Development and Evaluation of a Device for Optimum Quality Simultaneous Rheological and Morphological Characterisation of Complex Fluids

by

OURANIA GOUSETI

A thesis submitted to
The University of Birmingham
for the degree of

DOCTOR OF PHILOSOPHY

School of Chemical Engineering
The University of Birmingham
December 2011

ABSTRACT

With an increasing academic and industrial interest in complex, multiphase fluids, there is an associated interest in obtaining suitable methods for simultaneous characterisation of structure and rheology of such systems under flow. In the present work, development and evaluation of a prototype for optimum quality simultaneous rheological and morphological data acquisition has been considered. The work has been supported by Malvern Instruments, a leading company in laboratory and industrial instrumentation. The prototype was developed by combining optical geometries, designed and constructed during this project, with unique image acquisition unit and a standard rotational rheometer. Performance of the prototype has been extensively tested. First, accuracy of in house made geometries in rheological characterisation was found in very good agreement with standard geometries supplied by Malvern Instruments over a wide range of viscosities (0.01-10Pa s). Second, image acquisition was evaluated at high shears and for the first time reported images at shear rates as high as $20000s^{-1}$ have been acquired. Third, the potential of the new device in simultaneous rheo-structural measurements was demonstrated. Simultaneous rheology and structure of industrially relevant liquid / liquid systems was further investigated. Good agreement of rheological results was found with selected literature data and images of high quality were acquired. However, it has been difficult to compare combined rheology / morphology with literature as such data are not common in the literature yet. Development of the device as a marketable product was lastly considered and a complete experimental setup was suggested. Confirmation of the successful outcome of this work has been the recent filing of a provisional patent, approved under US regulations, and it is expected that a new instrument for optimum quality simultaneous rheo-structural measurements will be available in the market by Malvern Instruments in the near future.

To George, for his unconditional love and for his trust.

ACKNOWLEDGEMENTS

The present work would not have been realised without the invaluable support of Professor Andrzej Pacek, whose guidance throughout is gratefully acknowledged. Financial as well as technical support and guidance from Malvern Instruments is also thankfully acknowledged, many thanks in particular to Samiul, Fraser, Adrian and Darren. A great deal of thanks for their efficiency and timely help goes to the workshop team of chemical engineering, and especially to our dear Bob Sharpe, whose expertise and experience have significantly contributed in overcoming the numerous technical obstructions during those years. Phil Nelson is thankfully acknowledged for his unique contributions to the optical unit. Support from the administrative team of the department is also thankfully appreciated and I would be ungrateful if I didn't particularly thank Lynn Draper for providing help and sanity when necessary. Tom Eddelston is specially thanked for his support and advice in the lab.

I would like to thank Angel for supporting me when I so much needed it, for helping me with result analysis and thesis presentation and for being so special. I'm also very thankful to Adi for being a great lab companion and an exceptional scientist, ready to share his knowledge. I thank Marzena and Patricia for their very efficient support at a very difficult period. I will never forget the discussions and experiences I've had with Emily, my very special thanks goes to you for those. For their unique friendship during those years I would like to thank Isaac, Popi and Myrta, who are special for me. And Flora for her support those last months.

My final but definitely not least thanks goes to my family for their overall support throughout and for always being proud of me.

INDEX

LIST OF FIGURES

LIST OF TABLES

NOMENCLATURE

Latin characters

A	unit area. [m^2].
Ca	Capillary number.
Ca_{cr}^{eff}	effective critical Capillary number.
CC	coaxial cylinders geometry.
CP	cone/plate geometry.
d	distance. [m].
D	drop diameter; notations, wherever applicable, indicate the specific diameter as defined in the text. [m].
Def	deformation parameter.
f	force. [N].
G	rigidity modulus. [Pa].
Gl	glycerol.
h	sample height when loaded to the rheometer; notations, wherever applicable, indicate the specific sample height as defined in the text. [m].
HG	hexylene glycol.
H_S	hydration constant.
I	moment of inertia; notation, whenever applicable, indicates more details as explained in the text. [N m s^2].
J_{clamp}	compliance of the geometry's clamping system. [rad N^{-1} m^{-1}].
k, K	constants; notations, wherever applicable, indicate the specific constant as defined in the text or tables.
L_{maj}, L_{maj}	major and minor axis of the ellipsoid of a deformed drop under shear flow respectively (equation 2.17). [m].
n	power-law index.
n_i	number of drops with diameter equal to D_i.
PP	parallel plates geometry.
R	drop radius. [m].
Re_{pa}	particle's Reynolds number.
r	radius; notations, wherever applicable, indicate the specific radius as defined in the text. [m].
s	unit length. [m].
t	time. [s].
T	torque. [N m].
V	velocity. [m s^{-1}].
VPD	volume probability density. [m^{-1}].
W	water.

Greek characters

α	angular acceleration. [rad s^{-2}].
$\dot{\gamma}$	shear rate; notations, wherever applicable, indicate the specific shear rate as defined in the text. [s^{-1}].
δ	phase angle between the amplitudes of torque and displacement. [°].
ζ	deformation angle. [rad].
η	shear viscosity; notations, wherever applicable, indicate the specific shear viscosity as defined in the text. [Pa s].
$[\eta]$	intrinsic viscosity ($[\eta] = \lim_{\varphi \to 0} \frac{\eta - \eta_0}{\eta_0 \varphi}$).
θ	angular displacement. [rad].
Θ	temperature. [℃].
$\lambda = \eta_d / \eta_c$	viscosity ratio between dispersed and continuous phases.
$\mu_{friction}$	air bearing's friction coefficient. [N m s rad^{-1}].
ρ_C	density of continuous phase. [kg m^{-3}].
σ	stress. Pa.
τ	interfacial tension. [N m^{-1}].
φ	volume fraction of dispersed phase.
φ_m	maximum packing volume fraction where dispersed entities just touch each other.
χ	characteristic time. [s].
ω	angular velocity. [rad s^{-1}].

CHAPTER 1

INTRODUCTION

"Complex fluids" are a broad class of multiphase systems characterised by the presence of structures at the mesoscopic length scale, which is an intermediate between the molecular and the macroscopic length scales [Arratia 2011, Larson 1999, Gelbart & Ben-Shaul 1996]. The presence of mesoscopic structures provides the systems with unique characteristics and plays a significant role in determining the properties of the fluids, including rheology and structure.

The importance of rheological and morphological properties of complex fluids is well established in the literature [e.g. Arratia 2011, McCann et al 2011, Firoozmand 2009, Spyropoulos 2006, Jansseune et al 2003, Linden et al 2003; Yu et al 2002, Larson1999, Tadros 1994, etc] as well as in our everyday life, where for example, a mayonnaise that flows like a soup under gravity on a plate is rejected (by the consumer) as "too thin", while a toothpaste that is impossible to push out of the tube with gentle squeezing is rejected as "too thick".

Indeed, our perception of quality for many everyday products, such as food emulsions and gels, shampoos, hand creams, etc, is highly dependent on the link between rheology and structure. In the abovementioned mayonnaise, for example, which is essentially an emulsion of vegetable oil drops dispersed in a continuous aqueous phase (lemon or vinegar), the product should possess a certain yield stress, below which the product will not flow. The value of yield stress is known to greatly depend on the size of the oil drops and it has been reported that a good mayonnaise should contain oil drops of the order of $10\mu m$ [Larson 1999]. With the currently increasing trend in producing alternative foods, such as low and zero fat products, vegetarian substitutions of meat and cheap replacements of expensive foods such as synthetic caviar, it is also important to accurately control rheology and structure of the

substitute and, for a good quality alternative, to imitate the rheology and structure of the original food as close as possible.

Besides the food area, other examples of complex fluids where the mesoscopic structure plays an important role in determining quality, involve home and personal care products such as hand creams and body lotions, paints, inks, liquid crystals (present in many laptops and other flat panel screens), intermediates in the petroleum industry, bitumen, as well as vital biofluids such as blood [Larson 1999]. Indeed, blood can be considered as a suspension of $40\%\ vol/vol$ blood cells, which can be thought of as highly deformable discs with diameters of the order of $10\mu m$, in plasma [Larson 1999]. Blood cell aggregation is an important phenomenon, crucial in determining the rheological behaviour of blood, which in turn determines vascular flow and pressure. Understanding blood cell aggregation under shear is therefore significant for promoting health and it comes without surprise that simultaneous rheological and structural measurements have been employed in such investigations [e.g. Kaliviotis & Yanneskis 2007, Bransky et al 2006].

It is difficult to determine when the link between rheology and structure was first investigated systematically. Interestingly, among the first books on microscopy has been written by the same person who proposed the law of elasticity of ideal solids, Robert Hooke [Croft 1992]. The term "rheo-optics", however, is relatively new and has been ascribed to Professor R.S. Stein from the University of Massachusetts to generically describe the combination of electromagnetic radiation (optics) with rheological studies [Wilkes 1974].

Methods for characterising rheology and structure of (complex) fluids typically combine conventional rheological measurements with a suitable optical technique that gives information about the structure of the system under investigation. Depending on whether

optical recordings are simultaneous or follow rheological measurements, rheo-structural techniques can be categorized as direct and indirect, respectively. In indirect methodologies, rheological and morphological measurements are conducted separately and therefore no specifically designed instrumentation is required. However, the obvious advantage of direct methodologies is the real time nature of the measurements, which offers the potential for directly study the qualitative / quantitative link between rheology and structure.

In recent years, coupling of rotational rheometers with optical light microscopy has led to the development of devices for simultaneous rheological and microstructural measurements in individual laboratory scale as well as at commercial level by established companies such as Anton Paar, Thermo Fisher Scientific and Linkam Scientific [section 2.3.3 for more details]. Commercialisation of such instruments proves the significance of simultaneous rheological and optical microstructural measurements and their relevance to the industry as well as in research. However, reported images obtained with existing facilities are often of poor quality [see for example image 2.15], and, more importantly, reported images are typically imposed to shear rates of the order of $\dot{\gamma} < 100 s^{-1}$. There is no reported record in the open literature showing images at very high shear rates, which are relevant in many real industrial processes [Hall et al 2011; Utomo et al 2008].

For these reasons, Malvern Instruments has supported the present work aiming at the development and evaluation of a new rheo-structural apparatus with unique characteristics that will enable acquisition of optimum quality simultaneous rheological and morphological data at a wide range of shear rates, including very high shear rates of the order of $20000 s^{-1}$. Such a device requires adoption of novel approaches, especially in terms of image acquisition. Successful outcome of the present work is expected to be an important contribution in the

field of experimental studies of simultaneous rheology and structure of complex, multiphase fluids.

1.1 Objectives

The present project has aimed at the development and evaluation of a new device for simultaneous rheological and morphological recordings that ensures very high image quality without compromising accuracy in rheological characterisation, especially at high shear flow.

The main objectives set for this project are listed below:

(i) Design and construction of new hardware to combine with Malvern's standard rotational rheometer, unique image acquisition unit and existing software, for the development of a rheo-structural device for optimum quality simultaneous rheological and microstructural data acquisition. Such a device would ideally provide the operator with all the benefits of a standard rheometer coupled with the advantages of an imaging technique, without compromising the quality and accuracy of any of those two. Particular attention is given in obtaining high quality images at very high shear rates (up to the order of $20000s^{-1}$, set using the parallel plate geometry at very small gap size), which has never been reported before.

(ii) Evaluation of the new device in terms of accuracy in rheological measurements, clarity in image acquisition and simultaneous rheo-structural recordings. Extended applications, such as estimation of interfacial tension from direct rheo-structural observations, also to be considered.

(iii) Utilisation of the prototype to investigate simultaneously rheology and structure of selected two phase systems.

(iv) Examination of the potential of the newly developed rheo-structural device as a commercial product and suggestion of preliminary experimental setup that will incorporate all new features into a convenient design with improved marketability.

(v) Patent findings / parts of the present work if possible.

1.2 Layout of the Present Report

Work conducted during this project has been organised, and is presented, in six chapters. Chapter 2 introduces the relevant literature and it is divided into three sections. Section 2.1 reviews the basic principles of rheology for one phase system and further focuses on the effect of adding a second phase to the rheological properties of the system. This section also includes predictive viscosity models from the literature, which link system's viscosity with volume fraction of dispersed phase as well as with the viscosity ratio between dispersed and continuous phases, when relevant. Section 2.2 considers different possible microstructural configurations of two phase systems at quiescent conditions as well as under flow. From those configurations, focus is given predominately on morphologies consisting of drops dispersed in continuous phases. Deformation and breakage of a single, isolated drop immersed into an immiscible liquid under shear is discussed and the effect of increasing concentration of dispersed phase on microstructure is subsequently considered. Section 2.3 reviews different existing techniques for quantification of rheology and structure (separately) and further

presents reported instrumentation utilised for rheo-structural characterisation of investigated samples. A critical review of devices for simultaneous rheo-structural measurements where a rotational rheometer is combined with an optical light microscope is presented and main differences between existing, especially at a commercial level, facilities and the novel approach adopted at the present work are summarized.

Development of the new device is discussed in chapter 3. The overview of the developed experimental setup, including unique features of image acquisition unit, is schematically illustrated. Design and construction of new hardware is described in detail and photos of the newly developed device are shown. Existing image analysis software has been employed. This is discussed in detail elsewhere [e.g. Pacek et al 1994] and it is only briefly mentioned in this report.

In Chapter 4, evaluation of the newly developed device is considered. Accuracy in rheological measurements and quality of image acquisition are firstly tested separately and are presented in sections 4.2 and 4.3 respectively. Rheological response of all new measuring geometries, is assessed with one phase Newtonian liquids of known (by the supplier) viscosities, ranging between $0.1 - 1 Pa\ s$, and results are compared with values obtained with standard, stainless steel geometries. Quality of image acquisition is then tested at quiescence as well as under shear. Images of systems subjected to high shear rates (up to $20000 s^{-1}$) are shown. In section 4.4, examples of simultaneous rheological and microstructural recordings are considered and illustrate the potential of the device and the importance of simultaneous rheo-structural investigations. The potential of the device is further illustrated in section 4.5, where interfacial tension of an oil / aqueous system is estimated from direct rheo-structural observations (e.g. from the degree of deformation of an oil drop immersed into the aqueous

continuous phase at dilute systems and under controlled shear flow) and obtained results are compared with values obtained with the well established Wilhelmy plate tensiometer.

Chapter 5 further extends the evaluation of the newly developed device to include systematic investigation of rheology and structure of selected two phase systems. Such systems are important at both an industrial and a fundamental level, as they form the simplest model and the basis of many complex fluids. Investigated example systems cover all combinations of hydrophobic ("oil") and hydrophilic ("aqueous") phases. The effect of viscosity ratio between dispersed and continuous phases and of volume fraction of dispersed phase on rheology and structure of oil / aqueous systems is considered in section 5.2. Section 5.3 discusses the validity of implementing models developed for oil / aqueous dispersions to aqueous / oil systems, and it is indicated that such practice might not be entirely justified. Section 5.4 presents rheological and microstructural results obtained for oil / oil systems, while in section 5.5, considers the effect of shearing on the gel structure of an aqueous / aqueous system that gels on cooling.

Chapter 6 focuses on improving the newly developed device and considers its potential as a commercial, marketable product. At first, design and realization of a compact version where extension tubes are, for the first time in the context of rheo-structural experiments, utilised in the place of the large, bulky microscope is discussed. Finally, an experimental setup is suggested, where work and knowledge accumulated during the present project are combined with a standard rotational rhoemeter into a one piece instrument for simultaneous rheological and morphological measurements of optimum quality. In this setup, Malvern Instruments' latest rheometer, Kinexus, is used as a template. Key features of the proposed design are discussed.

Main conclusions from, and major outcomes of, the present study are summarised in chapter 7. Conclusions are sectionalized similarly as the chapters of this report. This final chapter concludes with some thoughts and suggestions for future work that are expected to improve the performance and / or commercial value of the developed device, thus extending the contribution of the present work.

1.3 Public Presentations and Additional Information

- Part of the findings of this project has been presented at the non-Newtonian Club meeting held at the University of Birmingham, 21 October 2008.

- Part of the findings of this project has been presented (as poster) at the British Society of Rheology Midwinter meeting held at the University of Leeds, 15-16 December 2008.

- Part of this project has been presented at the European Cooperation in Science and Technology (COST) and Food Structure design's working group meeting on "Food structure engineering and healthy functions: experimental approaches", 29-30 November 2011. This is considered as the first public presentation of the newly developed device. Proceedings of the meeting to be published in the web.

- Part of the project has been successfully filed for a patent under U.S. regulations (see appendix).

CHAPTER 2

LITERATURE REVIEW

2.1 Introduction

The main objective of the present work, as set in the previous chapter, has centred in the development and evaluation of a device for superior quality simultaneous rheological and microstructural data acquisition, especially at high shear rates. Such flow conditions are relevant to the industry, as they mimic the shear rates in processing apparatuses. It is relevant, therefore, that this chapter reviews literature about rheology, primarily in terms of shear viscosity, morphology, obtained by means of optical imaging, and experimental techniques for rheological and microstructural measurements.

The three aspects are addressed separately below. Thus, basic principles of rheology are discussed in the first section, where the fundamentals of rheology as a macroscopic property of systems considered as single phases are presented first. The effect of adding a second phase on system's rheology is then discussed. Discussion also includes a number of proposed model viscosity equations found in the literature, which correlate the relative viscosity (i.e. system's viscosity divided by the viscosity of continuous phase) of two phase systems with volume fraction of dispersed phase and, where relevant, with the viscosity ratio between dispersed and continuous phases.

Definitions and general features of microstructure and microstructural evolution in two-phase systems under shear are introduced in section 2.3. Here, the behaviour under shear of a single drop immersed in a continuous phase is considered first, followed by discussion on the effect of increasing volume fraction of dispersed phase on morphological properties of two phase systems.

Finally, in section 2.4, existing experimental techniques and instrumentation for quantification of rheology and morphology are revised separately. This section also includes a

critical review of recent advances on instrumentation for simultaneous rheological and structural measurements both at laboratory (in-house) and commercial level. Finally, major differences between existing devices and novel approaches adopted in this work are summarised.

2.2 Rheology

The term ‘rheology’, originating from the Greek work ‘rheo’ which implies flow, was introduced by Professor E.C. Bingham and his associates and they defined it as ‘the study of deformation and flow of matter’ [Barnes et al 1989]. The term was first accepted in 1929, when the American Society of Rheology was founded [Barnes et al 1989]. In its strictest sense, deformation pertains to solids and flow to liquids.

Today, rheology is widely acknowledged as an important property for many consumer products, including paints, inks, cosmetics, foods, pharmaceutical and agrochemical formulations, liquid detergents, etc, and it is generally recognised among the top determining factors of texture, quality and value [Tanner 2002]. For example, a good paint is expected to flow under shear as it is applied on a wall with a brush, but should resist flow under gravity once the application is completed, so as to prevent the paint from dripping; toothpaste should hold its shape when at rest in its tube but should flow easily when squeezed out of the tube, and many more.

Knowledge of rheology has also been identified as an integral part of product and process design as well as optimisation of industrial operation. Rheology is important, for example, in new product design, selection of processing equipment and operating conditions,

effect of length and time scales (scale up, scale down, time of processing), material handling, shelf life, mixing, transportation and storage [Pal 2001].

Although the term was introduced less than 100 years ago, the study of rheology has clearly preceded the invention of the name. The first references to a quantitative link between applied force and resulting deformation have been accredited to Robert Hooke and Isaac Newton [Tanner 2002]. In 1678 Robert Hook introduced his hypothesis on deformation of solids in his "True theory of Elasticity" and described that "the power of any spring is in the same proportion with the tension thereof" (i.e. deformation is proportional to exerted force); almost concurrently, in 1687, Isaac Newton proposed the hypothesis on flow of liquids in his "Principia", as "the resistance which arises from the lack of slipperiness of the parts of the liquid, other things being equal, is proportional to the velocity with which the parts of the liquid are separated from one another" [Barnes et al 1989]. Those two laws describe the behaviour of ideal materials and can be considered as the ancestors of modern rheology.

The behaviour of a material under shear forces (i.e. forces acting tangential on the surface of a material) is of great importance in rheological characterization. Shear deformation is the main type of deformation exerted on many everyday habits, such as swallowing of foods or application of a hand cream. In addition, shear flow is important in a number of process operations, such as mixing of raw ingredients or transportation of a product through a pipe. Shear deformation is also the type of deformation induced by rotational rheometers, perhaps the most common type of rheometers used in both industry and research (also employed in the present work), and it will be considered in some detail below. The other simple type of deformation, namely dilatational or elongational deformation, is caused by

forces acting perpendicular to the surface of the material and results in extension, but it will not be further discussed in detail in this review.

The response of a Hookean solid and a Newtonian liquid under shear forces is illustrated in figure 2.1, where shear stress σ (in $N\,m^{-2}$) is defined as the force f acting tangential to the surface A per unit area A and results in shear strain γ (equation 2.1). For the ideal, Hookean solid, σ is proportional to γ and the proportionality constant G is referred to as 'rigidity' (equation 2.2). For the ideal, Newtonian liquid σ is proportional to the velocity gradient, V/d (or rate of shear $\dot{\gamma}$, also often referred to simply as 'shear', although this is not considered accurate and will be avoided here) and the proportionality constant η is termed shear viscosity (equation 2.3). The angle ζ refers to the deformation angle of the solid block, as shown in figure 2.1.

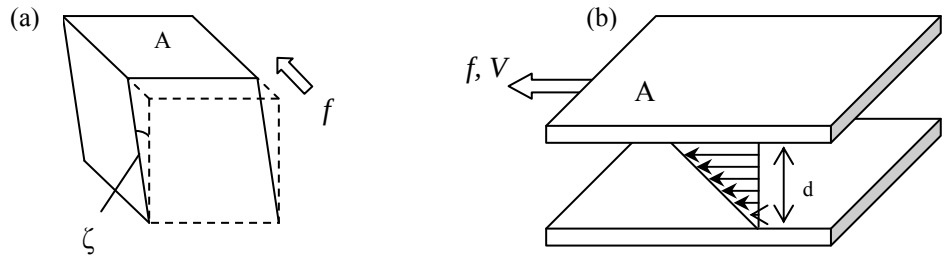

Figure 2.1: Effect of shearing on (a) Hookean solid; (b) Newtonian liquid [adapted after Dickinson 1992, Barnes et al 1989].

$$\sigma = f/A \tag{2.1}$$

Hookean solid: $\sigma = G(tan\zeta)$, $tan\zeta \cong \zeta$ if $\zeta < 0.1rad$ (2.2)

Newtonian liquid: $\sigma = \eta\dot{\gamma}, \dot{\gamma} = V/d$ (2.3)

The case of figure 2.1 is a rather simple picture, where only one stress component is considered. In fact, stress is a second order tensor, as it is illustrated in figure 2.2. Figure 2.2 shows a cubic, isotropic and structurally homogeneous volume element with edges parallel to the x, y and z axes of a three dimensional Cartesian coordinate system. This element is small enough for stress components to be regarded as constant throughout each surface and has identical properties in all surfaces. Stress components, σ_{ij}, acting on the element's surfaces from the external, surrounding environment are also illustrated in figure 2.2 [adapted from Sherman 1970 and Larson 1999]. In this notation, the first index, i, indicates the orientation of the surface's plane and the second, j, the direction of the stress. Stress is acting on all six surfaces, but stress components of opposite surfaces of the dm element are identical (although with different sign). The "state-of-stress" tensor is then given by equation 2.4 [Larson 1999].

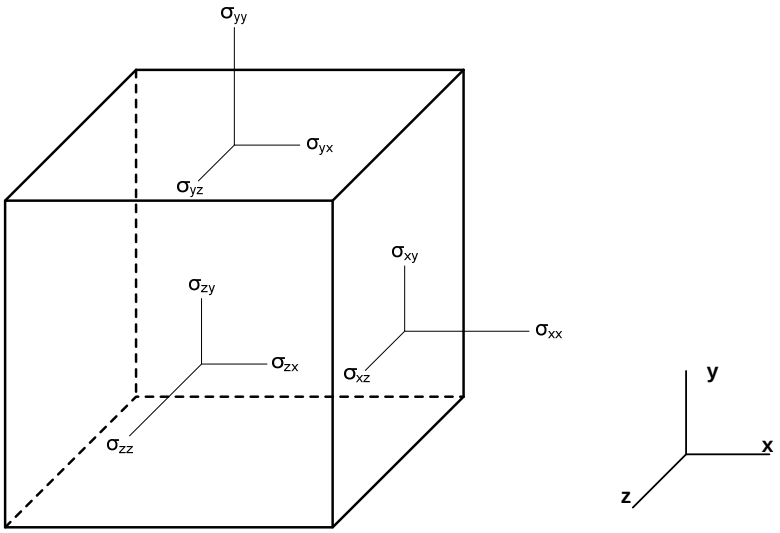

Figure 2.2: Stress components acting of the faces of a homogeneous and isotropic volume element of cubic shape [adapted after Sherman 1970, Larson 1999].

In equation 2.4, the components σ_{xx}, σ_{yy}, and σ_{zz} are the "normal" stresses, while σ_{xy}; σ_{xz}, etc are the "shear" stresses. For isotropic materials (i.e. those whose properties at rest are independent on the direction), it can be shown that $\sigma_{xy} = \sigma_{yx}$, $\sigma_{xz} = \sigma_{zx}$, and $\sigma_{yz} = \sigma_{zy}$ [Barnes et al 1989, Larson 1999]. For the simple shear flow of figure 2.1, there are at least two non-zero stress components, $\sigma_{xy} = \sigma_{yx}$, which in the case of Newtonian liquids are the only non-zero stress components and are expressed by equation 2.3. In the case of non-Newtonian liquids, however, the normal stresses are also non-zero. Due to the fact that the stress tensor is determined within an added isotropic pressure, it is common to express normal stresses in terms of normal stress differences, N_1 and N_2: $N_1 = \sigma_{xx} - \sigma_{yy}$, and $N_1 = \sigma_{yy} - \sigma_{zz}$.

$$State\ of\ stress\ tensor = \begin{pmatrix} \sigma_{xx} & \sigma_{xy} & \sigma_{xz} \\ \sigma_{yx} & \sigma_{yy} & \sigma_{yz} \\ \sigma_{zx} & \sigma_{zy} & \sigma_{zz} \end{pmatrix} \tag{2.4}$$

Velocity gradient is also a tensor, given by equation 2.5 [Larson 1999]. In simple shear, the only non zero component of the velocity gradient is the term $\frac{\partial v_x}{\partial s_y}$, which has been defined earlier as shear rate in equation 2.3. As the present work has been conducted using rotational rheometers, the following discussion is confined to the simple shear flow situation of figure 2.1.

$$\nabla V = \begin{pmatrix} \frac{\partial v_x}{\partial s_x} & \frac{\partial v_y}{\partial s_x} & \frac{\partial v_z}{\partial s_x} \\ \frac{\partial v_x}{\partial s_y} & \frac{\partial v_y}{\partial s_y} & \frac{\partial v_z}{\partial s_y} \\ \frac{\partial v_x}{\partial s_z} & \frac{\partial v_y}{\partial s_z} & \frac{\partial v_z}{\partial s_z} \end{pmatrix} \tag{2.5}$$

The laminar, simple shear flow of figure 2.1.b is often employed by rheometers for measuring shear viscosity, and is sometimes referred to as ‘viscometric flow’ [Barnes et al 1989]. Viscosity (or ‘apparent viscosity’) is an intrinsic parameter of the fluid that measures its resistance to flow. For Newtonian liquids measured at constant temperature and pressure, shear viscosity does not vary with shear rate and it is independent of shear history. However, for the majority of materials, viscosity is not a coefficient but rather a function of shear rates, $\eta(\dot{\gamma})$ and / or time $\eta(\dot{\gamma}, t)$. Materials whose viscosity decreases on increasing of shear rate are

called shear thinning (or pseudoplastic), whereas for those with increasing viscosity on increasing of shear rate, the term 'shear thickening' (or dilatant) is typically used. Figure 2.3 shows the characteristic relationship between shear stress and shear rate for shear-thinning, Newtonian and shear-thickening materials. Materials with yield stress (excluded from the graph) have zero $\dot{\gamma}$ until a certain value of σ (the so called yield stress) is reached.

For shear thinning materials, the typical flow curve showing viscosity as a function of shear rate is illustrated in figure 2.4 [Barnes et al 1989]. In the limits of very low and very high shear rate regions, viscosities of the material are η_0 and η_∞ respectively (the subscript referring to shear rate). Between those limits, viscosity decreases monotonically with shear rate.

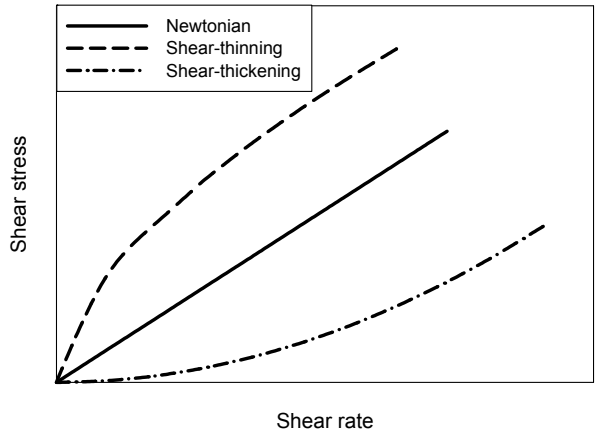

Figure 2.3: Flow curve for Newtonian, shear thinning and shear thickening material showing the relationship between shear stress and shear rate [Barnes et al 1989].

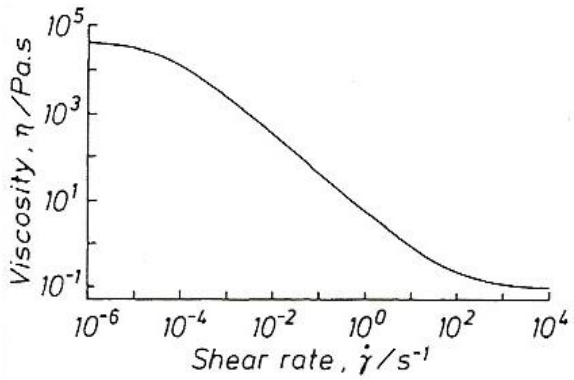

Figure 2.4: Flow curve of shear thinning material [Barnes et al 1989].

Equations that predict the shape of a material's flow curve typically require four parameters [Barnes et al 1989]. One such model is the Cross model of equation 2.6, where K_c is the Cross constant, with dimension of time, and n is the power law index, which is dimensionless. At the region where $\eta \ll \eta_0$ and $\eta \gg \eta_\infty$, equation 2.6 reduces to the popular power law model, given by equation 2.7. Power law index n is a measure of whether the material is shear thinning $(n < 1)$, Newtonian $(n = 1)$ or shear thickening $(n > 1)$. The power law constant, K_{PL}, has the strange dimensions of $Pa\ s^n$. It is important to note that the power law model is valid for the range between the limits of very low and very high shear rates. When used at the extremes of very low or very high shear rates (i.e. close to the limits of η_0 and η_∞) it might lead to questionable conclusions [Barnes et al 1989].

$$\frac{\eta-\eta_\infty}{\eta_0-\eta_\infty} = \frac{1}{1+(K_c\dot{\gamma})^n} \Leftrightarrow \frac{\eta_0-\eta}{\eta-\eta_\infty} = (K_c\dot{\gamma})^n \qquad \text{Cross model} \quad (2.6)$$

$$\eta = K_{PL}\dot{\gamma}^{n-1} \qquad \text{Power-law model} \quad (2.7)$$

Introduction of a second phase into the system may profoundly affect its rheological behaviour. Confining to liquid continuous phases, dispersed phases are typically in the form of solid rigid particles, liquid drops or air bubbles. The fraction of volume occupied by the dispersed phase determines the volume fraction of dispersed phase, φ. For liquid dispersed phases, viscosity ratio λ, defined as the ratio between viscosities of dispersed over continuous phases (equation 2.8), is frequently used as a parameter for the description of the system's rheology.

$$\lambda = \frac{\eta_d}{\eta_c} \tag{2.8}$$

Predicting the viscosity of two phase systems has received considerable attention in the literature due to its relevance in industrial applications as well as its importance in academic research. A selection of suggested viscosity models found in the literature is presented here, a number of which are summarised in table 2.1 (with references). The majority of suggested models presented in this section have empirical or semi empirical character, and have been developed within specific range of experimental conditions.

Table 2.1 is divided into two sections. The first section presents models developed for suspensions of solid particles in liquid continuous phases. All suspension models shown in table 2.1 have been derived assuming spherically shaped, rigid particles. In those models, relative viscosity η_r, defined as the viscosity of the system divided by viscosity of pure continuous phase, is correlated with the volume fraction of dispersed phase, φ. The second part of table 2.1 presents viscosity model equations developed for liquid / liquid dispersions. Here, relative viscosity is correlated with φ, as well as with the viscosity ratio between

dispersed and continuous phases, λ. Other models, which take into account other dimensionless numbers such as the dispersed entity's Reynolds number or the Capillary number, defined later in this chapter, are excluded from table 2.1 and are presented separately. In table 2.1 it has been attempted to follow a chronological order when possible.

Einstein's equation, introduced in 1906, was the first viscosity model to be widely known [Tadros 1994]. It has been theoretically obtained in the limit of infinitely dilute suspensions of spherically shaped, mono dispersed, non interacting rigid particles in liquid continuous phases. Rigid particles can be thought of as having infinite viscosities. At increasing volume fraction of dispersed phase, a more complex relationship between η_r and φ occurs, as interactions between particles can no longer be neglected. To account for this, an extended, power law version of Einstein's model has been used [from Khodakov 2004].

In 1917, Arrhenius proposed a logarithmic relationship between η_r and φ for solid / liquid suspensions of poly dispersed rigid particles. His model served as a starting point for the development of other logarithmic models, such as those of Richardson in 1933 [Pal 1992] and Broughton & Squires [1938]. Formulas later developed by Mooney [1951], Roscoe and Brinkman [Roscoe 1952], and Krieger & Dougherty [1959] were developed for suspensions of poly dispersed particles in liquid continuous phases over a range of φ (i.e. systems with finite φ). From those models, a particularly interesting approach has been proposed by Roscoe and Binkman. In their differential scheme, they have assumed that a concentrated system is formed by successive additions of infinitesimal small amounts of dispersed phase.

In 1967, Frankel and Acrivos proposed a model for very concentrated suspensions, where volume fraction of dispersed phase is of the order of the maximum packing volume

fraction, φ_m ($\varphi/\varphi_m \cong 1$). Few years later, in 1973, Barnea and Mizrahi suggested their own viscosity model for suspensions of finite volume fraction of dispersed phase [Pal 1992].

Maximum packing volume fraction of dispersed phase, which appears in the models of Krieger & Dougherty and Frankel & Akrivos, refers to the volume fraction where dispersed entities just touch each other. For mono dispersed systems of spherical particles the value of 0.74 is generally accepted and demonstrable as hexagonal close packing, whereas in the case of poly dispersed systems guidance for calculations can be found in the literature [for example Pal 1998 or Krynke & Sek 2004].

Equations developed for solid / liquid suspensions are often employed in the literature for liquid / liquid systems, where liquid drops are dispersed in liquid continuous phases [Pal 2001]. However, there are two main differences to consider when discussing liquid drops instead of rigid particles under shear: the first refers to their deformability, and the second to their non infinite viscosity. As a result, when subjected to shear flow, liquid dispersed phases deform, may orientate favourably to the direction of the flow and dispersed drops may also break or coalesce. Such changes may significantly affect the rheological, microstructural and textural characteristics of the system, indicating the importance of simultaneous rheological and microstructural measurements.

Predictive viscosity models derived for systems of two immiscible liquids, shown in the second part of table 2.1, typically correlate η_r with φ and λ. The earliest such model considered in table 2.1 is that of Hatscheck for dilute emulsions, introduced in 1911 [Sefton 2010]. In 1930, Sibree extended Hatscheck's model to account for higher concentrations of dispersed phases. Both models assume that the system's viscosity is independent of the viscosity of dispersed phase; hence the parameter λ is omitted. Although this may be true on

some occasions, it is an overall limiting factor. Taylor was the first to publish in 1932 a viscosity equation for liquid / liquid systems, where the viscosity of the dispersed phase is incorporated. Taylor's famous model assumes very dilute emulsions (non interacting drops) of slightly deformed Newtonian drops in Newtonian continuous phases. In 1941, Eilers proposed a viscosity correlation, which contains the empirical constant K_{ES} and has been developed to cover a wide range of dispersed phase concentrations. At the same year, 1941, Glasstone suggested a logarithmic relationship between relative viscosity and volume fraction of dispersed phase.

In 1972 and 1975, two models were proposed independently, by Yaron & Gal-Or and Choi & Schowalter, respectively, based on the cell theory. According to this theory, the dispersion is divided into identical individual cells of specific dimensions, composition and properties, and the suitable boundary conditions are then applied to the outer boundaries of the cells [Sherwood 2006]. For derivation of their model, Choi & Schowalter also assumed equal densities of the two phases, mono dispersed drops uniformly dispersed within the cells, and absence of surfactants.

The model proposed by Van Oene in 1978 was developed for phase separated polymer blends [Spyropoulos 2007]. It is interesting to note that together with Glasstone's model, it has been successfully employed to analyse the rheological response of aqueous / aqueous systems that deviate from the typical morphology of dispersed drops into a continuous phase and show other arrangements, such as string type formations [Jeon and Hobbie 2001, Spyropoulos et al 2007]. Some years later, in 1989, Pal & Rhodes introduced their equation developed for emulsions of non-Newtonian liquids.

Derivation of the models proposed by Phan-Thien & Pham (in 1997) and Pal (model 1 and model 2, in 2001) was based on a similar approach as the differential scheme of Roscoe and Birnkam, which assumes that a concentrated system is formed by successive additions of infinitesimal small amounts of dispersed phase (see above). According to this concept, the dispersed entities of every new step addition j 'feel' an effective continuous phase which consists of pure continuous phase plus the volume of dispersed phase added up to the previous step $(j-1)$. For their model, Phan-Thien & Pham also indicated that dispersed entities of increasing size are to be added in each consecutive step.

Pal [2001] has evaluated selected models of table 2.1 for emulsions over a wide range of viscosity ratios and volume fractions at small drop deformations. He reported that the model proposed by Choi / Schowalter over-predicted relative viscosities while the model of Phan-Thien / Pham gave good predictions only at low φ and under-predictions at high φ. He concluded that the model of Yaron / Gal-Or best agreed with a vast number of experimental data.

Table 2.1: Predictive viscosity models for two phase systems, including year it was suggested and reference (if not the original publication).

SOLID / LIQUID SYSTEMS

Author, year suggested & Reference	**Model equation**	**Author, year suggested & Reference**	**Model equation**
Einstein, 1906. [from Tadros 1994]	$\eta_r = 1 + 2.5\varphi$	Expanded Einstein [from Khodakov 2004]	$\eta_r = K_{E1} + K_{E2}\varphi + K_{E3}\varphi^2 + \cdots$ K_{E1}, K_{E2}, K_{E3}: constants
Arrhenius [1917]	$\eta_r = exp(2.5\varphi)$	Richardson, 1933 [from Pal et al 1992]	$ln(\eta_r) = K_R\varphi$ K_R: constant
Broughton and Squires [1938]	$ln(\eta_r) = K_{BS1}\varphi + K_{BS2}$ (K_{BS1} and K_{BS2}: constants)	Roscoe and Brinkman [Roscoe 1952]	$\eta_r = \frac{1}{(1-\varphi)^{2.5}}$
Mooney [1951]	$\eta_r = exp\left(\frac{2.5\varphi}{1 - K_M\varphi}\right)$ K_M: constant	Kreiger and Dougherty [1959]	$\eta_r = \frac{1}{[1-(\varphi/\varphi_m)]^{[\eta]\varphi_m}}$ [η]: intrinsic viscosity (equals 2.5 for rigid spheres) φ_m: maximum packing volume fraction
Frankel and Acrivos [1967]	$\eta_r = \frac{(9/8)(\varphi/\varphi_m)}{1-(\varphi/\varphi_m)^{1/3}}$	Barnea and Mizrahi, 1973 [from Pal et al 1992]	$\eta_r = exp\left(\frac{2.66\varphi}{1-\varphi}\right)$

LIQUID / LIQUID SYSTEMS

Hatschek [Sibree 1930]	$\eta_r = \frac{1}{1-\varphi^{1/3}}$	Sibree [1930]	$\eta_r = \frac{1}{1-(H_S\varphi)^{2.5}}$ (H_s: hydration constatnt)
Taylor [1932]	$\eta_r = 1 + 2.5\varphi\frac{\lambda+0.4}{\lambda+1}$	Eilers, 1941 [from Sefton et al 2010]	$\eta_r = \left(1+\frac{1.25\varphi}{1-K_{ES}\varphi}\right)^2$ (K_{ES}: constant)
Glasstone, 1941 [from Spyropoulos et al 2007]	$log(\eta) = \varphi_1 log(\eta_1) + \varphi_2 log(\eta_2)$ φ_i: volume fraction of liquid i of viscosity η_i	Yaron and Gal-Or, 1972 [Pal 2000]	$\eta_r = 1 + \frac{5.5\left[4\varphi^{7/3}+10-\left(\frac{84}{11}\right)\varphi^{2/3}+\left(\frac{4}{\lambda}\right)\left(1-\varphi^{7/3}\right)\right]}{10\left(1-\varphi^{10/3}\right)-25\varphi\left(1-\varphi^{4/3}\right)+\left(\frac{10}{\lambda}\right)(1-\varphi)\left(1-\varphi^{7/3}\right)}$
Choi-Schowalter , [1975]	$\eta_r = 1 + \varphi\frac{5\lambda+2}{2(\lambda+1)} + \varphi^2\frac{5(5\lambda+2)^2}{8(\lambda+1)^2} + \cdots$	Van Oene, 1978 [from Spyropoulos et al 2007]	$\eta_r = \left[1+\varphi\left(\frac{1}{\lambda}-1\right)\right]^{-1}$
Pal and Rhodes [1989]	$\eta_r = \left[1+\frac{(\varphi/\varphi^*)}{1.187-(\varphi/\varphi^*)}\right]^{2.49}$ φ^*: φ at which $\eta_r = 100$	Phan-Thien and Pham [1997]	$(\eta_r)^{2/5}\left(\frac{2\eta_r+5\lambda}{2+5\lambda}\right)^{3/5} = (1-\varphi)^{-1}$
Pal [2001] model 1	$\eta_r\left(\frac{2\eta_r+5\lambda}{2+5\lambda}\right)^{3/2} = exp\left[\frac{2.5\varphi}{1-(\varphi/\varphi_m)}\right]$	Pal [2001] model 2	$\eta_r\left(\frac{2\eta_r+5\lambda}{2+5\lambda}\right)^{3/2} = \left(1-\frac{\varphi}{\varphi_m}\right)^{-2.5\varphi_m}$

The list of viscosity models presented in table 2.1 is by no means exhaustive. Besides volume fraction of dispersed phase and viscosities of dispersed and continuous phases, viscosity of liquid / liquid systems is also known to depend on a number of other factors, such as temperature, average drop size and size distribution, densities of dispersed and continuous phases, nature and concentration of emulsifying agents (if present), presence of other entities such as solid particles in the dispersion, shear rate (for non-Newtonian systems), etc [Pal 2006, Krynke & Sek 2004, Johnsen & Ronningsen 2003, Pal 1998]. However, most of the suggested models are system and condition specific, and require determination of empirical constants. Indicatively, the model of Johnsen & Rooningsen [2003], which accounts for the effect of temperature on relative viscosity, contains four empirical constants (equation 2.9). It has been found in good agreement with results for water in crude oil dispersions at $50 - 70°C$ [Johnsen & Rooningsen 2003] as well as water in bitumen emulsions at temperatures $70 - 90°C$ [Sefton & Sinton 2010].

$$ln(\eta_r) = K_{JR1} + K_{JR2}T + K_{JR3}\varphi + K_{JR4}T\varphi \tag{2.9}$$

Predictive models where viscosity of liquid / liquid systems is correlated with morphological properties of the system, such as drop size, drop size distribution, deformation, or orientation of drops to the flow, are not common in the literature. One such example has been proposed by Pal [1998] and another later by Krynke & Sek [2004]. Those researchers have proposed viscosity models that correlate η_r with particle's Reynolds number, which they defined as $Re_P = \frac{\rho_c \dot{\gamma} R^2}{\eta_c}$. The general form of the two models is of the form of equation 2.10,

where Pal uses $\xi = [\eta]$ and Krynke & Sek define the constant as $\xi = -1.145 + 4.542\varphi$ [Pal 1998, Krykne & Sek 2004].

$$\varphi_m^{0.5}\left(1-\eta_r^{-1/\xi/\varphi_m}\right) = K_{KS4} + K_{KS5}log(Re_P) + K_{KS6}[log(Re_P)]^2 \tag{2.10}$$

Notably, Yu et al [2002] have developed a model for the dual, quantitative link between rheological and morphological parameters for mixtures of Newtonian fluids and morphologies of ellipsoidal drops dispersed in continuous phases. For simple shear flow they predicted shear-thinning behaviour at large shear rates. According to their model (equation 2.11) viscosity is a function, among others, of the Capillary number, Ca, which depends on drop size (full definition in the next section, equation 2.15). Correlation between viscosity and Capillary number permits (i) prediction of shear thinning and (ii) determination of drop size by knowledge of rheological data. Constants f_1, f_2, K_Y and characteristic time χ are calculated from equations 2.12 and 2.13. Substitution of f_1, f_2, K_Y and χ from equations 2.12 and 2.13 to equation 2.11 gives equation 2.14. A similar equation as 2.14 has also been proposed by Pal [2007] for dispersions of slightly deformed liquid droplets.

$$\eta = \frac{2\lambda+3+3(\lambda-1)\varphi}{2\lambda+3-2(\lambda-1)\varphi}\eta_c + \frac{10K_Y\chi f_1 f_2^2}{3[2\lambda+3-2(\lambda-1)\varphi](Ca^2+f_1^2)} \tag{2.11}$$

$$f_1 = \frac{40(\lambda+1)}{(2\lambda+3)(19\lambda+16)}, f_2 = \frac{5}{2\lambda+3}, K_Y = \frac{6\tau}{5R}\frac{(\lambda+1)(2\lambda+3)\varphi}{5(\lambda+1)-(5\lambda+2)\varphi} \tag{2.12}$$

$$\chi = \frac{\eta_c R}{\tau} \tag{2.13}$$

$$\eta_r = 1 + \varphi\left[\frac{5(\lambda-1)}{2\lambda+3} + \frac{5}{2\lambda+3}\frac{160(\lambda+1)(19\lambda+16)}{1600(\lambda+1)^2 + (19\lambda+16)^2(2\lambda+3)^2 Ca^2}\right] \quad (2.14)$$

From the above discussion it is evident that although many viscosity models correlating system's viscosity with volume fraction of dispersed phase and, when relevant, with viscosity ratio between dispersed and continuous phases, have been suggested in the literature, a quantitative link between rheology and morphology is yet to be understood. There are only few models where drop size is part of the equation, but there is a complete lack of models featuring other morphological parameters, such as drop deformation and orientation angle to the direction of the flow. To study the link between rheology and structure, and validate developed models, experimental data acquisition is important. The requirement for optimum quality simultaneous rheological and morphological measurements is therefore demonstrated.

2.3 Morphology

Morphology (from the Greek work 'morphi' which indicates shape) refers to the study of the (micro) structure of a material. It is an important parameter of matter and, linked with rheology, often crucial for characterisation of the sensory features, texture, process-ability and quality of a product. It is determined by material properties and processing parameters and it affects the rheological, optical, and transport properties of the system [Tucker and Moldenaers 2002, Mours et al 2003]. Although structure often plays a critical role in product quality and failure to successfully control morphology may result in poorly textured products, the topic has received relatively little attention in the open literature [Puyvelde et al 2003].

Typically, morphologies expected on blending of oil substances with aqueous phases as well as on mixing of a number of immiscible polymeric materials involve drops dispersed in continuous phases [Verhulst et al 2009, Huitric et al 2009]. However, other morphologies have also been reported. For example, aqueous two phase systems have been reported to exhibit structures that vary from simple drop type microstructures to multiple dispersions and steady string like arrangements, depending on their composition and flow conditions [Spyropoulos 2007]. By 'steady' it is meant here that those structures are stable under shear flow and distinct from transient elongational configurations occurring in sheared systems that lead to destabilisation and drop breakage. Examples of different microstructures for systems at rest are shown in figure 2.5.

Confining the following discussion to morphologies consisting of drops dispersed in continuous phases, the structural development of a single, Newtonian, liquid drop under shear flow is presented in the next section. The effect of increasing concentration of dispersed phase is subsequently briefly discussed in section 2.3.3.

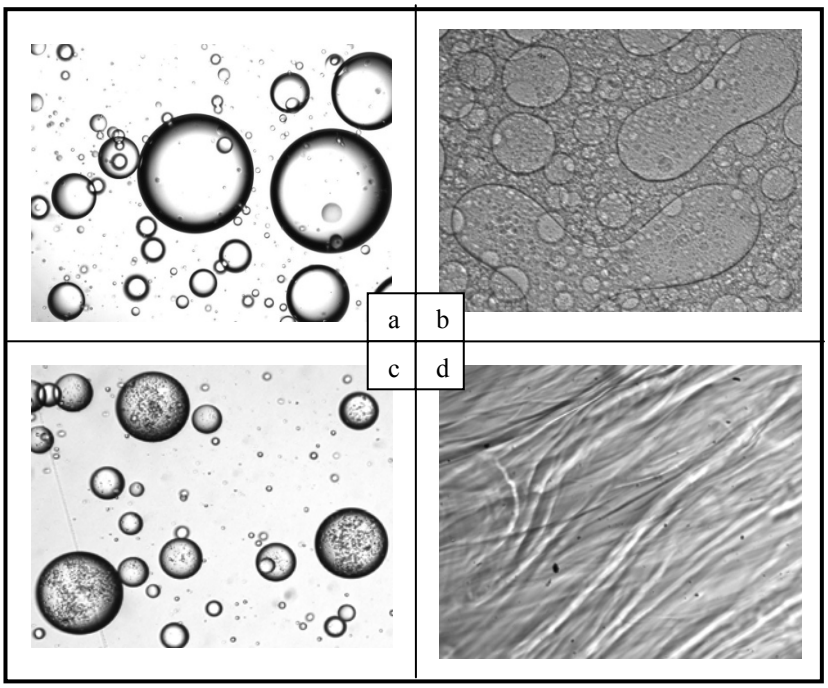

Figure 2.5: Examples of different microstructures at quiescence: (a) oil drops dispersed in aqueous continuous phase; (b) aqueous drops dispersed in aqueous phase; (c) double aqueous / oil / aqueous emulsion; (d) strings of aqueous / aqueous systems. [Images obtained with in house equipment developed during this project]. Image width $2.4mm$ except in (a), where it is $1.2mm$. Various geometries used.

2.3.1 Single Drop Under Simple Shear Flow

The shape of a single drop immersed to another fluid is determined by the forces acting upon and within it. At quiescent conditions and in the absence of other forces such as gravity it will assume a spherical shape, as dictated by the interfacial tension between the drop and its surroundings. When subjected to shear, the drop will deform as a result of the change in local stresses acting on it. Sheared drops in deformation studies are usually assumed to develop into symmetrical shapes, which in general is in good agreement with experimental observations [Jansseune et al 2000].

Deformation and breakage of a single drop immersed in a continuous phase and subjected to shear flow are governed by the balance between viscosity-driven deforming

stresses and the counteractive Laplace pressure-driven restoring stresses [Williams et al 1997, Janssen et al 1994]. The resulting dimensionless Capillary number is defined in equation 2.15. Interfacial tension τ is the force acting at a right angle to a line of unit length at the interface (tangential).

$$Ca = \frac{Viscous\ Stresses}{Laplace\ Pressure\ Stresses} = \frac{\eta_c \dot{\gamma} R}{\tau} \tag{2.15}$$

The type of shear deformation and breakage is determined by Ca as well as by viscosity ratio between dispersed and continuous phases λ. The critical Capillary number (Ca_{cr}) provides by definition a numerical barrier above which the drop becomes unstable and breaks. Grace curve (figure 2.6, adapted after Jansen et al 2000) is an experimentally obtained graph that correlates the critical capillary number with λ for initially spherical drops subjected to gradually increasing shear rate. Later attempts to fit the Curve into an equation include that of de Bruijn [Tucker et al 2002] given by equation 2.16, which is also shown in figure 2.6. Grace Curve suggests that drops subjected to simple shear flow break easier in the environment between $0.1 < \lambda < 1$ and that for viscosity ratios between dispersed and continuous phases above approximately 4, shearing does not result in drop breakage.

$$log Ca_{cr} = -0.506 - 0.0995 log\lambda + 0.124 (log\lambda)^2 - \frac{0.115}{log\lambda - log 4.08} \tag{2.16}$$

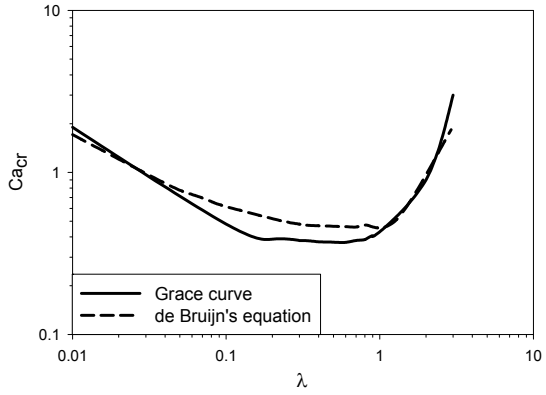

Figure 2.6: Grace curve and de Bruijn's fitting equation

Lin and Guo [2007] have studied experimentally the deformation and breakage of a single, Newtonian drop immersed in a Newtonian phase. They reported three distinctive mechanisms of drop breakage (figure 2.7), depending on the imposed capillary number. They observed that drops subjected to capillary numbers just above their Ca_{cr} broke via necking mechanism, which results in two practically equisized daughter drops and few satellites (figure 2.7.a). For drops subjected to medium capillary numbers, $Ca_{cr} < Ca < 2Ca_{cr}$, end pinching mechanism was dominant, where the initial drop deforms to a thread like shape with bulbous ends that eventually detach, showing also formation of small satellites. The process is repeated on the remaining part of the drop until no more breakage occurs (figure 2.7.b). The third breakage mechanism, namely capillary instabilities, was recorded for drops subjected to $Ca > 2Ca_{cr}$. In this case, initial drop again assumes a thread-like shape but this time instabilities occur both in the end and in the central part of the thread and as a result the drop in breaks into many uniformly sized daughter drops and small satellites (figure 2.7.c).

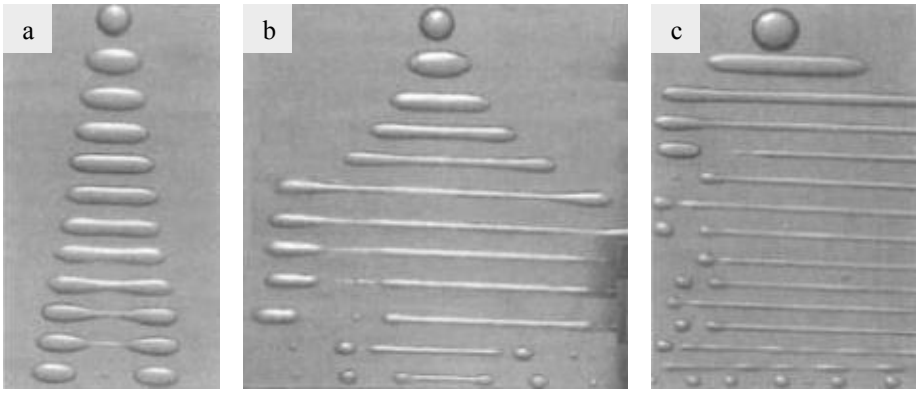

Figure 2.7: Drop deformation and breakage under shear: (a) necking; (b) end pinching; (c) capillary instabilities [Lin and Guo 2007].

De Bruijn [1989] has also described a fourth breakage mechanism, which he called tipstreaming (figure 2.8). He reported that drops with uneven interfacial tension along their surface deform into a sigmoidal shape and a stream of very small droplets is released off the pointed ends of the deformed drop. Uneven surface tension might develop, for example, in stirred emulsions, where the flow pushes the emulsifier towards the end of the drop [Groeneweg et al 1994]. Tipstreaming may occur in Capillary numbers well below the critical Capillary number of a system of identical viscosity ratio but free of surfactant, and therefore it might play an important role in emulsification.

Figure 2.8: Tipstreaming [de Bruijn 1989]

At low capillary numbers a drop exposed to simple shear flow typically deforms into an ellipsoid [Spyropoulos et al 2007, Ziegler & Wolf 1999]. The elliptical planar projection of the deformed drop with major and minor axes L_{maj} and L_{min} respectively, is characterised by Taylor's dimensionless deformation parameter Def, given by equation 2.17. Although the ellipsoidal deformation is widely accepted, other shapes have also been proposed and include slender structures with pointed ends or cylindrical formations with hemispherical ends, but are less common in the literature [Tucker et al 2002].

$$Def = \frac{L_{maj} - L_{min}}{L_{maj} + L_{min}} \tag{2.17}$$

For a Newtonian drop immersed into a Newtonian, equiviscous liquid, and subjected to small shear deformation, equation (2.18) gives Taylor's correlation between Def, Ca and λ. Cox later proposed a modified model (equation 2.19) to account for greater capillary numbers [Megias-Alguacil et al (2004); Sigillo (1997)].

$$Def = Ca\frac{19\lambda + 16}{16\lambda + 16} \tag{2.18}$$

$$Def = Ca\frac{19\lambda + 16}{16\lambda + 16}\left[1 + \left(\frac{19\lambda\, Ca}{20}\right)^2\right]^{-1/2} \tag{2.19}$$

It is evident from equations 2.15, 2.17 and 2.18 (or 2.19) that at steady state, ellipsoidal deformations of dilute systems of Newtonian drops immersed into Newtonian

continuous phases, interfacial tension τ can be determined from morphological measurements, provided that shear rate $\dot{\gamma}$ is well controlled and viscosities of the two phases are known [Sigillo et al 1997, Megías-Alguacil 2004]. This will be referred to as the 'steady drop deformation method' in section 4.5.

2.3.2 Concentrated Systems

Concentrated dispersions represent a wide range of materials important for many industries, including foods, pharmaceuticals and personal care. In addition, as the morphological behaviour of concentrated systems may differ substantially from that of their dilute counterparts, their study becomes both industrially important and theoretically challenging.

At high φ, increased interactions between dispersed entities become critical in determining morphology of the dispersion. As a result of high concentration drops deform and break easier (i.e. at smaller Ca) showing deviation from Grace Curve and de Bruijn's equation [Jansen et al 2001]. Steady drop size is then determined by the opposing processes of breakage and coalescence.

Jansen et al [2001] have experimentally investigated the behaviour of a drop under shear flow in concentrated emulsions of two immiscible Newtonian fluids. They reported a tenfold reduction in critical Capillary number for $\varphi = 0.7$ emulsions with respect to drops in dilute systems (Grace Curve) of the same $\lambda = 1.0$. They also observed drop breakage in concentrated systems occurring far above the limiting viscosity ratio for single drops ($\lambda \cong 4$). Further analysing their results they adopted the effective medium model (which they refer to

as 'mean field approximation') and recalculated an effective capillary number Ca^{eff}, where emulsion's viscosity replaces that of the continuous phase in equation 2.15, as shown in equation 2.20. They found good agreement between rescaled experimental data and points of Grace Curve and they suggested that the determining factor of drop breakage in concentrated emulsions is the average emulsion viscosity rather than viscosity of the continuous phase.

$$Ca^{eff} = \frac{\eta_{em}\dot{\gamma}R}{\tau} \tag{2.20}$$

2.4 Experimental Techniques - Instrumentation

Methods and relevant instrumentation for measuring rheology and morphology are presented in this section, focusing on shear rheometry and optical light microscopy, as those are the two main areas of interest for the present work. Recent advances on instruments for simultaneous rheological and morphological measurements are critically reviewed in the last section.

2.4.1 Measuring Rheology

Rheometry is the component of rheology that concerns experimental techniques used to determine the rheological response of a system under flow. It is part of many rheological books (e.g. Barnes et al 1989) and the main topic of others (e.g. Walters 1975). Accurate measurement of rheology is important in many industrial, experimental or theoretical applications and it is an inextricable component of rheological research. There are currently

many types of commercially available rheometers offering a variety of testing techniques and flow conditions. Selection of the appropriate device and operational mode depends on the required application that involves intended flow conditions and fluid's properties [Rides and Allen 2002]. Whatever the type, the general principle of a rheometer is based on applying a controlled stress and measuring the generated flow (controlled stress devices) or inversely, applying a controlled flow and measuring the required stress (controlled strain devices).

In relation to their operational flow conditions two major categories of rheometers are usually reported: shear and extensional. Typically, shear rheometers are either rotational or capillary. In the former, the sample under investigation is sheared between two surfaces one or both of which are rotating. Those will be discussed in more detail below due to the relevance with the present work. In capillary instruments, flow is generated by means of pressure gradient into a pipe in vertical (capillary) or horizontal (slit) positions. Unlike shear, extensional flows are generally considered difficult to generate and maintain in a well defined manner [Barnes et al 1989]. Forces acting on a drop subjected to the different types of flow conditions typically found in rheometers are summarised in figure 2.9.

Rotational instruments are perhaps the most common and developed type of rheometers. Recently, Barnes and Bell [2003] published an interesting review on the evolution of rotational instruments since their first commercial appearance, early 20^{th} century. At that time, both controlled stress and controlled strain devices were available. However, while controlled strain instrumentation rapidly evolved, controlled stress rheometers remained rather static until mid 60s – early 70s. Controlled stress rheometers, initially working with weights and pulleys, offered simplicity and economy, but posed limitations on the lower end of shear flows applied, the measurement duration and accuracy. An air turbine was then

introduced as the source of controlled stress and soon the whole system became automated. It took about 20 years (early 90s) for the new technology to spread and develop, and at present several industrial makes are commercially available, with minor differences between the devices. Currently, instruments of very high standards, rarely used to their full potential in standard rheological measurements, are common. Often, both controlled stress and controlled strain modes are offered by the same device. Significantly, modern instruments are capable of applying very low, stable shears and measure the corresponding response. Amongst other advantages, this allows easier determination of the apparent yield stress, with the relevant contribution to the debate questioning the very existence of real yield stress [Barnes 1999]. The next generation of rotational instruments may incorporate features for simultaneous optical microstructural measurements and it is towards this development that the present work wishes to contribute.

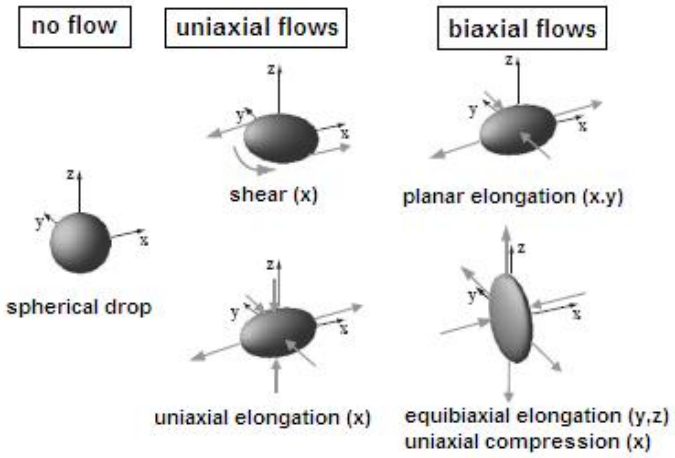

Figure 2.9: Drop subjected to rheometric flows [Windhab et al 2005]

2.4.2 Calibration of Rotational Rheometers

A schematic diagram showing the main components of a modern rotational rheometer is presented in figure 2.10 (not in scale). The sample is contained in the measuring geometry (parallel plates in figure 2.10 but any other geometry discussed below is applicable), whose rotational part is clamped to the motor's drive. The motor is responsible for application of torque, while angular displacement is determined by the optical encoders (with accuracy of the order of $0.5\mu rad$, Barnes & Bell 2003). In modern instruments, such as Malvern Instrument's CVO and Gemini used in this project, mechanical support for the rotating motor is provided by means of an air bearing.

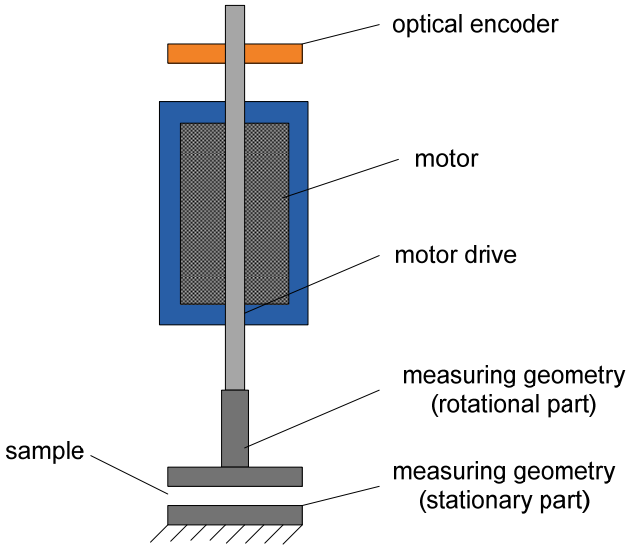

Figure 2.10: Sketch of a rotational controlled stress rheometer showing its main components [not in scale, adapted from Mezger 2006].

Typically, raw variables determined by rotational rheometers are the applied (by the instrument) torque and angular displacement, T_{raw} and θ_{raw} respectively. In order to translate obtained raw data into torque and displacement exerted onto the sample, T_{sample} and θ_{sample}

respectively, and further into shear stress and shear rate applicable to the sample, σ_{sample} and $\dot{\gamma}_{sample}$ respectively, additional information is required. Required information involves instrument's characteristics, including the moment of inertia, air bearing friction and clamp compliance, as well as the geometric characteristics of the loaded sample. Processing of raw variables is schematically shown in the flow diagram of figure 2.11 and it is usually carried out via the instrument's software. For standard geometries supplied together with the rheometer, required information is typically incorporated in the software and no further calibration is required. However, customised geometries require calibration of certain parameters if accuracy in rheological measurements is to be maintained.

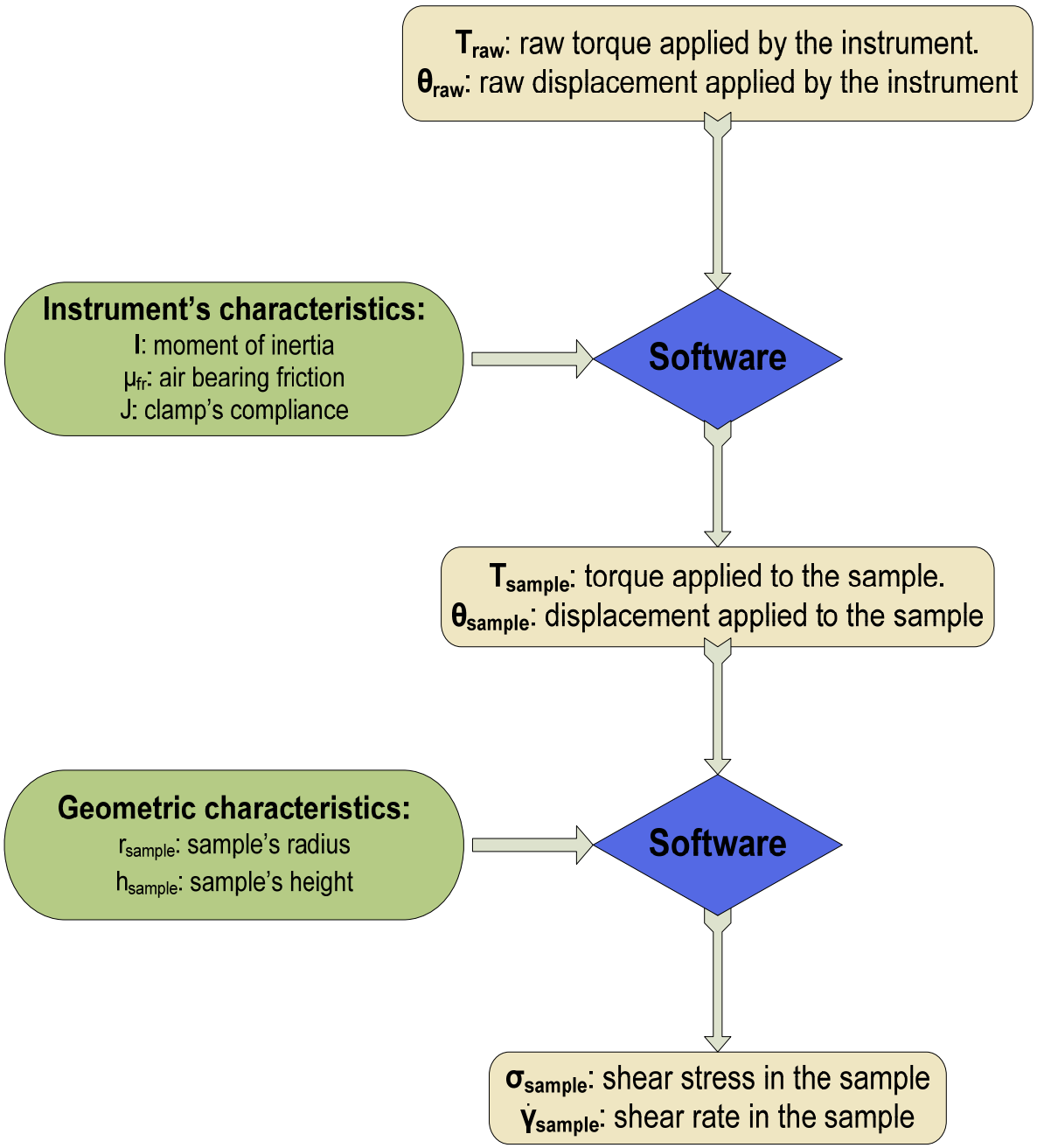

Figure 2.11: Flow chart showing processing of raw data in stress controlled rotational rheometers [adapted from Mo 2009]

2.4.2.1 Instrument's Characteristics

2.4.2.1.1 Moment of Inertia

The moment of inertia is a measure of an object's resistance to changes in its rotation rate and it is a function of its mass and mass distribution (shape). For a body rotating around an axis, the moment of inertia is given by equation 2.21, where r is the distance of the mass element dm from the rotation axis [Blake, 1985]. Moment of inertia can also be determined by division of the torque with the angular acceleration, α, as shown in equation 2.22 [Benenson et al 2002].

The part of applied torque that is used to rotate the motor's drive and the rotating part of the measuring geometry is referred to as $T_{inertia}$, and can be estimated by equation 2.23 if the instrument's inertia, $I_{instrument}$, and the angular acceleration are known. Obviously, instrument's inertia refers to the inertia of the motor's drive and the rotating part of the measuring geometry. As a result, it is unique for each geometry and requires calibration for new geometries.

$$I = \int r^2 dm \tag{2.21}$$

$$I = \frac{T}{\alpha} \tag{2.22}$$

$$T_{inertia} = I_{instrument}\alpha \tag{2.23}$$

2.4.2.1.2 Air Bearing Friction

Part of the applied torque is consumed by frictional resistance of the air bearing that supports the motor and its rotating parts. This frictional torque, $T_{friction}$, is velocity dependent and has opposite direction than the applied velocity. At low speed it is directly proportional to angular velocity, ω, with proportionality constant the coefficient of resistance, $\mu_{friction}$, as shown in equation 2.24 [Mo 2009].

$$T_{friction} = \mu_{friction}\omega \tag{2.24}$$

2.4.2.1.3 Compliance of Clamp

Clamping of the measuring geometry onto the motor's drive may induce an angular deformation θ_{clamp}, which is due to the clamp's compliance, J_{clamp}, and it is not directly applied to the sample. The magnitude of θ_{clamp} is approximately proportional to the applied torque, as shown in equation 2.25 [Mo 2009]. The value of J_{clamp} can be estimated from equation 2.25 if an experiment is carried out using a much stiffer sample than the clamping system. Raw angular displacement can then be approximated with θ_{clamp}. In modern instruments and for common experimental range, clamping is often considered rigid and is therefore ignored, or it is incorporated automatically in the instrument's software from the manufacturer.

$$\theta_{clamp} = T \times J_{clamp} \quad (2.25)$$

2.4.2.1.4 Calculation of T_{sample} and θ_{sample}

In rotational experiments, the total T_{raw} applied by the rheometer equals to the sum of the inertia induced torque, $T_{inertia}$, the torque consumed by the air bearing's friction, $T_{friction}$, and the torque applied to the sample, T_{sample}. The total θ_{raw} is the sum of the sample's angular displacement as well as the angular displacement of the clamp. As a result, T_{sample} and θ_{sample} can be calculated by equations 2.26 and 2.27, respectively. Substituting from equations 2.23, 2.24 and 2.25, equations 2.26 and 2.27 can be rewritten as 2.28 and 2.29.

$$T_{sample} = T_{raw} - T_{inertia} - T_{friction} \quad (2.26)$$

$$\theta_{sample} = \theta_{raw} - \theta_{clamp} \quad (2.27)$$

$$T_{sample} = T_{raw} - I_{instrument}\frac{d^2\theta_{raw}}{dt^2} - \mu_{friction}\frac{d\theta_{raw}}{dt} \quad (2.28)$$

$$\theta_{sample} = \theta_{raw} - T_{raw} \times J_{clamp} \quad (2.29)$$

If a sinusoidal torque of the form of equation 2.30 is applied, the resulting angular displacement will be given by equation 2.31, where δ is the phase angle between the amplitudes of torque and displacement, T_0 and θ_0 respectively. Sample's torque and displacement may then take the form of equations 2.32 and 2.33, respectively.

$$T_{raw}(t) = T_0 sin(\omega t) \tag{2.30}$$

$$\theta_{raw}(t) = \theta_0 sin(\omega t + \delta) \tag{2.31}$$

$$T_{sample}(t) = T_{raw}(t) - I_{instrument}\frac{d^2\theta_{raw}(t)}{dt^2} - \mu_{friction}\frac{d\theta_{raw}(t)}{dt} \tag{2.32}$$

$$\theta_{sample}(t) = \theta_{raw}(t) - T_{raw}(t) \times J_{clamp} \tag{2.33}$$

Computational results of sample's torque and displacement obtained from equations 2.32 and 2.33 for variables shown in table 2.2 have been presented by Mo [2009] and are plotted in figure 2.12. For the plot of figure 2.12, values of moment of inertia, friction coefficient and clamp's compliance of table 2.2 have been considered. Those are typical of the range found in rotational rheometers. As indicated by figure 2.12, the torque induced by friction in the air bearing is very small and can safely be neglected in most cases (or it is incorporated in the instrument's software).

Unlike frictional torque, the magnitude of inertia-induced torque in figure 2.12 is comparable to applied T_{raw}. It is essential, therefore, to calibrate instruments and measuring geometries in terms of their inertial contribution to the measurement.

Table 2.2: variables for computation of sample's torque and displacement from equations 2.32 and 2.33.

T_0	θ_0	δ	$I_{instrument}$	$\mu_{friction}$	J_{clamp}
11671	0.0504	96.9^o	16.64	1.046	0.006961

$(\mu N\ m)$	(rad)		$(\mu N\ m\ s^2)$	$(N\ m\ rad^{-1}\ s)$	$(rad\ N^{-1}\ m^{-1})$

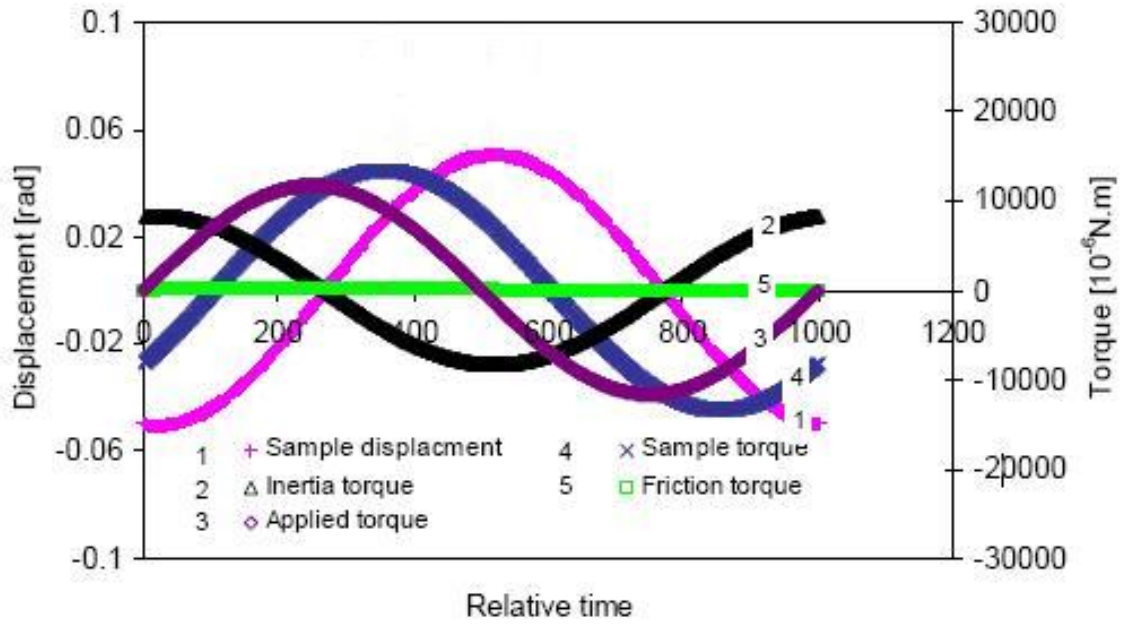

Figure 2.12: Computational results of torque and angular displacement from equations 2.32 and 2.33 and variables as in table A.1 [Mo 2009].

2.4.2.2 Geometric Characteristics

In rotational rheometers, commonly used coaxial cylinders (CC), parallel plates (PP) and cone / plate (CP) geometries are typically made of stainless steel or, more rarely, the lighter acrylic or aluminium materials are used. The instrument applies a controlled torque T and measures the corresponding angular velocity ω or vice versa, a controlled angular velocity is applied and the required torque is measured. Basic principles of those geometries

are presented below and refer to Barnes et al [1989], Chhabra & Richardson [2008] and Walters [1975], unless otherwise specified.

A loaded CC (or 'cup and bob') geometry is sketched in figure 2.13. In standard devices, loading of the investigated system typically overflows the cup. However, with the developed optical geometry, the sample is contained in the annular gap between the inner and the outer cylinders and at height h_{CC} from the bottom of the inner cylinder. Effort is made to maintain constant h_{CC} in all measurements. Shear flow is generated by the relative motion between the two cylinders. When the annular gap is narrow, $r_{in}/r_{out} \geq 0.97$ [Barnes et al 1989] (or $r_{in}/r_{out} \geq 0.99$ according to [Chhabra 2008]), curvature of the surface is usually ignored and shear rate is approximated to be constant throughout the gap, as in the simple shear flow of figure 2.1. One or both cylinders may rotate. Sometimes rotation of the outer cylinder is termed 'Couette' while that of the inner is called 'Searle'. Rotation of both cylinders is usually counter-directional, creating a stationary layer ($v = 0$) at a certain point in the gap.

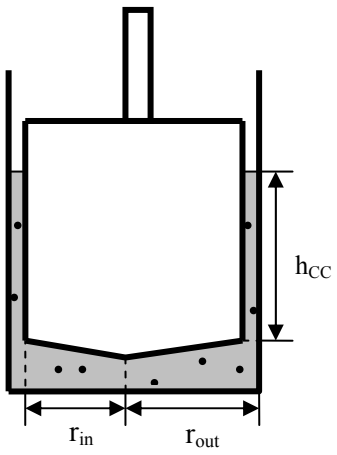

Figure 2.13: Schematic drawing of coaxial cylinders geometry

Errors in the measurements with CC are usually due to end effects, wall slip, inertia, presence of secondary flows, viscous heating and eccentricities of the cylinders due to misalignment. End-effects can be minimised through an appropriate design and manufacturing of the instrument / relevant software or by construction of a conical bottom surface (as in figure 2.13), although the effectiveness of the latter has been disputed [Kelessidis et al 2010]. Wall slip has been reported to occur above all in multiphase systems that exhibit a yield stress and roughened surfaces or specially constructed geometries, such as vane geometry, are sometimes preferentially employed to reduce the effect [Kelessidis et al 2010, Barnes & Nguyen 2001]. Development of secondary flows for a particular system depends on rotational speed and geometrical factors, often characterised by the dimensionless Taylor number (equation 2.34, Batten et al 2002, Lockett 1992). For long annuli, having small annular gap ($r_{out}/r_{in} > 0.8$), the critical Taylor number, Ta_{cr}, above which secondary flows occur can be approximated as shown in equation 2.34 [Lockett 1992]. Such flows may result in an overestimation of the torque due to energy being dissipated from the vortices. The effect of eccentricities is usually not an issue when the gap is narrow. The CC geometry poses an important restriction on the size of dispersed particles, droplets, or aggregates of investigated systems. To ensure adequate bulk measurements, a gap size $5-10$ times the size of the larger dispersed entity is recommended [Barnes 2000]. For a gap of the order of $1mm$ this practically translates to maximum dispersed size (diameter) of $100-200\mu m$.

$$Ta = Re^2 \frac{r_{out} - r_{in}}{r_{in}}, Re = \frac{v_{cyl}(r_{out} - r_{in})}{\eta_{kin}}$$
$$Ta_{cr} = \frac{\pi^4 (1 + r_{out}/r_{in})^2}{4P}, \qquad (2.34)$$
$$P = 0.0571\left(1 - 0.652(r_{out}/r_{in} - 1)\right) + \frac{0.00056}{1 - 0.652(r_{out}/r_{in} - 1)}$$

In the limit of narrow gap, shear rate and shear stress can be calculated from the angular velocity ω and the torque T by equations 2.35 and 2.36 respectively. Viscosity η is then calculated by division of σ with $\dot{\gamma}$ (equation 2.37). Equations 2.35 – 2.37 refer to rotating inner and stationary outer cylinder. If the outer cylinder rotates instead, the inner remaining stationary, r_{in} should be replaced by r_{out}, except when determining gap size.

$$\dot{\gamma} = \frac{r_{in}\omega}{r_{out} - r_{in}} \tag{2.35}$$

$$\sigma = \frac{T}{2\pi r_{in}^2 h_{CC}} \tag{2.36}$$

$$\eta = \frac{\sigma}{\dot{\gamma}} = \frac{(r_{out} - r_{in})T}{2\pi r_{in}^3 h_{CC}\omega} \tag{2.37}$$

The cone / plate (CP) geometry is schematically shown in figure 2.14 and consists of a stationary plate and a rotational, usually truncated, cone of radius r_c with its base parallel to the plate. The sample is loaded at the gap between the cone and the plate, where the plate forms the bottom boundary and the cone is in the top.

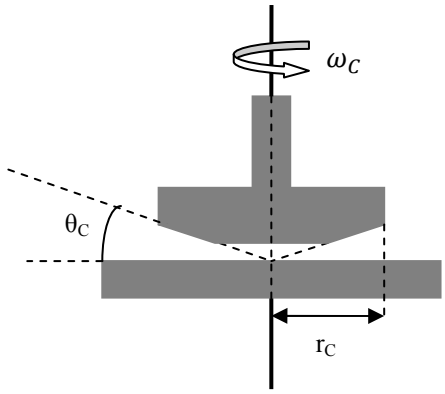

Figure 2.14: Schematic drawing of the cone / plate geometry

The velocity vector of the fluid loaded in a cone / plate geometry in spherical coordinates (r, θ, ψ) is described by equations (2.38), where the boundary conditions are also shown. Shear rate and shear stress are then given by equations (2.39) and (2.40) respectively, where K_{CP} is a constant determined by the boundary conditions.

$$\left.\begin{array}{l} v_{(r)} = 0, v_{(\theta)} = 0, v_{(\psi)} = r_C sin\theta\ \omega(\theta) \\ \omega(\pi/2) = 0, \omega[(\pi/2) - \theta_C] = \omega_C \end{array}\right\} \quad (2.38)$$

$$\dot{\gamma} = sin\theta_C \frac{d\omega}{d\theta} \quad (2.39)$$

$$\sigma = K_{CP} cosec^2 \theta_C \quad (2.40)$$

Assuming $cosec\theta_C = 1$ $(\theta_C < 4°)$, $\dot{\gamma}$ and σ can be calculated by equations 2.41 and 2.42 respectively. For derivation of those correlations it has also been assumed that the free surface of the fluid is part of a sphere with radius equal to r_C and centre at the cone vertex.

This is important when loading the sample into the geometry to avoid over-loading or under-loading. Viscosity equals with the division of stress with shear rate, as shown in equation 2.43.

$$\dot{\gamma} = \frac{\omega_C}{\theta_C} \tag{2.41}$$

$$\sigma = \frac{3T\theta_C}{2\pi r_C^3 \omega_C} \tag{2.42}$$

$$\eta = \frac{3T\theta_C^2}{2\pi r_C^3 \omega_C^2} \tag{2.43}$$

In CP shear rate is constant throughout the gap as with CC providing a clear advantage for measuring time or shear dependent systems. However, the requirement for small gap limits once more the applications of the geometry to systems with small particles / droplets / aggregates. For larger dispersed bodies the parallel plate geometry (PP) is preferred.

An illustrative drawing of PP geometry is shown in figure 2.15. The sample is placed between the upper, rotational, circular plate and a parallel, stationary bottom one. The gap size between the two plates equals to h_P. Unlike the CP geometry, shear rate in PP varies with the distance along the radius of the top plate from zero in the centre to maximum at the outer rim. There is no gap size limitation and therefore it is possible to study systems with large dispersed bodies by increasing the size of the measuring gap.

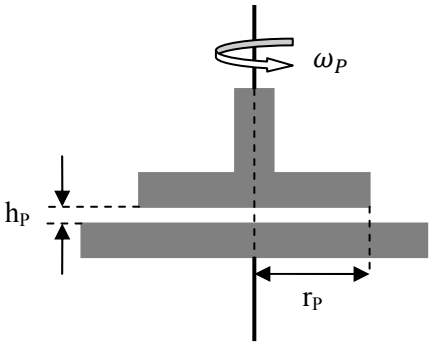

Figure 2.15: Schematic drawing of the parallel plate geometry

The velocity profile of PP is described in cylindrical coordinates (r, θ, z) in equations 2.44 where boundary conditions are also shown. At the rim of the upper plate, $\dot{\gamma}$ and σ are given by equations 2.45 and 2.46. Equation 2.45 indicates that shear rate changes proportionally along the radius of the plate r and angular velocity and reciprocally with gap size. Simplification of equation 2.46 to 2.47 is valid for power law systems [Barnes et al 1989, Walters 1975]. Viscosity is then calculated from the ratio between σ and $\dot{\gamma}$, as shown in equation 2.48. Evidently, sample loading is critical here as viscosity depends on the fourth power of r_P, which should equal to the radius of the loaded sample.

$$\left.\begin{array}{l} v_{(r)} = 0, v_{(\theta)} = r\,\omega(z), v_{(z)} = 0 \\ \omega(0) = 0, \omega(h_P) = \omega_P \end{array}\right\} \quad (2.44)$$

$$\dot{\gamma} = \frac{r_P \omega_P}{h_P} \quad (2.45)$$

$$\sigma = \frac{3T}{2\pi r_P^3}\left[1 + \frac{1}{3}\frac{d(lnT)}{d(ln\omega_P)}\right] \quad (2.46)$$

$$\sigma = \frac{3T}{2\pi r_P^3}\left(1 + \frac{n}{3}\right) \tag{2.47}$$

$$\eta = \frac{3Th_P}{2\pi r_P^4 \omega_P}\left(1 + \frac{n}{3}\right) \tag{2.48}$$

Other, less popular, geometries are also available for rotational instruments but will not be discussed here. More information can be found for example in the rheometer's manual. Measuring of viscoelasticity and normal stresses with rotational rheometers is also excluded from the present review but indicates the potential of the instrument. Those are discussed for example in Barnes [1989], Chhabra [2008], Walters [1975], Lakes [2004].

2.4.3 Optical Instruments / Techniques

Determination of microstructure is relevant to many rheologists, engineers, computer scientists, mathematicians, etc who study complex fluids. Several optical techniques have been employed up to date for microstructural characterisation of complex fluids, including light microscopy (LM), transmission electron microscopy (TEM), scanning electron microscopy (SEM), and scattering techniques, such as small-angle light scattering (SALS), small-angle X-ray scattering (SAXS), small-angle neutron scattering (SANS), etc. An exhaustive review on optical methods is beyond the scope of this work. Developments on the use of optical techniques in conjunction with rheological methods have been reviewed on several occasions in the literature [for example Linden et al 2003; Larson 1999; Wagner 1998; Sondergaard & Lyngaae-Jorgensen 1995; Fuller 1990].

Selecting the most appropriate optical technique depends on the required application, including the experimental length and time scales, and the relevant availability in the specific working environment. For example, light microscopy typically provides information for structures larger than $2\mu m$ and the corresponding time scale involved is larger than $0.01s$ [Linden et al 2003; Shaw 1994]. In scattering techniques, lengths of analysed structures are typically of the order of $10^{-3} - 1\mu m$ and the corresponding time scales range between $10^{-6}s$ and $1s$ [Linden et al 2003; Sondergaard & Lyngaae-Jorgensen 1995].

In SALS, SAXS and SANS, incident radiation, in the form of light beam, x-rays and free neutrons respectively, is directed to the sample and the scattered intensity is recorded as a function of the angle with the initial incident radiation [Linden et al 2003; Sondergaard & Lyngaae-Jorgensen 1995]. For photons, x-rays and neutrons, scattering depends on changes within the sample of refractive index, electron density and nuclear scattering cross section of molecules, respectively [Sondergaard & Lyngaae-Jorgensen 1995]. The scattered intensity as a function of scattered angle can be used to give information on the sample's microstructure, such as size, shape and orientation of polymer species in complex fluids [Linden et al 2003; Sondergaard & Lyngaae-Jorgensen 1995]. In the literature, rheological measurements have been combined with simultaneous structural characterisation using SALS [Gentile et al 2011; Azzum et al 2008; Lauger et al 2004; Xu et al 2004; Hong et al 1998], SAXS [Philippe et al 2011; Martin et al 2010; Hyun et al 2008; Panine et al 2003] and SANS [Takeda et al 2011; Stellbrink et al 2008; Erges et al 2006]. In addition, Anton Paar has developed commercial accessories for simultaneous rheological and optical scattering techniques [brochure].

In electron microscopy, EM, the image of the specimen under investigation is produced and magnified with the aid of a beam of electrons. The method offers very high

resolution potentially measuring down to less than a nanometer. In transmission EM (TEM), high energy electrons are transmitted through the sample, which causes part of them to scatter. The resulting image is the magnified projection of the beam electrons that have not been scattered. Magnification can reach very high levels, but due to the process of imaging meaningful results require very thin, layered samples. In scanning EM (SEM) the specimen is scanned by a focused electron beam, and electrons lose energy when encountered with the specimen's surface. Image is produced through a secondary signal, such as heat, secondary electrons, or x-rays, and represents a bulk picture of the sample. Both TEM and SEM function under vacuum. Recently, a new procedure has evolved, the environmental SEM, which does not require vacuum to operate thus permitting analysis of non-dry systems. EM produces images of high quality and has been combined with rheological measurements to visualise solidified structures [see for example Huitric et al 2009, Habeych et al [2008], Yang et al 2008, Wang and Zheng [2005], Jansseune et al 2003, Mours et al [2003], Hong et al 2000, Martin et al 2000, Wolf et al [2000]. However, the technique cannot offer morphological characterisation simultaneously with the rheological measurements, as image acquisition requires a solid-like material.

In the present work, light microscopy has been employed for visualisation of structures. From a historical point of view, the term "microscopy", from the Greek words for "small" and "to view", was first introduced in 1624 in Italy by the first Accademia dei Lincei, whose member included Galileo [Croft 2006]. As mentioned above, Robert Hooke was also among the first scientists to systematically study microscopy [Croft 2006].

In light microscopy, the subject under investigation is illuminated with light of visible wavelength and magnification is obtained by using a single or multiple lenses [Slayter &

Slayter 1992]. Lenses with different optical properties or in combination may be used to achieve the required magnification. The resolving power of optical microscopes (i.e. minimum separating distance between distinguishable objects) has been theoretically determined to about $0.2\mu m$, but it has been reported that reliable measurements are obtained for objects larger than about $2\mu m$ [Shaw 1994]. In practice, many industrial and research applications are well within this size range, establishing the technique among the most popular in structure analysis. Interestingly, the technology to visualise entities beyond the limit of $2\mu m$ has recently been reported [Want et al 2011]. In modern instruments images are usually recorded via a charge-coupled device (CCD) camera and stored in a computer for further analysis.

Experiments with light microscopes are simple, very reliable and offer direct visualisation of the object. Information on the size, shape and orientation of dispersed entities under flow can be obtained with appropriate image analysis using computer software. On the downside of the technique is the requirement for suitable optical properties of the sample., as a certain degree of transparency is essential. In addition, optical contrast between examined object and its surrounding background is required. Optimising the lighting conditions significantly improves the quality of acquired images, which is of particular importance for difficult samples, such as aqueous two phase systems where refractive indices of the ingredients are very similar, highly concentrated emulsions, or complex multiphase systems relevant to the industry. Optical light microscopy is adjustable to combine with rheometrical instruments and provides the potential of in situ recordings. Combined rheological and optical microstructural techniques are discussed in more detail the next section.

2.4.4 Rheo-Structural Instrumentation

Rheo-structural measurements refer to the linkage between rheological recordings and structural observations. Basic concepts of rheo-structural techniques have been reviewed elsewhere [Fuller 1995, Wagner 1998] and will not be included here. Their importance specifically in relation to food has been considered by Linden et al [2003]. Here, focus is given on recent instrumentation and commercial solutions of rheo-structural devices.

Rheo-structural instruments can be categorised based on whether optical characterisation is direct (simultaneous with rheological) or indirect (following rheological). In indirect methods rheology and structure are determined separately and structure solidification is often necessary prior to morphological observations, for example when electron microscopy is used for morphological observations. Structure immobilisation frequently occurs by means of gelation [Wolf et al 2000] or quenching [Jansseune et al 2003; Habeych et al 2008; Yang et al 2008; Wang & Zheng 2005, Mours et al 2003, Hong et al 2000 ; Martin et al 2000].

Indirect methodologies pose no specific restrictions on selection of rheometer and / or optical instrument / technique, as structure is determined separately from imposition of flow. For example, a rotational or extensional rheometer can equally be utilised and coupled with optical microscopy, scanning electron microscopy or any other optical technique. However, recorded morphologies generally differ from those generated by the flow, due to microstructural changes occurring in the time separating the rheological and morphological measurements or during the process of structure immobilisation. In addition, while observation of steady state morphologies is fairly straightforward, monitoring structure evolution in a detailed, real-time manner is impossible with indirect techniques due to the

nature of the experiments. Step structural changes may be observed in a laborious batch process where the experiment is halted and microstructure is determined at different stages of the measurement [Mours et al 2003].

Direct rheo-structural methods, on the contrary, offer simultaneous rheological and morphological data recordings and therefore the potential of directly investigate the link between rheology and structure. Extended applications of direct techniques [reviewed by Puyvelde & Moldenaers 2006] also include studies of different structural formations, drop deformation and breakage under controlled flow fields, detailed investigation of the process of coalescence, observation of structure relaxation after cessation of well controlled flow, and estimation of interfacial tension from measurements of steady drop deformation under controlled shear flow.

Direct rheo-structural instruments typically join a rheometer with an optical technique into a single device and have been reported in relevance to a number of different flow conditions, including rotational flow [discussed in more detail below] complex flows [Soulages et al 2008; Testa et al 2001], capillary [Lee & Mackley 2001] and optical micro-rheometry [Biesiada et al 2006; Bransky et al 2006]. In recent years, rotational rheometers have been combined with optical microscopes in realisation of both home-made [Erni et al 2011; Keshtkar et al 2010; Desse et al 2009; Lin & Guo 2007; Mighri and Huneault 2006; Vervoort and Budtova 2005; Jeon & Hobbie 2001; Guido and Villone 1998] and commercial [Linkam Scientific Instruments; Anton Paar; Thermo Fisher Scientific] devices for simultaneous rheological and morphological measurements.

Commercialisation of direct rheo-structural instruments reflects the response of established companies in the field of rheometry to the growing interest for simultaneous

rheological and morphological observations. The most flexible solution has been designed by Linkam Scientific Instruments [Mobuchon et al 2009; Guo et al 2005; Puyvelde et al 2003; Wolf & Frith 2003] and consists of an optical shearing stage supplied by quartz glass parallel plates geometry (figure 2.16). The stage can be mounted onto an optical microscope to allow contemporaneous visualisation of the sheared system. Although flexible, this design has the disadvantage of not offering a complete solution for simultaneous recordings, requiring additional microscopic equipment and assembly.

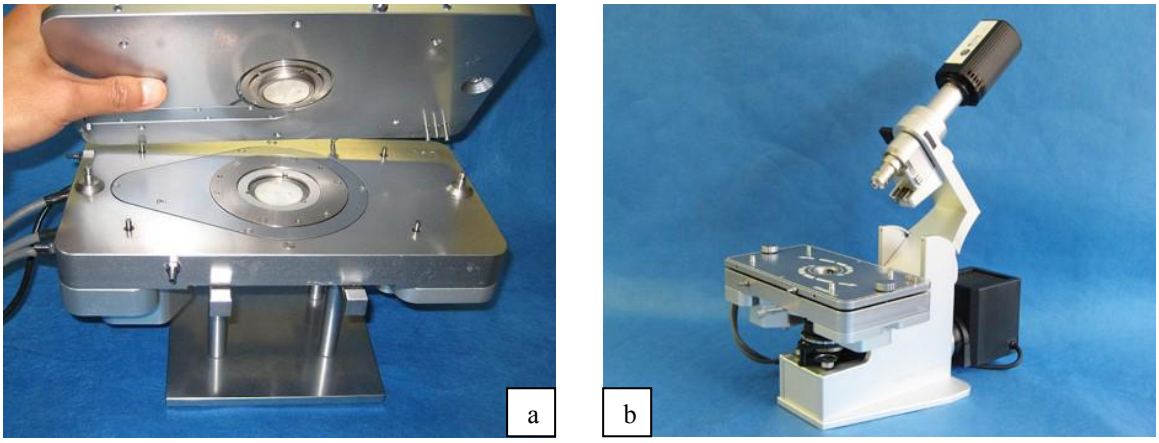

Figure 2.16: Linkam Scientific's optical shearing stage (a) close up view; (b) mounted on optical microscope [relevant brochure].

Anton Paar and Thermo Fisher Scientific have developed optical microstructural accessories that can be combined with their Physica MCR and HAAKE Mars rheometers respectively, to produce complete direct rheo-structural devices [Morishita & Kawaguchi 2009, Oldorp 2007, Lauger & Heyer 2006, Kawaguchi & Kubota 2004]. These are shown in figure 2.17. For both designs of figure 2.17, experimental process involves illumination of the sheared sample and image recordings via CCD camera. Key features of both units are similar: (a) an optical measuring geometry, which replaces the standard stainless steel and consists of

fully transparent glass PP for Anton Paar's rheo-microscope, or an open quartz 'window' in the bottom plate of PP and CP geometries for Thermo Fisher Scientific's rheoscope (figure 2.17); (b) samples are illuminated by constant light source; (c) both light and camera are positioned at the bottom of the measuring geometry; and (d) constant magnification is provided by objective lenses claimed to give standard x20 and optional x5, x10 and x50 [Anton Paar and Thermo Scientific brochures].

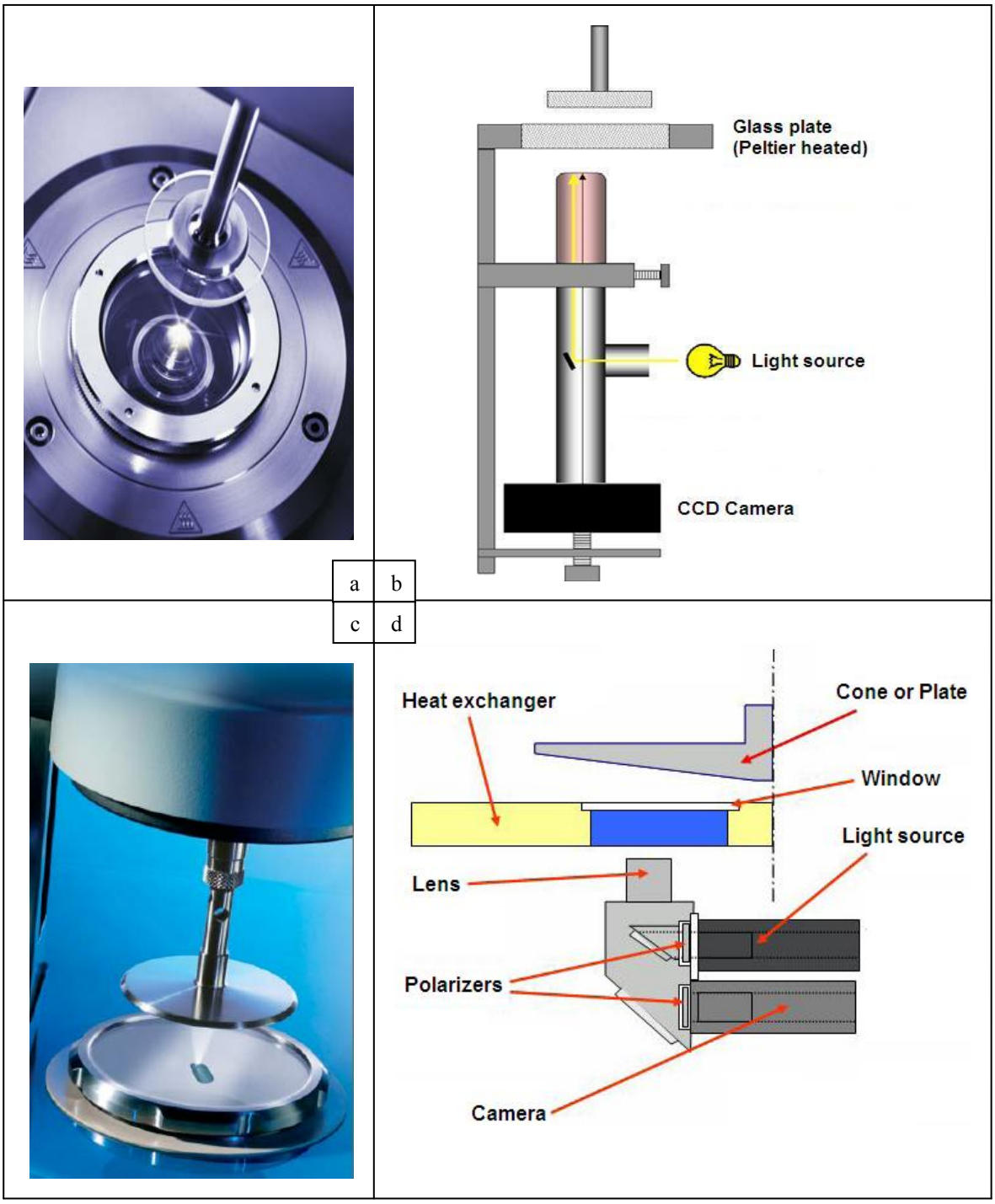

Figure 2.17: Commercial devices for simultaneous rheo-structural measurements by (a) and (b) Anton Paar; (c) and (d) Thermo Fisher Scientific [(a) and (c) from relevant brochures; (b) and (d) from Lauger & Heyer 2006 and Oldorp 2007, respectively].

Figure 2.18 shows images of polymer blends / emulsions obtained with Anton Paar's rheo-microscope and Thermo Fisher Scientific's rheoscope, displayed in the brochures of the

two companies. Those will be referred to in chapter 4 for comparison of image quality between images obtained with the two commercially available devices and those achieved with the new device developed in this project. Also for comparison, images of other systems obtained with the three commercial devices are depicted in figure 2.19.

Figures 2.18 and 2.19 illustrate drops with blunt boundaries, especially under deformation, that may pose difficulties in automated analysis with computer software even at low concentrations of dispersed phase. In addition, maximum shear rates of simultaneous rheo-structural recordings reported in the literature are of the order of $\dot{\gamma} = 100s^{-1}$, but higher shears are frequently relevant with industrial processes, especially in the range of products where high shear mixing is involved [Hall et al 2011; Utomo et al 2008]

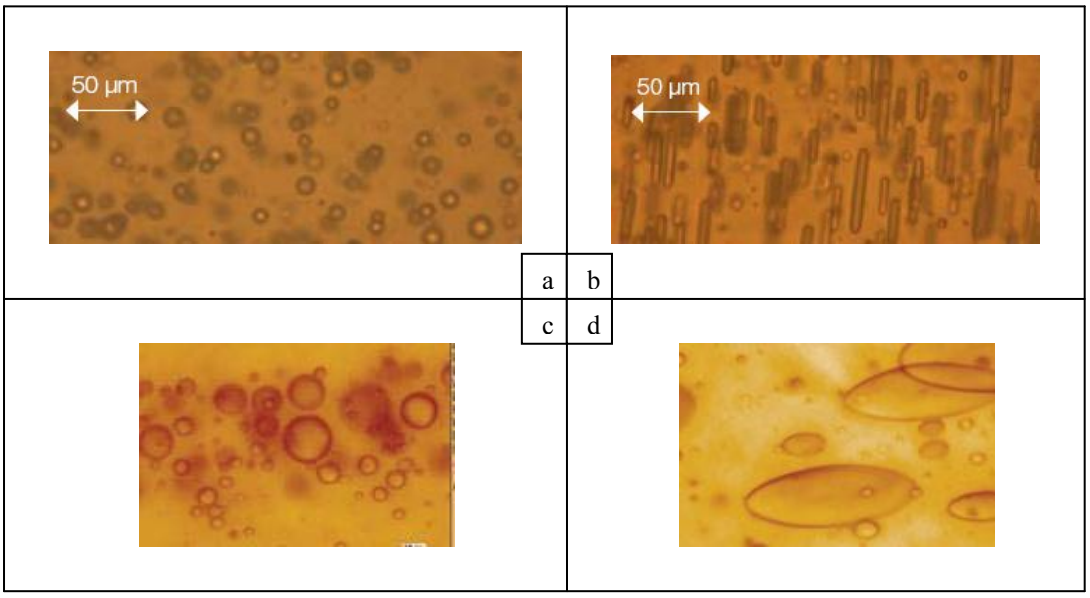

Figure 2.18: Images of polymer blends / emulsions obtained by (a) and (b) Anton Paar rheo-microscope; (c) and (d) Thermo Fisher Scientific rheoscope [relevant brochures].

Figure 2.19: images of (a) liquid crystals obtained by Linkam Scientific optical cell; (b) liquid crystals obtained by Anton Paar rheo-microscope; (c) starch granules in water obtained by Thermo Fisher Scientifric rheoscope [(a) Guo et al 2005; (b) and (c) relevant brochures].

For those reasons, a different approach has been considered in the development of the new instrument in our lab targeting in superior image quality, especially in high shears. Key features differ from the two commercial ones: (a) optical geometries of all typical measuring systems (PP, CP and CC) have been constructed, offering the full range of choices of standard rheometers. Working surfaces are made of glass providing optical transparency at low price; (b) a stroboscopic lighting system synchronised to flash with the camera's shutter opening is employed to ensure optimal illumination; (c) light and camera are positioned on opposite sides of the sample (facing each other) to enhance image quality by eliminating shadows and reflections; and (d) magnification, defined as pixel size, can rapidly change during the experiment to allow flexible observations of microstructural evolution according to the characteristic size of the microstructure. With the current arrangement, high quality images are for the first time obtained at shear rates of the order of $2 \cdot 10^4\ s^{-1}$, set using the parallel plate geometry at small gap size (100µm).

CHAPTER 3

DEVELOPMENT OF THE RHEO-STRUCTURAL DEVICE

3.1 Introduction

New hardware has been developed for construction of an instrument for simultaneous rheological and morphological measurements that improves the limitations of existing experimental facilities, discussed in the previous chapter. The new device incorporates all benefits of a modern rheometer and high quality time / spatial resolution recordings of the system's microstructure / morphology. Particular attention has been given to obtain sharp images at different shear rates for a variety of two phase liquid / liquid systems, by optimising the image acquisition unit.

In this chapter, development of the experimental setup is presented and critical features of hardware are described in some detail. Existing software has been employed in image analysis and is also discussed briefly.

3.2 Experimental Setup and Hardware

3.2.1 Setup Overview

The proposed experimental setup with a parallel plate geometry is illustrated in figure 3.1. Similar arrangements have been configured for cone / plate and coaxial cylinder measuring systems.

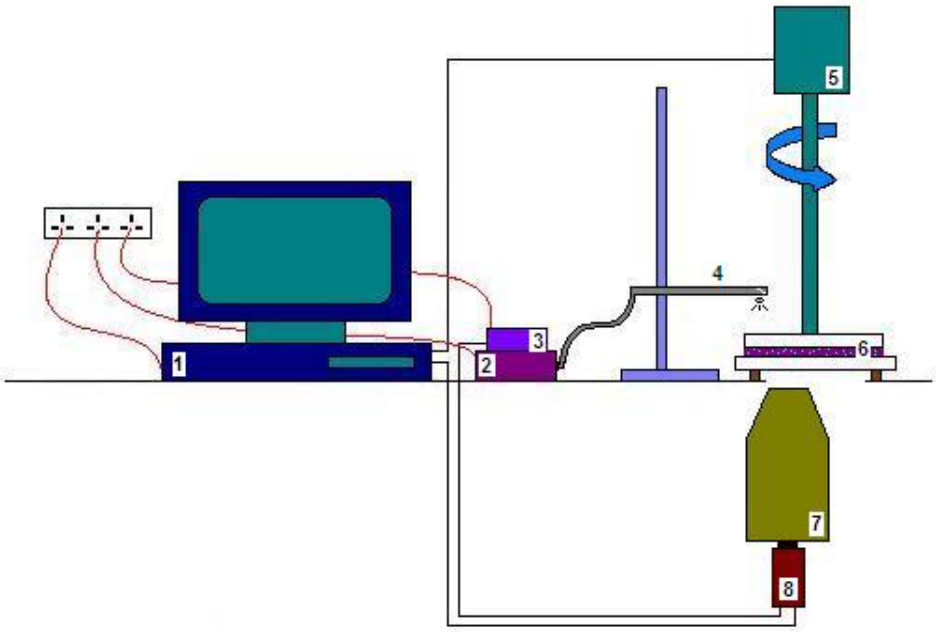

Figure 3.1: Diagram of experimental setup. (1) PC; (2) strobe flash; (3) synchronising trigger, synchronises pulsating frequency of strobe light with camera's framing speed; (4) strobe light directed to geometry; (5) standard Malvern rotational rheometer; (6) optical measuring geometry with glass working surfaces (parallel plates in the particular case) and loaded sample; (7) stereo microscope; (8) CCD high resolution camera. Similar designs have been employed for all new geometries.

The setup combines a rheometer with an optical unit. The former consists of a standard rotational controlled stress rheometer with control rate facilities and optical measuring geometries designed and constructed during this project (see next section). A CVO and Gemini 2 rheometers, both supplied by Malvern Instruments, have been used. The change of rheometer was considered necessary over repeated technical failures observed with the first model, especially at shear rate $400s^{-1}$, where discontinuous rotation was visually evident. There was no significant difference between the rheological results obtained with those two rheometers for a range of tested systems (data not shown), therefore no further distinction between them will be made.

The optical unit, besides the geometries, is comprised of a stroboscopic lighting system and a stereo microscope connected to a CCD camera (arrangement of different parts to be discussed below). Gathering of simultaneous data as well as data analysis are controlled by relevant PC software. Photos of the assembled experimental setup are shown in figure 3.2 for the parallel plate and the coaxial cylinders geometries.

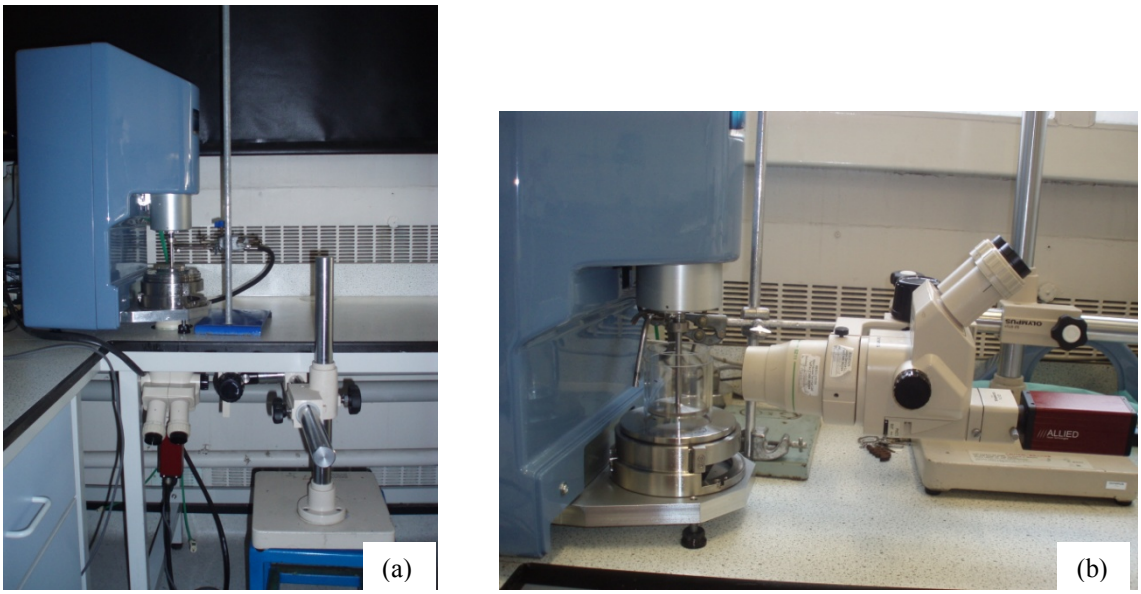

Figure 3.2: Photos of experimental setup with (a) parallel plates and (b) coaxial cylinders geometries (detail).

3.2.2 Optical Measuring Geometries

Design of new geometries has aimed at ensuring very high optical properties without compromising accuracy of the rheological measurements, at a reasonable cost if possible. To meet those aims, standard geometric designs were employed but working parts were partially made of glass. Technical drawings of the new geometries are shown in figure 3.3.

Optical glass, polished when necessary, ensures sufficient transparency for visualisation purposes, and it is considerably cheaper than quartz, used in other solutions for simultaneous rheological and morphological measurements [see for example Thermo Fisher Scientific optical unit, Linkam Scientific's optical cell, Malvern Instrument's optical cell for birefringence measurements, Lin & Guo 2007].

Frames and shafts that hold the glass and fix the cone / top plates / inner cylinder in the rheometer are made of stainless steel and provide robustness with negligible obstruction in optical recordings. Optical obstructions occur when the shaft that holds the glass passes between the light and the camera at the moment when images are captured, overshadowing the acquired picture. 222At shear rate of $250s^{-1}$, shadowed images were found to be less than 15% of the total acquired images, what translates to one out of seven, or approximately two shadowed images per one second.

Shafts were constructed in house to precisely fit the already shaped glass parts so that accuracy in rheological measurements is not affected by misfits between shafts and glass. For convenience, fixing of customised geometries to the rheometer was designed to mimic the technique used by standard geometries supplied by manufacturer.

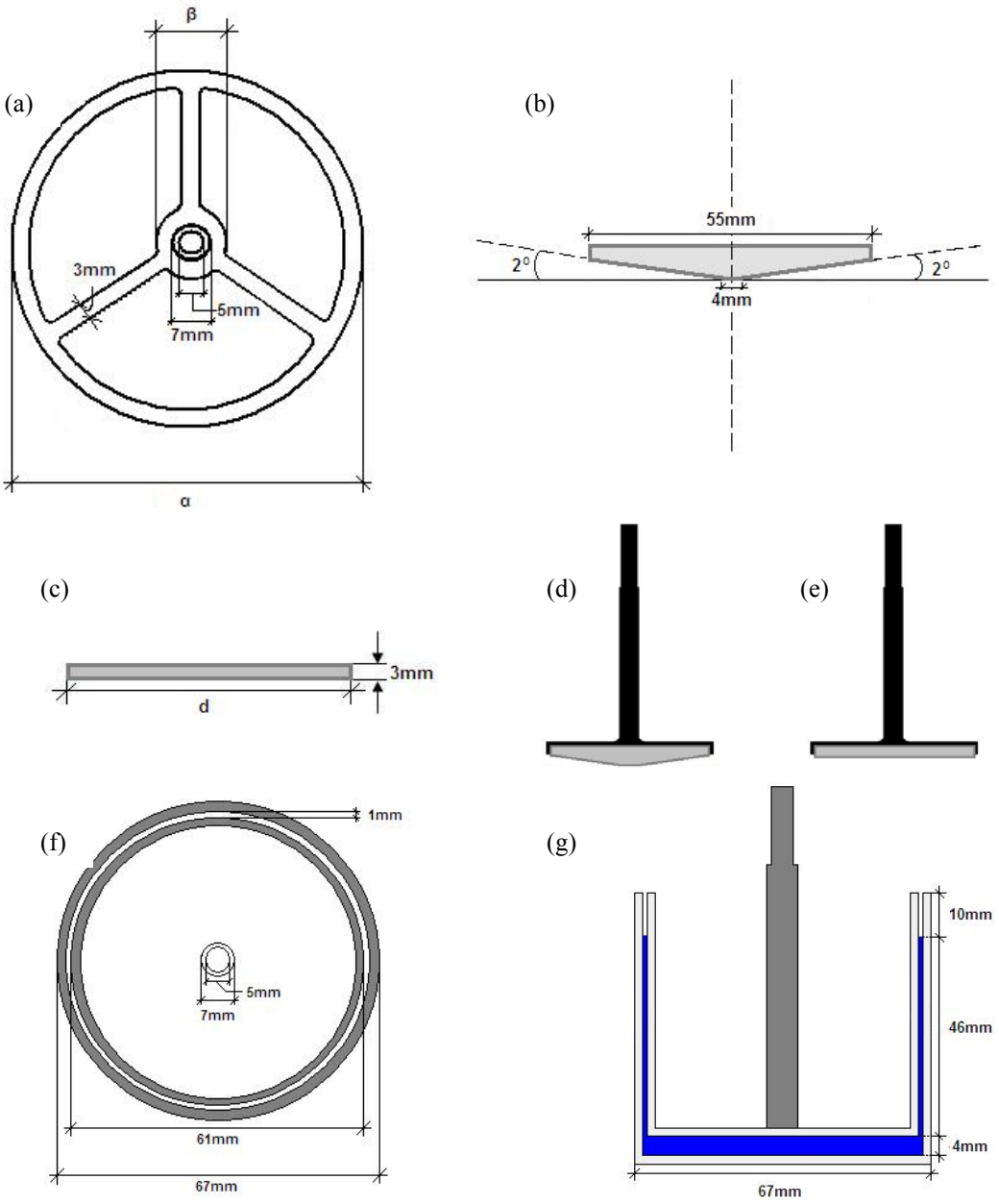

Figure 3.3: Drawings of new geometries; (a) top view of parallel plates and cone / plate (for PP40, PP60 and CP55/2 respectively: α=43mm, 63mm, 58mm and β=11mm, 14mm, 13mm); (b) side view of glass cone; (c) side views of glass top plates (d=40mm and 60mm for PP40 and PP60 respectively); (d) and (e) side views of cone and top plates, respectively, with shafts; (f) and (g) top and side views of CC respectively.

Four new geometries have been constructed. The two parallel plates, with top plate diameters of $60mm$ and$40mm$, from now on referred to as PP60 and PP40 respectively, are conveniently suited for measurements of samples with different viscosities and a range of particle / drop sizes. The bottom glass plate of $66mm$ is also utilised for the cone / plate geometry (CP55/2 from now on), the cone having $55mm$ base diameter, 2° angle and $0.7mm$ truncation. Dimensions of top plates and cone have been selected to equal the sizes of their counterparts found in standard rheometric accessories kits and the small cone angle ensures that the relevant geometric requirements, discussed in chapter 2, are met. Narrow gap coaxial cylinders geometry (referred to as CC from now on) has annular gap of $1mm$ and inner to outer radius ratio 0.97. In CP55/2 and CC shear rate is approximated to be constant throughout the gap. Photos of the new geometries are shown in figure 3.4.

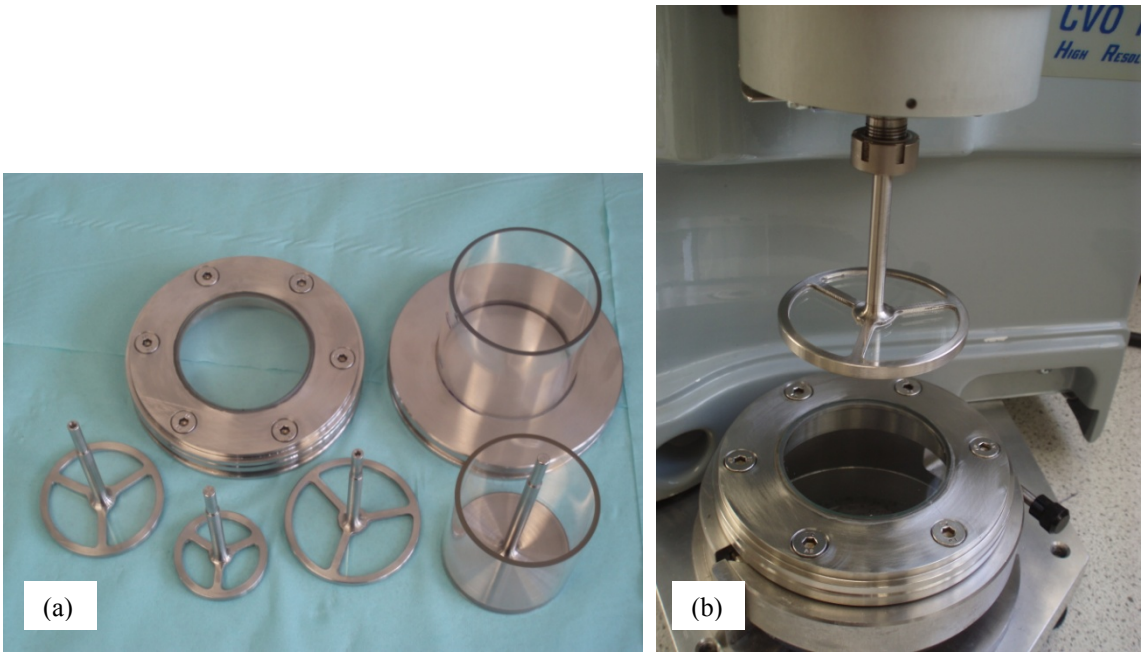

Figure 3.4: Photos of (a) constructed measuring geometries; (b) PP60 fixed on rheometer

Gap size is critical in determining flow properties and subsequent rheometric calculations in parallel plates and cone / plate units. Shaft heights for the particular geometries and position of bottom plate have therefore been appropriately adjusted to ensure accurate control of the gap within the working limits of the instrument. Working limits are posed by the limits of the rheometer's head vertical movement, which controls the position of the upper platen. In CC geometry, sample height was manually maintained to $\cong 46mm$. Accuracy of manual height control was tested by measuring various samples at $42mm$ and $50mm$ height. Small difference, $< 10\%$, was observed for the two extreme heights, and therefore it was concluded that for current use, manual determination of sample height is acceptable.

3.2.3 Image Acquisition Unit

Besides geometries, other critical parts of the image acquisition unit include stroboscopic illumination, magnification / camera, and the relevant software for image recording.

Lighting system consists of a strobe light source and an electronic trigger / synchroniser that is connected to both the CCD camera and the strobe light source and matches the pulsating frequency of the light with the camera's framing speed (see figure 3.1 above). The working principle of the synchronised strobe light is schematically illustrated in figure 3.5. The strobe flash occurs concurrently with the opening of the camera's shutter, thus providing strong and short illumination of the subject under examination. Synchronisation of the light's flashing frequency with the camera's shutter opening ensures that all images are uniformly and strongly illuminated. This illumination setup permits minimisation of both the camera's gain and shutter's opening time and therefore guarantees maximisation of control

over lighting conditions of the sample, independently of the lighting conditions of the environment.

Utilising stroboscopic illumination, a technique pioneered in this lab, produces very high quality sharp images, especially at high shears where image clarity is significantly affected by the fast motion of the sample. Stroboscopic illumination used in this project has been generated by a Perkin Elmer Inc. xenon strobe flash system (supplied by Metax).

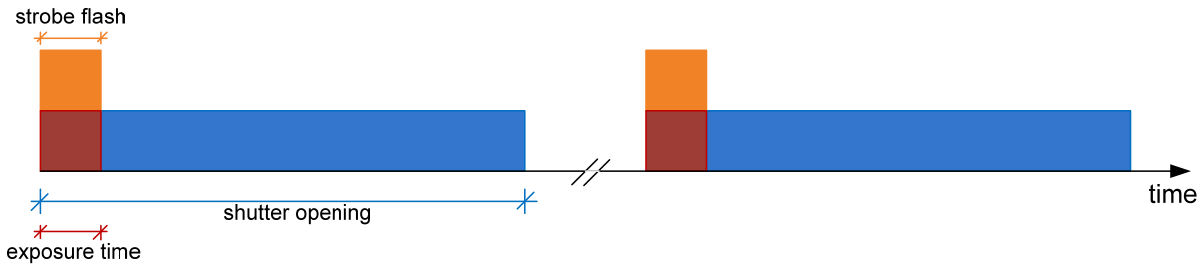

Figure 3.5: Working principle of the strobe light synchronised to flash with the camera's shutter opening.

The light is positioned to flash through the sample and directly into the microscope / camera lens (figure 3.1). This setup differs than those of existing devices, where light and camera are located at the same side of the measuring geometry [chapter 2]. The proposed setup considerably enhances image clarity by eliminating light reflections as well as interfering shadows of neighboring drops. Example images that demonstrate enhanced image clarity of the current setup compared to other commercial solutions are shown in figure 3.6.

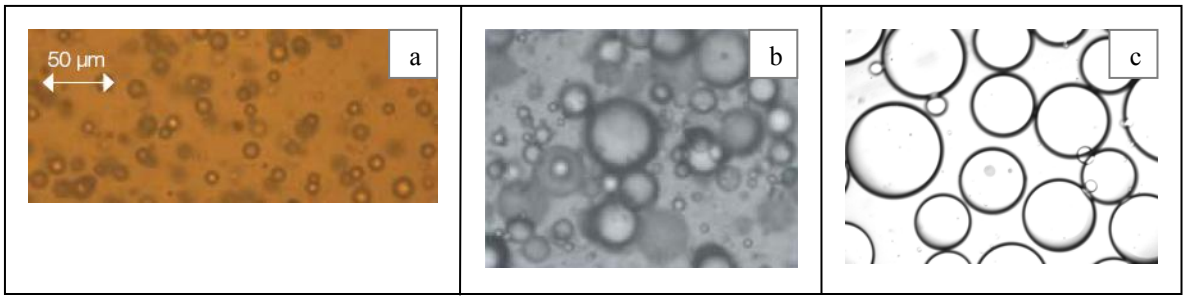

Figure 3.6: Images taken with (a) Anton Paar's Rheo-Microscope; (b) Fisher Scientific's Rheoscope; (c) current setup (image width in (c) is 2.4mm). Improved image quality with current setup is demonstrated. [Pictures (a) and (b) are taken from the brochures of the companies]

Magnification in the current setting of the device is accomplished with a zoom stereo microscope (SZ1145TR-CTV supplied by Olympus), which is connected to a CCD high resolution Dolphin F145B firewire black and white camera supplied by Allied Vision Technologies, AVT. According to the camera's specifications, capturing frame rate is 15fps, image width 1280 pixels and height 960 pixels. Images are recorded using the AVT software.

Magnification is defined in terms of the size of a pixel rather than number of enlargement times found in commercial devices [Anton Paar and Thermo Fischer Scientific]. For the current setting maximum achieved magnification was $1.3 \mu m\ pixel^{-1}$.

Unlike existing commercial devices, in the proposed setup magnification can be rapidly adjusted according to the characteristic dimension of the analysed evolving morphology. The morphological response to the change of shear rate can therefore be followed in real time with required accuracy / spatial resolution. In a possible future commercialisation of the device, this feature can be automated for better control and ease of use.

3.3 Inertial Calibration of Optical Geometries

As mentioned in section 2.3.2, translation of raw torque applied by the device, T_{raw}, to stress and shear rate applied to the sample requires information about the instrument's characteristics as well as the sample's geometric features. For standard measuring geometries, typically made of stainless steel or acrylic, required information is usually intrinsically incorporated in the software and stress / strain are given automatically. However, constructed glass geometries used in this project necessitate precise calibration if accuracy in rheological measurements is to be maintained.

From the three main required instrument parameters, described in section 2.3.2, instrument's moment of inertia $I_{instrument}$ and compliance of clamp J_{clamp} are geometry specific, whereas the air bearing's friction coefficient $\mu_{friction}$ is independent of the employed geometry. As the clamping system of new geometries was designed identically to the standard clamp, the same compliance has been assumed and no further correction of clamp was introduced.

The instrument's moment of inertia has been calibrated for each of the new geometries. The two components of $I_{instrument}$ are the individual moments of inertia of the motor's drive, I_{motor}, and that of the measuring geometry, $I_{geometry}$, as shown in equation 3.1. Both motor's and geometry's moments of inertia are required by the instrument's software. The former, I_{motor}, is independent of the geometry and it was obtained directly from the software, to equal $1.5 \cdot 10^{-5} kg\ m^2$, as shown in equation 3.2. The latter, $I_{geometry}$, was estimated separately for each geometry by performing a sinusoidal (torque) amplitude sweep experiment without any loaded sample. The resulting angular acceleration was measured and the total $I_{instrument}$ was determined by equation 3.3. The value of $I_{geometry}$

was then calculated from equation 3.1 by substituting the values of I_{motor}, from equation 3.2, and $I_{instrument}$.

$$I_{instrument} = I_{motor} + I_{geometry} \quad 3.1$$

$$I_{motor} = 1.5 \cdot 10^{-5} kg\ m^2 \quad 3.2$$

$$I_{instrument} = \frac{T_{raw}}{\alpha} = \frac{T_{raw}}{\omega^2 \theta} \quad 3.3$$

The plot of applied torque against resulting angular acceleration is shown in figure 3.7 for all newly constructed optical geometries. The value of $I_{instrument}$ equals to the slope of the linear regression passing through the origin of coordinates. Calculated moments of inertia [excel 2007] are shown in table 3.1.

Table 3.1: Estimated moments of inertia of optical geometries

Coaxial cylinders	**Cone / plate**	**Parallel plate 40mm diameter**	**Parallel plate 60mm diameter**
$9.5 \cdot 10^{-5} kg\ m^2$	$1.9 \cdot 10^{-5} kg\ m^2$	$7.1 \cdot 10^{-6} kg\ m^2$	$2.6 \cdot 10^{-5} kg\ m^2$

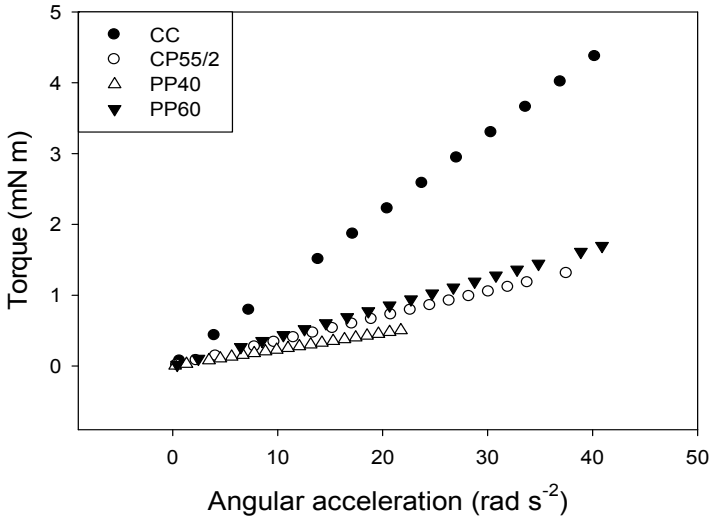

Figure 3.7: inertial calibration of the optical geometries. A sinusoidal amplitude sweep experiment was performed with each of the geometries and the calculated angular acceleration is plotted against applied torque. The slope of linear regression passing through the origin equals $I_{instrument}$ CC: coaxial cylinders; CP: cone / plate; PP40 and PP60: parallel plate with 40mm and 60mm diameter respectively.

3.4 Image Analysis Software

Existing software has been employed for image analysis. Two software programmes have been used. Calibration of size using an object of known dimensions is essential prior to image analysis in both programmes.

In Morphologi G3, supplied by Malvern Instruments, loaded images are automatically analysed. Image analysis includes measurements of drop size and size distributions, as well as shape descriptors of individual drops, such as aspect ratio, circularity, and convexity. Automatic analysis is simple, fast and rather effortless. However, the software poses certain limitations on quality of the image that is being analysed in order to enable identification of drops. Sufficiently clear contrast between boundaries of dispersed entities and background is required so that the relevant threshold can be set. Blunt edges or other objects in close

proximity with the drop, such as other drops or small dust entities that do not interfere with rheological measurements, disrupt recognition. As a result, only very dilute samples, where drop overlapping is limited, can be analysed.

Bubble Pro, a semi-automated software developed in this department [Pacek 1994], has been employed for analysis of images outside of the requirements of Morphologi G3. In BubblePro drops are manually selected. Circular drops are appointed either by clicking on three points of the drops' perimeter or by sliding a set of two perpendicular lines to form a square with sides tangential to the circle. Elliptically deformed drops are drawn manually using again a set of two lines at right angle and dragging a rectangle tangential to the drop. Selected drops remain coloured (yellow) so as to avoid repeated selections of the same drops. Further analysis automatically gives drop sizes, average drop sizes, and drop size distributions, as well as volume and number density probability functions. Shape analysis with Bubble Pro is possible and without difficulties, but it is relatively laborious, as it requires a considerable amount of manual input. Bubble Pro can be used for analysis of all images with easily identifiable drops independently of dispersed phase concentration and drop overlapping.

CHAPTER 4

EVALUATION OF THE NEW DEVICE

4.1 Introduction

The newly developed device, described in the previous chapter, was subsequently evaluated for the quality and potential of obtained rheological and morphological data. Evaluation is divided into four sections, presented in this chapter. Rheometric performance and image acquisition, tested separately, are discussed in sections 4.2 and 4.3 respectively. The former requires accurate rheological characterisation of the investigated system, while high quality images are characterised by clarity in morphological features and sharp boundaries between dispersed and continuous phases, when relevant.

Section 4.4 considers simultaneous rheological and morphological recordings for a variety of different systems, including oil / aqueous dispersions and aqueous / oil / aqueous double emulsions. Selected examples and case studies are presented and demonstrate the potential of the device in terms of simultaneous rheo-structural measurements. Extending the applications of the device, section 4.5 illustrates how interfacial tension between two phases can be estimated experimentally from direct observations of a drop of one phase immersed into the other and subjected to controlled steady shear flow. Experimental results are compared with values obtained with a Wilhelmy plate tensiometer for the same oil / aqueous systems.

4.2 Rheometry

Accuracy of rheological measurements is important for the new device. All constructed geometries were calibrated in terms of their inertial contribution to the measurements prior to their rheometric evaluation (as discussed in chapter 3). The latter

involves comparison between measurements carried out with the new optical geometries and standard stainless steel geometries, supplied by Malvern Instruments. Everything else being constant, the results should be identical.

A series of Newtonian silicone oils (SO) has been employed for measurements of shear viscosity. Viscosity of the oil depends on its molecular chain length and the range of tested viscosities covered two orders of magnitude, from $0.01 Pa\ s$ to $1 Pa\ s$. Many systems of industrial interest, such as emulsions and dispersions used in cosmetics and foods, fall well within this range. The oils were subjected to an increasing-decreasing shear rate, extending from $5 s^{-1}$ to $500 s^{-1}$. Comparison between obtained results with the optical glass geometries – cone / plate of $2°$ angle and $55 mm$ diameter (CP 2/55 glass), parallel plate of $40 mm$ diameter (PP40 glass) and with $60 mm$ diameter (PP60 glass) and coaxial cylinders (CC glass) – and viscosities measured with the stainless steel cone / plate of $2°$ angle and $55 mm$ diameter (CP 2/55 steel) and parallel plate of $40 mm$ diameter (PP40 steel), is shown in figure 4.1.

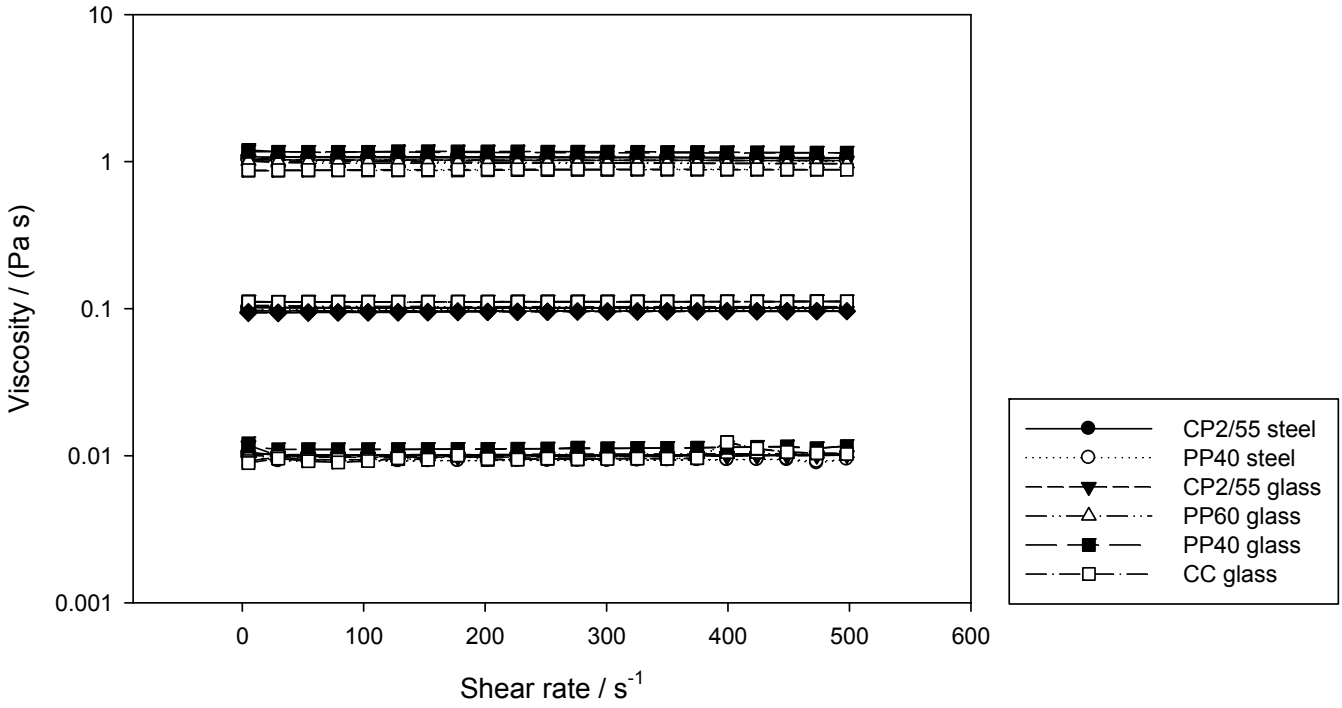

Figure 4.1: Shear viscosity of silicone oils of 0.0096, 0.096, and 0.97 $Pa\ s$ (supplier's values at 25℃) measured with standard stainless steel and customised glass geometries at room temperature, maintained between $20 - 28$℃.

Excellent agreement between measurements with all geometries is demonstrated, suggesting that newly constructed geometries are as good as standard ones in rheological characterisation of liquids. All measurements reveal the Newtonian nature of the liquid and display viscosity values very close to those claimed by the supplier, with average error as low as 8%.

Errors in the measurements may be partially attributed to temperature fluctuations. Variations of viscosity with temperature for Newtonian liquids are typically considered to follow the Arrhenius relationship (equation 4.1), where K_{Ar1} and K_{Ar2} are constants. In the case of water, 3% per 1℃ temperature sensitivity is expected at room temperature [Barnes et

al 1989]. It is remarked that rheological tests were performed at different days for the different geometries, depending on required time for their construction. Room temperature during the tests was recorded between $20-28℃$, varying notably from the supplier's reference temperature of $25℃$.

$$\eta = K_{Ar} e^{-K_{Ar2}/\Theta} \tag{4.1}$$

Other factors contributing to the total error may include geometric factors, such as minor dimensional errors, deviation from parallelism and / or concentricity, or imprecise determination of gap size, as well as experimental errors.

4.3 Image Acquisition

High quality image acquisition is among the major targets of the present project (section 1.2). Image quality has been tested with a variety of different liquid systems and flow conditions. The optical unit has been assessed at quiescent conditions as well as at increasing shear. For the first time reported, clear images of morphologies with resolution of the order of several microns are shown at very high shears, set as high as $20000 s^{-1}$.

4.3.1 Sample at Rest

The main criterion of a good quality image requires that all structures are easily identifiable by visual observations. In the case of discrete droplets, sharp boundaries between continuous and dispersed phases enable automation of image analysis and automatic quantification of size / shape in dilute systems, thus offering an additional advantage, as discussed in chapter 3.

Example images of oil / aqueous dispersions obtained at quiescent conditions with the four new geometries are shown in figure 4.2, ordered from low to high volume fraction of dispersed phase. Samples have been prepared by gentle mixing of relevant quantities of silicone oil and mixtures of hexylene glycol / water or hexylene glycol / glycerol (referred to as HGW and HGG respectively from now on) to prepare samples of $50mL$. Detailed description of sample preparation is not considered essential here as it is presented in section 5.2. Images have been captured just before or after cessation of a $5min$ shearing at $250s^{-1}$. Parallel plate images refer to the rim of the top plate, where actual pre-shearing rate was $330s^{-1}$ (see section 4.4.1 and equation 4.2). Gap size between the plates was maintained to a standard $1mm$.

Figure 4.2 demonstrates very good quality images for all new geometries with good contrast between drops and continuous phases. Dilute samples of $\varphi \leq 0.05$ show clear, discrete drops and are easily analysed by automated computer software. At higher volume fractions of dispersed phase images can be quantified with the semi-automated software Bubble Pro, where drops are identified manually and analysed automatically (chapter 3).

Geometry	$\varphi = 0.02$	$\varphi = 0.1$	$\varphi = 0.3$
CC	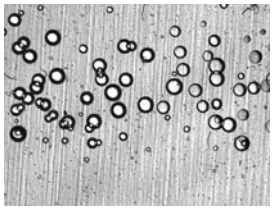	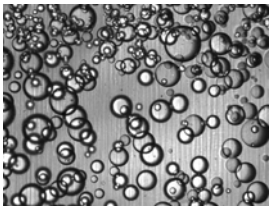	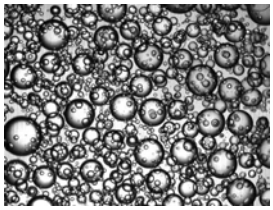
PP40	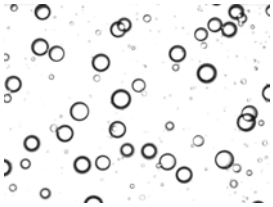	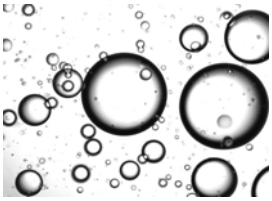	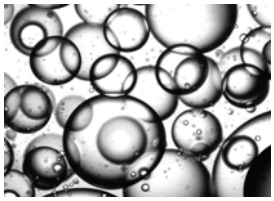
PP60	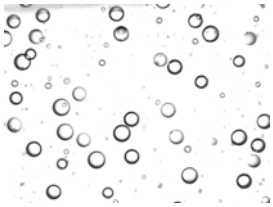	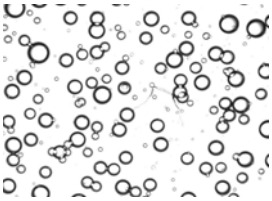	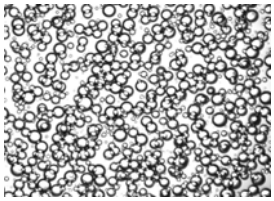
2/sdfasd	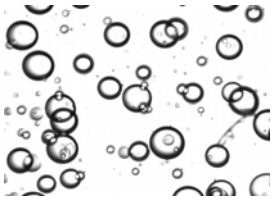	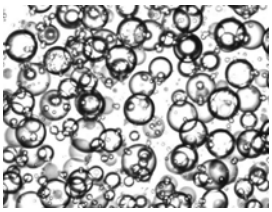	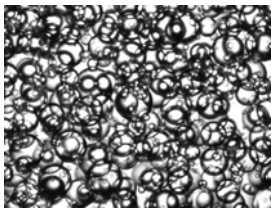

Figure 4.2: Images of dispersions of silicone oil in hexylene glycol / water or hexylene glycol / glycerol mixtures at rest captured with the four new geometries, CC, PP40, PP60 and CP2/55 and at $\varphi = 0.02$, 0.1, and 0.3. (Image width $2.4mm$)

Image quality depends, among other factors, on concentration of the recorded dispersed entities in the image (number of entities per unit area). Large numbers of recorded drops per unit area of the image result in unclear images with high degree of drop overlapping and, in the case of large gap sizes, a significant number of out-of-focus drops. In those cases, image analysis may then be prohibited unless the number of recorded drops in the captured

image is reduced either by sample dilution or minimisation of sample volume (smaller gap). The effect of reducing gap size in PP geometries is shown in figure 4.3.

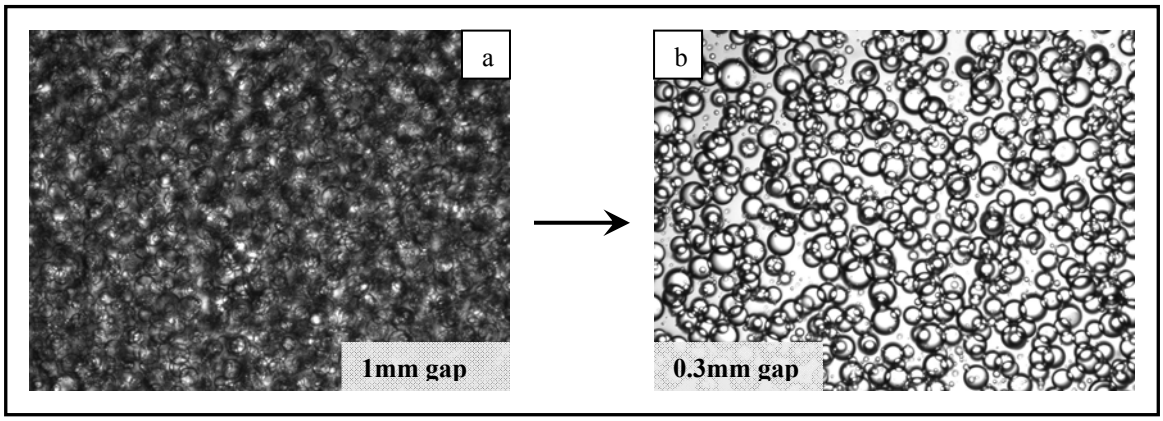

Figure 4.3: Effect of gap size reduction in image quality of an oil / aqueous dispersion. Images were captured with PP60 at (a) $1mm$ and (b) $0.3mm$ gap. (Image width $2.4mm$)

Lowering of gap size, which may substantially improve image quality (as illustrated in figure 4.3), is straightforwardly offered by the plate / plate geometries, but may involve several complexities if implemented with other geometries. Small gap sizes may also be obtained with measurements at low radius of the cone / plate geometries. Considerations dictating the lower limit of gap sizes practically valid for an experiment include the requirement for a $5-10$ times difference between maximum drop diameter and gap size [section 2.3.2] as well as errors in rheological measurements due to possible inaccuracies in determination of gap dimensions and / or parallelism. It should be kept in mind that the significance of geometric as well as wall slip errors is magnified as gap decreases. Gap size reduction has also been employed to improve image quality at increasing shear rates, discussed later in this chapter. For the case of figure 4.3, it appears that drop size is

comparable to the small gap size (0.3mm), and therefore the validity of any rheological measurements obtained with the small gap size is questionable and should be carefully tested.

Image acquisition has been further tested with systems that are generally considered more difficult to capture than single oil / aqueous dispersions. Figure 4.4 illustrates very good quality images of double emulsions and aqueous / aqueous systems at rest. Double emulsions are characterised by a drop-in-drop structure, as the primary emulsion, already containing droplets, is dispersed in a secondary continuous phase. Aqueous / aqueous systems are often considered more difficult to capture because of similar refractive indices between the two aqueous components. In addition, structures frequently deviate from the strict morphology of drops dispersed in continuous phases, seen so far [Spyropoulos 2007, also evident in figure 4.4].

Primary emulsion of aqueous / oil / aqueous sample was prepared by mixing $170g$ of continuous phase (10% span 85 in sunflower oil) with $30g$ HG at $800rpm$ for $5min$ with a Silverson mixer. Secondary emulsion was then prepared by gentle mixing of $7.5g$ primary emulsion with $42.5g$ secondary continuous phase (2% triton in HG), to produce 15% dispersion. Concentrations of surfactants have been chosen empirically to produce kinetically stable systems for the duration of the experiment.

Aqueous / aqueous systems of dextran (10% wt/wt) / gelatine (10% wt/wt), SDS (10% wt/wt) / gelatine (10% wt/wt) and SDS (12% wt/wt) / pullulan (12% wt/wt) were produced by gentle mixing of $7.5g$ dispersed phases with $42.5g$ continuous phases. Gelatine was dissolved at 80℃, immediately mixed with dispersed phase and rapidly loaded to the geometry. Images were taken within $3min$ from sample preparation to avoid gelation occurring at cooling of sample to room temperature.

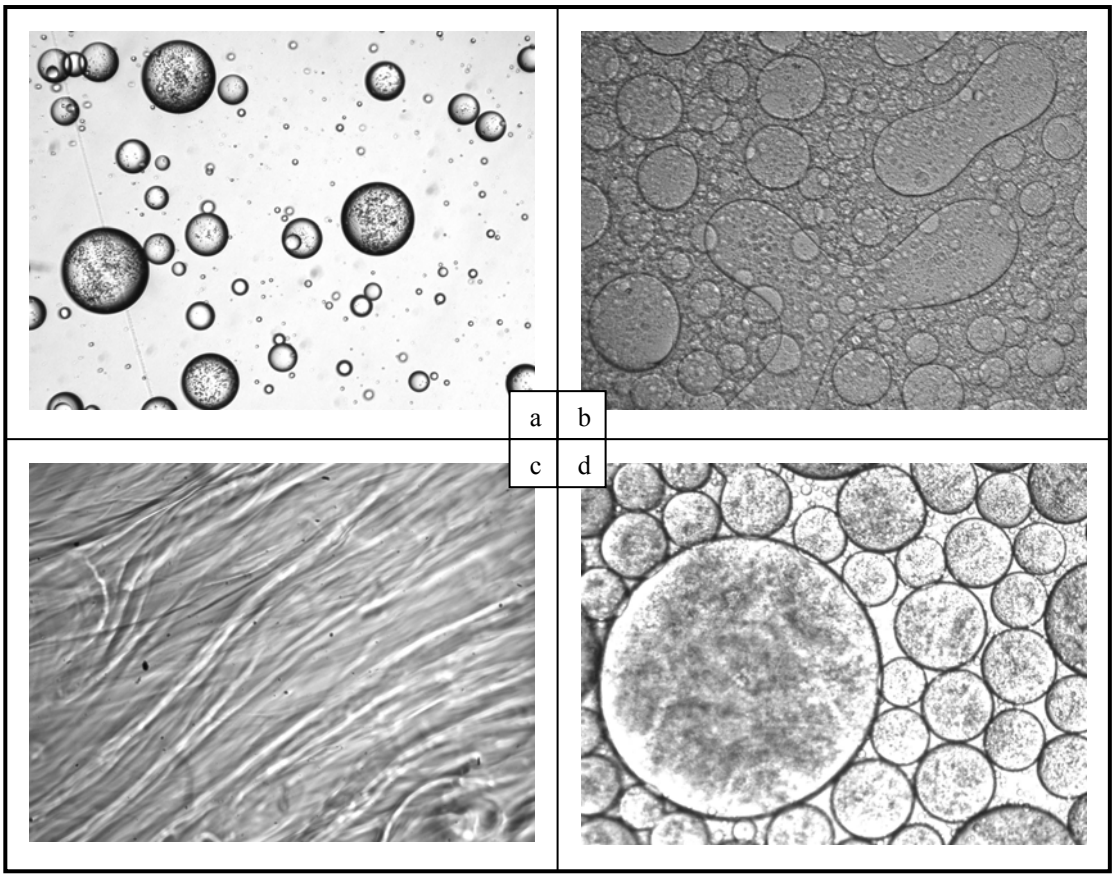

Figure 4.4: Image evaluation in complex structures: (a) aqueous / oil / aqueous double emulsion; (b) dextran / gelatine system; (c) SDS / gelatine; (d) Dextran / PEG. (Image width $1.2mm$, various geometries used.)

4.3.2 Sample Under Shear Flow

When a sample is subjected to shear, different types of microstructure can form depending on properties of the sample such as volume fraction of dispersed phase, φ, viscosity ratio between dispersed and continuous phases, λ, and interfacial tension, τ. Possible morphologies range from deformed drops to thread-like formations and bi-continuous structures [Spyropoulos 2007].

Figure 4.5 demonstrates high image quality at medium shear rates for a variety of different systems and morphologies. Oil / oil dispersion was prepared by gently dispersing $5g$ sunflower oil into a $45g$ mixture of silicone oils ($5cSt: 10cSt = 4:1\ wt/wt$). Aqueous / oil / aqueous double emulsion and aqueous / aqueous systems were prepared as described previously.

The structure of image 4.5.a, showing deformed drops orientated to the direction of the flow, is typical for single oil / aqueous and aqueous / oil dispersions. Quantification as well as prediction of the drop's deformation and / or orientation under shear has drawn the attention of a number of researchers due to its relevance in determination of morphology and therefore to a certain extend texture of industrially relevant systems [for example Lin & Guo 2007, Yu et al 2002, Jansen et al 2000, Maffettone & Minale 1998, De Bruijn 1989, Bentley & Leal 1986]. Studies on drop behaviour under shear require optimum quality experimental data, where the shape of the drops is clearly indicated, and figure 4.5.a demonstrates the suitability of the new device for such experiments.

The typical sheared double emulsion of image 4.5.b shows the characteristic drop in drop structure. For the specific system and under current optic specifications, drop deformation is only evident in the secondary (oil / aqueous) emulsion, while aqueous drops of the primary emulsion are seen as small dots.

The two images showing aqueous / aqueous systems, figures 4.5.c and 4.5.d, illustrate morphologies that deviate from the typical microstructure of drops dispersed in continuous phase. Such morphologies can be solidified for example by gelation or temperature reduction and are potentially of importance in industries such as the food industry, where manufacturing

of a required microstructure is often determinant of the quality of the final product. Gelation of aqueous / aqueous systems is discussed in more detail in section 5.5.

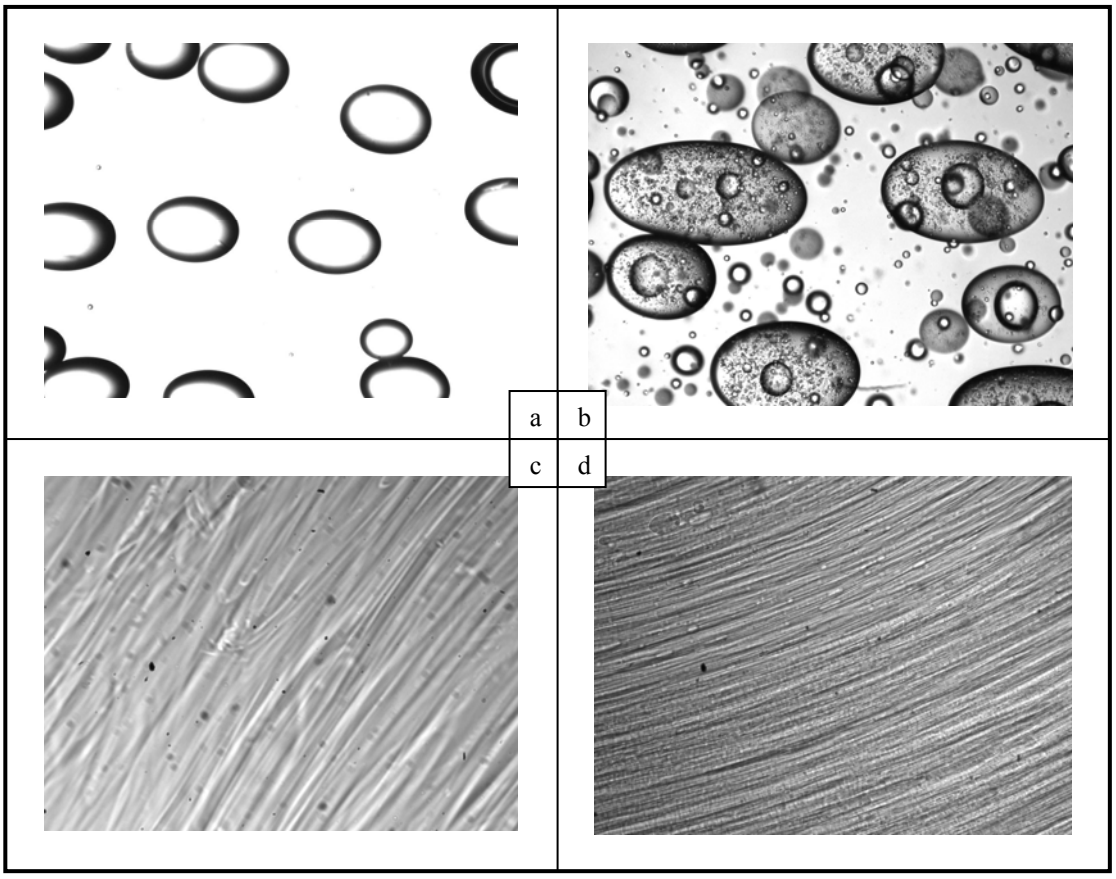

Figure 4.5: Systems under shear: (a) oil / oil dispersion at $250s^{-1}$; (b) aqueous / oil / aqueous double emulsion at $20s^{-1}$; (c) SDS / gelatine at $10s^{-1}$; and (d) dextran / gelatine at $100s^{-1}$. (Image width $1.2mm$, various geometries used.)

As shear rate further increases, there are additional difficulties involved with image acquisition, often related to drop size reduction and increase in number as well as the rapid movement of the fluid. As a result, there is a lack of simultaneous rheological and microstructural observations at very high shears in the literature.

With the current setup it was possible to attain high quality images at shears set as high as $20000s^{-1}$. Such high shear rates were achieved using the plate / plate geometries and reducing gap size as required (see equations 2.3 and 2.45). Selected images are shown in figure 4.6 (i). Measurements have been carried out with the parallel plate arrangement and gap size was adjusted as required to optimise image clarity. It is remarked that although image quality in figure 4.6 has been electronically enhanced, pictures on full screen appeared significantly clearer, therefore easier to quantify / analyse.

It is evident from figures 4.5 and 4.6 that very high quality images can be acquired with the new device for a range of different samples and flow conditions. For morphologies of the investigated systems, images taken at medium and high shear rates up to $10000s^{-1}$ can be quantified (determine size, description of shape, etc), as shown in figure 4.6 (ii). At higher shear rates it appears that with the current optics only qualitative analysis can be obtained. It should be noted, however, that at such high shear rates and small gap sizes, it becomes questionable whether rheological measurements using rotational rheometers are reliable and more work is required before reaching specific conclusions and recommendations.

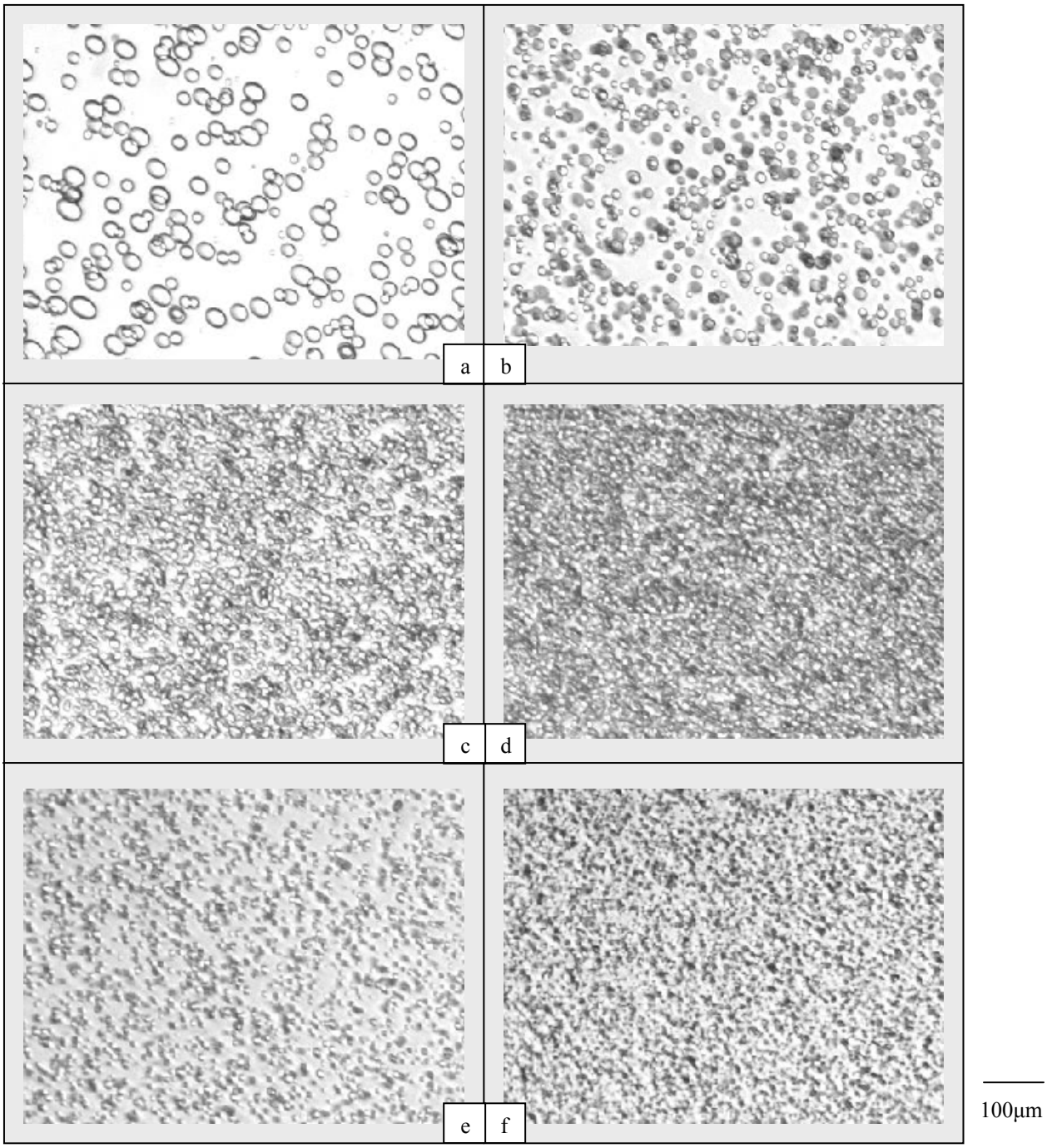

Figure 4.6 (i): Images of oil/aqueous dispersions at increasing shears. (a) $5000s^{-1}$; (b) $10000s^{-1}$; (c) $10000s^{-1}$; (d) $13000s^{-1}$; (e) $16000s^{-1}$; (f) $20000s^{-1}$. Volume fraction is 0.1 (a), (b) and (e); 0.2 for (c), (d) and (f). Images captured with PP60 geometry.

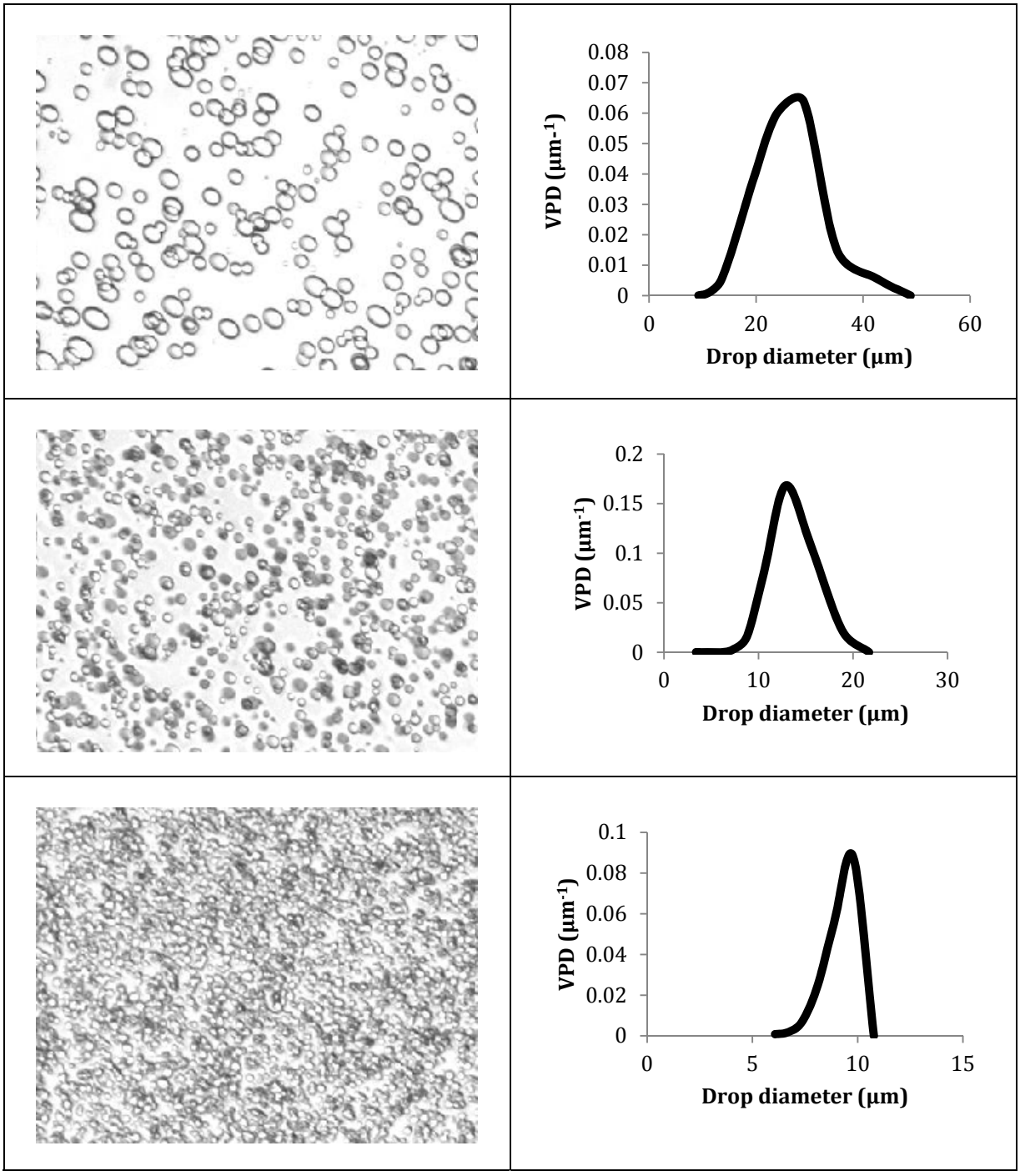

Figure 4.6 (ii): Drop size distributions (Volume Probability Density) of sheared O/W systems corresponding to images of figure 4.6 (i). (a) $5000s^{-1}$, φ=0.1; (b) $10000s^{-1}$, φ=0.1; (c) $10000s^{-1}$, φ=0.2. Images captured with PP60 geometry.

4.4 Simultaneous Recordings

Simultaneous rheological and microstructural recordings of different systems and flow conditions are presented below and the link between structure evolution and shear is illustrated.

4.4.1 Shear Profile of Parallel Plates: a Case Study

Good control of flow conditions is critical in rheo-structural experiments. Unlike CC and CP, where constant shear rate is assumed throughout the gap, shear rate in PP varies with distance along the radius of the top rotating plate from zero in the centre to maximum at the perimeter (chapter 2). The non uniform application of stress has been cited as a disadvantage for rheological measurements because the sample is subjected to a varied shear and the value of imposed shear rate is therefore an average value [see for example Mezger 2006, Rosenthal 1999].

In simultaneous rheological and morphological experiments, however, the same feature may prove to be advantageous as it offers the possibility of visual inspection of the investigated sample under a range of shear rates in a single measurement, simply by capturing images at different positions along the radius of the top plate. This is illustrated below for the two extreme positions, close to the centre ($r_c = 7mm$) and at the rim of the plate ($r_p = 30mm$) in figure 4.7.

In parallel plates geometries, shear rate is controlled by the software at position $r = \frac{3}{4} r_p$, where r_p is the radius of the top plate [personal communication with Malvern Instruments]. In any other position, imposed shear rate can be calculated from equation 4.2.

$$\dot{\gamma}_x = \dot{\gamma}_p \cdot \frac{4}{3} \cdot \frac{r_x}{r_p} \tag{4.2}$$

Figure 4.7 shows images recorded at r_P and r_c for a 5% oil / aqueous dispersion (20cSt silicone oil dispersed in hexylene glycol / glycerol mixture). Shear rate was set to increase from $5s^{-1}$ to $500s^{-1}$. According to equation 4.2, therefore, shear rate at the two positions r_c and r_P ranged between $1.6 - 156s^{-1}$ and $6.7 - 667s^{-1}$ respectively. The results in figure 4.7 are from two separate experiments, each conducted with freshly prepared system, where images were recorded at the edge and centre of the plate, respectively. The system exhibited Newtonian behaviour with relative viscosity of the order of 1. In figure 4.7, the image captured at $67s^{-1}$ was selected as an example showing an elongated, unstable drop, which further deformed and broke into smaller droplets and it is not representative of the steady drop shape / size.

The difference in structural evolution recorded at the edge and centre of the parallel plate geometry clearly demonstrates the potential of the device for simultaneous rheo-structural recordings at selected shear rates or at a continuous ramp of shear rates simply by altering the position of the image-capturing unit along the radius of the plates. Automation of

the feature would offer easy and accurate investigations of a sample at different shear rates with a single measurement, offering an advantage for future commercialisation.

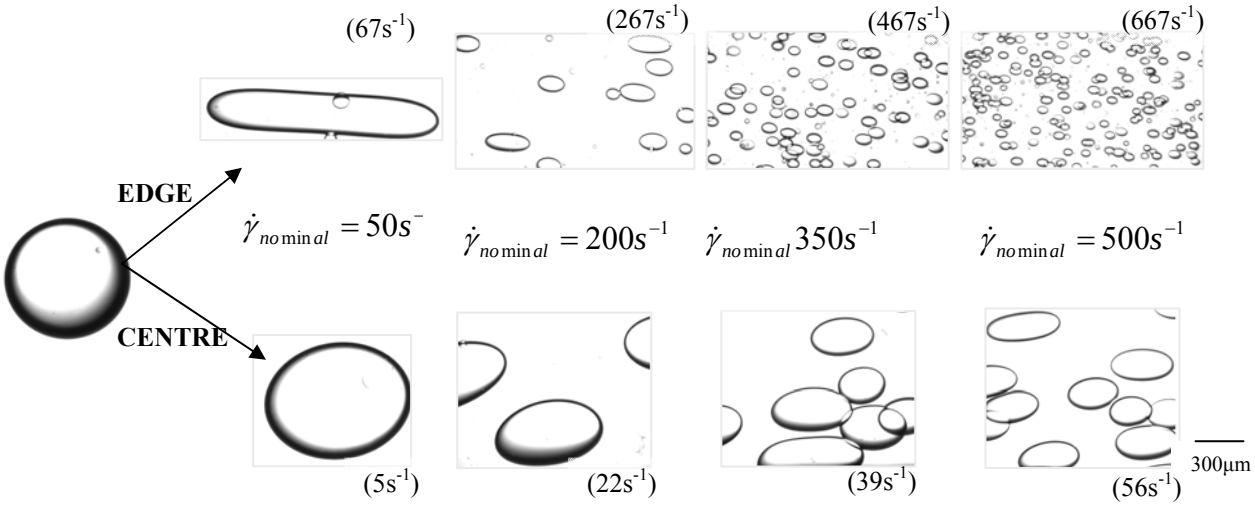

Figure 4.7: Drop deformation of 5% oil/aqueous dispersion at the rim and near the centre of a PP of $60mm$ diameter. Nominal shear rates refer to set shear rates imposed by the rheometer; actual shear rates (shown in brackets) are calculated from eq. 4.2.

4.4.2 Oil / Aqueous Dispersions: Non-Newtonian Behaviour Induced at Increasing φ

It is well established in the literature that microstructural changes occurring during shearing of oil / aqueous dispersions at increasing concentration of dispersed phase may induce shear thinning behaviour [Barnes 1989, Pal 1996]. Experimentally, Teipel [2002] observed shear thinning in emulsions of paraffin oil in water for $\varphi > 0.15$ and Krynke and Sek [2004] reported power-law index of the order of 0.81 for a $\varphi = 0.5$ system of sunflower oil in rokafenol (all phases Newtonian). Interestingly, Jansen et al [2001] showed, but did not comment on, increasing shear thinning behaviour for systems at increasing φ and phase

composition very similar to systems of the present study: silicone oil dispersed in aqueous mixtures of hexylene glycol with water and polyacrilic acid. From a theoretical approach, Pal [2007] and Yu et al [2002] have suggested model equations that correlate the viscosity of the two phase dispersion with φ and Ca, which predict shear thinning behaviour as volume fraction of dispersed phase increases (section 2.2). However, morphological characteristics are generally absent from model equations predicting the relative viscosity of two phase systems (table 2.1).

Despite considerable progress, the relationship between rheology and morphology is still a subject of extensive investigation [Saiki et al 2007]. Experimentally, there is limited information on the effect of certain emulsion properties, such as drop size and / or drop deformability, on rheology, which may be partially attributed to the limited methodology available. As those properties are often system specific, they are difficult to study without optimum quality simultaneous rheo-structural methods. The suitability of the new device for such studies is illustrated here with an example of shear thinning induced at increasing volume fraction of dispersed phase ($0.05 \leq \varphi \leq 0.3$) for an oil / aqueous dispersion.

Dispersions of silicone oil (of $100cSt$, $\eta_d = 0.095Pa\ s$) in hexylene glycol / glycerol mixture ($wt/wt = 5.45$, $\eta_c = 0.072Pa\ s$) had viscosity ratio $\lambda = 1.3$ and were prepared by gentle mixing of the two phases as described in section 4.3, to produce systems of $\varphi = 0.05$, 0.1, 0.2 and 0.3. Experiments have been conducted with the optical coaxial cylinders geometry.

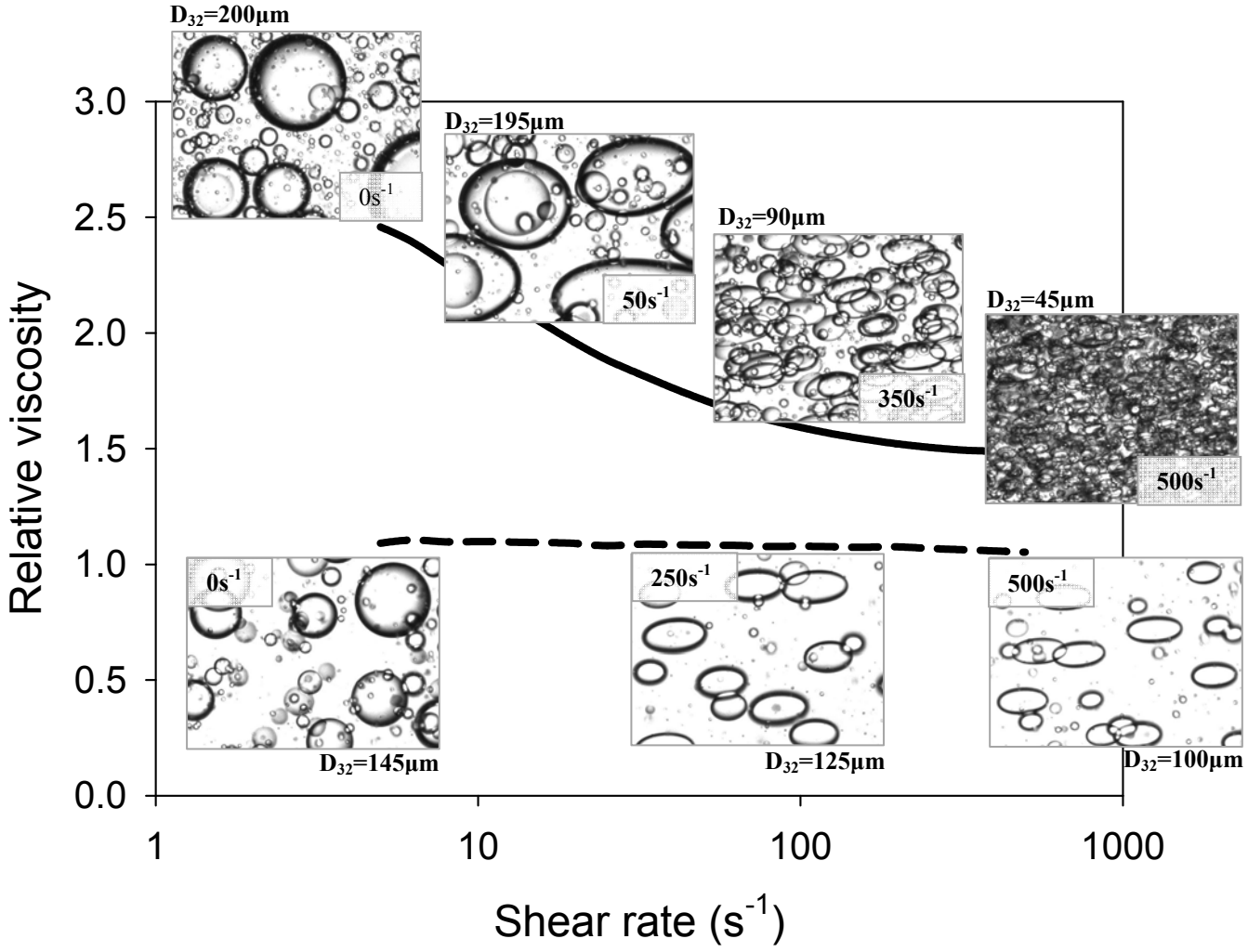

Figure 4.8: Rheology and structure of oil / aqueous dispersion of $\lambda = 1.3$, at $\varphi = 0.05$ (dashed line) and $\varphi = 0.3$ (solid line) under increasing shear. Enhanced shear thinning is observed at high φ. Image width $1.2mm$. (note: rheological data and images at $\varphi = 0.05$ were obtained with gap size $1mm$; images at $\varphi = 0.3$ were captured at gap size of $0.5mm$). Experiments with CC geometry.

Figure 4.8 shows flow curves and associated microstructures of the system at $\varphi = 0.05$ and $\varphi = 0.3$ at increasing shear rate from $5s^{-1}$ to $500s^{-1}$. At $\varphi = 0.3$, enhanced shear thinning behaviour is observed $(n = 0.85)$. Intermediate volume fractions ($\varphi = 0.1$ and $\varphi = 0.2$) demonstrated gradual shear thinning enhancement as φ increased (not shown).

At $\varphi = 0.05$, shear viscosity was only slightly affected by the presence of dispersed phase, and relative viscosity was just above unity. The system showed near-Newtonian behaviour with power-law index of $n > 0.95$. Sauter mean diameters, defined in equation 4.3 where $p = 3$ and $q = 2$ [Leng & Calabrese 2004], were $165\mu m$ before shearing and $100\mu m$ at $\dot{\gamma} = 250s^{-1}$.

$$D_{pq} = \left(\frac{\sum n_i D_i^p}{\sum n_i D_i^q}\right)^{1/(p-q)} \tag{4.3}$$

At $\varphi = 0.3$, enhanced shear thinning response was recorded on increase of shear rate from $5s^{-1}$ to $500s^{-1}$ and power law index reduced to $n = 0.85$. For this experiment, calculated Taylor number (of the order of 1, equation 2.34) is much smaller than the critical Taylor number (of the order of 1700, equation 2.34) and therefore inertial instabilities and Taylor vortices are unlikely to have occurred. In addition, the effect of centrifugal phase separation is also considered small, as the densities of continuous and dispersed phases were matched to ensure (kinetic) stability of the system. It is suggested that observed shear thinning is at least partially associated with significant microstructural changes occurring at increasing of shear rate, as shown in figure 4.8, causing the system to be practically processed. Drop breakage resulted in a 80% reduction in D_{32}, from $200\mu m$ before shearing to $45\mu m$ at $\dot{\gamma} = 500s^{-1}$. It should be remarked, however, that large drops present at high φ might have interferred with the measurement, through bridging and end effects, causing an artificial increase in measured viscosity, especially at the initial stages of the experiment. Favourable orientation of drops to the direction of flow is also evident in figure 4.8 and it is expected to

play a key role in observed shear thinning. However, it has been difficult to quantify with the current setup due to the fact that position of the camera is not accurately controlled. It is therefore difficult to accurately identify the direction of the flow in the captured images.

4.4.3 Shear Induced Destabilisation of a Double emulsion

Double emulsions are emulsions of emulsions, with a droplet-in-droplet structure (section 4.3.1). They are used in a plethora of applications, foods, pharmaceuticals, cosmetics and detergents to name but a few [Dickinson 2011, Jiao and Burgess 2003]. Often in commercial products the internal dispersed droplets contain a functional substance required to be released under specific conditions, and it is said to be encapsulated. A detergent's perfume, for example, is required to be preserved during washing and released upon rubbing of the cloth with the body, while a hand cream is expected to provide its moisturising molecules on application to the hand.

The effect of well controlled shear flow on destabilisation of a double emulsion and release of the innermost phase can be easily investigated with simultaneous rheological and microstructural measurements. In the present study, the freshly prepared aqueous / oil / aqueous double emulsion was subjected to shear rate of $20s^{-1}$ for $10min$. Destabilisation of the double emulsion and release of internal drops with time of shearing is shown in figure 4.9. Aqueous / oil / aqueous samples were prepared in a two step process, as described in section 4.3.1. Experiments have been conducted with the PP40 geometry and images have been recorded at the rim of the top plate. Nominal set shear rate was $15s^{-1}$.

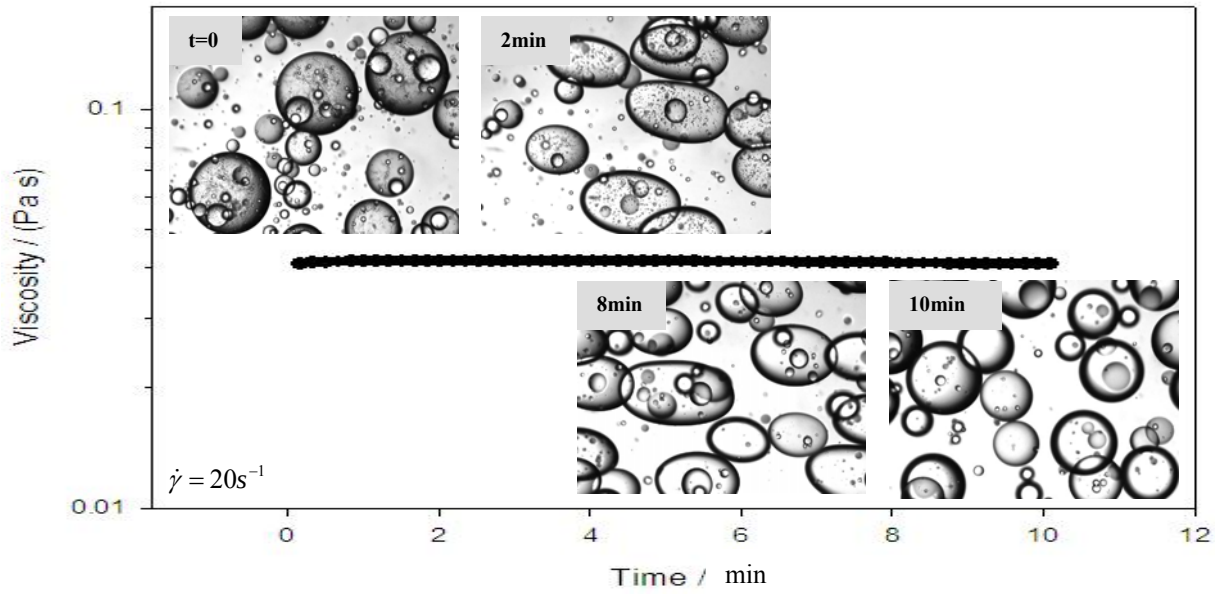

Figure 4.9: Simultaneous rheology and microstructure of an aqueous / oil / aqueous sample sheared at $20s^{-1}$ for $10min$ reveals gradual destabilisation of the double emulsion and release of inner drops with time of shearing whilst viscosity remains practically constant. (Image width $1.2mm$, experiments with PP40 geometry.).

Figure 4.9 demonstrates gradual reduction of the inner drops concentration with time of shearing. After 8 minutes of shearing the double emulsion is effectively destabilised to produce a single oil / aqueous dispersion. This destabilisation process only marginally affects viscosity of the system, which remains practically constant throughout the duration of the experiment. Emulsion destabilisation, therefore, could not be detected by rheological measurements alone. The effect of shearing on destabilisation of the primary emulsion is illustrated more clearly in figure 4.10, where initial morphology of the freshly prepared aqueous / oil / aqueous double emulsion is compared with the structures of (i) sheared and (ii) un-sheared sample observed 10 minutes later.

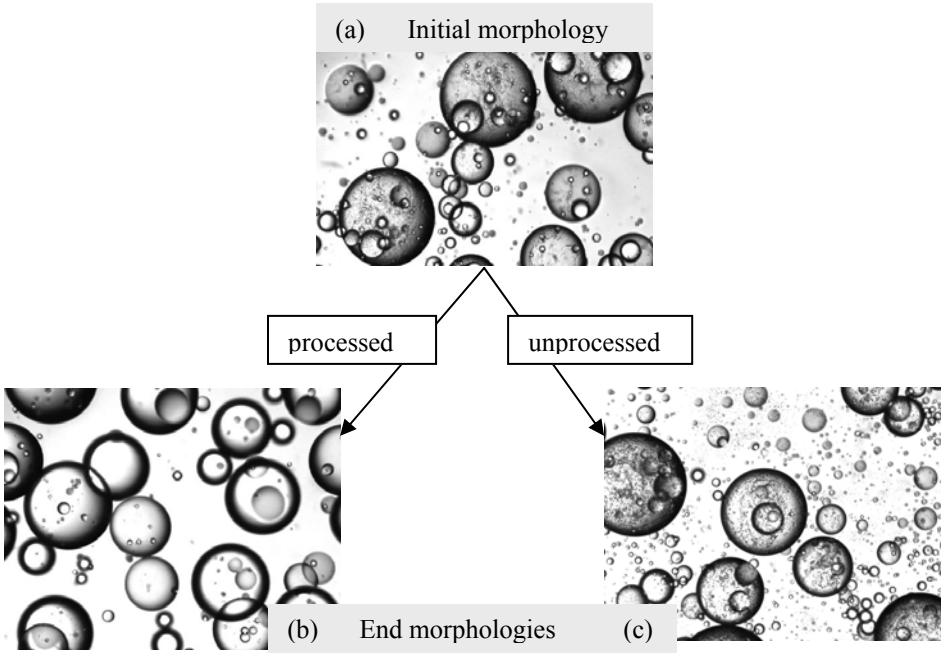

Figure 4.10: Images of an aqueous / oil / aqueous double emulsion (a) freshly prepared; (b) after 10min of shearing at $20s^{-1}$; (c) after 10min at quiescence. The effect of shearing on release of inner drops is very clear. (Image width $1.2mm$, experiments with PP40 geometry).

Comparison between the three images of figure 4.10 shows that for the particular product, 10 minutes of processing at low to medium shear rates ($\dot{\gamma} = 20s^{-1}$) practically destabilised completely a system that without shearing appears stable. In addition, it seems that while shearing released nearly 100% of drops of the primary emulsion, the viscosity of the product is maintained practically unchanged. However, further quantification of destabilisation rate seems difficult with the current optics.

The present study illustrated the potential of the device in studying the effect of flow on double emulsion destabilisation. By carefully choosing applied flow conditions, different industrial or medical / biological processes can be simulated, and their effect on stability of double emulsions investigated. Similar experiments, therefore, may provide a highly promising methodology in the field of controlled release technology.

4.4.4 Shear Induced Coalescence

Coalescence, i.e. the physical merging of dispersed entities, is an important phenomenon, often playing a crucial role in the determination of the morphology of multiphase liquid systems [Lyu et al 2000]. It may occur at quiescence, when it is sometimes termed as static coalescence, or under flow [Utracki 2002; Lyu et al 2000]. Despite its great importance, the extent of published literature on experimental studies of drop coalescence is still limited [Leal 2004; Lyu et al 2000]. Lack of experimental data has been partially attributed to technical difficulties involved with measurements of drop sizes and drop size distributions under well controlled flow conditions [Lyu 2000]. In this section, the suitability of the new device on such recordings is considered.

The investigated system for this study consisted of $100cSt$ silicone oil ($0.1Pa\,s$ measured with the customised cone / plate optical geometry) dispersed in a mixture of hexylene glycol (84.5%) with glycerol (15.5%). Continuous phase viscosity was measured, $0.085Pa\,s$, and viscosity ratio was determined, $\lambda = 1.2$. Volume fraction of the silicone oil was kept constant at $\varphi = 0.2$. Experiments have been conducted with the cone / plate optical geometry.

The effect of gentle shearing on coalescence was monitored by pre-shearing the dispersion at $\dot{\gamma}_1 = 500s^{-1}$, thus inducing considerable drop breakage, followed by a subsequent single step reduction in shear rate to $\dot{\gamma}_2 = 1s^{-1}$. Structure evolution was recorded at $8fps$ to allow accurate capturing of drop coalescence. For comparison, the same experiment was repeated, but this time the sheared dispersion was left at quiescence, $\dot{\gamma}_2 = 0s^{-1}$.

Recorded increase in Sauter mean diameter for the two experimental conditions is presented in figure 4.11. Selected images supporting findings of figure 4.11 are shown in figure 4.12. Both figures prove the suitability of the new device in experimental studies of drop coalescence and suggest that, at least for the specific oil / aqueous system, coalescence was significantly facilitated by gentle shearing.

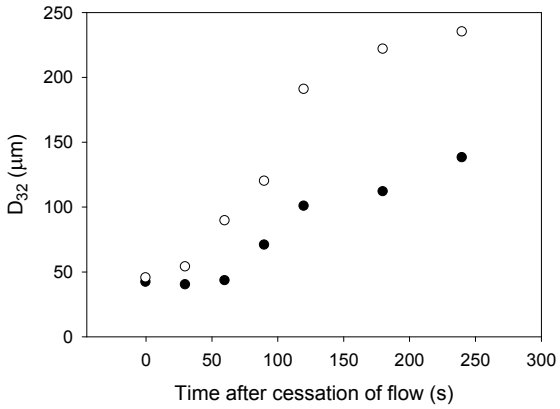

Figure 4.11: Shows the effect of (gentle) shearing on drop coalescence after structure breakage by shearing at $\dot{\gamma}_1 = 500s^{-1}$. Sauter mean diameters are plotted against time after cessation of $\dot{\gamma}_1$ and subsequent $\dot{\gamma}_2 = 0s^{-1}$ (black dots) or $\dot{\gamma}_2 = 1s^{-1}$ (white dots). Experiments with CP2/55 geometry.

Time (s)	$\dot{\gamma}_2 = 0s^{-1}$	$\dot{\gamma}_2 = 1s^{-1}$
0	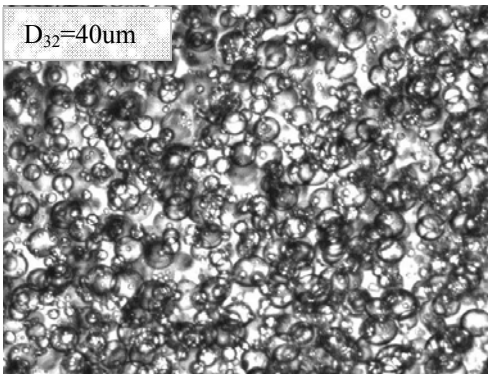	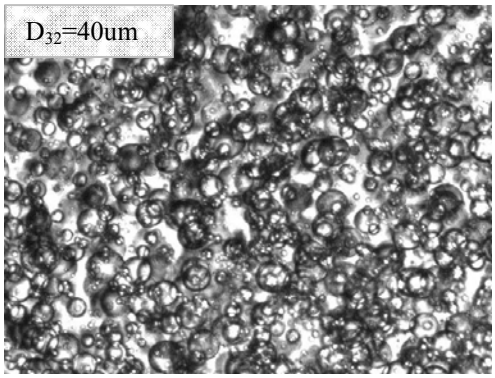
60	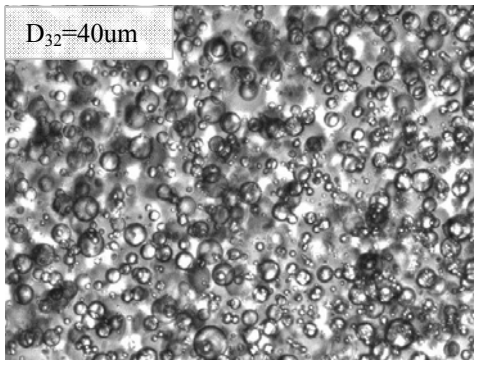	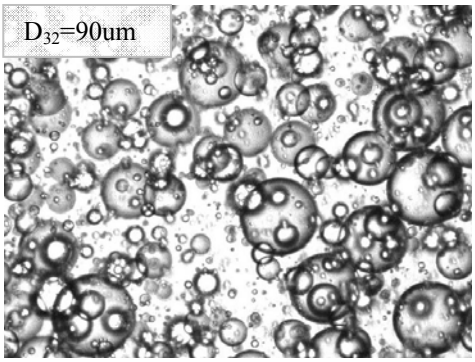
120	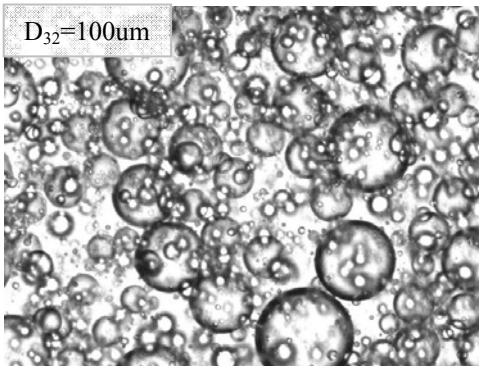	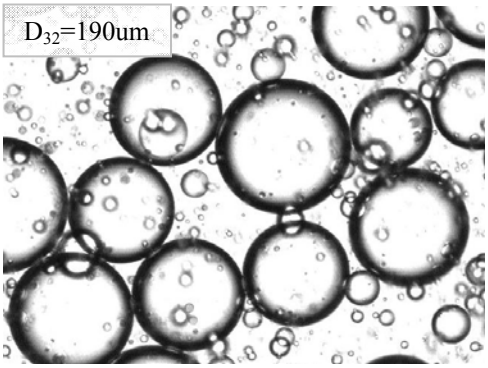

Figure 4.12: Indicative images of oil / aqueous dispersion showing coalescence after shearing at $\dot{\gamma}_1 = 500s^{-1}$, and subsequent $\dot{\gamma}_2 = 0s^{-1}$ (2nd column) or $\dot{\gamma}_2 = 1s^{-1}$ (3rd column). Fist column shows time after cessation of $\dot{\gamma}_1$. (Image width $1.2mm$, experiments with CP2/55 geometry)

Figure 4.12 also indicates that coalescence caused changes in drop size distributions over time. For coalescence under gentle flow of $1s^{-1}$ this is more clearly illustrated in figures 4.13 and 4.14. Figure 4.13 shows the evolution of different mean drop sizes, as defined by equation 4.3, with time of coalescence. Variation between different mean diameters is an indication of the degree of poly-disparity, them being equal only in the case of purely mono dispersed systems [Padron-Aldana 2005]. Figure 4.13 therefore indicates gradual widening of drop size distributions with time of coalescence.

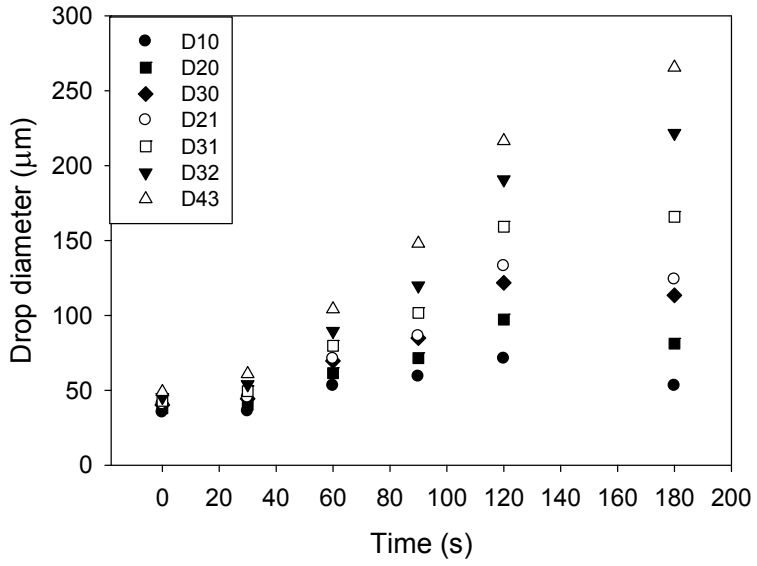

Figure 4.13: Mean drop diameters against time of coalescence at $\dot{\gamma} = 1s^{-1}$. Experiments with CP2/55 geometry.

Figure 4.14 shows the measured drop size distributions, corresponding to images and conditions shown in figure 4.12, i.e. at times $t = 0s$, $60s$ and $120s$ after cessation of shearing. Clearly, figure 4.14 illustrates an increase of drop sizes as well as widening of drop

size distributions as drops coalesce with time. Closer inspection of figure 4.14 shows that drop size distribution evolves from a narrow normal-shaped to bimodal (at $t = 60s$) and further to wide normal-shaped (at $t = 120s$). Transition from small to large drops via bimodal distribution may indicate that coalescence initially occurred in a fraction of small drops, of the order of $60\mu m$, which by coupling together resulted in the formation of few larger entities, of the order of $120\mu m$. The remaining small drops subsequently merged to the larger drops with time. Hence, the population of small drops sees gradually reduction simultaneously with a corresponding increase in average drop size. However, in order to draw solid conclusions about the coalescing mechanism, more work is required.

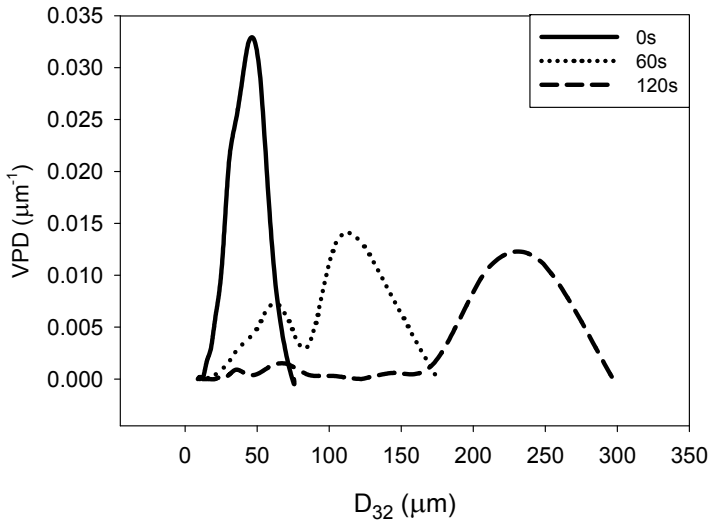

Figure 4.14: Drop size distributions (Volume Probability Density) of the coalescing system under gentle shear ($\dot{\gamma} = 1s^{-1}$) at times $t = 0s$ (solid line), $60s$ (dotted line) and $120s$ (dashed line) after cessation of a $\dot{\gamma} = 500s^{-1}$ flow. Experiments with CP2/55 geometry.

4.4.5 From Shelf to Lab: French Style Dressing

In this section, rheology and microstructure of a real commercial product found at the shelves of supermarkets are shown. French style dressing is a popular salad dressing, essentially consisting of an oil / aqueous (vegetable oil in vinegar) system. A typical, full fat French style dressing found in a shelf of a supermarket has oil concentration of the order of $40-50\%\, wt/vol$ [according to the manufacturers]. Under shearing flow conditions, full fat salad dressings undergo shear thinning, partially due to their high oil concentration, as also discussed in section 4.4.2. In recent years, due to the trend for healthier and less fattening foods, low fat or zero fat substitutes of French dressing are available in the market. Those options should mimic the properties of the original food as closely as possible, and therefore there is a requirement for similar shear thinning behaviour.

To illustrate the similar rheological response between the original food and the less fattening substitute, a full fat ($45\%\, wt/vol$) and a low fat ($2\%\, wt/vol$) French style dressings, perchased from local supermarket, were subjected to increasing shear rate between $5s^{-1}$ and $500s^{-1}$. Obtained flow curves of the two products are shown in figure 4.15, where images of the full fat version at increasing shear are also shown. For comparison, the recorded image of the low fat product, showing absence of oil drops, is also included. Experiments were conducted with the cone / plate geometry.

In figure 4.15, the two products show qualitatively the same viscosity response on imposition of shear. Curves are not very smooth, and this might be the effect of wall slip at such high oil volume fractions. Power law indices for the full and low fat versions were estimated at $n = 0.37$ and $n = 0.34$, respectively, confirming their similarity in terms of shear thinning. Franco et al [1995] have studied the rheological response of salad dressing

emulsions with oil content of 55% wt/vol at increasing shear rate between $1\,s^{-1}$ and $300s^{-1}$. For the range of $5s^{-1} \leq \dot{\gamma} \leq 300s^{-1}$, they reported a power law decrease in recorded viscosity similar to that shown in figure 4.15. Reported viscosities ranged approximately between $2Pa\ s$ and $0.2Pa\ s$, and power law index was of the order of $n = 0.3$.

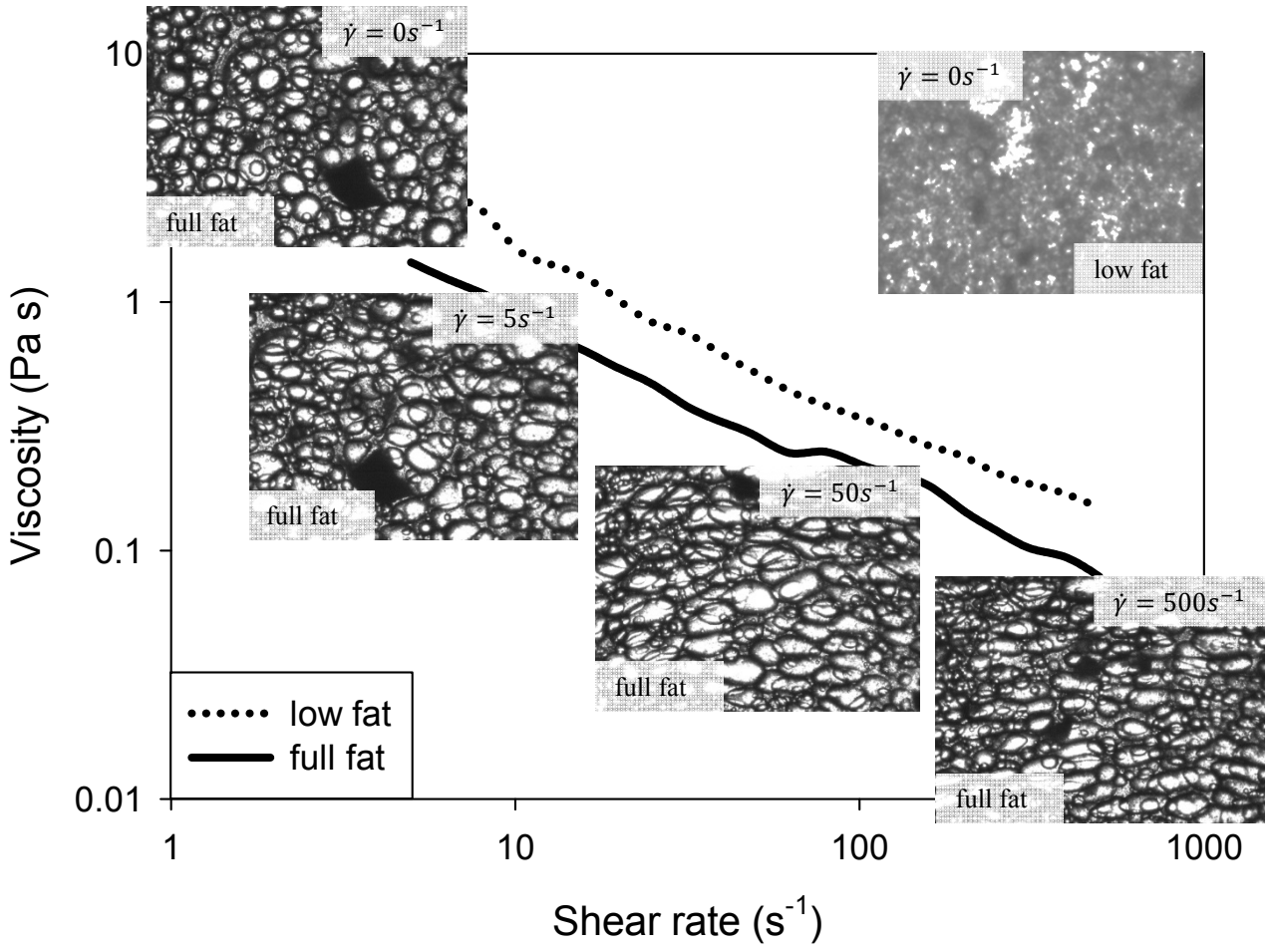

Figure 4.15: Flow curves and images of full fat and low fat French style salad dressings. Image width $2.4mm$. Experiments with CP2/55 geometry.

Figure 4.15 also illustrates the potential of the device to capture high quality images at high dispersed phase concentrations. As shear rate increases, oil drops of the full fat product

are shown to structure themselves to the flow, deform, break, and favourably orientate to the flow direction, thus inducing the observed shear thinning. By contrast, there are virtually no oil drops in the image corresponding to the low fat version, and rheological response is engineered artificially by addition of fat mimetic agents. Indeed, there is a number of works dedicated to the production of fat mimetic agents for salad dressings, where agents of different composition and properties are suggested [for example Bauer et al 1991].

4.5 Estimation of Interfacial Tension with Simultaneous Rheo-Structural Observations

Interfacial tension, τ, plays a vital role in determining the behaviour of an interface, therefore the morphology, quality and performance, of immiscible blends. Knowledge of interfacial tension is also important for quality control and optimisation of processing conditions in many industries such as foods, coatings, cosmetics, detergents, etc.

Measurements of interfacial tension have been broadly classified into three main categories [Ding et al 2002]: (i) methods based on the balance between gravitational and interfacial forces, such as Du Noüy ring or Wilhelmy plate tensiometer, or pendant drop method [Arashiro et al 1998]; (ii) techniques based on measurements of equilibrium shape / size of drops, such as the maximum liquid drop volume method [Pu and Chen 2001]; (iii) flow related methods based on direct optical observations between the interface, involving analysis of deformation and breakage of a thin thread of one phase ‘sandwiched’ into the other [Puyvelde Van et al 2002], or analysis of steady drop deformation under well controlled shear [Guido et al 2002], or analysis of retraction of a deformed drop after cessation of shear [Spyropoulos 2006, Ito et al 2008]. It is interesting to note that all flow related methods

correlate interfacial tension (an interfacial property) with viscosity (a bulk property). In principle, the two properties are independent, e.g. knowledge of viscosity is not required for measurements with the Wilhelmy plate or du Nouy ring tensiometer. It is through their combined effect on a third feature, such as the degree of steady drop deformation, that they can be related and the relationship used to estimate interfacial tension.

Sigillo et al [1997] compared the three techniques of flow related methods and found good agreement between them for a polymer blend composed of poly-isomutylene and poly-dimethylsiloxane. Comparison between the fibril break up technique with the drop retraction method has also been reported [Puyvelde et al 2002] and good agreement has been demonstrated for an aqueous gelatine / dextran polymer mixture. Verdier & Brizard [2002] have described a method to measure interfacial tension, which involves examination of the characteristic time of drop coalescence in blends of poly-isobutylene with silicone oil. Such experiments are possible with the current device.

In this section, interfacial tension between silicone oils and mixtures of hexylene glycol / water has been measured using the steady drop deformation method (SDDM, described in chapter 2) and results are compared with values obtained experimentally with Wilhelmy plate tensiometer. The latter is a well established technique involving slow lifting of a metallic (often made of Pt) plate from the interface, measuring the required force and dividing it with the perimeter of the width of the plate.

Drop deformation experiments have been conducted using very dilute systems of (almost) isolated drops, prepared by gentle mixing of continuous and dispersed phases, as described above (section 4.3). A series of aqueous phases was prepared by increasing water concentration in the hexyelen glycol / water mixture from 0% (pure HG) to 100% (pure

water). As water is heavier than HG, aqueous mixtures of increasing densities were produced. To best match the density of each continuous phase, silicone oils of increasing molecular chain lengths were used, a choice supported by the fact that interfacial tension between silicone oils and aqueous media is known to be independent of the oil's chain length [Calabrese 1986, Pu and Chen 2001, also confirmed here experimentally, data not shown]. Experiments were conducted at steady shear rate $250s^{-1}$ and reported results have been obtained using the coaxial cylinders geometry. Similar results were obtained with the parallel plates and cone / plate geometries [not shown].

Figure 4.16 shows the comparison between interfacial tension values determined by SDDM and Wilhelmy plate tensiometer at increasing water content in the continuous phase. Overall good agreement is illustrated between the two methods for systems with water concentration up to ca. 30% in the aqueous phases, albeit SDDM resulted in slightly higher results. For aqueous phases with higher water content, however, SDDM failed to accurately determine interfacial tension and resulted in significant overestimations.

Observed discrepancies at water concentration above 30% wt/wt may be due to inaccurate determination of the deformation parameter, Def (equation 2.17), which is critical for the SDDM. As longer oil molecules were used in this part of the graph for gravitational reasons (as described above), dispersed drops became progressively more viscous and difficult to deform under shear, as predicted by Grace Curve (near-spherical drops). At lower deformations, however, deformation becomes low as well as difficult to accurately determine. Overestimation of interfacial tension may therefore be attributed to underestimation of Def.

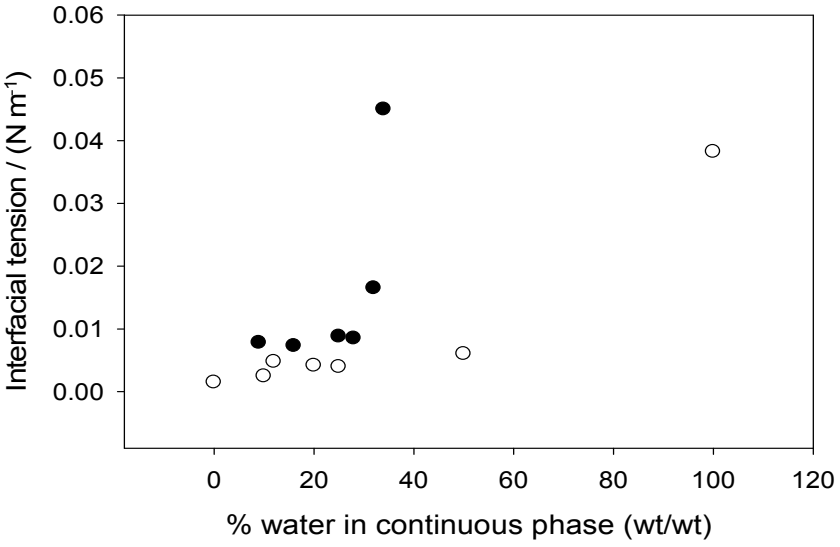

Figure 4.16: interfacial tension measurements of oil / aqueous system obtained with the steady deformation method (black dots) and Wilhelmy plate tensiometer (white dots) at increasing water concentration in the aqueous phase.

Figure 4.16 also illustrates that in the presence of hexylene glycol there was a significant reduction in interfacial tension. Interfacial tension between silicone oil and pure water obtained with Wilhelmy plate tensiometer ($42mN\ m^{-1}$) is in good agreement with the $45mN\ m^{-1}$ reported by Calabrese [1986]. In the presence of hexylene glycol, however, measured interfacial tension was reduced to $3.8mN\ m^{-1}$, indicating that hexylene glycol has a stabilising effect on oil droplets. This observation is important as silicone oil drop coalescence might be significantly limited at aqueous phases where hexylene glycol is the main component, as those employed in the present work.

Results similar to figure 4.16 were also obtained for systems where silicone oils were dispersed in aqueous phases consisting of mixtures of hexylene glycol with glycerol (not shown). In the presence of hexylene glycol / glycerol mixture, interfacial tension was

estimated at $2.2mN\ m^{-1}$. It is noted that interfacial tension values reported here are used in the next two chapters.

4.6 Summary

Evaluation of the device in terms of accuracy in rheological measurements, image clarity and simultaneous rheo-structural recordings has proven the reliability of the setup on rheo-structural studies of complex systems, even when tested at high shear rates and / or volume fractions of dispersed phase. Excellent rheometric performance was demonstrated when optical measuring geometries were compared with standard stainless steel geometries supplied by Malvern Instruments at the range of investigated Newtonian viscosities, $0.01 - 1Pa\ s$, and shear rates, $5 - 500s^{-1}$. In addition, high quality images of required resolution were obtained for a variety of systems both at quiescence and under different flow conditions. Very clear images of aqueous / aqueous systems, inherently considered difficult to capture due to similar refraction indices of the ingredients, were obtained. On certain occasions, especially at high volume fractions of small dispersed entities, reduction of gap size was shown to substantially improved image quality, providing a clear advantage to the parallel plate geometries, where reduction of gap size is readily available. Optical recordings under d shear of $20000s^{-1}$ have for the first time been reported, adding a novelty to the present work and providing a successful outcome for the project. However, at these high shear rates, achieved at extremely small gap sizes, accuracy in rheological measurements becomes questionable and an interesting subject to consider in future work.

Simultaneous rheological and microstructural measurements demonstrated the potential of the device and the link between rheology and structure. Experiments with the parallel plate geometries illustrated how images of the investigated system can be captured under a range of shear rates with a single measurement simply by moving the image capturing unit along the plate's radius. As the image capturing unit moves towards the centre of the plates, acquired images correspond to lower shear rates. This feature requires automisation for exploitation of its full potential.

An oil / aqueous dispersion was subsequently shown to shear thin at $\varphi = 0.3$, while at $\varphi = 0.05$ the same system showed Newtonian behaviour. It was suggested that observed shear thinning could be linked to significant morphological changes occurring on increasing of shear flow, leading to re-arrangement of the drops to the flow direction, deformation, drop orientation, and breakage. While drop breakage was easily followed with simultaneous rheological and morphological recordings, the effect of orientation of drops to the flow direction was difficult to study with the current setup.

A study with an aqueous / oil / aqueous double emulsion illustrated that small-to-medium shearing may cause de-stabilisation of the double emulsion and release of the inner aqueous phase. This observation could not possibly be determined by rheological measurements alone, as the viscosity of the system was maintained constant. Such studies may be relevant in investigations of controlled release systems, where the inner phase may contain an active compound, required to be released under certain conditions.

The device was further used to illustrate the effect of gentle shearing on coalescence. Shear-induced coalescence was successfully recorded for an oil / aqueous dispersion pre-

sheared at $500s^{-1}$. The same system showed slower coalescence when kept at rest after pre-shearing.

Simultaneous rheological and morphological recordings of a product directly from the supermarket shelf were then considered. Rheology and structure of full fat and low fat versions of French style salad dressing demonstrated similar rheological response but significantly different microstructures due to the reduced amount of oil drops in the light version.

The potential of the device in estimation of interfacial tension by simultaneous rheo-structural observations was lastly demonstrated. Estimated interfacial tension values using the steady drop deformation method showed good agreement with values obtained with the Wilhelmy plate tensiometer.

CHAPTER 5

RHEOLOGY AND STRUCTURE OF SELECTED TWO PHASE SYSTEMS

5.1 Introduction

In the previous chapter, the newly developed experimental setup was evaluated in terms of quality of rheological and microstructural data acquisition. To further demonstrate the potential of the device, this chapter presents simultaneous rheological and morphological results obtained for selected two phase systems under shear flow. Those systems are formed by mixing of two immiscible or partially miscible components and they are important for both industrial applications and in fundamental research [Tardos 1994]. In the industry, many consumer products are manufactured based on the processing of such systems, including food and other emulsions, pharmaceuticals, cleaning creams, body lotions, inks, paints, pastes, liquid crystals etc [Tadros 1994, Larson 1999]. On a fundamental level, two phase systems are usually the simplest model systems that are theoretically or numerically investigated from researchers working on understanding the interactions between dispersed entities and the relationship between properties in the micro-scale and macro-scale [Tadros 1994].

In two phase liquid / liquid systems, one phase is typically dispersed in the other, the continuous phase, in the form of drops, though, as discussed in chapter 4, other morphologies are also possible, for example formation of thread like arrangements. Dispersed and continuous phases may be predominantly hydrophobic (‘oil’) or essentially hydrophilic (‘aqueous’), and therefore their combinations result in oil / aqueous, aqueous / oil, oil / oil and aqueous / aqueous dispersions. In the present chapter, rheology and structure of example liquid / liquid systems covering all combinations of "oil" and "aqueous" phases are presented. Each type of dispersion is presented in a separate section. Oil / aqueous systems are considered in section 5.2, aqueous / oil dispersions in section 5.3, oil / oil systems in section

5.3 and section 5.4 presents results on an aqueous / aqueous system. Contents of the chapter are summarised in section 5.5.

5.2 Oil / Aqueous Systems

Rheology and structure of systems of silicone oil dispersed in Newtonian aqueous phases have been measured and results are presented in this section. Focus is specifically given on the effect of volume fraction of dispersed phase, φ, and viscosity ratio between dispersed and continuous phases, λ, on rheology and microstructure of the oil / aqueous systems. It is noted that the term "aqueous" here is used to conveniently describe hydrophilic phases fully miscible with water, but which might not contain water.

Materials and methods are briefly described in the next section. Measurements over a wide range of λ ($0.2 \leq \lambda \leq 67$) and volume fraction of dispersed phase between $0.02 \leq \varphi \leq 0.3$ have been conducted under steady as well as at increasing-decreasing shear rate. Results are presented separately for the two shearing profiles in sections 5.2.2 and 5.2.3, respectively.

5.2.1 Materials and Methods

Investigated systems were required to (i) have Newtonian oil and aqueous phases; (ii) be kinetically stable for the duration of the experiment; (iii) be easy to prepare; and (iv) enable isolated investigation of the effect of φ and λ on rheology and structure.

Stability of the dispersions was ensured by matching the densities of the dispersed and continuous phases, therefore eliminating the driving force for creaming and / or sedimentation. Stability of all systems was tested by monitoring the degree of separation by visual observation of the dispersion in a beaker and also by careful microscopic observations of a system loaded to the rheometer. Systems that remained stable for minimum 3 hours after preparation were characterised as 'stable' and were used for further analysis.

Silicone oils have been chosen as oil phases. Those are Newtonian liquids available in a vast range of viscosities (from $10^{-3} - 10^{4} Pa\ s$), which depends on their molecular chain length. Silicone oils used in the present study had viscosities ranging between $0.01 Pa\ s$ and $1 Pa\ s$.

Silicone oils have nearly constant densities independently of their viscosity. Investigated silicone oils displayed densities between $930 - 970 kgm^{-3}$, the lower density corresponding to the smaller molecular chain length and the lower viscosity oil. Due to the nearly constant densities of dispersed phases, kinetically stable systems could be prepared over a wide range of λ by altering the viscosity of the oil only, while maintaining the same (or nearly the same) aqueous phase. In addition, interfacial tension between silicone oils and aqueous phases is known to be independent of the viscosity of the oil [Calabrese 1986, also confirmed here experimentally (section 4.5)], which facilitated the isolated study of the effect of φ and λ on rheology and sturcture (requirement (iv)).

Mixtures of hexylene glycol (HG) with water or with glycerol were used as continuous phases. HG was chosen due to its low density, lower than the density of the oil. Water and glycerol are fully miscible with HG and can increase the density of the mixture as required to kinetically stabilize the system.

Individual rheological measurements of oil and aqueous phases indicated that they were all Newtonian, e.g. power law indices were above 0.98 (equation 2.7). Interfacial tension of silicone oil with HG / water and HG / glycerol was measured with a Wilhelmy plate at $0.0038 Nm^{-1}$ and $0.0022 Nm^{-1}$, respectively as described in section 4.5. As glycerol is more viscous than water, systems where aqueous phases were mixtures of HG with glycerol were generally of lower λ than systems of similar densities with aqueous phases consisting of mixtures of HG with water.

Twelve oil / aqueous systems have been prepared and used for simultaneous rheological and morphological measurements. Viscosity ratios of the systems covered the range between $0.2 - 68$, as shown in table 5.1. Each system was measured at volume fractions of dispersed phase of 0.02, 0.05, 0.1, 0.2 and 0.3 following the same experimental procedure, which is described below. Preparation of each $50mL$ involved addition of the relevant amounts of continuous and dispersed phases in a $200mL$ beaker and subsequent gentle mixing for $15s$. Freshly made samples were measured well within the limit of 3 hours from preparation, where samples have been proven stable.

Table 5.1: Composition and properties of investigates systems.

Dispersed phase	**Continuous phase**	η_d $(Pa\ s)$	η_c $(Pa\ s)$	λ
10cSt SO*	$94.4\%HG^* + 5.6\%Gl^*$	0.0095	0.041	0.2
10cSt SO	$91\%HG + 9\%W^*$	0.0095	0.029	0.3
20cSt SO	$90\%HG + 10\%Gl$	0.019	0.053	0.4
50cSt SO	$85\%HG + 15\%Gl$	0.049	0.071	0.7
20cSt SO	$84\%HG + 16\%W$	0.019	0.022	0.9
100cSt SO	$84.5\%HG + 15.5\%Gl$	0.095	0.072	1.3
50cSt SO	$75\%HG + 25\%W$	0.049	0.017	2.9
350cSt SO	$83\%HG + 17\%Gl$	0.35	0.076	4.6
100cSt SO	$72\%HG + 28\%W$	0.095	0.017	5.6
1000cSt SO	$80.4\%HG + 19.6\%Gl$	0.88	0.080	11
350cSt SO	$68\%HG + 32\%W$	0.35	0.013	27
1000cSt SO	$66\%HG + 34\%W$	0.88	0.013	68

*HG: Hexylene glycol; Gl: Glycerol; W: Water; SO: Silicone oil

Rheology and structure of all systems of table 5.1 were studied under (i) steady shear rate of $250s^{-1}$ and (ii) increasing shear rate from $5s^{-1}$ to $500s^{-1}$ followed by decreasing shear rate from $500s^{-1}$ to $5s^{-1}$. Rheology of each flow curve experiment was measured at 42 fixed shear rate points in total (i.e. 21 in each direction of increasing and decreasing shear rate), at logarithmic intervals, as shown in table 5.2.

Table 5.2: Table of investigated shear rates at the flow curve experiments (in s^{-1})

5.0	10.0	19.9	39.7	79.2	158.1	315.5
6.3	12.6	25.1	50.0	99.8	199.1	397.2
7.9	15.8	31.6	63.0	125.6	250.6	500

Measurement of each experimental point involved 10s “waiting time”, where the system was sheared at the corresponding shear rate without recording rheological properties, followed by 10s “integration time”, where viscosity was measured and averaged. Experiments have been conducted using the coaxial cylinders geometry. The range of studied shear rates is

typical for pipe flow in pumping applications as well as polymer extrusion and it is relevant in physiological research, as it is representative of the venous shear rate [Barnes 1989, Haynes et al 2011]. Shear step experiments are relevant to industrial applications, where systems are usually subjected to complex, often transient flows. Experiments under steady shear flow are relevant for example for fundamental studies of drop dynamics and interactions under equilibrium conditions.

5.2.2 Rheology and Structure Under Steady Shear Rate of 250s^{-1}

Rheo-structural results obtained for oil / aqueous systems at steady shear rate of $250s^{-1}$ are presented in terms of (i) time to develop steady state structure, especially at high viscosity ratio between dispersed and continuous phases, (section 5.2.2.1); (ii) comparison of obtained steady state relative viscosities with viscosity models found in the literature, discussed in section 2.2 (section 5.2.2.2); (iii) comparison of recorded microstructure and obtained drop sizes with Grace Curve (section 5.2.2.3); (iv) relationship between Sauter mean and maximum obtained drop diameter (section 5.2.2.4); and (v) effect of volume fraction of dispersed phase and viscosity ratio between dispersed and continuous phases on drop size (section 5.2.2.5).

5.2.2.1 Time to Develop Steady State Structure

The majority of investigated systems showed time independent viscosities and very fast development of steady morphologies at $\dot{\gamma} = 250s^{-1}$. However, systems of high φ and λ

required finite time, sometimes of the order of $10min$, to develop steady state structure, resulting in a corresponding time to develop steady state viscosity.

For the $\varphi = 0.3$, $\lambda = 27$ system, figure 5.1 illustrates gradual deformation, breakage and favourable orientation to the flow direction of drops after imposition of flow, until a steady structure and viscosity plateau were reached at around $10min$. Left at quiescence for long enough time after shearing, drops slowly coalesced back to the initial, coarse morphology, which reproduced similar curves as in figure 5.1 on repetition of the experiment. However, when the system was left for too long (e.g. overnight) complete phase separation occurred, where oil and aqueous phases formed two distinctive parts.

The term "thixotropy" has been used to characterise the property of a material whose viscosity decreases with time of shearing and then increases when shearing is removed [Barnes 1997]. In his review on thixotropy, Barnes [1997] described the typical characteristics of a thixotropic behaviour, where similarities with the response of the $\varphi = 0.3$, $\lambda = 27$ system of figure 5.1 are evident. According to this review, viscosity of a typical thixotropic system decreases with time of shearing and eventually levels out to a constant value; further, if the shear flow is stopped and the material rests for a long time then on subsequent shearing at the same shear rate viscosity should initially be higher and gradually reduced to the same constant value [Barnes 1997].

Although such behaviour was observed for systems of high φ and λ, it was not systematically investigated further. However, figure 5.1 illustrates the potential of the device for such investigations. For systems that showed finite time to develop steady state microstructure, such as the $\varphi = 0.3$, $\lambda = 27$ system of figure 5.1, the constant viscosity value

of the plateau has been taken into consideration in the discussion of the next section, where obtained viscosities at are compared with predictive viscosity models of chapter 2.

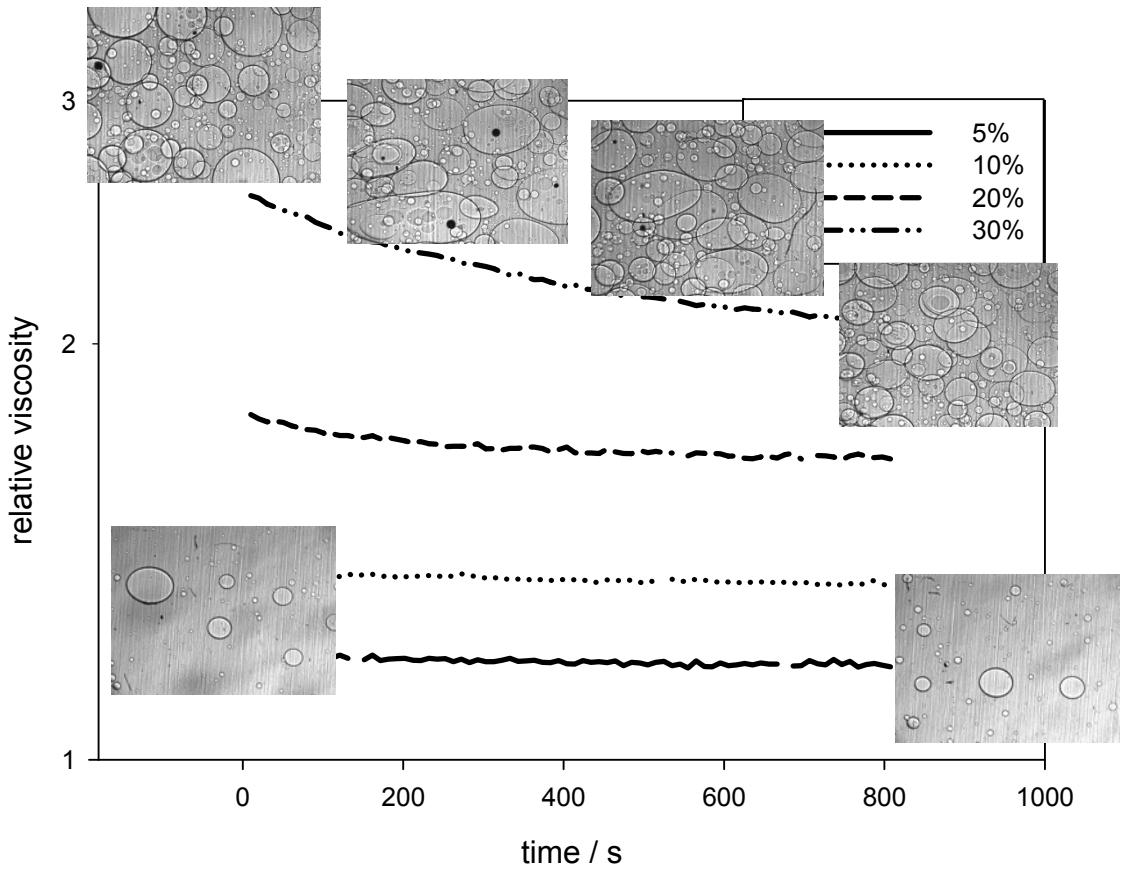

Figure 5.1: Time to develop steady state structure observed at for system of . At , microstructural changes occurring on imposition of shear, until steady state structure is obtained, result in a corresponding change in viscosity until a plateau is reached (at). Image width . Experiments with CC geometry.

5.2.2.2 Shear Viscosity at $250s^{-1}$: Comparison with Viscosity Models from the Literature

All correlations given in section 2.2 have been tested against experimental data and three have been chosen for detailed discussion. Selection has been based on good agreement

between predicted values and experimental data as well as on relevance between investigated and considered by the model systems.

The Choi & Schowalter's model [1975] (equation 5.1) will be referred to as 'model 1' for the rest of the chapter. This cell model was developed for systems similar to those measured in the present study: two immiscible, Newtonian liquids of equal densities and finite volume fractions of dispersed phase. The model of Phan-Thien & Pham [1997] (equation 5.2) will be referred to as 'model 2' for the remaining of the chapter. Model 2 has been developed following the concept of the effective medium theory (described in chapter 2) and considering Taylor's equation to describe each successive addition of infinitesimally small amounts of dispersed phase (chapter 2 for more details). 'Model 3' (equation 5.3) will denote the model proposed by Pal [2001], which is also based on the concept of effective medium but describes each dispersed phase addition step by the equation proposed by Krieger & Dougherty (chapter 2 for more details). All models have been developed for drops with small deformations (small Ca), a requirement which has been confirmed by simultaneous visual observations of the system under the microscope throughout the duration of the experiments.

$$\eta_r = 1 + \varphi \frac{5\lambda + 2}{2(\lambda + 1)} + \varphi^2 \frac{5(5\lambda + 2)^2}{8(\lambda + 1)^2} \tag{5.1}$$

$$(\eta_r)^{2/5} \left(\frac{2\eta_r + 5\lambda}{2 + 5\lambda}\right)^{3/5} = (1 - \varphi)^{-1} \tag{5.2}$$

$$\eta_r \left(\frac{2\eta_r + 5\lambda}{2 + 5\lambda}\right)^{\frac{3}{2}} = \left(1 - \frac{\varphi}{\varphi_m}\right)^{-2.5\varphi} \tag{5.3}$$

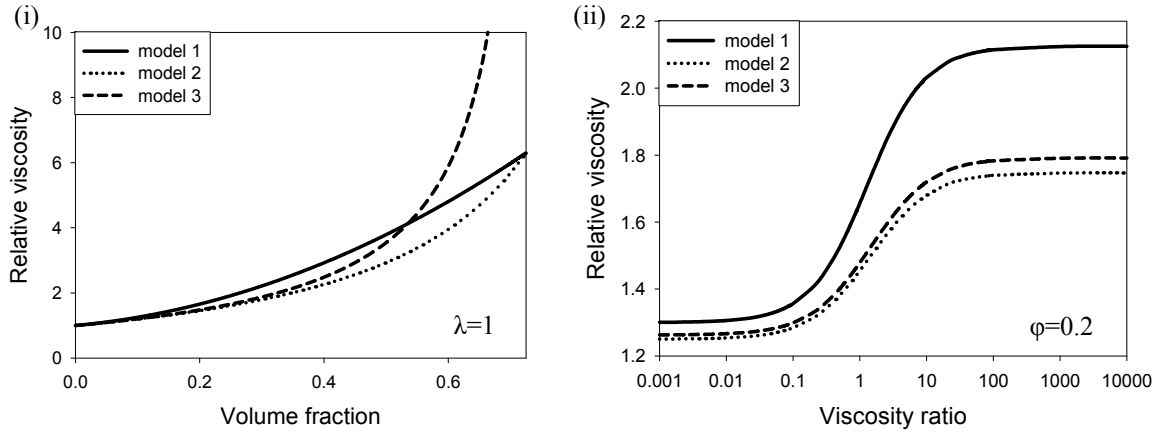

Figure 5.2: Relative viscosity predictions from Choi & Showalter's model 1 [1975], Phan Thien & Pham's model 2 [1997], and Pal's model 3 [2001] at (i) constant $\lambda = 1$ (equi viscous dispersed and continuous phases) and varying φ; (ii) constant $\varphi = 0.2$ and varying λ; (note: fixed values of λ and φ have been arbitrary chosen as examples).

The three models follow the same pattern, which is evident in figure 5.2, and has been discussed in detail by Pal [2001]. In figure 5.2, the value of 0.74 has been assumed as maximum packing volume fraction of dispersed phase for model 3, which corresponds to the maximum volume fraction of rigid spheres. Although higher φ_m might be achievable for deformable droplets, the graph of figure 5.2 is illustrative of the patterns of the three models. At a fixed λ, all models predict that relative viscosity increases with increasing φ. At a fixed value of φ and for the range of investigated viscosity ratios, the three models predict relative viscosity to increase with λ, but increasing rate reduces for $\lambda > 10$. At $\lambda > 100$ relative viscosity becomes nearly constant and independent of λ (figure 5.2). Spyropoulos et al [2007] have found good agreement between model 1 and aqueous / aqueous two phase systems of morphologies displaying drops dispersed in continuous phases, but Pal [2001] has reported that model 1 over predicts and model 2 under predicts relative viscosity.

Comparison between experimental results and the three models at $\varphi = 0.05, 0.1, 0.2$ and 0.3 is shown in figure 5.3. The difference between predicted and experimental relative viscosities for the 12 investigated systems of different viscosity ratios was measured as root mean square deviation (RMSD), calculated from equation 5.4 [Calabrese 1986 part II]. Calculated RMSD values for the three models are shown in table 5.3.

It is evident from figure 5.3 that for the investigated systems, viscosity increased at increasing viscosity ratio between dispersed and continuous phases, as predicted by all models of figure 5.2. Moreover, the effect of λ on relative viscosity was found enhanced at increasing volume fraction of dispersed phase. Overall, significant scatter of experimental points was observed at low φ and at increasing φ models were shown to over-predict obtained viscosity data.

Comparison of experimental data with equation 5.1 shows that model 1 generally over predicted experimental results, yet showing a similar shape/slope. For this model, deviations above 20% were observed for $\varphi \geq 0.2$ and at $\varphi = 0.3$ predicted relative viscosities were nearly double the experimental values (figure 5.3 and table 5.2). Better agreement was found with the effective medium based models 2 and 3. Model 2 showed overall best fit with $RMSD^{model\,2} < 20\%$ at all investigated volume fractions. Reasonably good predictions were also obtained by model 3 at $\varphi \leq 0.2$, but deviations of the order of 30% were found at $\varphi = 0.3$, where the model over predicted experimental data.

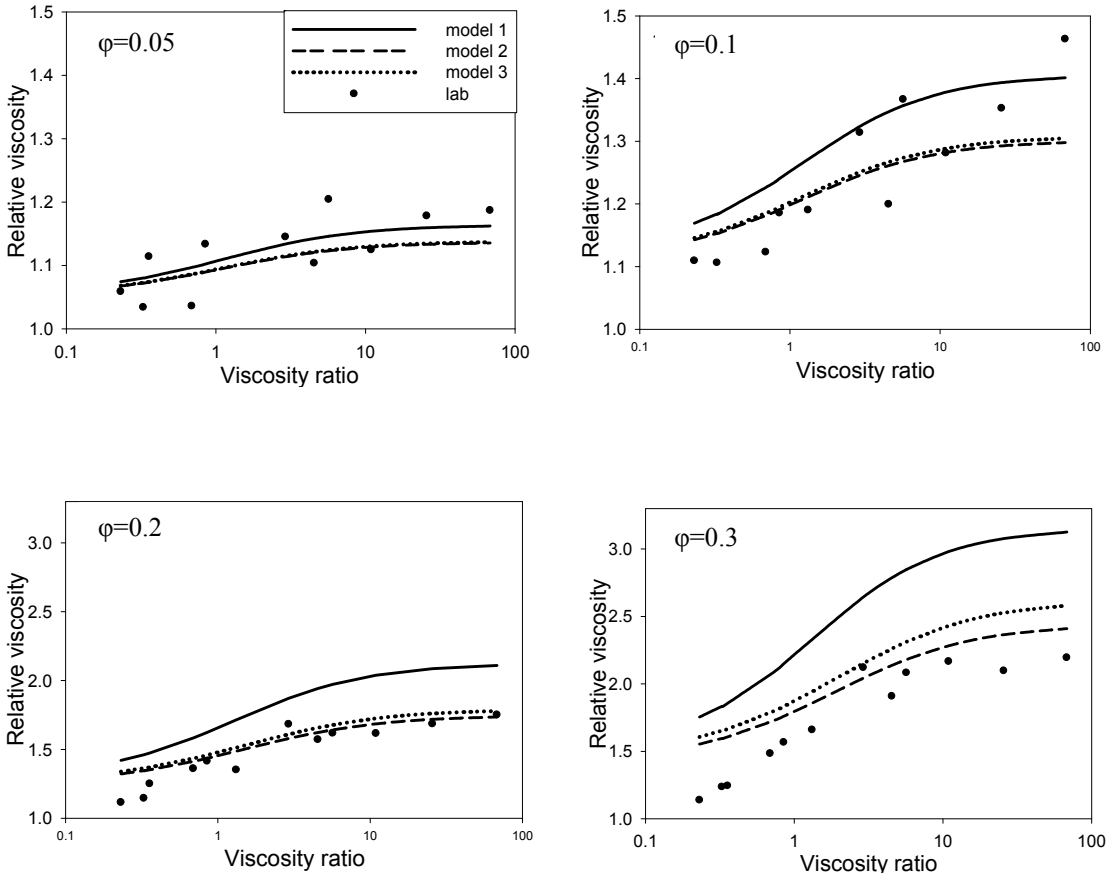

Figure 5.3: Comparison of experimental data (solid symbols) with model 1 (Choi & Showalter [1975], solid line), model 2 (Phan-Thien & Pham [1997], dashed line) and model 3 (Pal [2001], dotted line) at $\varphi = 0.05$, 0.1, 0.2 and 0.3. Experiments with CC geometry.

$$RMSD = \left\{ \frac{\sum_{i=1}^{12} \left[\left(\frac{\eta_{r(\lambda_i)}^{model} - \eta_{r(\lambda_i)}^{experiment}}{\eta_{r(\lambda_i)}^{experiment}} \right)^2 \right]}{12} \right\}^{1/2} \tag{5.4}$$

Table 5.3: RMSC between experiment and the three models.

Model No	**RMSD**			
	$\varphi = 0.05$	$\varphi = 0.1$	$\varphi = 0.2$	$\varphi = 0.3$
model 1	3%	7%	21%	40%
model 2	4%	5%	10%	18%
model 3	4%	5%	10%	30%

Results indicate better agreement of experimental data with the effective medium than the cell theory. It is reminded that the former assumes formation of a concentrated system by successive additions of infinitesimally small amounts of dispersed phase, while the cell model involves division of the system into identical unit cells that are uniformly occupied by mono-dispersed drops (chapter 2).

Discrepancies between experimental data and predictions from model 1 may therefore be partially due to non uniform, poly dispersed morphologies, which have been observed with simultaneous optical recordings. An illustrative example of a captured image of the $\lambda = 0.9$, $\varphi = 0.2$ system under shear rate $250s^{-1}$ and the corresponding drop size distribution is shown in figure 5.4. This figure illustrates deviations from mono disparity and uniformity required for the cell theory. Additional to morphological deviations, for the development of equation 5.2 the authors have also assumed complete absence of surfactants. An additional error might therefore be caused by the surface active properties of hexylene glycol (and glycerol when present) on the oil, as described in section 4.5.

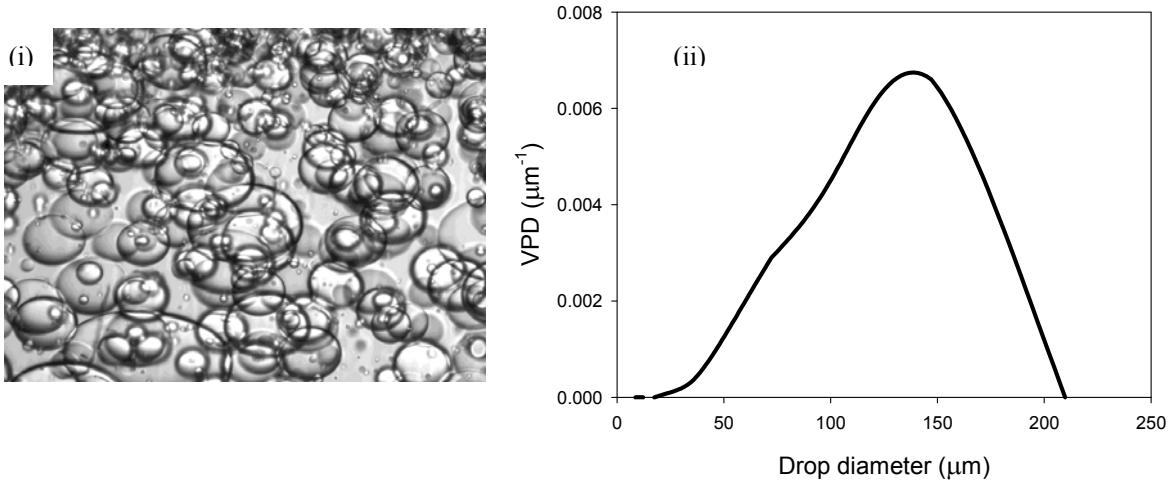

Figure 5.4: Example of obtained morphology for the $\lambda = 0.9$, $\varphi = 0.2$ system under shear rate $250s^{-1}$ illustrating deviations from mono disparity and uniformity assumed by the cell model: (i) captured image; (ii) determined drop size distribution. Image width $1.2mm$. Experiments with CC geometry.

All models shown in figure 5.3 over predicted obtained results, especially at increasing φ, and they systematically failed to successfully predict experimental data at low λ, in particular for $\varphi \geq 0.1$. For this reason, an empirical equation that correlates η_r with φ and λ has been developed with non-linear regression [Sigmaplot 11.0] to best fit all experimental points. Equation 5.5, derived from Choi & Schowalter's model 1, has been taken as a template. By doing so, it was presumed that the model might be system specific and that by changing the constants it can be extended to accommodate the investigated systems. With k_1, k_2, k_3 and k_4 constants, the empirical equation would be of the form of equation 5.6. It was found that experimental data fit well to equation 5.6 when $k_1 = 7$, $k_2 = -1$, $k_3 = 7/4$ and $k_4 = 1$, as shown in equation 5.7. The corresponding graph confirming the (expected) good agreement between equation 5.7 and experimental data is shown in figure 5.5.

$$\eta_r = 1 + \varphi \frac{5\lambda + 2}{2\lambda + 2} \tag{5.5}$$

$$\eta_r = 1 + \varphi \frac{k_1\lambda + k_2}{k_3\lambda + k_4} \tag{5.6}$$

$$\eta_r = 1 + \varphi \frac{7\lambda - 1}{1 + (7/4)\lambda} \tag{5.7}$$

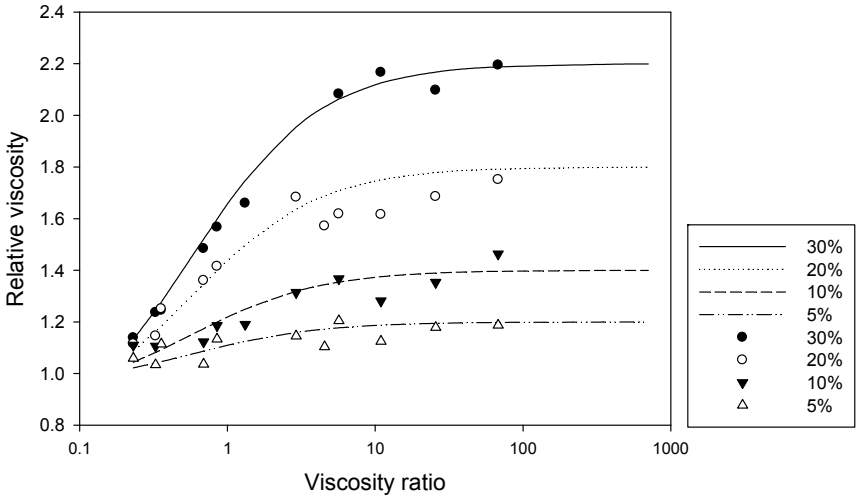

Figure 5.5: The best fit curves (equation 5.7, shown as lines) with experimental data (shown as scattered dots) at volume fraction of dispersed phase between 0.05 and 0.3 (shown as percentages in the legend). Experiments with CC geometry.

As equation 5.7 is purely empirical, its implementation on a physical basis is rather limited. However, comparison with equation 5.5, which served as a template, has been considered and it is illustrated in the graph of figure 5.6 for $\varphi = 0.3$. Figure 5.6 also includes the plot of equation 5.1 for comparison.

It is evident from figure 5.6 that at $\varphi = 0.3$, all plotted equations (5.1, 5.5, and 5.7) predict monotonically increasing relative viscosity with increasing λ. At low λ, the derived

equation 5.7 predicts the lowest η_r, suggesting that for investigated systems inviscid dispersed phases, compared to viscous continuous phases, marginally affected the system's viscosity. In addition, compared to equation 5.5, the derived equation 5.7 predicts lower relative viscosities at $\lambda < 0.5$, whereas the opposite is observed for $\lambda \geq 0.5$, where it is equation 5.5 that predicts lower relative viscosities. Compared to equation 5.1, the best fit equation 5.7 predicts lower relative viscosities at all viscosity ratios between dispersed and continuous phases. At $\lambda > 100$ all models of figure 5.5 show relative viscosities independent of λ.

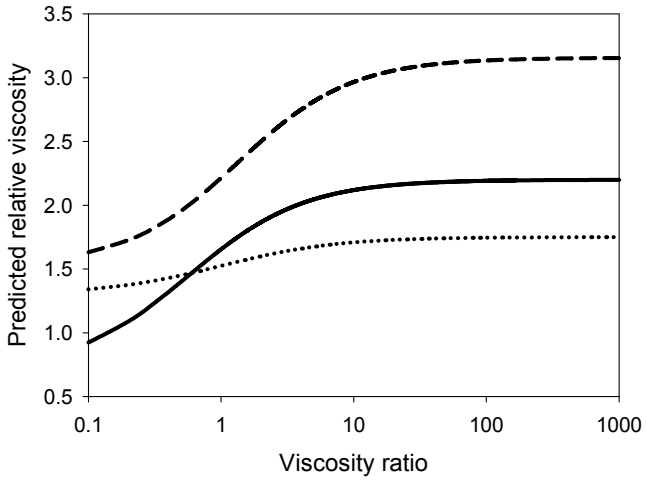

Figure 5.6: Comparison between empirically developed equation 5.7 (solid line), the template equation 5.5 (dotted line) and equation 5.1 (dashed line). Experiments with CC geometry.

5.2.2.3 Comparison of Obtained Morphology with Grace Curve

Experimental critical Capillary numbers have been calculated from equation 2.9 using the maximum recorded drop size of each sample. Comparison of acquired results with Grace

Curve, as expressed by de Bruijn's equation 5.8 (also as equation 2.16 in chapter 2), is shown in figure 5.7 for $\varphi = 0.02$ and $\varphi = 0.3$, where excellent agreement is observed at low φ. However, at increasing volume fraction of dispersed phase, lower Ca_{cr} numbers were obtained experimentally than predicted.

$$log(Ca_{cr}) = -0.506 - 0.0995log(\lambda) + 0.124[log(\lambda)]^2 - \frac{0.115}{log(\lambda) - log(4.08)} \qquad (5.8)$$

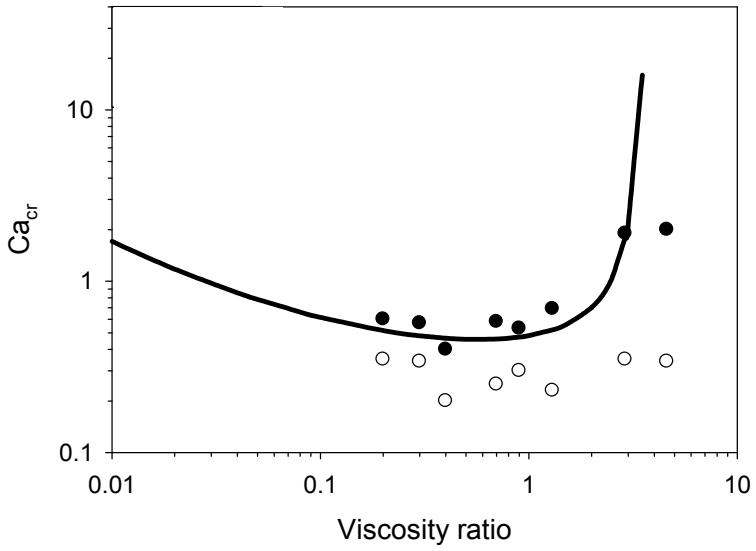

Figure 5.7: Dependence of critical Capillary number on viscosity ratio. Line represents predicted** values (equation 5.8); experimental data are shown as scattered dots at $\varphi = 0.02$ (black dots) and $\varphi = 0.3$ (white dots). Experiments with CC geometry.

The effect of increasing volume fraction of dispersed phase on breakage of emulsion drops has been experimentally studied by Jansen et al [2001] for concentrated systems with

$\varphi \leq 0.7$ using a counter-rotating coaxial cylinders geometry. They reported that at increasing φ drop breakage was determined by the average emulsion viscosity rather than viscosity of continuous phase, as anticipated by the effective medium model. They found reasonably good agreement of their results with Grace Curve at all investigated volume fractions, by replacing Ca_{cr} with its "effective" equivalent Ca^{eff} (where η_{em} replaces η_c in equation 2.15). Caserta et al [2007] investigated drop deformation and breakage of polymer blends at $0 \leq \varphi \leq 0.1$ under shear and also found good agreement of their experimental data with the effective medium approach at increasing volume fraction of dispersed phase.

The effective medium model has also been employed here to analyse the experimental data of the present work. The re-calculated Ca_{cr}^{eff} is compared with Grace Curve in figure 5.8 for $\varphi = 0.3$. The values of Ca_{cr} at $\varphi = 0.3$ as well as at $\varphi = 0.02$ are also shown for comparison. Figure 5.8 demonstrates good agreement between Grace curve, obtained Ca_{cr} at dilute systems and re-calculated Ca_{cr}^{eff} at $\varphi = 0.3$, suggesting that the effective medium theory can successfully explain experimental morphological results. This is supplementary to the previous section, where the effective medium theory was found to agree well with obtained rheological data. In figure 5.8 (ii), improved agreement is shown when besides Ca_{cr}^{eff}, viscosity ratio is also replaced by λ^{eff}.

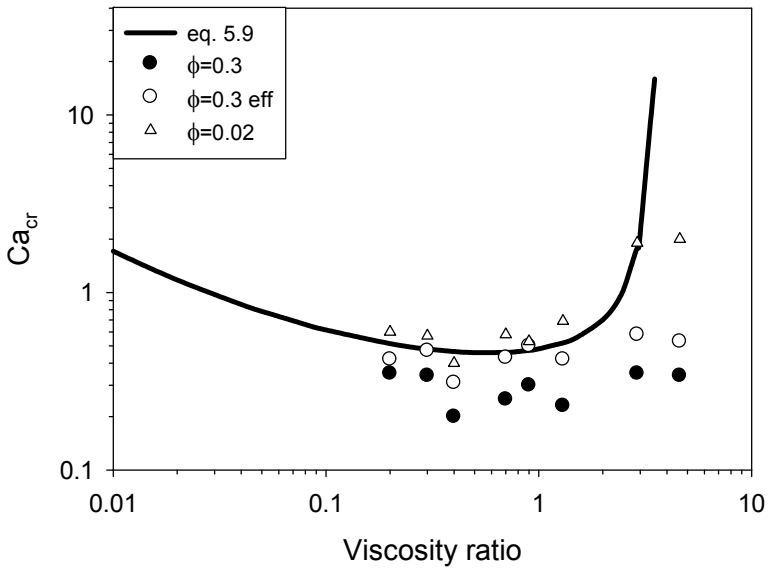

Figure 5.8 (i): Comparison of experimental morphological data with Grace Curve (solid line) at (triangles) and (dots). Improved agreement is shown at when values of are replaced by (white dots). Experiments with CC geometry.

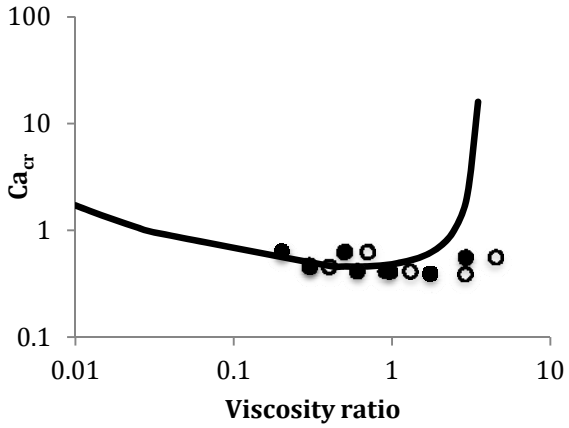

Figure 5.8 (ii): Correlation between Grace Curve (solid line) and effective critical Capillary number at . Improved agreement is shown when viscosity ratio (white dots) is replaced by effective viscosity ratio (black dots). Experiments with CC geometry.

5.2.2.4 Effect of φ on D_{32} at different λ

Figure 5.9 presents the variation of D_{32} with λ at $\varphi = 0.02$ and $\varphi = 0.3$ for selected systems under steady shear rate of $\dot{\gamma} = 250s^{-1}$. All systems shown in figure 5.9 have continuous phases comprising mixtures of hexylene glycol with glycerol, and consequently they have the same interfacial tension between the two phases ($2.2mN\ m^{-1}$, section 4.5).

Figure 5.9 shows that increasing the volume fraction of dispersed phase resulted in a reduction of Sauter mean drop sizes for all investigated systems. This behaviour is believed to be linked with increased drop breakage and number of created small satellite drops at increasing φ (discussed in the previous section), combined with the fact that coalescence was largely restricted at $\varphi \leq 0.3$ due to the observed surface activity of hexylene glycol and glycerol on oil drops (section 4.5). As a result, for investigated range of φ and λ, droplet size was primarily determined by breakage.

The behaviour of drops under shear flow in concentrated systems has been numerically simulated by Loewenberg & Hinch [1996] and experimentally investigated by Jansen et al [2001]. Both works suggest increased drop breakage at increasing φ. Loewenberg & Hinch reported for emulsions with $\varphi \leq 0.3$ and $0 \leq \lambda \leq 5$ and suggested that the shear stress applied on a drop at $\varphi = 0.3$ is 35% higher than that applied by pure continuous phase, due to the contribution of the surrounding drops. Increased drop breakage at higher φ was therefore linked with higher shear stress "felt" by drops at concentrated systems. Jansen et al [2001] experimentally examined systems of $\varphi \leq 0.7$ and reported a reduction of Ca_{cr} at increasing dispersed phase concentration up to one order of magnitude for high φ (of the order of $\varphi = 0.7$). In addition, as mentioned in section 5.2.2.3, Caserta et al [2007] and Jansen et al [2001] have employed the effective medium model to explain observed increase

in drop breakage at higher φ, and they suggested that drops at increasing dispersed phase concentration are subjected to increased effective capillary numbers, calculated by equation 2.20 rather than equation 2.15. As increased applied capillary numbers are associated with longer deformations and production of larger in number and smaller in size daughter droplets (and satellites) during rupture, it is therefore suggested that those effects will be intensified at increasing φ. Those observations are in good agreement with obtained experimental data of figure 5.9.

Figure 5.9 also indicates that at increasing λ, the difference in obtained D_{32} between dilute and concentrated systems also increases. This observation may be linked with the fact that at $\lambda > 4$ drops did not break at dilute systems, in accordance with Grace Curve. As a result, large drops were observed at $\varphi = 0.02$, as drop size was determined by breakage during the gentle pre-treatment.

In addition, at both low and high φ there is a characteristic minimum in D_{32}, occurring at around $\lambda \cong 0.4$ and $\lambda \cong 2$, respectively. At dilute systems, this minimum is in good agreement with Grace Curve (figure 2.6), where a minimum of Ca_{cr} is observed at similar λ. As viscosity of continuous phase, shear rate and interfacial tension were maintained nearly constant in all experiments, lower Ca_{cr} is expected to be linked with lower drop sizes (equation 2.15). On increasing volume fraction of dispersed phase, the shift of observed minimum towards higher λ can be explained by means of the effective medium theory, which predicts breakage at higher λ.

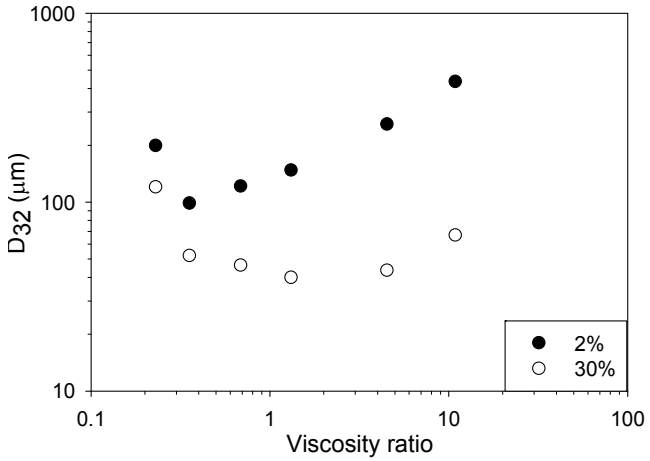

Figure 5.9: Effect of volume fraction on D_{32} for selected systems at $250s^{-1}$. Experiments with CC geometry.

5.2.2.5 Relationship between D_{32} and D_{max}

Although linear relationship between D_{32} (defined in equation 4.3) and D_{max} passing through the origin of coordinates ($D_{32} = kD_{max}$) has been reported on several occasions for mixing of two immiscible liquids [Padron-Aldana 2005, Zefra & Brooks 1996, Calabrese et al 1986, Brown & Pitt 1972, Sprow 1967], generalisation of linearity as such is not justified, as the relationship between the two diameters depends on the exact shape of size distribution [Pacek et al 1998]. The relationship between D_{32} and D_{max} should therefore be determined on the basis of each specific mixture and experimental conditions.

In the present section the relationship between measured D_{32} and D_{max} for investigated oil / aqueous systems under steady shear rate of $250s^{-1}$ is discussed. Although it is understood that recorded D_{max} might not correspond exactly to the maximum drop diameter of the entire system, as monitoring was spatially limited to a small part of the geometry, it is considered that it statistically gives a good estimate of the real situation due to

the large number of images recorded. Obtained D_{32} and D_{max} at $\varphi = 0.02$ and $\varphi = 0.3$ are plotted in figure 5.10.

It appears in figure 5.8 that the linear relationship between D_{32} and D_{max}, observed on several occasions in the literature, is also applicable in the present study. Estimated proportionality constants are within the range of $0.4 - 0.7$ reported in the literature for other systems / flow conditions.

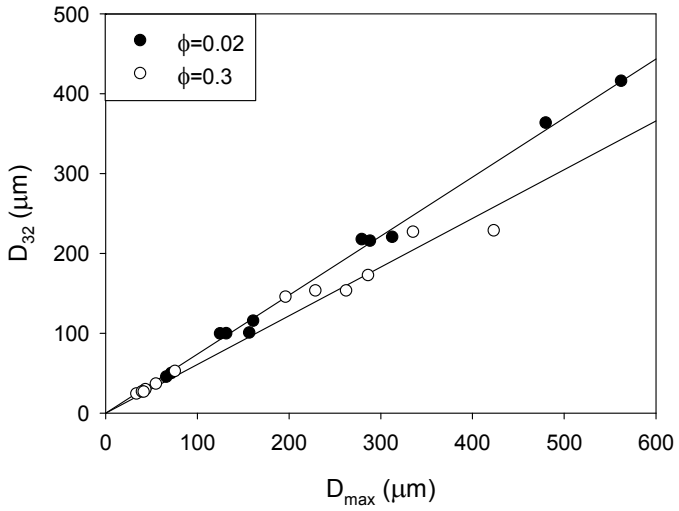

Figure 5.10: D_{32} against D_{max} at $\varphi = 0.02$ (black dots) and $\varphi = 0.3$ (white dots). Experiments with CC geometry.

Linear regression forced to pass through the origin of coordinates [Sigmaplot 11.0] at low and high volume fractions of dispersed phase gave proportionality constants of 0.74 (coefficient of determination $R^2 = 0.99$) and 0.61 ($R^2 = 0.97$) for $\varphi = 0.02$ and $\varphi = 0.3$ respectively, indicating larger population of small drops produced at increased φ (evident in

figure 5.10). The difference between low and higher volume fraction of dispersed phase may be explained by examining the principal drop breakage mechanism occurring at each φ. As described in section 2.3, the two main breakage mechanisms involve [Lin & Guo 2007]: (i) deformation to dumbbell shape and breakage into two equisized daughter drops and few satellites; (ii) formation of thread like shapes that will rupture into many smaller drops and their satellites (more details found in chapter 2). Janssen & Meijer [1993] and Padron Aldana [2005] have reported formation of increased number of small sized satellite drops when breakage mechanism involved thread like structures (unlike dumbbell breakage). In addition, they both observed that longer threads resulted in larger number of satellite drops. Renardy et al [2002] have further simulated breakage of a drop in an equi-viscous, equi-dense system focusing specifically on the formation of satellite fragments. They reported that when the drop is subjected to high capillary numbers (e.g. high shear rates or higher viscosity of continuous phase), approximately 10-17% of its volume forms large satellites of roughly mono-dispersed size accompanied by additional formation of smaller fragments.

It may therefore be suggested that the higher proportionality constant (i.e. fewer small drops) obtained at $\varphi = 0.02$ compared to $\varphi = 0.3$, may be linked with increased degree of "necking" breakage (i.e. through dumbbell shapes) at dilute systems, in comparison with a higher degree of "thread-like" breakage at higher volume fractions of dispersed phase. Taking into consideration the effective medium concept, this difference may also be explained by increased effective viscosity of continuous phase "felt" by the drops at increasing φ, which promotes the "thread like" breakage, as drops are subjected to higher capillary numbers. Images illustrating dumbbell type drop breakage at $\varphi = 0.02$ and thread-like type drop breakage at $\varphi = 0.3$ ($\lambda = 0.4$) are shown in figure 5.11.

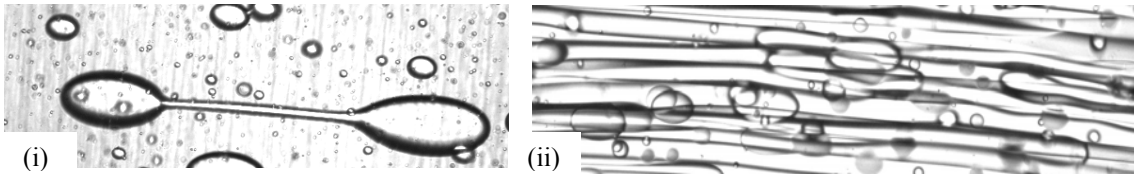

Figure 5.11: Drop breakage at $\dot{\gamma} = 250s^{-1}$ for the $\lambda = 0.4$ system at (i) $\varphi = 0.02$ and (ii) $\varphi = 0.3$, showing dumbbell mechanism at low φ and thread-like mechanism at higher φ. Images captured with CC geometry.

5.2.3 Rheology and Structure Under Flow Curve at 5-500-5s^{-1}

Dilute dispersions observed under flow of increasing-decreasing shear between $5s^{-1}$ and $500s^{-1}$ showed Newtonian behaviour with marginal effect of the presence dispersed phase on systems' viscosity (data not shown). On increasing φ, significant enhancement of the effect of dispersed phase on measured relative viscosities was observed, as it is illustrated in figure 5.12 where selected flow curves for systems at $\varphi = 0.3$ are shown. At $\varphi = 0.3$, increasing λ caused relative viscosities to increase in value and deviate from Newtonian behaviour. Results for the rest of the samples and conditions described in section 5.2 confirmed the observed trends.

Accuracy of rheological measurements was considered in terms of inertial and centrifugal instabilities, as well as end effects and microstructural requirement for small drops compared to the gap size (see chapter 2). In all experiments, the effect of inertial instabilities and Taylor vortices was considered low, as calculated Taylor numbers were overall one order of magnitude smaller than the estimated critical Taylor number of the experimental setup (maximum calculated Taylor number was of the order of 100, while critical Taylor number was of the order of 1700, determined by equations 2.34). In addition, the effect of centrifugal forces on the measurements was considered low, as the value of $r\omega^2$ was low (below 10) in all

experiments, and inhomogeneity was also prevented by the similar densities of continuous and dispersed phases (see section 5.2.1). However, large drops were observed in some experiments, especially at initial stages and with systems of high viscosity dispersed phase, as it can be seen for example in figure 5.14. These large, viscous drops might interfere with viscosity measurements, resulting in increased recorded viscosities, wherever present. On those occasions, accuracy of rheological measurements becomes questionable. Although the possible effect of large drop sizes in the cases of systems with viscous dispersed phases should not be neglected, it is noted that the discussion below focuses on the effect of other microstructural observations on the recorded viscosity data, as most systems showed drop sizes below the limit of 5-10 times smaller of the gap size (see section 2.4.2.2).

At least three interesting features are observed in figure 5.12. The first refers to the fact that systems with increasing λ showed an overall stronger shear thinning response (lower power law indices) as shear rate increased (black lines); the second to the intersection between the two curves corresponding to increasing (black line) and decreasing (green line) shear rates (cross points marked in circles in figure 5.12); and the third to the fact that zero-shear viscosities of dispersions were higher initially (black line) than after shearing (green line), although reduction of drop size was recorded; it should be noted here that smaller drops are generally associated with rise in shear viscosity at constant volume fraction of dispersed phase [Teipel 2002, Barnes et al 1989, Pal 1996]. Those observations will be discussed below in some detail. It is remarked that all absolute values of viscosities were above $0.01 Pa\,s$, ensuring a certain degree of accuracy in rheological measurements.

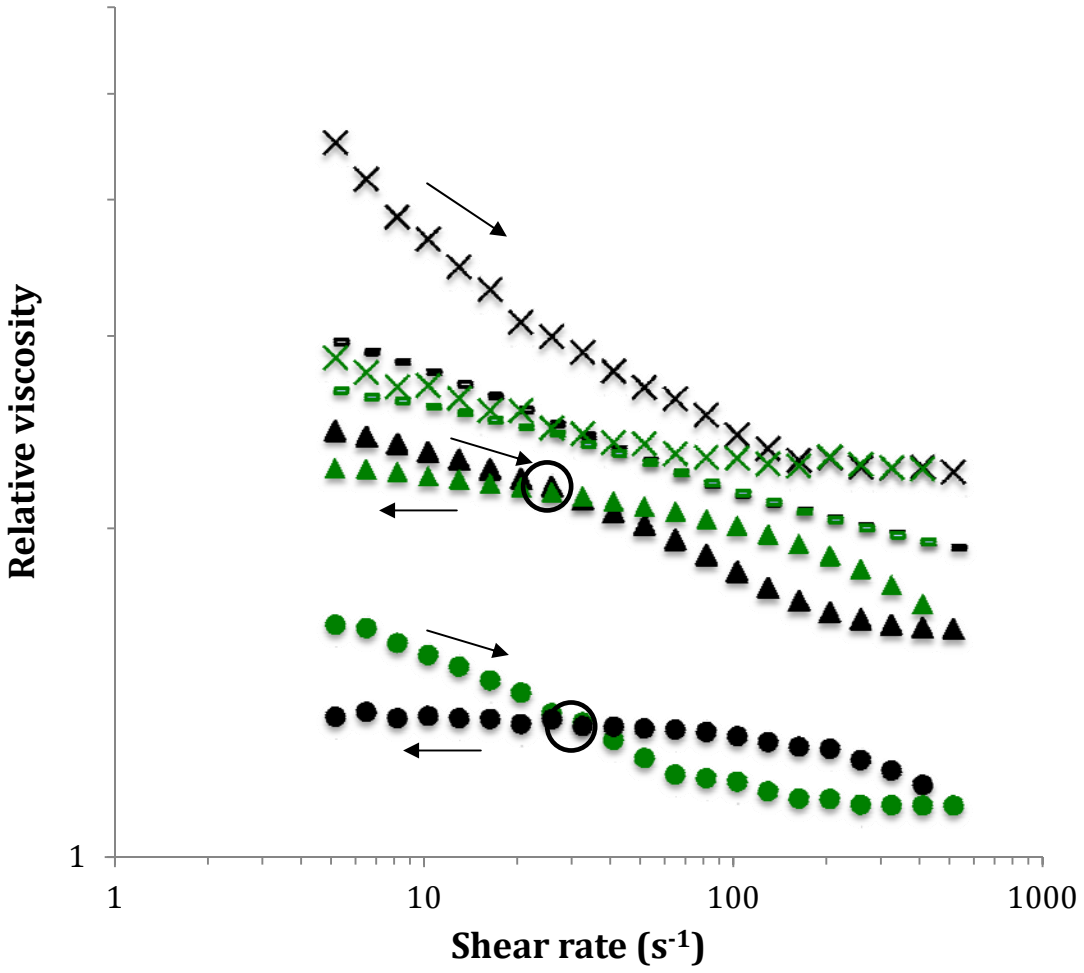

Figure 5.12: Selected relative viscosity curves of oil / aqueous dispersions of Newtonian phases at subjected to an increasing (black symbols) then decreasing (green symbols) shearing profile. Viscosity ratios between dispersed and continuous phases were (circles); (triangles); (dashes); (crosses). Experiments with CC geometry.

Shear thinning behaviour induced with increasing volume fraction of dispersed phase has been discussed in some detail in chapter 4, where the system of was chosen as an example. Here, results obtained for all investigated systems at constant are considered in an attempt to understand the effect of viscosity ratio between dispersed and continuous phases on the degree of induced shear thinning.

Figure 5.13 shows the dependence of power-law index n on λ for fixed $\varphi = 0.3$ for selected systems subjected to increasing-decreasing shear rate. It is observed that as $\dot{\gamma}$ increases (black dots), power law index decreases monotonically for systems with increasing λ. At $\lambda = 68$, power law index of the order of $n = 0.82$ was estimated, clearly indicating shear thinning behaviour. Krynke & Sek [2004], Teipel [2002] and Jansen et al [2001] have also reported similar power law indices for oil / water systems of similar φ and λ (also mentioned in section 4.4.2). Interestingly, on subsequent decrease of shear (white dots in figure 5.13) all investigated systems showed near Newtonian behaviour with power law indices $n \geq 0.94$. Observed Newtonian behaviour may be associated with the absence of significant microstructural changes occurring as the sheared systems are subjected to a decreasing shear rate. Example images illustrating minimal morphological changes on decrease of shear rate of two sheared systems with low and high viscosity ratio between dispersed and continuous phases can be found in figure 5.14. In figure 5.14, images at initial stage, maximum shear rate and after cessation of shear flow are shown at fixed $\varphi = 0.3$ for two systems, one with low and one with high viscosity ratio between dispersed and continuous phases ($\lambda = 0.2$ and $\lambda = 27$ respectively). Significant drop size reduction is illustrated on increase of shear followed by mild microstructural changes on decrease of shear. A step-by-step presentation of structural evolution during this experiment has been shown in figure 4.8. It is believed that principal role in the absence of major microstructural changes on decrease of shear rate, plays the fact that at all investigated systems oil drops were stabilised by the surface active properties of the continuous phases, which significantly limited coalescence, as already discussed in section 4.5.

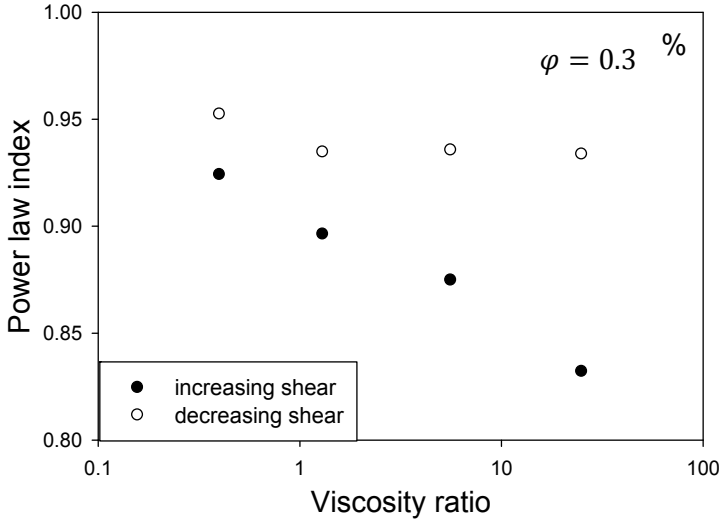

Figure 5.13: Dependence of power law index on viscosity ratio for fixed $\varphi = 0.3$. An increasing-decreasing shear profile was imposed in all experiments. Experiments with CC geometry.

Although the cause-effect relationship between microstructure and shear thinning is well established, the exact nature of the relationship is still not well understood (quantified), which has also been remarked in the literature [for example Keshtkar 2010, Saiki 2007, Yu et al 2002, Teipel 2002, Mason 1999, Pal 1996]. In addition, morphological features (drop size / shape) are generally absent from predictive viscosity models of two-phase systems, which link relative viscosity with η_c, φ and λ but contain no morphological variables (e.g. models presented in chapter 2). Investigations of the quantitative link between morphology and shear thinning should certainly benefit from optimum quality simultaneous rheological and morphological measurements, proposed with the new device of this work.

For low to medium concentration dispersions, shear thinning has been qualitatively associated to the deformability of drops, which enables orientation to the flow direction [Pal 1996]. It is therefore likely that reduction of n at increasing λ may be linked to the presence of more viscous, large, deformable drops, as illustrated in figure 5.14. However, as mentioned

in section 4.4.2, systematic study of the orientation of drops to the direction of the flow has been difficult with the current setup, as the camera was positioned manually, thus obstructing accurate determination of the flow direction.

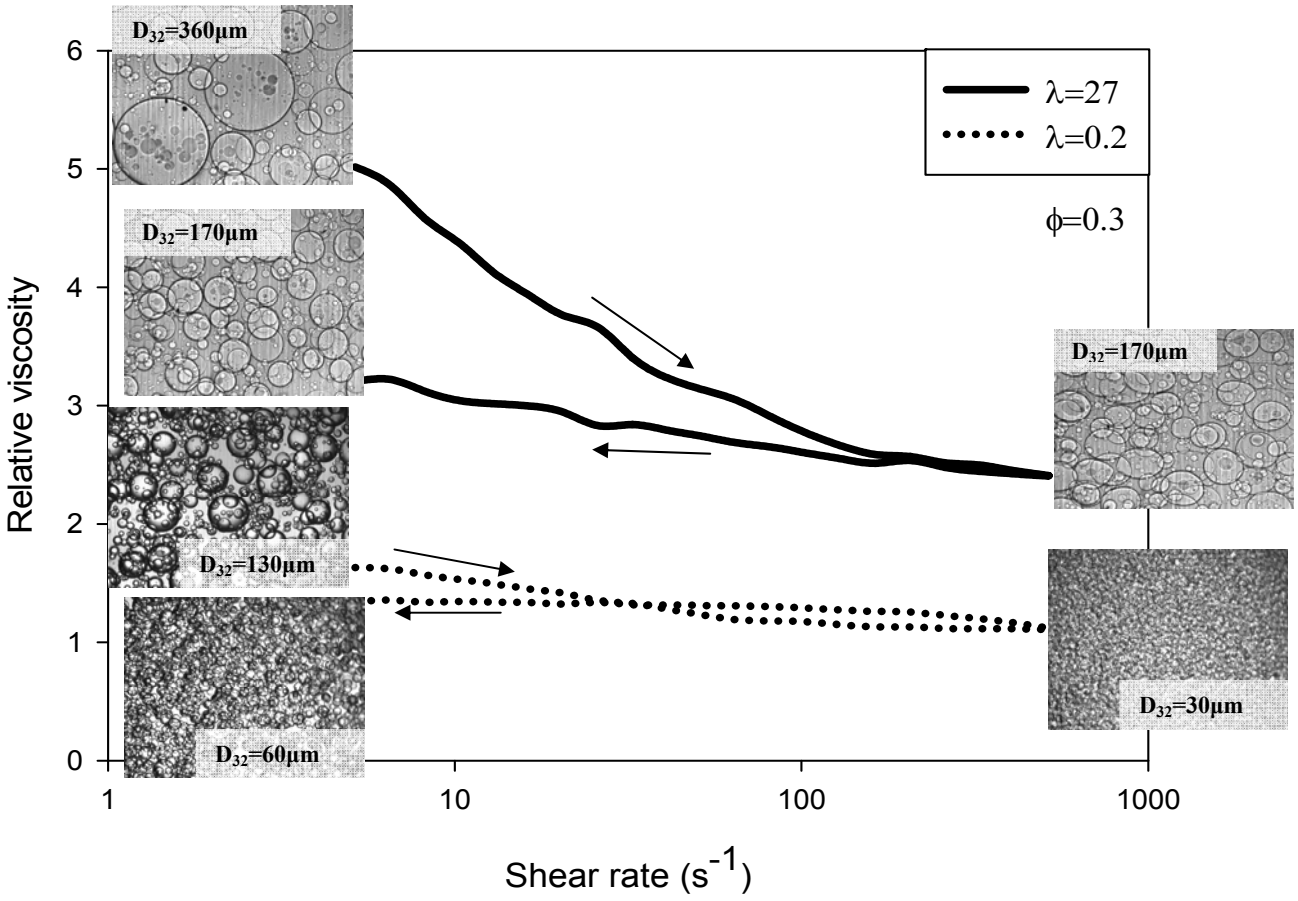

Figure 5.14: Rheology and structure of oil / aqueous systems at $\lambda = 0.2$ and $\lambda = 27$ for fixed $\varphi = 0.3$. Significant morphological changes at increasing shear caused shear thinning, followed by near Newtonian behaviour on subsequent shear decrease as minimal structural changes were observed. Image width $1.2mm$. Experiments with CC geometry. (Note: images on computer screen are easily quantifiable).

Observed shear thinning may also be linked with the intersection of flow curves observed in figure 5.12, a feature that is generally not indicated in the literature. It should be

noted that although observed hysteresis in viscosities in figure 5.12 is marginal, and on occasions hardly noticed (e.g. at $\lambda = 11$), its occurrence was frequent and therefore requires some discussion.

Crossing of flow curves can be interpreted as the result of the following characteristics. At first, shear thinning response, caused by microstructural changes on imposition of flow, produced a negative slope to the curves of increasing shear, as discussed above. The shape of the black (increasing shear) lines corresponds well with the typical shear thinning curve shown in figure 2.4 [Barnes et al 1989]. On subsequent decrease of shear (green lines in figure 5.12), viscosity initially increased slightly, and further maintained an almost zero (Newtonian) slope, causing the observed hysteresis and line intersection. Initial small increase in viscosity can be related to the stabilising effect of the continuous phase on oil drops (section 4.5), which largely prevented coalescence and resulted in small drop sizes. Smaller drops are associated with higher viscosities, as mentioned above. Subsequent near-Newtonian behaviour (almost zero slope of green lines) has been linked to absence of significant microstructural changes, as illustrated in figure 5.14.

Although investigated systems were not thermodynamically stabilised, it appears that shearing also caused narrowing of the drop size distributions (DSD). Figure 5.15 presents DSD of the $\lambda = 0.2$, $\varphi = 0.3$ system (also shown in figure 5.14 in terms of rheology and images) before shearing, at maximum shear rate ($\dot{\gamma} = 500s^{-1}$) and just after cessation of shear flow. It shows that the initially broad drop size distribution, produced by gentle pre treatment of the sample, significantly narrowed as shear rate increased, showing narrower peak at maximum shear rate. Subsequent decrease of shear rate resulted in further broadening of the narrow DSD. This was typical for all examined systems. It is noted that DSD of final

dispersions were narrower than those of initial systems. For example, for the $\lambda = 0.2$, $\varphi = 0.3$ system, breadth of the peaks has been determined as its span, calculated by equation 5.9 [Malvern Instrument's Mastersizer manual], where $D_{0.9}$, $D_{0.1}$, and $D_{0.5}$ refer to the diameter of a drop that is the largest between the 90%, 10%, and 50% of analysed drop population respectively. Initial (before shearing), at maximum shear rate and final (after cessation of shearing) spans were determined at 1.9, 0.4, and 1.0, respectively, showing initial narrowing and subsequent widening of peaks.

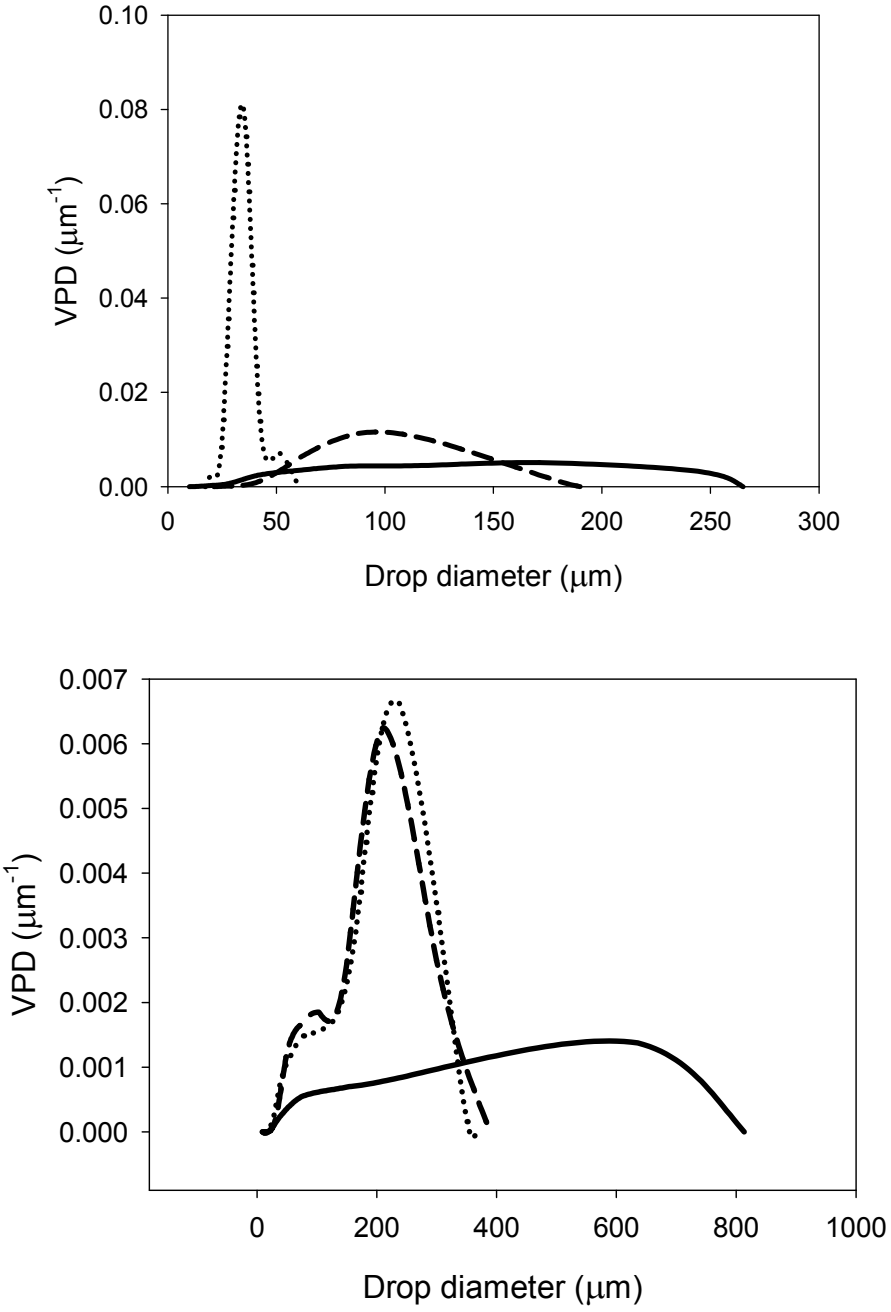

Figure 5.15: Drop size distribution before shearing (solid line), at maximum shear (dotted line) and after cessation of shear (dashed line) for the systems of figure 5.11 at fixed $\varphi = 0.3$ and (a) $\lambda = 0.2$; (b) $\lambda = 27$ (corresponding images shown in figure 5.11). Experiments with CC geometry.

$$span = \frac{d(0.9) - d(0.1)}{d(0.5)} \tag{5.9}$$

Differences in drop size distributions may also be linked to the observed reduction in zero shear viscosities between the pre-sheared and post-sheared systems ($\eta_{r0,initial} > \eta_{r0,final}$), which seems to contradict with the contemporaneous reduction in drop sizes ($D_{32,initial} > D_{32,final}$). The effect of drop size distribution on rheology is not yet well understood, e.g. none of the equations presented in chapter 2 accounts for the impact of size distributions on relative viscosity. However, it has been suggested that wide distributions may cause an increase in viscosity [Pal 1996]. In the present work it appears that the role of size distribution on system's viscosity may be significant, and requires further systematic investigation, which is made possible with simultaneous rheological and microstructural recordings offered by the device of the present work.

Figure 5.15 also indicates occurrence of shear-induced coalescence on gradual decrease of shear, which was widely observed during the experiments and more particularly at low λ (thinner drops). More detailed presentation of shear-induced coalescence (including recorded images) has been presented in section 4.4.4. Although the present study has not intensively focused on investigation of drop coalescence, some remarks will be attempted.

Shear-induced coalescence has been reviewed by Leal [2004] and simulated by Borschig et al [2000]. From those reviews it can be concluded that (i) gentle flow promotes gentle collisions, which was found to enhance drop coalescence; (ii) coalescence is increasingly difficult at high values of viscosity ratio between dispersed and continuous phase; (iii) coalescence rate increases with increasing volume fraction of dispersed phase.

The first two observations are evident in section 4.4.4 as well as in figure 5.15, where it is shown that decreasing shear rate (hence imposing gentle shearing conditions) induced coalescence at $\lambda = 0.2$ but not at $\lambda = 27$. Figure 5.15 also demonstrates that coalescence

resulted in broader size distributions, as the span of the peak increased from 0.4 (at $\dot{\gamma} = 500s^{-1}$) to 1.0 (after cessation of shear flow). Similar results have been reported by Caserta et al [2005], who systematically studied shear-induced coalescence in aqueous biopolymer mixtures and reported that on gradual decrease of a high shear rate, average drop size increased and size distribution progressively broadened.

The effect of φ on observed drop coalescence is presented in figure 5.16 for the $\lambda = 0.2$ system. It is demonstrated in figure 5.16 that at all investigated volume fractions of dispersed phase, shearing at $500s^{-1}$ resulted in drop sizes of the order of $35\mu m$, but increasing φ caused increasing coalescence on decrease of shear rate. The rate of increase, however, declined above $\varphi = 0.1$.

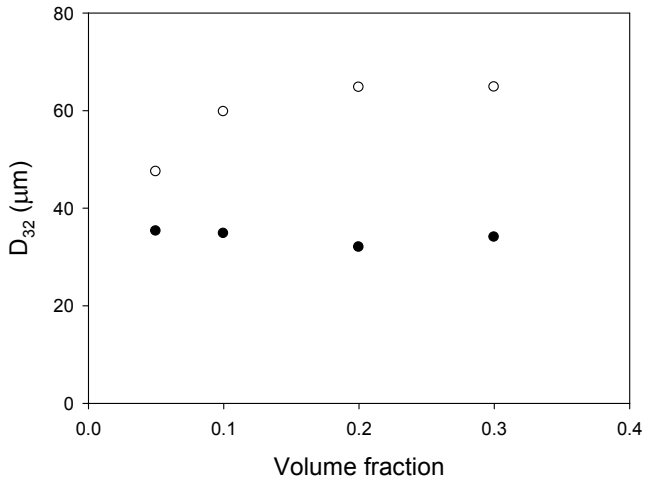

Figure 5.16: Effect of volume fraction of dispersed phase on shear-induced coalescence. Experiments with CC geometry.

5.3 Aqueous / Oil systems

The device was further utilised for experiments with aqueous / oil systems, where aqueous phases are dispersed in oil continuous phases. Besides foods (e.g. margarine), such systems are also relevant to the petroleum industry, and therefore their mechanical properties are of great interest to petroleum engineers [Arhuoma et al 2009]. Nevertheless, published research on aqueous / oil systems and their direct comparison with oil / aqueous mixtures is limited in the literature. Often, researchers assume identical rheological response for oil / aqueous and aqueous / oil systems with similar properties (interfacial tension, viscosity ratio, volume fraction, shearing conditions, etc) [Farah et al 2005; Pal 1998; Lee et al 1997]. The validity of this assumption is tested in the present section for selected systems.

5.3.1 Materials and Methods

System selection was based on table 5.1, where aqueous and oil phases with equal densities, thus capable of forming kinetically stable dispersions, are shown. As in the previous section, the word “aqueous” is conventionally used to denote hydrophilic phases that are fully miscible with water but which may not contain water. Continuous phases were silicone oils with viscosities ranging between $10 - 350 cSt$, while aqueous phases comprised mixtures of hexylene glycol with glycerol. Interfacial tension between the oils and aqueous phases has been previously estimated at $\cong 2 mN\, m^{-1}$ (section 4.5).

Aqueous / oil dispersions were prepared by gentle mixing of the aqueous phases into the oil, a similar pre treatment to that applied in the oil / aqueous systems of the previous section 5.2. Properties of the resulting aqueous / oil systems are shown in table 5.3.

Experiments presented in this section have been conducted with the optical plate / plate geometry of $40mm$ diameter, gap size $1mm$ (unless otherwise stated). For direct comparison, experiments of oil / aqueous systems with exactly the same phase compositions have been conducted using the same geometry. Properties of the investigated oil / aqueous dispersions are also shown in table 5.3. Aqueous / oil and oil / aqueous systems of $\varphi = 0.02$, 0.1, 0.2 and 0.3 have been measured at steady shear rate of $250s^{-1}$ as well as at increasing-decreasing shear rate between $\dot{\gamma} = 5s^{-1}$ and $\dot{\gamma} = 500s^{-1}$, similarly as in the previous section 5.2.

Table 5.4: Composition and viscosities of investigates aqueous / oil systems.

Aqueous phase	**Oil phase**	η_{aq}	η_{oil}	$\lambda_1 = \eta_{aq}/\eta_{oil}$	$\lambda_2 = \eta_{oil}/\eta_{aq}$
$94.4\%HG + 5.6\%Gl$*	$10cSt$ SO*	0.041	0.0095	4.3	0.2
$85\%HG + 15\%Gl$	$50cSt$ SO	0.071	0.049	1.4	0.7
$84.5\%HG + 15.5\%Gl$	$100cSt$ SO	0.072	0.095	0.8	1.3
$83\%HG + 17\%Gl$	$350cSt$ SO	0.076	0.35	0.2	4.6

*HG: Hexylene glycol; Gl: Glycerol; W: Water; SO: Silicone oil

5.3.2 Shear Viscosity at 250s^{-1}

At $\dot{\gamma} = 250s^{-1}$, obtained viscosities of dilute dispersions were very little affected by the presence of dispersed phase for both aqueous / oil and oil / aqueous systems (measured relative viscosities close to unity, data not shown). Interestingly, at increasing volume fraction of dispersed phase, relative viscosities of aqueous / oil and oil / aqueous dispersions of similar λ appeared to gradually deviate from one another, as it is illustrated in figure 5.17 for the $\varphi = 0.3$ systems (data at $\varphi = 0.02$ confirmed observed trend whereas at $\varphi = 0.1$, similarly as at $\varphi = 0.02$, no significant differences between oil / aqueous and aqueous / oil systems were observed and recorded relative viscosities were near to unity). If valid, this

result implies that the abovementioned generalisation of correlations obtained for solid suspensions and / or oil / aqueous dispersions to aqueous / oil systems might not be necessarily justified at all times. This observation was reproducible, and average standard deviation of triplicates was calculated at 12%, ranging between 5% and 22%.

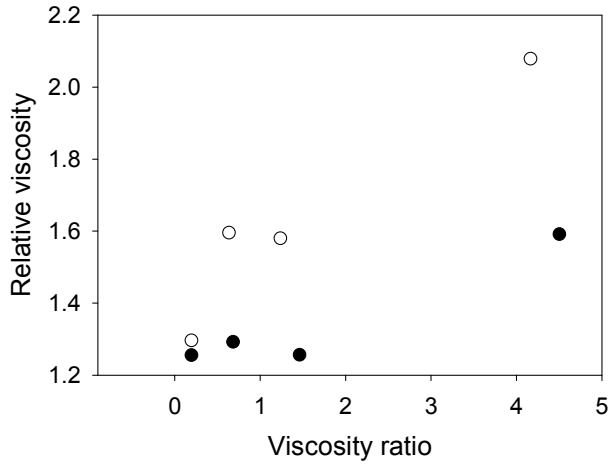

Figure 5.17: Relative viscosities of aqueous / oil (black dots) and oil / aqueous (white dots) systems at $\varphi = 0.3$ obtained with the optical plate / plate $40mm$ diameter geometry.

Validity of results was further tested by an additional set of experiments identical to those shown in figure 5.17, conducted with the standard stainless steel geometry supplied by Malvern Instruments (parallel plate, $40mm$ diameter, gap size $1mm$). The aim of those experiments was to test the effect of changing material of the geometry (glass instead of stainless steel) on the measurements. Results obtained with the two geometries are shown in figure 5.18, where non linear regressions (Sigmaplot 11.0) are also shown to facilitate differentiation between the two types of dispersions.

In figure 5.18 it is evident that regardless of the material that the geometry is made of, aqueous / oil systems of $\varphi = 0.3$ showed lower relative viscosities than the corresponding oil / aqueous type of dispersions of similar φ and λ.

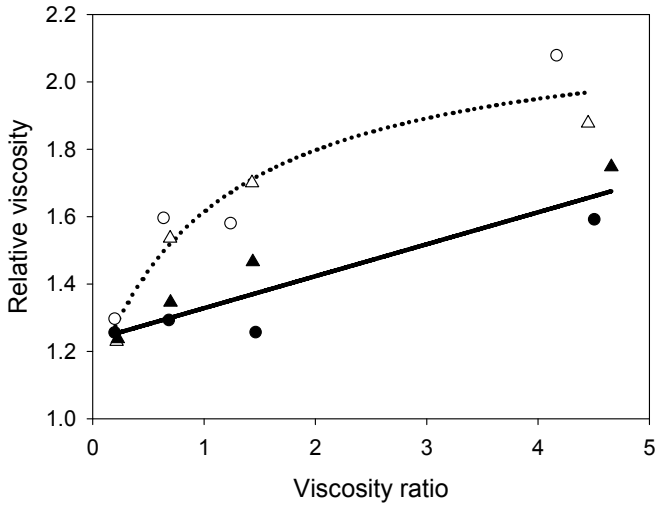

Figure 5.18: Relative viscosities of aqueous / oil (black symbols) and oil / aqueous (white symbols) dispersions obtained with the plate / plate (40mm diameter) optical glass (dots) and stainless steel (triangles) geometries.

The same observation was also evident at increasing-decreasing profile of shear rate between $5s^{-1}$ and $500s^{-1}$. Figure 5.19 shows selected flow curves and confirms higher relative viscosities for oil / aqueous than aqueous / oil dispersions of similar φ and λ. It is noted that flow curves of figure 5.19 have generally similar shapes to those of figure 5.12 (obtained with coaxial cylinders optical geometry for oil / aqueous systems).

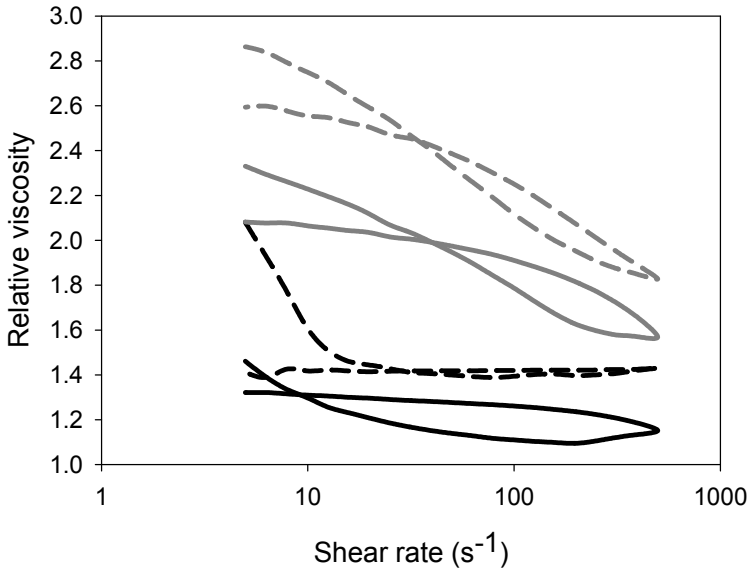

Figure 5.19: Relative viscosities at increasing-decreasing profile of shear rate between $5s^{-1}$ and $500s^{-1}$ for selected oil / aqueous (grey lines) and aqueous / oil (black lines) systems at $\varphi = 0.3$ and viscosity ratios $\lambda = 0.8$ (solid lines) and $\lambda = 4.3$ (dashed lines) showing higher relative viscosities for oil / aqueous than aqueous / oil systems. Experiments with PP40 geometry.

Observed variations between aqueous / oil and oil / aqueous systems have been further examined in association with simultaneously recorded microstructural data. It was observed that aqueous / oil systems of high λ, which showed lower relative viscosities in figure 5.17, were characterised by larger drops than the corresponding oil / aqueous dispersions of similar λ, as it is illustrated in figure 5.20. As larger drops are generally associated with lower viscosities (section 5.2.3), this observation further confirms the link between rheology and morphology and the importance of simultaneous rheo-structural experiments. The differences in obtained drop sizes may suggest that for the investigated systems, morphology significantly depended on viscosity of continuous phase, as viscous continuous phases caused increased drop breakage. The effect of viscosity of continuous phase on drop size is discussed in more detail in the next section.

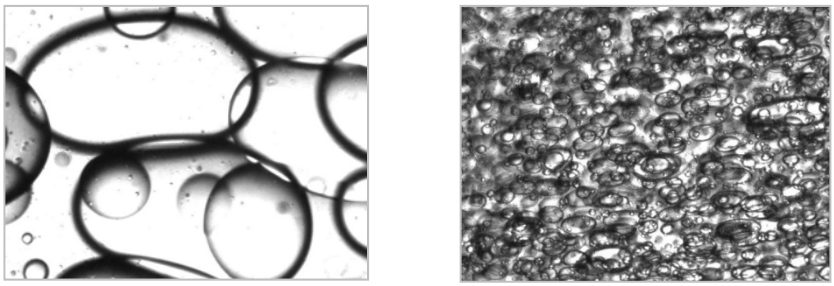

Figure 5.20: Images of aqueous / oil (left) and oil / aqueous (right) dispersions with $\varphi = 0.3$ and $\lambda = 4$ at $\dot{\gamma} = 250s^{-1}$. Note: images of oil / aqueous systems were recorded at reduced gap size of $0.5mm$. Image width $1.2mm$, captured with PP40 geometry.

5.3.3. Mean Drop Size

The aim of this section is to stress the importance of viscosity of continuous phase on system's microstructure for investigated oil / aqueous and aqueous / oil systems, which in turn is closely linked with the observed relative viscosity, as discussed in section 5.3.2. It is noted that the relationship of Capillary number (equation 2.15) with viscosity ratio is not considered in this section, as focus is directed on the potential effect of drop size on viscosity. To enable direct comparison between rheology at $\dot{\gamma} = 250s^{-1}$ and corresponding morphological recordings, an additional set of experiments was conducted where the plate / plate geometry ($40mm$ diameter) was subjected to nominal shear rate of $\dot{\gamma} = 187.5s^{-1}$ and images were recorded at the rim of the top plate. It can therefore be calculated from equation 4.2 that applied shear rate at the rim of the top plate, where morphological data were recorded, was $250s^{-1}$. It is noted that automated positioning of the light / camera unit along the plate's radius would have enabled direct comparison without requiring the additional experiments by positioning the image acquisition system at $r = (3/4)r_P$, where r_P is the radius of the top plate.

Measured Sauter mean drop diameters of aqueous / oil and oil / aqueous dispersions at $\varphi = 0.3$ are plotted against viscosity of continuous phase in figure 5.21 and against viscosity ratio between dispersed and continuous phases in figure 5.22. Figure 5.21 shows that large drops were difficult to break by continuous phases of very low viscosity ($0.0095 Pa\ s$). This is expected from Grace Curve, as drops immersed to continuous phases of low viscosities are subjected to low Capillary numbers, possibly below the critical Capillary number (equation 2.15). At increasing viscosity of continuous phase, smaller drops were acquired for both aqueous / oil and oil / aqueous dispersions.

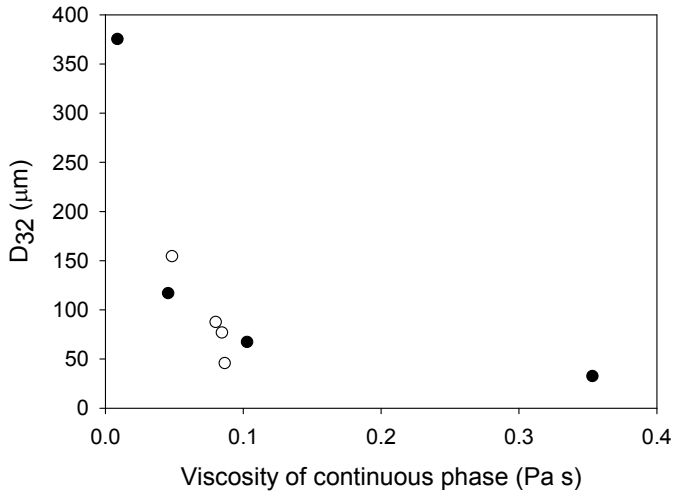

Figure 5.21: Sauter mean diameter of aqueous/oil (black dots) and oil/aqueous (white dots) dispersions against viscosity of dispersed phase. Experiments with PP40 geometry.

Figure 5.22, on the other hand, illustrates that for the investigated systems there was no evident correlation between drop breakage and λ, as different trends were observed for oil / aqueous and aqueous / oil systems. For the oil / aqueous systems, where increase of λ is

linked with decrease in viscosity of continuous phase (table 5.3), drop size decreased at increasing λ. For the aqueous / oil systems, on the other hand, the opposite was observed and larger drops have been acquired at increasing λ, which can be associated with the significant increase in viscosity of continuous phase (table 5.3). Results from figures 5.21 and 5.22 may suggest that viscosity of continuous phase might play a key role in drop breakage. These results were also associated with obtained rheological observations in section 5.3.2, where at increasing λ oil / aqueous systems were found to display higher relative viscosities than the corresponding aqueous / oil dispersions of similar λ, which is generally not predicted by viscosity models of chapter 2.

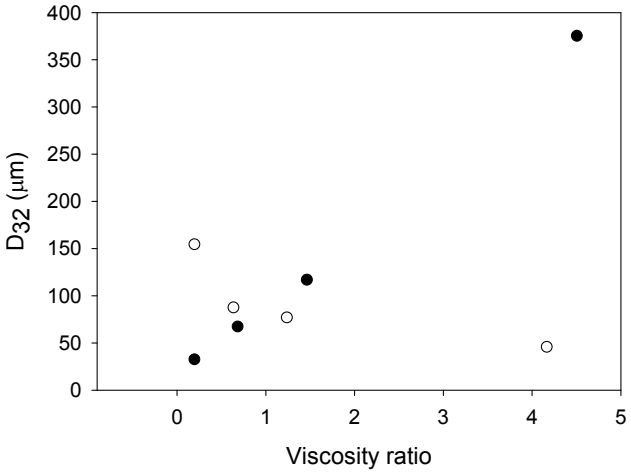

Figure 5.22: Sauter mean diameter of aqueous / oil (black dots) and oil / aqueous (white dots) dispersions obtained at $\dot{\gamma} = 250s^{-1}$ against viscosity ratio between dispersed and continuous phases. Experiments with PP40 geometry.

5.3.4 Relationship Between D_{32} and D_{max}

Similarly with the oil / aqueous mixtures in the previous section the relationship between D_{32} and D_{max} in aqueous / oil mixtures at $\dot{\gamma} = 250s^{-1}$ (nominal shear $\dot{\gamma} =$

$187.5s^{-1}$, image acquisition at the rim of the top plate) is examined in this section. Results at $\varphi = 0.3$ appear to suggest a linear correlation between D_{32} and D_{max} for investigated systems with proportionality constant 0.87, as illustrated in figure 5.23. The high value of proportionality constant indicates that mean drop size was primarily determined by large drops, with limited contribution from small satellites. Consequently, it can be suggested that drop breakage was dominated by necking mechanism, which lead to the production of two equi-sized daughter drops and small number of satellites.

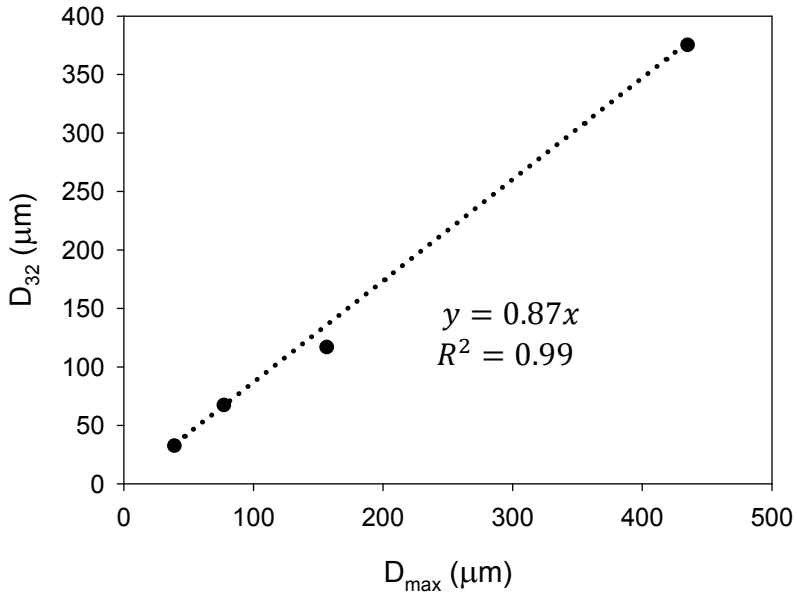

Figure 5.23: Relationship between D_{32} and D_{max} for investigated aqueous / oil systems and linear regression passing through the origin of coordinates. Experiments with PP40 geometry.

5.4 Oil / Oil systems

Studies on liquid / liquid two phase systems where both liquids are oils are scarce in the open literature [Suitthimeathegorn et al 2005; Jaitely et al 2004]. In addition, a considerable amount of research work has focused on fat replacement techniques, especially in the food industry, which encourages scientific emphasis on aqueous / aqueous systems instead [McCann et al 2011; Mistry 2001; Lucca & Tepper 1994]. However, the potential of oil in oil dispersions has recently been recognised in many fields such as formation of nanoparticles [Klapper et al 2008], microencapsulation [Kobaslija et al 2006] and pharmaceutical formulations for controlled drug release [Brown 2004; Jaitely et al 2004]. The study of oil in oil systems therefore becomes important and relevant in research and the industry.

In this section, results obtained with the new device on oil / oil systems are presented. Rheology and structure of dispersions of sunflower oil in silicone oil as well as its reverse (silicone in sunflower oil) under shear flow are considered. Results are compared with observations for oil / aqueous systems of similar viscosity ratio between dispersed and continuous phases.

5.4.1 Materials and Methods

As with oil / aqueous systems, stability was obtained by matching the densities of the two individual phases, thus eliminating the tendency for creaming and sedimentaion. For this reason, silicone oils of $5cSt$ and $10cSt$ (Dow Corning Corporation, Sigma Aldrich) were mixed in proportion $4:1$ to obtain an equi-dense phase with the sunflower oil (purchased from

local supermarket), which had density of $920kg\ m^{-3}$. The exact composition of purchased sunflower oil is not known, but its major constituents are triglycerides, which are surface active components due to the presence of the glycerol- (hydrophilic) and the long fatty acid (hydrophobic) parts in the same molecule. Interfacial tension between sunflower and silicone oils was determined with the steady drop deformation method, which has previously been used to measure interfacial tension of silicone oils with aqueous mixtures of hexylene glycol with water and with glycerol [section 4.5]. Determination of interfacial tension was repeated in triplicates and an average value of $2mN\ m^{-1}$ ($\pm 0.2mN\ m^{-1}$) was estimated. It is reminded that similar interfacial tension was measured for oil / aqueous systems where silicone oils are dispersed in mixtures of hexylene glycol with glycerol (section 4.5).

Experiments presented in this section were conducted with the optical plate / plate geometry of $60mm$ diameter, $1mm$ gap, unless otherwise stated. Viscosities of the two individual oil phases were measured using the same geometric configuration, sunflower oil $0.055Pa\ s$, silicone oil mixture $0.0055Pa\ s$. Viscosity ratios for the two types of dispersions, sunflower in silicone oil and silicone in sunflower oil, were therefore determined at $\lambda = 10$ and $\lambda = 0.1$ respectively.

Coarse dispersions of $\varphi = 0.02$, 0.1, 0.2 and 0.3 were prepared by gentle mixing of required amounts of the two phases to produce a $50mL$ sample, as in the previous section. Rheology and structure of dispersions were measured under steady shear of $\dot{\gamma} = 250s^{-1}$. For direct comparison, an oil / aqueous dispersion of $\lambda = 10$ ($1000cSt$ silicone oil dispersed in a mixture of 80.4% hexylene glycol and 19.6% glycerol) was also prepared and measured at the same shear rate and with the same parallel plate $60mm$ diameter geometry.

5.4.2 Shear Viscosity at 250s^{-1}

Relative viscosities of the two oil / oil systems (sunflower in silicone oil, $\lambda = 10$, and silicone in sunflower oil, $\lambda = 0.1$) at different volume fractions of dispersed phase are presented in figure 5.24. For direct comparison, results for the oil / aqueous mixture of $\lambda \cong 10$ obtained with the same geometry are also shown.

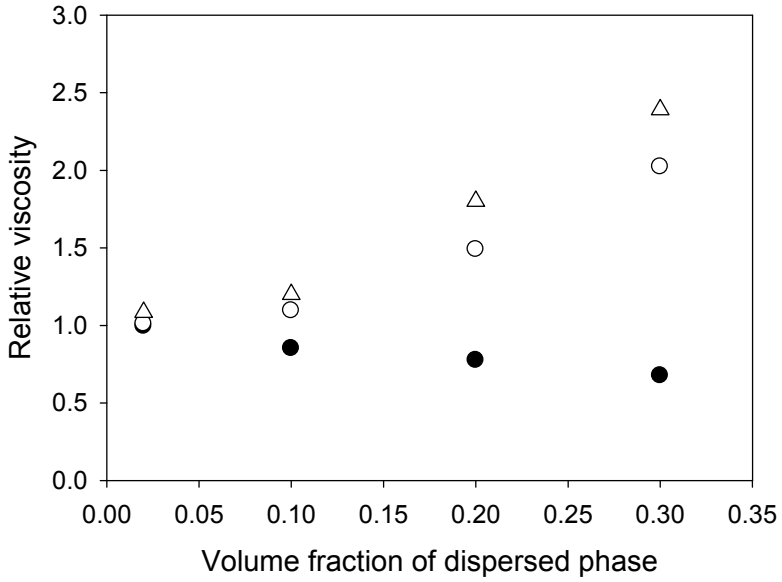

Figure 5.24: Relative viscosities of silicone in sunflower oil ($\lambda = 0.1$, black dots) and sunflower in silicone oil ($\lambda = 10$, white dots) at different volume fractions. Results for the corresponding oil in water system of $\lambda = 10$ are also shown for comparison (white triangles). Experiments with PP60 geometry.

Surprisingly, it was found that dispersing the less viscous silicone oil in sunflower oil ($\lambda = 0.1$) resulted in an unexpected drop in viscosity, the reduction being greater at increasing volume fraction of dispersed phase (solid dots in figure 6.8). Similar results were invariably obtained on several repetitions of the experiment (standard deviation 5%).

A number of possible explanations for these unexpected results have been considered. At first, simultaneous morphological recordings were examined and revealed a microstructure of drops dispersed in continuous phases, which is typical for single dispersions of the investigated volume fractions of dispersed phase and shear rates. Formation of string like structures or other favourable morphological configurations under shear flow, possibly causing viscosity reduction, was not evidenced. Images of the silicone in sunflower oil dispersion at $\varphi = 0.02$, $\varphi = 0.1$ and $\varphi = 0.2$ are shown in figure 5.25. At $\varphi = 0.3$, extensive drop breakage caused deterioration of image quality and reduction of gap size would have been necessary to determine drop size (as discussed in chapter 4). Hence, there is no image shown for this φ. It is noted that at $\varphi = 0.2$, acquired images were easily quantified on a computer screen.

The possibility of phase separation in terms of creaming or sedimentation, which would result in inhomogeneous coverage of the stationary or rotating plates thus interfering with the measurement, was also examined as a plausible reason for the observed decrease of relative viscosity with increasing φ. At $\varphi \leq 0.02$ no such phase separation was observed, while at $\varphi = 0.3$ a low degree of phase separation (shear banding) was occasionally noticed by visual observation of the shearing geometry. However, observed phase separation was excluded as a reason for the viscosity reduction due to its low level, its un-repeatability and the fact that viscosity drop was also evident at $\varphi \leq 0.2$, where no phase separation occurred.

Bridging between the two plates by large dispersed phase drops was also eliminated as a plausible reason due to the small drop sizes (of the order of $50\mu m$) with respect to the large gap size ($1mm$). Furthermore, the possibility that viscosity reduction might be linked with the presence of very low viscosity dispersed phase was considered. However, it was found that

literature on liquid foams, which represent the systems with the less viscous dispersed phases, suggests that for a given shear rate relative viscosity increases with increasing volume fraction of the gas phase ("foam quality") [Herzhaft 1999, Hohler & Cohen-Addad 2005]

The observed $\eta_r < 1$ might have therefore been the result of partial miscibility between dispersed and continuous phases, where solubilisation of the less viscous dispersed phase in the more viscous continuous phase caused lowering of the system's viscosity. In this case, knowledge of the exact composition of the two phases in the system would require employment of analytical chemistry for the construction of the appropriate phase diagram. The main weaknesses of this hypothesis are related to the presence of silicone oil drops at volume fraction as low as $\varphi = 0.02$, as well as the fact that viscosity continued to decrease at increasing φ. Although with evident weaknesses, partial miscibility of the two phases appeared to be the most plausible explanation so far for the reduction of viscosity on addition of the less viscous dispersed phase.

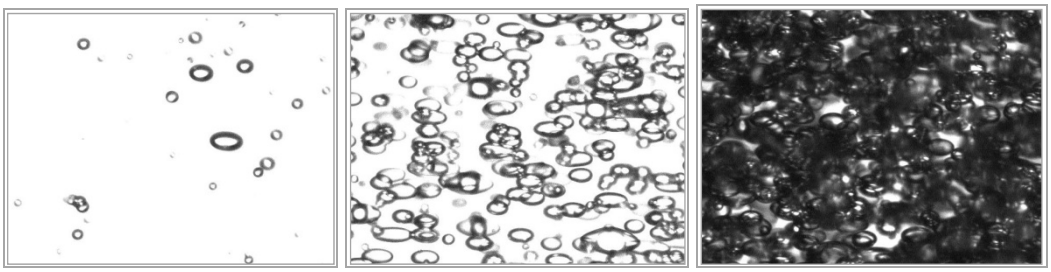

$\varphi = 0.02$ $\varphi = 0.1$ $\varphi = 0.2$

Figure 5.25: Silicon oil drops in sunflower oil continuous phase ($\lambda = 0.1$) at increasing volume fraction of dispersed phase and $\dot{\gamma} = 250s^{-1}$ showing drop-matrix morphology. (Image width $1.2mm$, images captured with PP60 geometry).

At $\lambda = 10$, dispersion of the viscous sunflower oil in silicone oil caused increase in viscosity (white dots in figure 5.24). Comparison with the oil / aqueous mixture of similar λ (white triangles in figure 5.24) demonstrated that in the case of sunflower / silicone oil the increase was less significant. The difference between oil / oil and oil / aqueous systems may be linked to (i) solubilisation of the two phases in the case of the oil / oil system; (ii) smaller drops in the case of the oil / aqueous system, shown in the next section and generally associated with higher viscosities [chapter 5, Teipel 2002, Barnes 1989, Pal 1996].

5.4.3 Drop Breakage at λ=10: Comparison Between Oil / Oil and Oil / Aqueous systems

Very good quality images were obtained for both investigated oil / oil systems. Example images of silicone oil drops in sunflower oil were shown in figure 5.25 above, while images of the reverse system at increasing volume fraction of dispersed phase are shown in figure 5.26 below.

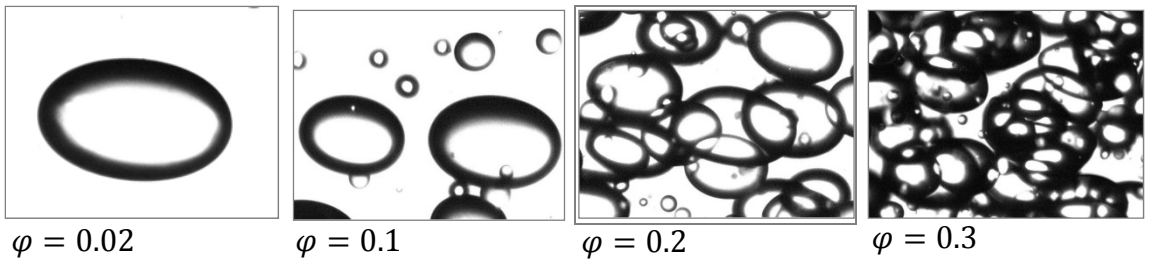

Figure 5.26: Sunflower oil drops in silicone oil ($\lambda = 10$) at increasing volume fraction of dispersed phase and $\dot{\gamma} = 250s^{-1}$. (Image width $1.2mm$, images captured with PP60 geometry.).

At $\lambda = 10$, drops of sunflower oil immersed into silicone oil at dilute dispersions did not break and drop size was predominately determined by mixing during sample preparation. Similar observations were discussed in section 5.2 for the dilute oil / aqueous system of $\lambda = 10$, which did not show drop rupture under shear, as predicted by Grace Curve (figure 2.6). At increasing volume fraction of dispersed phase, observed drop breakage resulted in a reduction of obtained drop size showing deviation from Grace Curve, in both oil / oil and oil / aqueous dispersions (see also section 5.2).

However, morphological recordings at $\dot{\gamma} = 250s^{-1}$ revealed a significant difference in obtained drop sizes between the oil / oil and the corresponding oil / aqueous systems of similar φ and λ. At $\varphi = 0.3$, Sauter mean diameters of the oil / oil system were estimated at $210\mu m$, about 2.5 times larger than the oil / aqueous system's $80\mu m$. Measured drop size distributions were of similar shape, as illustrated in figure 5.27, and indicate similar breakage mechanisms. The difference in obtained drop sizes between the oil / oil and oil / aqueous dispersions may be associated with the ($20\ fold$) difference in the viscosity between the two continuous phases, as the more viscous aqueous continuous phase exerted significantly higher distortive stress ($\eta_c \cdot \dot{\gamma}$) to the dispersed drops than the less viscous oil continuous phase. As such, the imposed Capillary number was higher. A similar observation was discussed in the previous section for aqueous / oil systems, where viscosity of continuous phase appeared to play a key role in drop breakage. Smaller drop sizes of the oil / aqueous system have been linked with the higher acquired relative viscosities.

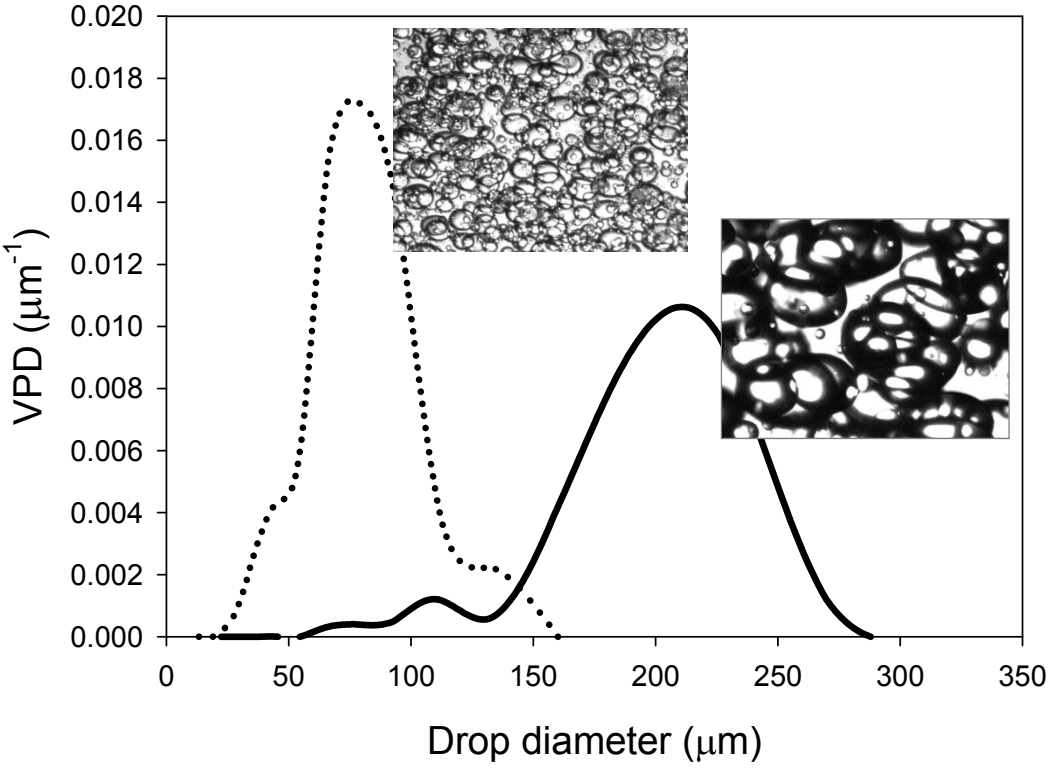

Figure 5.27: Drop size distributions of sunflower-in-silicone oil and silicone oil-in-aqueous media at $\varphi = 0.3$ and $\dot{\gamma} = 250s^{-1}$. (Image width $1.2mm$, experiments with PP60 geometry).

5.5 Aqueous / Aqueous Systems: Structure Stabilisation by Gelation

The reason for choosing to investigate aqueous two phase systems is their importance in many commercial products, and especially in the low fat foods and home and personal care industries [Spyropoulos et al 2007, Puyvelde Van et al 2003]. They are often used to produce the required product texture or to substitute an oil ingredient without compromising textural requirements. As rheology and structure determine texture and product quality, simultaneous rheological and microstructural studies of aqueous / aqueous systems might be very valuable for industrial and research purposes. However, such systems are often more demanding in terms of image acquisition as refractive indices of both ingredients are often very similar and

clear contrast between the two phases becomes difficult to obtain. With the present setup, very high quality images of aqueous / aqueous mixtures were recorded. An example of a gelling system is presented in the present section.

One way to generate kinetically stable morphologies is to entrap the required structure into a gel formed by a gelling component in the mixture. In the present study, temperature induced gelation of a polysaccharide / protein mixture has been monitored at different shear rates. Sample preparation involved very gentle mixing of dextran (solution $15\%\ wt/wt$) with gelatine (solution $10\%\ wt/wt$) in ratio 1:4. Gelatine was dissolved under constant heating conditions to avoid premature gelation. After reaching $80℃$, it was gently mixed with the relevant volume of dextran solution and subsequently very rapidly loaded to the cone / plate geometry. Shear flow and rheo-structural recordings began almost immediately. As temperature control is important for these experiments, it is critical to maintain all sample preparations and pre-treatment conditions as constant as possible. Cooling of the mixture induced gelation, followed by the characteristic increase in viscosity. An example of sample gelation and associated structures is illustrated in figure 5.28.

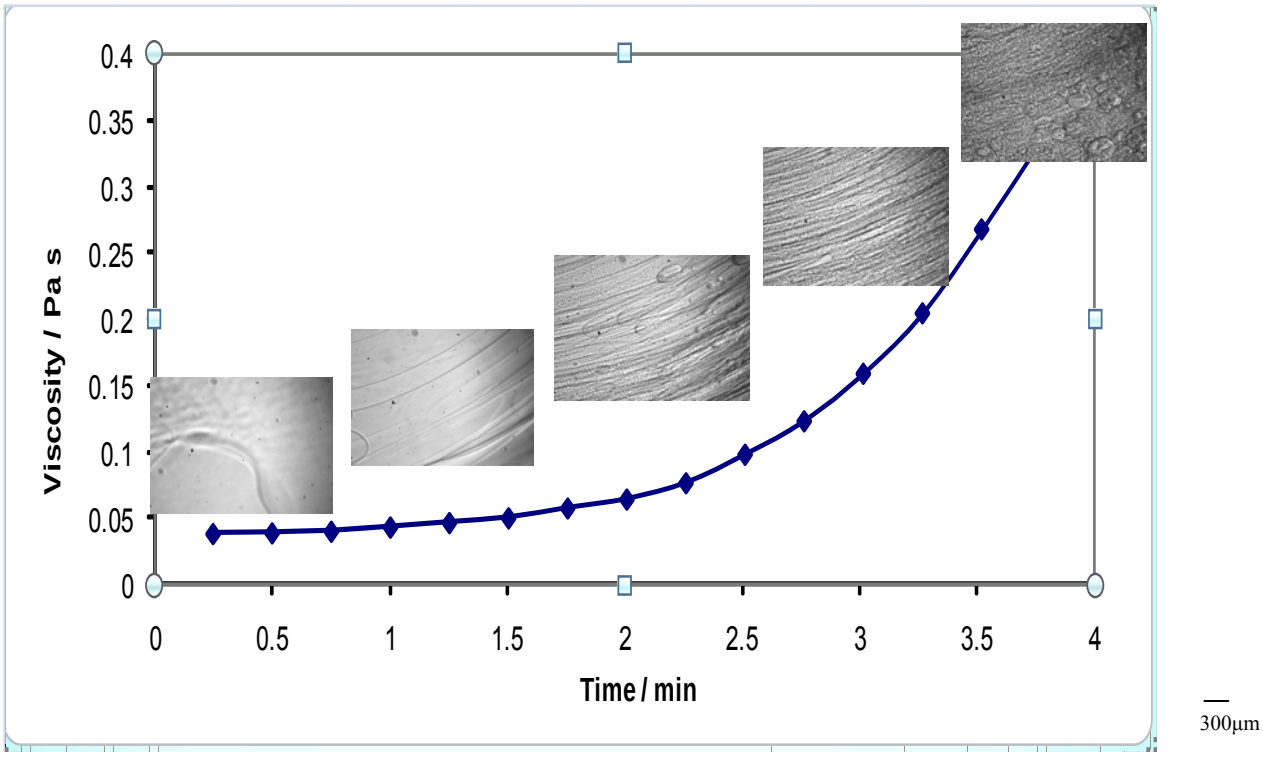

Figure 5.28: Simultaneous rheological and microstructural data of a dextran / gelatine system during gelation induced by lowering of temperature from ca 60℃ to room temperature; shear rate $10s^{-1}$. Experiments with CP2/55 geometry.

Shearing induced structure organisation and alignment to the direction of the flow (figure 5.28). Continuation of shearing beyond $4min$ resulted in a temporal viscosity plateau at $0.4Pa\ s$ (gelled structure), followed by structure breakdown and consequential reduction in viscosity (data not shown). As structure development strongly depends on flow conditions, the effect of shear rate on gel structure formation at a range of well controlled shears has been considered and it is illustrated in figure 5.29. At present, temperature is excluded from figure 5.29, as it was not accurately controlled / monitored.

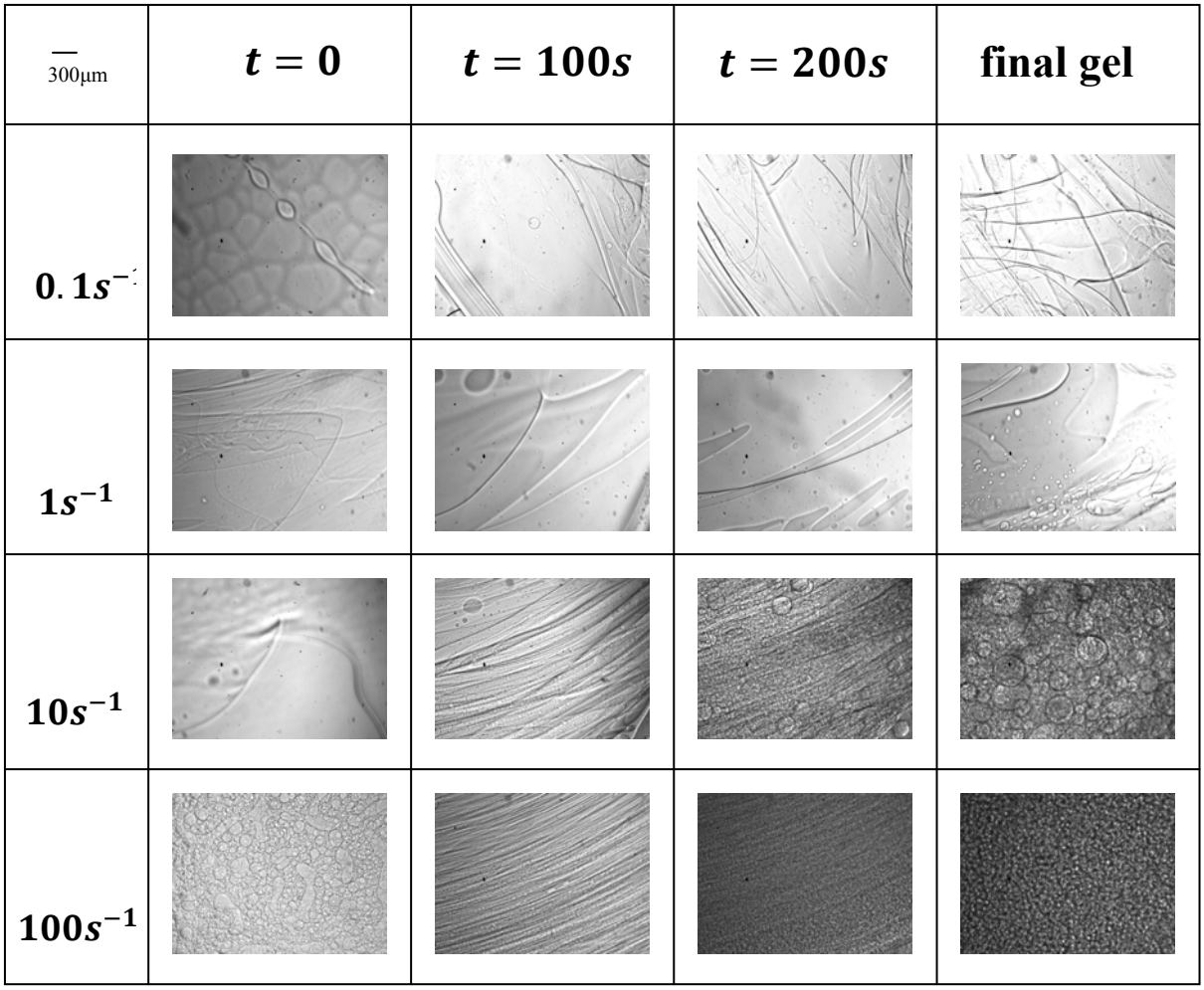

Figure 5.29: Effect of shear rate on structure evolution of temperature induced gelation of a dextran / gelatine system (dextran 15% wt/wt gently dispersed in gelatine 10% wt/wt; weight fraction of dispersed phase 0.2). Experiments with CP2/55 geometry.

Various different morphologies are shown in figure 5.29. Gels of entangled curved strings were formed at shear rates below $1s^{-1}$, while finer gel formations were produced at increasing shear rate. Figure 5.29 therefore illustrates that gel structure is determined by the applied shear flow conditions on gelation. Control of cooling rate and / or gelatine concentration is expected to further contribute in the final microstructure control by altering gelling rate.

5.6 Summary

In this chapter, evaluation of the newly developed device, discussed in the previous chapter, was extended to include examination of its potential in systematic simultaneous rheological and microstructural investigations of two phase systems. Example systems covering all combinations of hydrophobic ("oil") and hydrophilic ("aqueous") phases have been measured under shear, i.e. oil / aqueous, aqueous / oil, oil / oil, and aqueous / aqueous dispersions. Such systems are relevant to both industrial applications and fundamental research.

All constructed geometries have been considered in this chapter. Oil / aqueous dispersions were measured using the coaxial cylinders geometry, while the parallel plates of $40mm$ geometry was employed for measuring aqueous / oil systems. Experiments with oil / oil and aqueous / aqueous systems were conducted using the parallel plates of $60mm$ diameter and cone / plate geometries, respectively.

Examined oil / aqueous dispersions had Newtonian individual phases, viscosity ratios between dispersed and continuous phases in the range of $0.2 \leq \lambda \leq 67$ and volume fractions of dispersed phase between $0.02 \leq \varphi \leq 0.3$. Rheology and structure ere measured systematically at steady shear rate of $250s^{-1}$ as well as at increasing-decreasing shear rate profile between $5s^{-1}$ and $500s^{-1}$.

Obtained relative viscosities at $250s^{-1}$ were compared with predictive viscosity models found in the literature and showed good agreement with the effective medium theory, which assumes that concentrated systems are formed by consecutive additions of very small quantities of dispersed phase in initially pure continuous phase. Taking the Choi /

Schowalter's model as a template, a viscosity equation was further developed to best fit experimental data. According to the new equation, the effect of dispersed phase on system's viscosity was very low at low λ, increasingly stronger at increasing λ and constant at $\lambda \geq 10$ for all investigated volume fractions of dispersed phase.

Obtained critical Capillary numbers were further calculated by equation 2.9, where recorded maximum drop radius was taken into consideration, and results were compared with Grace Curve, as expressed by de Bruijn's equation 5.9. Very good agreement between experimental data and Grace Curve was found for dilute systems. At increasing volume fraction of dispersed phase, however, recorded data deviated from Grace Curve, e.g. drop breakage under simple shear flow was observed at $\lambda > 4$. Deviations were explained by means of the effective medium theory, which associates drop breakage with the average system's viscosity rather than the viscosity of continuous phase.

The relationship between Sauter mean and maximum drop diameter at $250s^{-1}$ was subsequently examined and found to be linear with proportionality constant of the order of 0.7 (slightly reduced at higher volume fractions of dispersed phase, attributed to increased interactions between droplets, which promoted production of increased number of small satellite drops during breakage). In addition, drop diameter was found to decrease at increasing volume fractions of dispersed phase, which was attributed to a combination of increased level of drop breakage and limited coalescence, for $\varphi \leq 0.3$, linked with the stabilizing effect of continuous phase on oil drops (discussed in section 4.5).

Flow curves at increasing-decreasing shear rate of non dilute oil / aqueous dispersions showed induced shear thinning behaviour on initial increase of shear, followed by near Newtonian response on subsequent decrease of shear. Results were examined in conjunction

with simultaneous microstructural observations and a close link between recorded viscosity and morphology was suggested. Shear thinning was linked with breakage as well as deformation and favourable orientation of drops to the flow direction. Subsequent near Newtonian behaviour on decrease of shear rate was further associated with minimal microstructural changes observed due to the stabilising effect of the continuous phase on oil drops, largely limiting coalescence.

The fact that zero-shear viscosities were lower prior to shearing than after shearing, despite contemporaneous reduction in drop size generally associated with higher viscosities, was also discussed. It was suggested that the effect of drop size distribution might be of importance and that more (future) work on the link between poly disparity and rheology would be beneficial for in depth understanding of the lack between poly disparity and rheology would be beneficial

Experiments with aqueous / oil dispersions aimed primarily at investigating the validity of implementing viscosity models developed for oil / aqueous systems (discussed in chapter 2) to aqueous / oil type of systems. Examined aqueous / oil systems had viscosity ratio between dispersed and continuous phases ranging between 0.2 and 4, while volume fraction of dispersed phase was between 0.02 and 0.3. For direct comparison, oil / aqueous dispersions of similar λ, φ and interfacial tension were measured with the same geometry.

At $\varphi \leq 0.1$, the two types of dispersions showed no significant differences in obtained relative viscosities, which maintained a value close to unity. However, at increasing volume fraction of dispersed phase, oil / aqueous dispersions of high λ showed increasingly higher relative viscosities than the corresponding aqueous / oil systems of similar φ and λ. This observation was further confirmed with measurements conducted using a standard stainless

steel geometry of the same configuration (plate plate of $40mm$ diameter, supplied by Malvern Instruments).

Results were examined in association with simultaneous microstructural recordings, where a close link between rheology and structure was indicated. Viscosities of individual phases were identified as a potentially significant factor in determination of drop deformation and breakage of systems with similar λ. It was suggested that at high λ, the higher viscosity of continuous phase in oil / aqueous compared to aqueous / oil systems (at $\lambda = 4$ the difference was of the order of 10) induced extended drop breakage, hence smaller drops, which are associated with higher η_r.

Overall, it can be concluded that implementing viscosity models developed for oil / aqueous dispersions to aqueous / oil systems, although found in the literature, might not be entirely justifiable. Observed differences confirmed the strong link between rheology and structure.

The two phases of investigated oil / oil dispersions were sunflower oil ($\eta = 0.055Pa\,s$) and a mixture of silicone oils with equal density ($\eta = 0.0055Pa\,s$). Resulting systems had viscosity ratios 0.1 and 10, depending on which phase was dispersed in the other.

It was found that whereas dispersing sunflower oil in silicone oil resulted in an expected rise in relative viscosity, the opposite was observed when the less viscous silicone oil was dispersed in sunflower oil. This was an unexpected result, as addition of dispersed phase is generally associated with increase in relative viscosity. Simultaneous microstructural recordings confirmed that silicone oil was dispersed in the form of drops in the continuous

sunflower oil and therefore the observed viscosity reduction cannot be attributed to other favourable morphological configurations, such as thread like formations, which might result in viscosity decrease. From the possible explanations examined, the possibility of partial miscibility between the two phases, although not readily confirmed by visual observations, was considered as the most plausible. If true, then construction of a phase diagram is required to understand the behaviour of mixtures of silicone and sunflower oil.

The last system presented in this chapter is the polysaccharide / protein system of dextran / gelatine. Concentration of gelatine was chosen high enough to ensure gelation of the system on cooling. Experiments with the temperature induced gels indicated that controlled gelation may provide a way to ensure required morphologies are entrapped within the gel structure. Obtained gel morphologies were found to strongly depend on applied shear rate during cooling.

Concluding this chapter, the potential of the device to produce high quality simultaneous rheological and morphological data was demonstrated for selected two phase systems. It should be noted, however, that manual input is relatively high at present and automation of the operating environment of the device will substantially improve quality of acquired data as well as convenience of use. The development of a fully automated, complete rheo-structural instrument is discussed in the next chapter.

CHAPTER 6

PRODUCT DEVELOPMENT & SUGGESTED DESIGN

6.1 Introduction

The experimental setup considered so far in this report has been the design of figure 3.1, where simultaneous rheo-structural measurements are achieved by the combination of a standard rotational rheometer with optical glass geometries and an image acquisition unit consisting of strobe lighting, a microscope and a CCD camera (chapter 3). Evaluation of the developed device was discussed in chapters 4 and 5, and has aimed at demonstrating its high quality performance in terms of simultaneous rheological and morphological data acquisition, for a wide range of different systems. Having examined its performance and the improved qualities that features developed during this project have added, attention is now centred on the instrument itself.

Work presented in this chapter has focused on further developing the current setup of the device with the aim of improving its user friendliness and automated control as well as increasing its commercial value and its potential as a marketable product. In the next section, design and realisation of a compact version of the instrument, where small extension tubes are utilised in the place of the large, bulky microscope, is presented. Preliminary evaluation of data acquisition for the new setup is also shown. Section 6.3 discusses the design of a rheo-structural instrument that incorporates and extends features studied during this project. The suggested solution uses the latest model of Malvern's rheometers (Kinexus) as a template and proposes certain additions and / or alternations aiming at providing the new design with targeted specifications for simultaneous rheological and microstructural measurements of optimum quality and ease of use for the operator.

6.2 Compact Setup

6.2.1 Description and Development

Reducing the size of the device would increase its convenience / ease of use and therefore it is beneficial for the development of the instrument and its potential commercialisation. It is an inevitable step for improving the experimental setup if the construction of a bench top instrument is examined. For this reason, a compact version has been designed and developed, and is illustrated in figure 6.1.

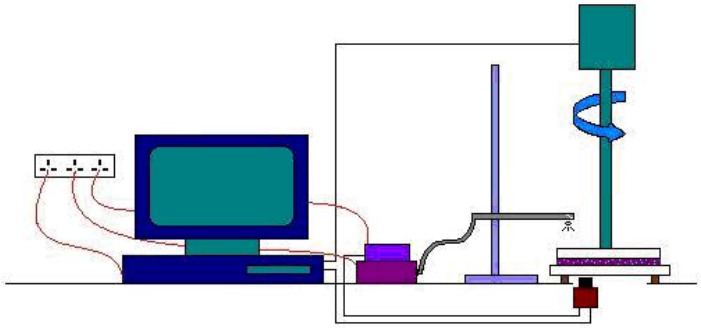

Figure 6.1: Diagram of compact experimental setup where bulky microscope has been replaced by extension tubes and a smaller camera is utilised (to be compared with figure 3.1).

The main modification introduced in the compact version of figure 6.1, compared to the standard version of figure 3.1, is the use of extension tubes to replace the bulky microscope. Such an alternation has never been attempted before in the context of rheo-structural measurements described in the literature and as such is a novelty of this work.

Extension tubes are essentially hollow rings that are typically made of metal or plastic (see for example figure 6.2.a). They are introduced, often by simple screwing, between the camera and the lens, thus extending the space that separates them, as shown in figure 6.2 (b and c). Their working principle can by understood from figure 6.3 [adapted after Hornberg 2006], where the model of a thin lens is schematically outlined. The model is described by equations 6.1 – 6.3. It is anticipated that the same principles, although described by more complex equations, are followed when using thicker lenses, as in real applications.

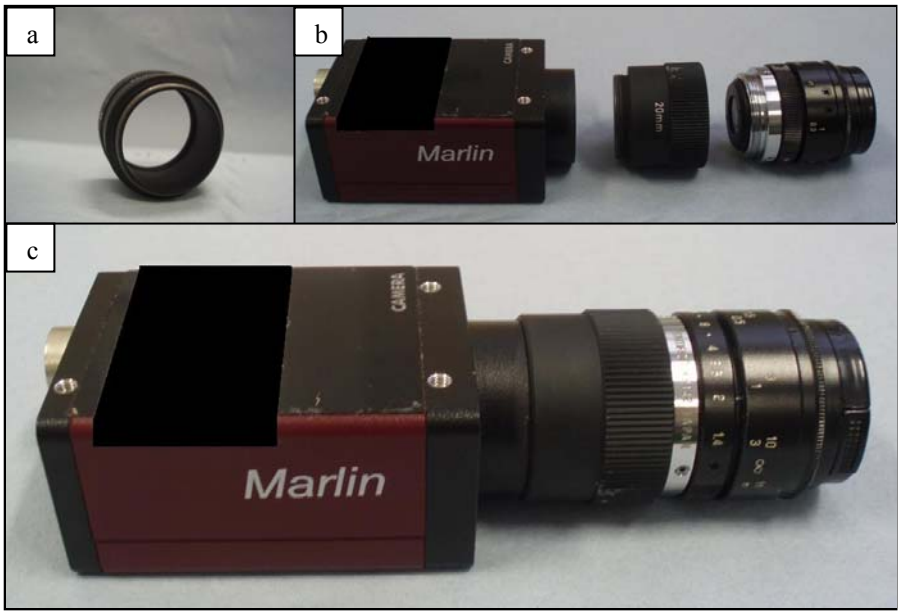

Figure 6.2: Detailed parts of compact setup; (a) $20mm$ long metallic extension tube; (b) camera, tube and lens shown separately; (c) camera, tube and lens assembled.

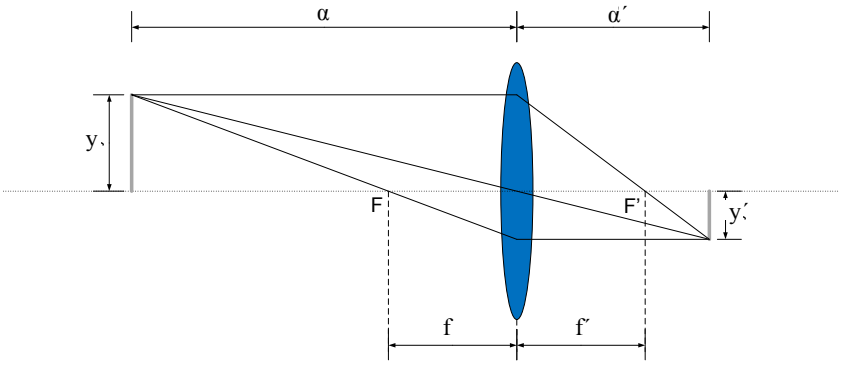

Figure 6.3: Model of a thin lens [adapted after Hornberg 2006].

$$\frac{1}{f} = \frac{1}{f'} = \frac{1}{\alpha} + \frac{1}{a'} \tag{6.1}$$

$$M = \frac{y'}{y} = \frac{\alpha'}{a} \tag{6.2}$$

$$M = \frac{\alpha'}{\alpha} = \alpha' \left(\frac{1}{f} - \frac{1}{a'}\right) = \frac{\alpha'}{f} - 1 \tag{6.3}$$

In figure 6.3, a real object of size y is mapped through a thin lens (shown in blue) to an image of size y´. Three specific light rays of the top side of the object are shown in figure 6.3. The first ray travels parallel to the optical axis towards the lens, where it is deflected and subsequently passes through F´; the second ray passes through the lens centre and is not deflected; and the third ray passes through F and after deflection from the lens continues parallel to the optical axis.

The distance between the object and the lens is α, while the lens is at α´ distance from the image plane (plane where the image is projected). In absolute numbers, the focal length f

(distance between the centre of the lens and the point where a refracted ray of light initially parallel to the optical axis crosses the optical axis) can then be calculated by equation 6.1. Magnification, defined as the ratio between image and real object size, is given in equation 6.2 and can be related with the distances α and α′ by simple geometrical proportions, also shown in equation 6.2. From equations 6.1 and 6.2 it is evident that by increasing the length between the lens and the image plane, α′, higher magnifications are obtained, as expressed in equation 6.3. In the case of figure 6.2, the image plane is located in the camera, and therefore use of extension tubes, which extend the space that separates the camera and the lens, induces higher magnifications.

Extension tubes are generally the simplest (and cheapest) accessory in photography, containing no optical elements, hence their initial low price. They usually have their inner surfaces blackened so that reflections of light are avoided (as in figure 6.2). As light has to travel an additional distance from the real object to the image plane, exposure tends to be reduced. This is typically compensated by use of strong illumination, a prerequisite that is met in the design of figure 6.1 by use of strong, strobe lighting. Extension tubes are also common in macro photography (i.e. close up photography of very small subjects) due to their simplicity, efficiency and ease of use.

Besides extension tubes, the compact setup is also complemented with the use of a smaller camera (Marlin by Allied Vision Technologies) to replace the bigger one (Dolphin, by the same supplier) and further reduce the total size of the device. The two, Marlin and Dolphin, cameras have external dimensions (in mm) of 72 x 44 x 29 and 115 x 45 x 45 (Length x Width x Height) respectively and are shown in figure 6.4 for comparison. From a technical point of view, table 6.1 summarises the comparison of main features, similarities

and differences of the two cameras. Dolphin offers higher image resolution, reaching a maximum of 1392 x 1040 pixels, compared to the 656 x 494 pixels of Marlin, but shows lower recording frequency. It should be noted, however, that new generations of cameras with smaller sizes and improved specifications are continuously being developed, offering a wide range of choices to the interested user.

Figure 6.4: Larger Dolphin and smaller Marlin cameras (both supplied by AVT)

Table 6.1: Specifications of the larger Dolphin and the smaller Marlin cameras [from relevant brochures]

	Dolphin CCD camera	**Marlin CCD camera**
Image device	1/2 inches, progressive scan	2/3 inches, progressive scan
Lens mount	C-mount	C-mount
Picture size (max)	1392 x 1040 (H x W) pixels	656 x 494 (H x W) pixels
Recording frequency (max)	30fps	60fps

Realisation of the compact design with a 20mm long extension tube is pictured in figure 6.5, where the standard version is also shown for comparison. Due to its small size, smaller than the desk's width, the camera-tube-lens unit of the compact version is not visible in figure 6.5b.

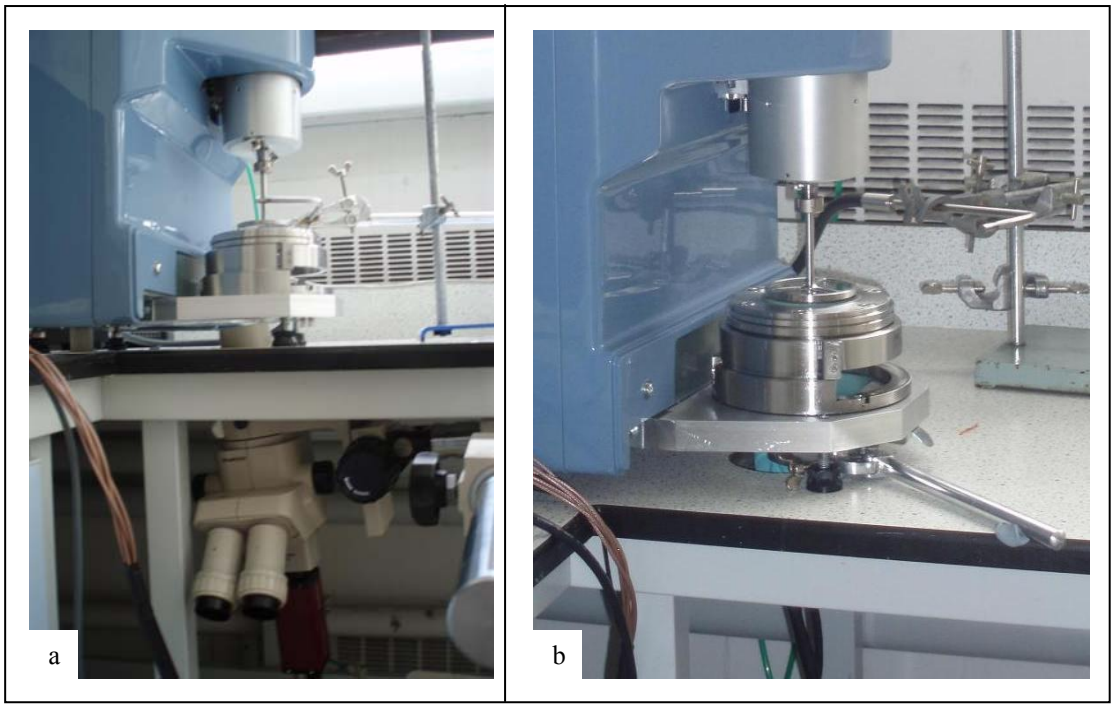

Figure 6.5: Detail of the device showing (a) standard version with microscope and Dolphin (large) camera; (b) compact version using extension tubes ($20mm$ in length) and Marlin (small) camera. In compact version tube and camera are hidden by the desk's width.

6.2.2 Evaluation of Data Acquisition

Accuracy of acquired rheological data has already been discussed in chapter 4 and will not be repeated here, as the rheological unit (rheometer and measuring geometries) has remained unchanged. Preliminary image acquisition quality evaluation is presented in this

section. Both cameras, the small Marlin and the bigger Dolphin, have been considered in the compact version and images have been obtained using the $20mm$ long extension tube in the place of the microscope. Figure 6.6 shows (a) air bubbles in silicone oil under shear rate of $10s^{-1}$ taken with the Marlin camera and (b) retraction of an air bubble in silicone oil after cessation of $10s^{-1}$ shear rate, as recorded with the Dolphin camera.

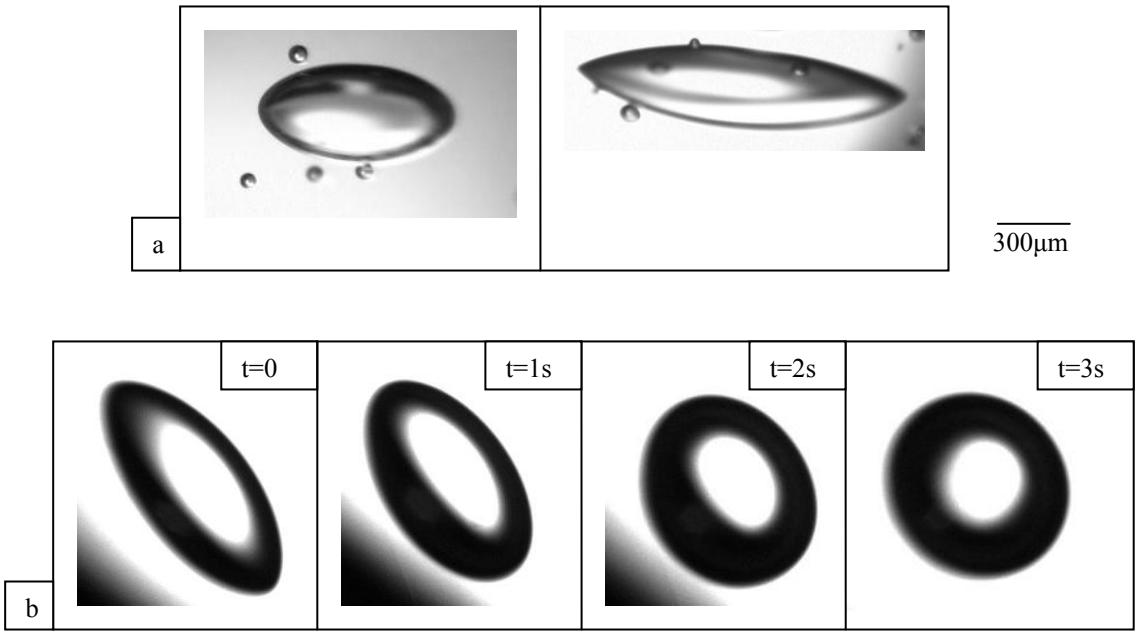

Figure 6.6: Images of bubbles in silicone oil obtained with a 20mm long extension tube in the place of the microscope; (a) deformed air bubbles captured with small (Marlin) camera; (b) air bubble retraction after cessation of shear flow captured with Dolphin camera.

Images of figure 6.6 show bubbles with sharp boundaries and good contrast with the background, which are easy to analyse both semi-automatically (for example with Bubble Pro) or with software such as Malvern's Morphologi G3, or later versions, where required manual input is minimal (see chapter 3 for description of software).

It appears therefore that replacing the bulky microscope with extension tubes may provide a promising technique to substantially reduce the size as well as the cost of the instrument. However, there are technical / design details which still require to be solved before the method can be successfully incorporated in a complete rheo-structural instrument. For example, the required range of lengths of the extension tubes needs to be established.

6.3 Suggested Experimental Setup

At this stage, and partially due to the fact that this project has been financially supported by an established company in the field of instrumentation, it is considered constructive to discuss the development of, and suggest a design for, an instrument for simultaneous rheological and morphological measurements, which will incorporate information and knowledge accumulated during this project in a setup with increased marketability and commercial potential. Such a setup is expected to produce optimum quality simultaneous rheological and morphological data over a wide range of systems (e.g. two or multi phase systems, other complex fluids, etc), measuring conditions (e.g. temperature, shearing or oscillatory profiles, etc) and characteristic dimensions. In addition, it is expected to provide a fully automated working environment with maximal use of computer software and minimal manual input requirements. Supplementary features, such as the presence of a capillary with the ability to inject in situ drops or bubbles of a dispersed phase, which has never been implemented in a commercial level, would add extra value to the future instrument.

Figure 6.7 illustrates a schematic drawing of a suggested design which combines a standard rotational rheometer with an image acquisition unit featuring characteristics

discussed in the previous chapters as well as certain additional elements, some of which have not been studied during this project, in the form of a one-piece rheo-structural instrument. This design is by no means a conclusive solution, and it is well understood that a substantial amount of future work is required before a complete design can be developed. However, the suggested design demonstrates the potential of the work carried out during this project to integrate into a commercially valuable product. It should be noted that the size of the PC in figure 6.7 has been deliberately drawn disproportionally small compared to the size of the opto-rheometer so as to allow for a more detailed representation of the latter. The components of the rheo-structural instrument, excluding the PC, are designed in scale, i.e. the proportions of the rheometer and cameras illustrate real proportions as acquired by manufacturers' information.

A series of attributes and features have been implemented in the design of figure 6.7. Firstly, external dimensions and overall layout of the rheo-structural instrument have been chosen to match the size and layout of Malvern Instrument's latest rheometer, Kinexus (680mm × 490mm × 485mm, $height \times width \times depth$ (depth dimension obviously not shown in figure 6.7). Although this was considered as the most appropriate model to adopt as a template, it should be noted that all additional features are equally applicable to any standard rotational rheometer.

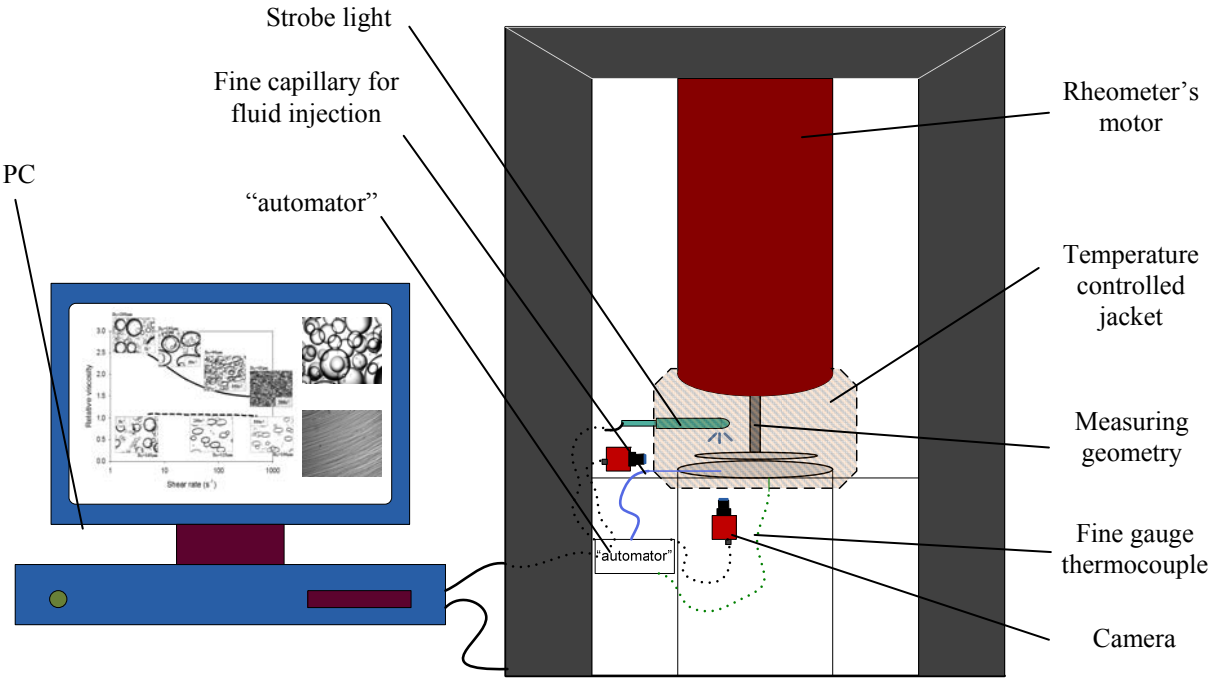

Figure 6.7: Schematic drawing of a device for simultaneous rheological and structural measurements of optimum quality. A standard rheometer is combined with an optical unit featuring characteristics studied during this project as well as additional features not studied during the project. External dimensions: 680mm x 490mm, $height \times width$, standard for Malvern's latest rheometer, Kinexus. (For more details see text). Note that proposed opto-rheometer has been designed at scale to keep proportions between rheometer, cameras, light, etc.

One of the strongest, and possibly the most important feature of the device of figure 6.7 is its unique image acquisition unit, which shows a number of novelties compared to existing commercial or in house constructed instruments for simultaneous rheological and morphological recordings found in the literature. Main components of the image acquisition unit include optical glass geometries, anticipated to be similarly constructed as in the designs of figure 3.3, two separate cameras and a stroboscopic illuminator positioned opposite of one of the cameras. The two cameras have been positioned in such a way so as to enable image capturing from a horizontal (shear rate) as well as vertical (vorticity) plane of the sample at a

single experiment, thus providing more complete microstructural information and the means to create a three dimensional image of the sheared sample. Dimensions of the cameras have been selected according to modern models available in the market, with the criterion of combining small size with the minimum, at least, targeted specifications of image resolution and image capturing frequency, as summarised in table 6.2.

Simultaneous rheological and optical microstructural experiments showing images from different directions are generally scarce in the literature due to the lack of appropriate instrumentation. Guido et al [1997 and 2003] have shown images captured at both shear rate and vorticity planes by performing separate experiments and altering their in house experimental configuration to acquire the required images. Although successful, this approach requires double effort than the solution of figure 6.7.

Each of the cameras pictured in figure 6.7 are equipped with an extension tube featuring easily and rapidly alternating lengths. A detail showing the adjustable extension tubes and lens mounted in a camera is shown in figure 6.8. As discussed in section 6.2, altering the length of an extension tube offers the possibility to change the acquired magnification, thus providing the means to follow microstructural evolution according to a characteristic evolving length scale of the image. It is anticipated that positioning of the two cameras as well as control of the tube's length is automated by using relevant software.

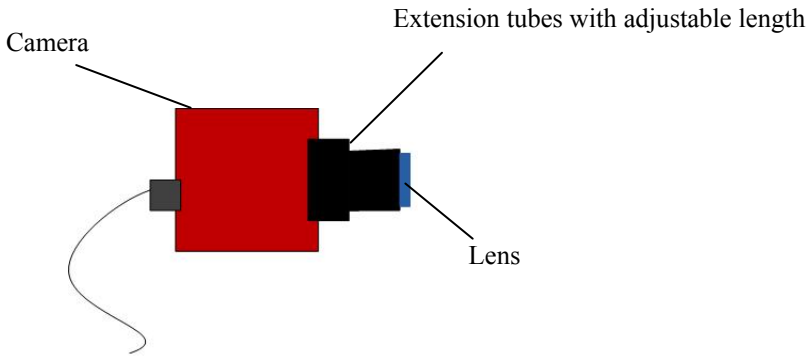

Figure 6.8: Detail of camera with extension tube of alternating length attached. Camera dimensions (excluding extension tube and lens): 29mm (height) x 29mm (width) x 19mm (depth)

Similarly, the strobe illuminator of figure 6.7 is designed to be positioned automatically according to the location of the camera situated opposite. Cameras' shutter opening and light flashing are expected to be synchronised, as it is in the current setup. Strong illumination is expected for both cameras with minimal interference from shadows due to position and the strength of the light.

The design of figure 6.7 is also equipped with an insulated temperature jacket and a fine gauge thermocouple probe for temperature control and monitoring, respectively. Care has been taken to exclude the cameras from the jacketed area, as they have limited operating temperatures between 5℃ and 45℃ [manufacturer's information]. However, for measurements at around room temperature and within the cameras' working limits, care is no longer required.

Fine gauge thermocouples have diameters as low as $0.013mm$ [omega's brochure, which is one of the suppliers] and are therefore expected to have minimal interference in rheological measurements. In figure 6.7, the thermocouple is shown embedded in the bottom plate, while its measuring end is positioned into the sample and as close to the surface of the

plate as possible, thus providing a direct temperature reading of the sample without obstructing shearing. A similar approach has been adopted by Guido et al [2003], who immersed the finely thin probe into their sheared system.

The same research team [Guido et al 2003] has also employed a fine capillary tube to introduce drops of dispersed phase into the loaded sample, in order to study binary collisions of coupled drops under simple shear (in their case loaded sample was pure continuous phase). A similar feature is also included in the setup of figure 6.7, where controlled amount of fluid dispersed phase is designed to pass through the capillary tube and get injected into the loaded sample, at a convenient position for image capturing. Injection of dispersed phase into the sheared system in a well controlled manner facilitates, for example, direct investigation of the behaviour of isolated, or paired, drops immersed into the required continuous phase, under controlled shearing conditions. Such experiments are important in the fundamental understanding of drop-drop as well as drop-continuous phase interactions or in studies of the effect of type and concentration of surfactant in drop stabilisation.

Finally the box generically termed as “automator” in figure 6.7 requires some discussion. It can be thought of as the “brain” of automation, the representation of a central coordinator and the connector between different parts of the device as well as between the device and the PC. Its tasks are very specific and crucial for the automated operation of the instrument. As such, it is considered responsible for synchronising the strobe flash to the camera’s shutter opening as well as providing, in conjunction with the relevant software, automated control of the light’s and camera’s positions. This tool is also expected to play a role in accurate control of the length of each extension tube, i.e. management of acquired magnification, in communicating temperature readings to the PC and in automatically

synchronising rheological and morphological data recordings. It is noted that the latter was performed manually in the present setup.

Although briefly discussed above, it is beyond the scope of this work to provide details on how the required degree of automation can be achieved, and it is understood that a better coordination might be possible. This is considered as part of future work, where realisation of the suggested design might be further examined.

Table 6.2 below summarises the main targeted specifications of the suggested experimental setup, as expected within the limitations of the present knowledge and experience. It is anticipated that specifications may alter on expanding acquired information and knowledge. Rheological specifications of table 6.2 are identical to Malvern Instrument's Kinexus and are therefore only briefly mentioned. Specifications for sample visualisation are as identified in the brochure of the XCD-MV6, Miniature Digital Video Camera model of Sony, which has been chosen due to its combination of small size with accomplishments of the minimum targeted performance requirements as set in table 6.2 (minimum 640 x 480 output pixels, 30 frames per second). It should be noted here that the specific camera brand has been chosen arbitrary and there is no intention of specifically advertising it. Other cameras with smaller size, including spy cameras or miniature cameras, have also been considered, but offer much lower pixel and image resolution than the Sony's model shown below. Borosilicate glass is recommended for construction of optical geometries, as it is highly resistant to heating and is therefore considered suitable for measurements at high temperatures.

Table 6.2: Minimum targeted main specifications

	Feature	**Specification**
Rheology	Rheometer model dimensions	Malvern's latest Kinexus: 490mm (w) x 680mm (h) x 485mm (d)
	Torque range	0.05μNm to 200mNm
	Angular Velocity range	10nrad/s to 500rad/s
	Frequency range	1μHz to 150 Hz
	Temperature range	-40℃ to 200℃*
Visualisation	Camera	2 x cameras (specifications as indicated in Sony's XCD-MV6, Miniature Digital Video Camera)
	Magnification mechanism	Extension tubes of adjustable lengths
	Standard Output pixels	640 x 480
	Standard Frame Rate	60 frames per second
	Shutter speed range	1s to (1/50000)s
	Lens mount	C mount
	Operating Temperature	-5^{o}C to 45^{o}C
	Camera dimensions	29mm (h) x 29mm (w) x 19mm (d) (excluding protruding parts)
Additional features	Temperature monitoring through fine gauge thermocouple probes inserted in the sample without interfering to the flow and rheological measurement	
	Fine capillary for injection of fluids (drops and bubbles) into the loaded geometry	

* working at such high temperatures requires the use of special glass materials, such as borosilicate glass, which are resistant to extreme high temperatures.

6.4 Summary

The potential of developing a user friendly device, which will incorporate all features studied during this project into a one piece, compact, automated, and easy to use instrument with increased marketability for simultaneous rheological and structural measurements has been considered in this chapter. A setup of reduced size has been designed, developed and tested in terms of optical data acquisition. In this setup, the voluminous microscope was replaced by small, inexpensive extension tubes, which extend the distance between the lens and the image plane, hence imparting magnifying properties. The compact setup was complimented with the use of a smaller camera for further size reduction. Preliminary evaluation of data acquisition proved that the method's prospects as an alternative to the bulky microscope for magnification with improved convenience and ease of use for the operator.

A design that brings together features studied in the present project, extends them to include further improvements and combines them with the latest model of Malvern's rheometer has been suggested, although a complete, marketable solution undoubtedly requires further research and development. The proposed design incorporates two cameras, for horizontal (shear rate plane) and vertical (vorticity plane) imaging, which enable more spherical visualisation of the sample under investigation, and a three dimensional representation. The setup is also complemented with a jacket for temperature control and a fine gauge thermocouple for accurate temperature monitoring. Strobe light is automatically positioned to flash directly into the camera. Further automations are also anticipated, regarding positioning of the camera at a required location below the geometry, controlling magnification by altering the length of the extension tube, and synchronising rheological and

structural recordings for easier interpretation of the results. A capillary tube able to introduce controlled amounts of dispersed phase into the system at an automated, controlled manner further supplements the suggested design with additional features.

CHAPTER 7

CONCLUSIONS AND FUTURE WORK

7.1 Conclusions

The present project has focused primarily on the development and evaluation of a device for improved quality simultaneous rheological and morphological measurements. The new device has been developed by combining new hardware, designed and constructed during this project, with unique image acquisition unit and a standard rotational rheometer. Optimisation of acquired data has been achieved by incorporating novel approaches, primarily in terms of image capturing, which enabled high quality images to be produced. For the first time reported, images at very high shear rates, of the order of $20000s^{-1}$, have been shown. Confirmation of the successful outcome of the main objective of this project has been the recent filing of a provisional patent, approved under US regulations, and it is expected that a new instrument for optimum quality simultaneous rheological and morphological measurements will be available in the market by Malvern Instruments in the near future.

This section considers the main conclusions and summarises the main outcomes of the present project. Its layout mimics the layout of the report. Key features related to the development of the device are presented in the next (sub) section, where main differences between the current project's experimental setup and existing commercial instrumentation are also outlined. Next, conclusions on the evaluation of the newly developed device in terms of quality of acquired rheological and morphological data, both separately and simultaneously, as well as its potential as a rheo-structural instrument are considered. Results on rheology and structure of selected two phase systems, including oil / aqueous, aqueous / oil, oil / oil and aqueous / aqueous systems, are subsequently summarized. Finally, main points and suggestions for the development of a complete instrument for optimum quality simultaneous

rheological and morphological measurements, with increased commercial potential are outlined.

7.1.1 Development of the Device

New hardware has been successfully designed, constructed and combined with Malvern's standard rotational rheometers for the development of a direct rheo-structural instrument for simultaneous acquisition of rheological and structural data. Constructed optical geometries are identical in shape and dimensions with standard stainless steel geometries typically used with rotational rheometers, but are partially made of glass to allow optical observations. Glass has sufficient optical properties for the intended use and is considerably cheaper than quartz, encountered in other instruments for simultaneous rheological and optical microstructural measurements found in the literature and in the market [see chapter 2].

Key features of the new device include: (i) robust optical geometries, with fully transparent working surfaces and stainless steel shafts; (ii) stroboscopic illumination synchronised to flash together with the camera's shutter opening, providing strong and uniform lighting conditions, able to capture sharp images of moving elements, even when the system under investigation is subjected to high shear rates; (iii) positioning of light and camera on opposite sides of the sample (facing each other) thus enhancing image quality by eliminating reflections and shadows; (iv) magnification determined by pixel size that can be rapidly altered during the experiment to allow studies of morphological evolution according to a characteristic structural size.

Utilization of stroboscopic illumination in conjunction with all typical measuring geometries of rotational rheometry, in the context of simultaneous rheological and morphological measurements, is an important novelty of this work. Combined with positioning of the light opposite of the camera, it provides optimum lighting conditions, ideal for image capturing under fast motion. Existing commercial instruments to present employ continuously illuminated environment, which does not particularly facilitate image acquisition under high shear flow.

As constructed geometries have different weights and weight distributions from standard stainless steel geometries, their inertial contribution to the rheological measurements (i.e. part of the applied torque used to rotate the geometry) was determined and added as a constant to the rheometer software, which is designed to subtract it from the total applied torque for calculation of applied (to the sample) shear stress.

7.1.2 Evaluation of the Device

The developed experimental setup produced very high quality images simultaneously with reliable rheological data. Quality of rheometric performance and image acquisition were firstly examined separately. Rheological accuracy was tested for viscosities ranging between $0.01 Pa\ s$ and $1 Pa\ s$, using one phase silicone oils of known (from the supplier) viscosities. Many consumer products (e.g. food emulstions, creams) and fluids of industrial interest (e.g. petroleum oils) fall well within this range. Good agreement between obtained and known viscosities was obtained, as differences below 8% were recorded for all new optical geometries developed for this project.

Image acquisition was tested with different types of systems, including oil / aqueous dispersions, double emulsions and aqueous / aqueous mixtures, the latter being generally considered difficult to capture due to similar refractive indices of the system's components. Very clear images were obtained on all occasions. In addition, image acquisition under shear produced qualitative images at shear rates of the order of $20000s^{-1}$, relevant to many industrial processes involving liquid mixtures. With the current optics, quantification of obtained structures (drop size / shape, size distribution) was possible at shear rates up to $10000s^{-1}$, whereas at higher shears images could be analysed on a qualitative basis.

At high volume fractions of dispersed phase, reduction of gap size in the plate / plate geometries was found to significantly improve image quality by reducing the number of projected drops per unit area. This feature is difficult to implement with other measuring geometries, suggesting a clear advantage for parallel plates when gap size reduction is required.

Simultaneous rheo-structural measurements of selected systems further demonstrated the potential of the device and highlighted the importance of simultaneous acquisition of rheological and microstructural data with specific examples. At first, the possibility of studying a sample under a range of shear rates with a single experiment was illustrated by two sets of experiments conducted with the same plate / plate geometry, where images were captured at the centre and at the rim of the top plate respectively. As shear rate is zero in the centre and maximum at the rim, images recorded while moving the image acquisition unit along the plate's radius will represent morphologies of the sample at different shear rates.

An oil / aqueous system was then shown to undergo shear thinning behaviour at increasing volume fraction of dispersed phase (up to $\varphi = 0.3$). This behaviour was linked to

significant morphological changes (e.g. orientation of dispersed phase to the flow direction, reduction in drop size, deformation of drops) occurring on increasing of shear, observed simultaneously under the microscope. When diluted, the same systems showed minimal microstructural changes and Newtonian behaviour (at low φ).

Further, a kinetically stable at quiescence aqueous / oil / aqueous double emulsion was monitored to destabilise to a simple oil / aqueous dispersion under shear, while maintaining constant rheological properties. Although this information is potentially very important, for example for the release profile of an active compound solubilised in the internal aqueous phase, it would not have been revealed only by rheological measurements.

Finally, shear induced coalescence was monitored. Images of the same sample and identical shearing pre-treatment were recorded under quiescence as well as under gentle sher flow conditions, and it was shown that coalescence was significantly facilitated in the latter case.

Additional applications of the device were also considered and estimation of interfacial tension between silicone oil and aqueous mixtures from the steady state deformation under shear flow was found to agree well with values obtained with the Wilhelmy plate tensiometer for the same systems. Measurements indicated that presence of hexylene glycol in the aqueous mixtures caused a significant ($20\,fold$) reduction in interfacial tension between the silicone oil and the aqueous phases, hence stabilising the oil droplets against coalescence.

7.1.3 Extended Evaluation of the Device: Rheology and Structure of Selected Two Phase Systems

The device was further evaluated for its potential for systematic rheological and structural investigations of selected two phase systems. Examples of oil / aqueous, aqueous / oil, oil / oil and aqueous / aqueous systems were considered. All constructed geometries, coaxial cylinders, parallel plates of $40mm$ and $60mm$ diameters and cone / plate of $2°$ angle and $55mm$ base diameter, were utilised for these experiments.

Rheology and structure of oil / aqueous systems with viscosity ratios between dispersed and continuous phases ranging from 0.2 to 68 and volume fractions of dispersed phase from 0.02 to 0.3 were examined at steady shear rate of $250s^{-1}$ as well as increasing-decreasing shear between $5s^{-1}$ and $500s^{-1}$.

At steady shear flow, obtained relative viscosities were compared with a number of predictive rheological models found in the literature [discussed in chapter 2]. The effective medium theory, which assumes formation of a non dilute system by successive additions of infinitesimal small amounts of dispersed phase, was found to best agree with obtained results. An empirical equation was further developed to best fit experimental points using the model proposed by Choi & Schowalter [1975] as a template. The new equation suggested that at fixed volume fraction of dispersed phase, the effect of dispersed phase on system's viscosity was very low at low λ, increasingly stronger at increasing λ and almost constant at $\lambda \geq 10$.

Simultaneous microstructural observations of oil / aqueous systems at $250s^{-1}$ showed deviations from Grace Curve at increasing volume fraction of dispersed phase. Observed drop breakage of non dilute systems at viscosity ratio between dispersed and continuous phases as

high as 27, not predicted by Grace Curve, was explained by means of the effective medium theory and have therefore been associated with the average system's viscosity rather than viscosity of continuous phase.

The relationship between acquired Sauter mean diameters and maximum recorded drop diameters of oil / aqueous systems under steady $250s^{-1}$ was further examined and it was found to be linear with proportionality constant of the order of $0.6 - 0.7$. In addition, drop size was found to decrease at increasing φ. This was associated with increased drop breakage, due to increased interactions between neighbouring drops, and limited coalescence, due to the stabilising effect of the continuous phase on oil drops at investigated volume fractions of dispersed phase (≤ 0.3).

Systems were further subjected to an increasing then decreasing shear rate of $5s^{-1} - 500s^{-1} - 5s^{-1}$. Under this shearing profile, non dilute oil / aqueous systems were found to shear thin on initial increase of shear rate and showed near Newtonian behaviour on subsequent decrease of shear rate. It was suggested that shear thinning might have been the result of drop breakage as well as their deformation and favourable orientation to the flow direction. On subsequent decrease of shear rate, observed near Newtonian behaviour was associated with minimal microstructural changes, as coalescence was largely prevented by the stabilising effect of continuous phase on oil drops.

At the same, increasing then decreasing, shear rate profile, it was observed that zero shear viscosities of investigated oil / aqueous samples were higher before shearing, where coarse dispersions were recorded, than after shearing, where dispersions were characterised by smaller drops. As smaller drops are generally associated with higher viscosities, this observation was unexpected and it was suggested that drop size distribution might

significantly influence the sample's viscosity. Although detailed information on the effect of drop size distribution on viscosity is generally lacking from the literature, it was shown that experimental investigations are feasible with the current setup and are expected to contribute to a more in depth understanding of the link between structure and rheology.

Experiments with aqueous / oil dispersions were carried out and obtained rheology and structure at $250s^{-1}$ as well as at increasing-decreasing shear rate between $5s^{-1}$ and $500s^{-1}$ were compared with results of oil / aqueous systems of similar λ and φ, acquired with the same geometry. The two types of dispersions showed differences in relative viscosities measured under similar experimental conditions and especially at increasing viscosity ratio between dispersed and continuous phases. Oil / aqueous dispersions showed generally higher relative viscosities than the corresponding aqueous / oil systems of equal φ and λ.

These differences were linked with corresponding differences in recorded microstructures and it was implied that the viscosities of individual phases may play a significant role in determination of both rheology and morphology of the investigated system. However, it was suggested that more work would be beneficial in order to draw solid conclusions (see section 7.6.5).

In the experiments with oil / oil systems it was found that while dispersing the viscous sunflower oil in silicone oil resulted in an expected increase of the system's viscosity, the opposite was true when silicone oil was dispersed in sunflower oil. At increasing volume fraction of the dispersed, less viscous silicone oil, an enhanced reduction in relative viscosity was observed ($\eta_r < 1$). Simultaneous morphological recordings did not indicate an obvious reason for this reduction, and it was suggested that the two phases might partially miscible,

although this was not obvious by visual observations. Experiments with oil / oil systems also suggested that viscosities of individual phases may significantly affect rheology and structure, as indicated previously for aqueous / oil and oil / oil systems.

Experimented aqueous / aqueous system consisted of polysaccharide / protein mixtures, where the continuous phase was a gelling solution of gelatine. The systems were loaded to the device at elevated temperature and were left to gel by cooling under different shear rates. It was shown that the link between imposed shear rate during cooling and morphology of the final gel can be investigated using the developed rheo-structural device.

7.1.4 Product Development and Suggested Design

After evaluation of the device for selected two phase systems, attention was set on further developing the device itself as a product of optimum performance with increased marketability. Assembly of a compact version was at first considered, where the bulky microscope was substituted by metallic extension tubes and the large camera was replaced by a smaller one. Utilisation of extension tubes to induce magnification in the context of rheo-structural measurements is a novelty of the present work. The compact version was realised and images acquired with this reduced size arrangement proved its suitability to produce high quality, clear images of dispersed entities with sharp boundaries. However, further work is considered essential if extension tubes are to be established as a preferred method for acquiring magnification.

An experimental setup which will incorporate work and knowledge accumulated during this project was lastly suggested. Proposed design was built based on Kinexus,

Malvern Instrument's latest model of rheometers, as a template. All features described in (sub) section 7.1.1, as well as additional features not experimented in the present study, were considered.

The suggested design presented a one piece instrument with maximal automation and minimal manual input. In the proposed setup, utilisation of two cameras, whose positions are expected to be automatically controlled, was suggested to enable simultaneous morphological recordings of the investigated system from different planes. Furthermore, magnification was obtained by means of extension tubes with (automatically) adjustable lengths in order to enable rapid alternation of the magnifying power according to the investigated characteristic length scale. Strobe light was also automatically positioned opposite of one of the cameras to ensure optimum illumination.

An important feature of the suggested design is the accurate temperature control and monitoring. In the suggested design, controlled temperature environment was guaranteed by use of an insulating jacket with automatic temperature regulation. Actual temperatures in the sample were recorded by a fine thermocouple which, although situated in the sample, is not expected to obstruct rheological measurements due to its minute size. Finally, the design was complemented by a capillary tube, entrusted with the task of injecting fluid elements in the loaded sample.

7.2 Future Work

Suggested future work, presented in this section, is expected to improve the performance and / or to increase the commercial value of the new device, thus extending the contribution of the present project. Parts of the suggested work have also been mentioned in the previous section, especially when the proposed experimental setup was described. However, they are included here as well, as they are believed to be important for the development of a reliable instrument with improved properties and marketability.

7.2.1 Accurate Temperature Control and Monitoring

It is well established that rheology highly depends on temperature, and the Arrhenius equation has been proposed to describe the relationship between viscosity and temperature. Therefore, lack of accurate temperature control limits the applications of the new instrument to measurements at ambient temperatures or unmonitored temperature changes. At present, temperature is recorded with a probe positioned manually close to the measuring geometry. Although this setup provides general information about the temperature surrounding the system under investigation, it fails to accurately inform on, or control, the temperature of the system itself.

In the suggested design described above, temperature control and monitoring was achieved by using a jacket and a fine gauge thermocouple. However, future work is required to realise and evaluate the potential of this, or any other, method for accurate temperature management.

7.2.2 Automation

Performance, marketability, commercial value, and ease of use of the developed device would significantly benefit from automation of its features. As an example, automated positioning of the light / microscope / camera unit would save considerable time and effort when setting up an experiment. When combined with plate / plate geometries, this feature could also enable easy observations of a system under a range of well controlled shear rates by altering the position of the image acquisition unit along the radius of the geometry. In addition, automated control of magnification would enable effortless flexibility and accuracy in measuring structure evolution according to the characteristic microstructural dimensions. Overall, maximisation of computer controlled features translates to a better product.

7.2.3 Size Reduction / Convenience

Although of high quality performance, the current setup is large and difficult to assemble in a bench top instrument. Size reduction is therefore essential. A step towards this direction, i.e. replacing the bulky microscope with extension tubes and utilisation of a smaller camera, has been considered, however more work is required to establish the compact setup.

7.2.4 Optical Resolution

Recent advances in optical sciences involve optical microscopy with nanoscale resolution [Wang et al 2011]. It would be interesting therefore to investigate the potential of incorporating such state-of-the-art technologies with the developed rheo-structural instrument,

thus significantly enhancing the optical specifications of the device. Higher magnifying power would extend the applications of the device, as it would increase the range of systems that can be investigated.

7.2.5 Is Generalisation of Models Developed for Solid / Liquid Suspensions and Oil / Aqueous Dispersions to Non Oil / Aqueous Systems Justifiable?

In the course of the present work, it appeared that relative viscosities of non oil / aqueous (for example aqueous / oil or oil / oil) systems deviated, sometimes significantly, from empirical or semi-empirical viscosity models developed for solid / liquid suspensions or oil / water dispersions [discussed in chapter 2]. If valid, these observations may suggest that generalisation of rheological models developed for solid / liquid suspensions and / or oil / aqueous dispersions to non oil / aqueous systems, although not uncommon in the literature [Farah et al 2005; Pal 1998; Lee et al 1997], may not be entirely justifiable. This observation initiates an idea which, if confirmed with further investigations, might develop to an interesting and important contribution to rheology and structure of two phase liquid systems.

LIST OF REFERENCES

ANTON PAAR. Brochures: Rheo-Microscope accessory for the Physica MCR Rheometer; MCR, Application-specific accessories for structure analysis.

ARASHIRO, E.Y., DEMARQUETTE, N.R., 1999. Use of pendant drop method to measure interfacial tension between molten polymers. *Materials Research*, 2(1), 23-32.

ARHUOAMA, M., DONG, M., YANG, D., IDEM, R., 2009. Determination of water-in-oil emulsion viscosity in porous media. *Industrial & Engineering Chemistry Research*, 48, 7092-7102.

ARRATIA, P.E., 2011. Complex fluids at work. Physics, 4, 9.

ARRHENIUS, S., 1917. The viscosity of solutions. *Biochemical Journal*, 11 (2), 112-133.

AZZURRI, F., STANGARO, P., CONZATTI, L., CAVALLO, D., REPETTO, L., SCATTO, M., ANDREOTTI, L., COIAI, S., 200. In situ rheo-SALS experiments on Ldpe nanocomposites: a preliminary study. IV *Intermational Conference Times of Polymers (TOP) and Composites, American Institute of Physics (AIP) Conference Proceedings*, 1042, 204-206.

BARNES, H.A., 2000. *A Handbook of Elementary Rheology*. The University of Wales Institute of Non Newtonian Fluid Mechanics, UK.

BARNES, H. A., 1994. Rheology of emulsions – a review. *Colloids and Surfaces A: Physicochemical and Engineering Aspects*, 91, 89-95.

BARNES, H.A., 1997. Thixotropy – a review. *Journal of Non-Newtonian Fluid Mechanics*, 70, 1-33.

BARNES, H.A., 1999. The yield stress – a review or 'τα πάντα ρει' – everything flows? *Journal of Non-Newtonian Fluid Mechanics*, 81, 133-178.

BARNES, H.A., BELL, D., 2003. Controlled-stress rotational rheometry: An historical review. *Korea – Australia Rheology Journal*, 15(4), 187-196.

BARNES, H.A., HUTTON, J.F., WALTERS, K., 1989. *An Introduction to Rheology*. Elsevier Ltd., UK.

BARNES, H.A., NGUYEN, Q.D., 2001. Rotating vane rheometry - a review. *Journal of Non-Newtonian Fluid Mechanics*, 98 (1), 1-14.

BASKARAN, R., SUBRAMANIAN, V., SELVAKUMARAN, T.S., 2006. Real-time measurement of aerosol size distribution using mastersizer. *Indian Journal of Pure and Applied Physics*, 44, 576-580.

BATTEN, W.M.J., BRESSLOFF, N.W., TURNOCK, S.R., 2002. Transition from vortex to wall driven turbulence production in the Taylor-Couette system with a rotating inner cylinder. *International Journal for Numerical Methods in Fluids*, 38, 207-226.

BAUER, R., CUCCURULLO, J.A., DAZO, P.E., KICHAKJI, K.J., RIKON, S.M., RUDOW, R.E., (inventors), 1991. Low fat/no fat salad dressing having mimetic functional properties fat and a process therefor. Patent US5209942.

BENENSON, W., HARRIS, J.W., STOCKER, H., LUTZ, H. (ed). 2002. Handbook of physics. Springer-Verlag, USA.

BENTLEY, B.J., LEAL, L.G., 1986. An experimental investigation of drop deformation and breakup in steady, two-dimensional linear flows. *Journal of Fluid Mechanics*, 167, 241-283.

BIESIADA, G., KRZEMIEN, J., CZEPIEL, J., TELEGLOW, A., DABROWSKI, Z., SPODARYK, K., MACH, T., 2006. Rheological properties of erythrocytes in patients suffering from erysipelas. Examination with LORCA device. *Clinical Hemorheology and Microcirculation*, 34(3), 383-390.

BLAKE, A. (ed.), 1985. Handbook of mechanics, materials, and structure. John Wiley & Sons, Inc.,USA.

BLONDIAUX, N., JENEY, S., LILEY, M., PUGIN, R., SIGRIST, H., HEINZELMANN, H., SPENCER, N.D., 2003. Structured peg=dextran surfaces for bio-applications. *European Cells and Materials*, 6 (Suppl 1), 62.

BORSCHIG, C., FRIES, B., GRONSKI, W., WEIS, C., FRIEDRICH, C., 2000. Shear-induced coalescence in polymer blends – simulations and rheo small angle light scattering. *Polymer*, 41, 3029-3035.

BRANSKY, A., KORIN, N., NEMIROVSKI, Y., DINNAR, U., 2006. An automated cell analysis sensing system based on microfabricated rheoscope for the study of red blood cells physiology. *Biosensors and Bioelectronics*, 22, 165-169.

BROUGHTON, G., SQUIRES, L., 1938. The viscosity of oil-water emulsions. Journal of Physical Chemistry, 20 (2), 253-263.

BROWN, D.M., 2004. Drug delivery systems in cancer therapy. Humana Press Inc., New Jersey, U.S.A..

BROWN, D.E., PITT, K., 1972. Drop size distribution of stirred non-coalescing liquid-liquid system. *Chemical Engineering Science*, 27, 577-583.

CALABRESE, R.V., WANG C.Y., BRYNER, M.P., 1986. Drop breakup in turbulent stirred-tank contactors Part III: correlations for mean size and drop size distribution. *American Institute of Chemical Engineers (AIChE) Journal, 32(4), 677-681.*

CASERTA, S., REYNAUD, S., SIMEONE, M.,, GUIDO, S., 2007. Drop deformation in sheared polymer blends. *Journal of Rheology*, 51 (4), 761-774.

CASERTA, S., SABETTA, L., SIMEONE, M., GUIDO, S., 2005. Shear-induced coalescence in aqueous biopolymer mixtures. *Chemical Engineering Science*, 60, 1019-1027.

CHHABRA, R. P., RICHARDSON, J. F., 1999. *Non-Newtonian Flow in the Process Industries. Fundamentals and Engineering Applications*. Buzzztterworth-Heinemann, UK.

CHOI, S.J., SCHOWALTER, W.R., 1975. Rheological properties of nondilute suspensions of deformable particles. *Physics of Fluids*, 18, 420-427

CROFT, W.J., 2006. Under the microscope: a brief history of microscopy. World Scientific Publishing Co. Pte. Ltd, Singapore.

CUSSLER, E. L., MOGGRIDGE, G, D., 2001. *Chemical Product Design*, Cambridge University Press, Published by the press syndicate of the university of Cambridge, Printed in USA.

DE BRUIJN, R. A., 1989. *Deformation and Breakup of Drops in Simple Shear Flows*. PhD Thesis.

DESSE, M., WOLF, B., MITCHELL, J., BUDTOVA, T., 2009. Experimental study of the break-up of starch suspension droplets in step-up shear flow. *Journal of Rheology*, 53(4), 943-955.

DESSE, M., WOLF, B., MITCHELL, J., BUDTOVA, T., 2009. Experimental study of the break-up of starch suspension droplets in step-up shear flow. *Journal of Rheology*, 53(4), 943-955.

DICKINSON, E., 2011. Double emulsions stabilized by food biopolymers. *Food Biophysics*, 6, 1-11.

DICKINSON, E., 1992. *An introduction to food colloids*. Oxford University Press, USA.

DING, P., WOLF, B., FRITH, W. J., CLARK, A. H., NORTON, I. T., PACEK, A. W., 2002. Interfacial tension in phase-separated gelatin/dextran aqueous mixtures. *Journal of Colloid and Interface Science*, 253, 367-376.

ERGES, R.G., NETTENSHEIM, F., WAGNER, N.J., 2006. Rheo-SANS investigation of acucular-precipitated calcium carbonate colloidal suspensions through the shear thickening transition. *Journal of Rheology*, 50, 685-709.

ERNI, P., WINDHAB, E.J., FISCHER, P., 2011. Emulsion drops with complex interfaces: Globular versus flexible proteins. Macromolecular Materials and Engineering, 296, DOI: 10.1002/mame.201000290.

FARAH, M.A., OLIVEIRA, R.C., CALDAS, J.N., RAJAGOPAL, K., 2005. Viscosity of water-in-oil emulsions: variation with temperature and water volume fraction. *Journal of Petroleum Science and Engineering*, 48, 169-184.

FIROOZMAND, H., MURRAY, B.S., DICKINSON, E., 2009. Microstructure and rheology of phase-separated gels of gelatine + oxidized starch. Food Hydrocolloids, 23, 1081-1088.

FRANCO, J.M., GUERRERO, A., GALLEGOS, C., 1995. Rheology and processing of salad dressing emulsions. *Rheologica Acta*, 34, 513-524.

FRANKEL, N.A., ACRIVOS, A., 1967. On the viscosity of a concentrated suspension of solid spheres. *Chemical Engineering Science*, 22, 847-853.

FISCHER, P., ERNI, P., 2007. Emulsion drops in external flow fields – The role of liquid interfaces. *Current Opinion in Colloid & Interface Science*, 12, 196-205.

FULLER, G.G., 1995. *Optical Rheometry of Complex Fluids*. Oxford University Press.

FULLER G.G., 1990. Optical Rheometry. *Annual Review of Fluid Mechanics*, 22, 387-417.

GALLEGOS, C., FRANCO, J.M., 1999. Rheology of Food Emulsions. IN: Advances in the Flow and Rheology of Non-Newtonian Fluids, Siginer, D.A., De Kee, D., Chhabra, R.P., (eds), volume 8, pages 87-118, ebook exclusively (no longer available in print).

GELBART, W.M., BEN=SHAUL, A., 1996. The "new" science of "complex fluids". *The Journal of Physical Chemistry*, 100, 13169-13189.

GENTILE, L., OLIVIERO ROSSI, C., OLSSON, U., 2012 (electronically published November 2011). Rheological and rheo-SALS investigation of the multi-lamellar vesicle formation in the C(12)E(£)/D(@)O system. *Journal of Colloid and Interface Science*, 367 (1) 537-539

GROENEWEG, F., DIEREN, F.VAN, AGTEROF, W.G.M., 1994. Droplet break-up in a stirred water-in-oil emulsion in the presence of emulsifiers. *Colloids and Surfaces A: Physicochemical and Engineering Aspects*, 91, 207-214.

GONZALEZ-TELLO, P., CAMACHO, F., BLAZQUEZ, G., 1994. Density and viscosity of concentrated aqueous solutions of polyethylene glycol. *Journal of Chemical Engineering Data*, 39, 611-614.

GOSH, R., 2006. *Principles of Bioseparations Engineering*. World Scientific Publishing Co., Singapore.

GUIDO, S., SIMENOE, M., 1998. Binary collision of drops in simple shear flow by computer-assisted video optical microscopy. Journal of Fluid Mechanics, 357, 1-20.

GUIDO, S., SIMEONE, M., ALFANI. A., 2002. Interfacial tension of aqueous mixtures of Na-caseinate and Na-alginate by drop deformation in shear flow. *Carbohydrate polymers*, 48, 143-152.

GUIDO, S., SIMENONE, M., GRECO, F., 2003. Deformation of a Newtonian drop in a viscoelastic matrix under steady shear flow: Experimental validation of slow flow theory. *Journal of Non-Newtonian Fluid Mech*anics, 114 (1), 65-82.

GUIDO, S., VILLONE M., 1998. Three-dimensional shape of a drop under simple shear flow. *Journal of Rheology*, 42, 395-415.

GUO, T., HARRISON, G.M., OGALE, A.A., 2005. Transient shear rheology and rheo-optical microstructural characterization of a thermotropic liquid crystalline polymer. *Polymer Engineering and Science*, 45(2, 187-197.

HABEYCH, E., DEKKERS, B., VAN DER GOOT, A.J., BOOM, R., 2008. Starch-zein blends formed by shear flow. *Chemical Engineering Science*, 63(21), 5229-5238.

HALL, S., COOKE, M., EL-HAMOUZ, A., KOWALSKI, A.J., 2011. Droplet break-up by in-line Silverson rotor-stator mixer. *Chemical Engineering Science*, 66, 2068-2079.

HAYNES, L.M., DUBIEF, Y.C., ORFEO, T., MANN, K.G., 2011. Dilutional control of prothrombin activation at physiologically relevant shear rates. *Biophysical Journal*, 100 (3), 765-773.

HERZHAFT, B., 1999. Rheology of aqueous foams: a literature review of some experimental works. *Oil & Gas Science and Technology – Review IFP*, 54, 587-596.

HOHLER, R., COHEN-ADDAD, S., 2005. Rheology of liquid foam. Journal of Physics: Condensed Matter, 17, R1041-R1069.

HONG, Z., SHAW, M.T., WEISS, R.A., 1998. Effect of shear flow on the morphology and phase behavior of a near-critical SAN/PMMA blend. *Macromolecules*, 31 (18), 6211-6216.

HORNBERG, A., (ed.), 2006. Handbook of Machine Vision. WILEY-VCH Verlag GmbH & Co. KGaA, Federal Republic of Germany.

HUITRIC, J., VILLE, J., MEDERIC, P., MOAN, M., AUBRY, T., 2009. Rheological, morphological and structural properties of PE/PA/nanoclay ternary blends: Effect of clay weight fraction. *Journal of Rheology*, 53(5), 1101-1119.

HYUN, K., STRUTH, B., MEINS, T., WILHELM, M., 2008. In-situ rheo-SAXS study on shear induced alignment of liquid crystal (8CB) in the smectic phase under LAOS. *The XV International Congress on Rheology: The Society of Rheology 80th Annual Meeting. American Institute of Physics Conference Proceedings*, 1027, 1423-1425.

ITO, E.N., UEKI, M.M., BRETAS, R.E.S., HAGE E.Jr, 2008. Interfacial tension of PBT/SAN blends by the drop retraction method. *Materials Research*, 11(2), 165-169.

JAITELY, V., SAKTHIVEL T., MAGEE G., FLORENCEA T., 2004. Formulation of oil in oil emulsions: potential drug reservoirs for slow release. *Journal of Drug Delivery Science and Technology*, 14(2), 113-117.

JANSEN, K. M. B., AGTEROF, W. G. M., MELLEMA, J., 2000. Droplet breakup in concentrated emulsions. *Journal of Rheology*, 45(1), 227-236.

JANSSEN, J.J.M., BOON, A., AGTEROF, W.G.M., 1994. Influence of dynamic interfacial properties on droplet breakup in simple shear flow. *American Institute of Chemical Engineers (AIChE) Jounral*, 40(12), 1929-1939.

JANSSEN, J.J.M., BOON, A., AGTEROF, W.G.M., 1997. Influence of dynamic interfacial properties on droplet breakup in plane hyperbolic flow. *American Institute of Chemical Engineers (AIChE) Jounral, 43 (6), 1436-1447.*

JANSSEUNE, T., MOLDENAERS, P., MEWIS, J., 2003. Morphology and rheology of concentrated biphasic blends in steady shear flow. *Journal of Rheology*, 47(4), 829-845.

JEON, H.S., HOBBIE, E.K., 2001. Shear viscosity of phase-separating polymer blends with viscous asymmetry. Physical Review E Statistical, Nonlinear and Soft Matter Physics, 63, 061403.

JIAO, J., BURGESS, D.J., 2003. Rheology and stability of water-in-oil-in-water multiple emulsions containing Span 83 and Tween 80. *The American Association of Pharmaceutical Sciences Journal*, 5(1), Article 7.

JOHNSEN, E.E., RONNINGSEN, H.P., 2003. Viscosity of 'live' wter-in-crude-oil emulsions: experimental work and validation of correlations. *Journal of Petroleum Science and Engineering*, 30 (1-2), 23-36.

KALIVIOTIS, E., YANNESKIS, M., 2007. On the effect of dynamic flow conditions on blood microstructure investigated with optical shearing microscopy and rheometry. Procedings of the Institution of Mechanical Engineers, Part H: Journal of Engineering in Medicine, 221, 887-897.

KAWAGUCHI, M., KUBOTA, K., 2004. Rheo-optical properties of silicone oil emulsions in the presence of polymer emulsifiers. *Langmuir*, 20(4), 1126-1129.

KELESSIDIS, V.C., HATZISTAMOU, V., MAGLIONE, R., 2010. Wall slip phenomenon assessment of yield stress pseudoplastic fluids in Couette geometry. *Applied Rheology*, 20(5), 52656.

KELESSIDIS, V.C., MAGLIONE, R., BANDELIS, G., 2010. On the end-effect correlation for Couette type oil-field direct-indicating viscometers for Newtonian and non-Newtonian fluids. *Journal of Petroleum Science and Engineering*, 71, 37-46.

KESHTKAR, M., HEUZEY, M.C., CARREAU, P.J., RAJABIAN, M., DUBOIS, C., 2010. Rheological properties and microstructural evolution of semi-flexible fiber suspensions under shear flow. *Journal of Rheology*, 54(2), 197-222.

KHODAKOV, G.S., 2004. On suspension rheology. *Theoretical Foundations of Chemical Engineering*, 38(4)430-439.

KLAPPER M., NENOV S., HASCHICK R., MULLER K., MULLEN K., 2008. Oil-in-oil emulsions: a unique tool for the formation of polymer nanoparticles. *Accounts of Chemical Research*, 41(9), 1190-1201.

KOBASLIJA, M., McQUADE, D.T., 2006. Polyurea microcapsules from oil-in-oil emulsions via interfacial polymerization. *Macromolecules*, 39(19), 6371-6375.

KRIEGER, I.M., DOUGHERTY, T.J., 1959. A mechanism of non-Newtonian flow in suspensions of rigid spheres. *Transactions of the Society of Rheology*, 3, 137-152.

KRYNKE, K. K., SEK, J. P., 2004. Predicting viscosity of emulsions in the broad range of inner phase concentrations. *Colloids and Surfaces A: Physicochemical Engineering Aspects*, 245, 81-92.

LARSON, R.G., 1999. *The Structure and Rheology of Complex Fluids*. Oxford University Press, Inc, U.S.A..

LAUGER, J., HEYER, P., 2006. Rheo small angle light scattering (rheo-SALS0, and rheo-microscopy as tools for investigations of structure-property relations in complex fluids. *Annual Transactions of the Nordic Rheology Society*, vol. 14.

LEAL, L.G., 2004. Flow induced coalescence of drops in a viscous fluid. *Physics of fluids*, 16 (6), 1833-1851.

LEE, H.M., LEE, J.W., PARK, OO., 1997. Rheology and dynamics of water-in-oil emulsions under steady and dynamic shear flow. *Journal of Colloid and Interface Science*, 185, 297-305.

LEE, K., MACKLEY, M.R., 2001. The application of the multi-pass rheometer for precise rheo-optic characterisation of polyethylene melts. *Chemical Engineering Science*, 56(19), 5653-5661.

LENG, D., CALABRESE, R., 2004. Immiscible liquid-liquid systems. In: PAUL, E.L., ATIEMO-OBENG, V.A., KRESTA, S.M., eds, Handbook of Industrial Mixing: Science and Practice, *John Wiley & Sons Inc*., Chapter 12, 639-754.

LIN, C., GUO, L., 2007. Experimental study of drop deformation and breakup in simple shear flows. *Chinese Journal of Chemical Engineering,* 15(1), 1-5.

LINDEN van der, E., SAGIS, L., VENEMA, P., 2003. Rheo-optics and food systems. *Current Opinion in Colloid and Interface Science* 8, 349-358.

LIU, H., XU, X.M., GUO, S.D., 2007. Rheological, texture and sensory properties of low-fat mayonnaise with different fat mimetics. Food Science and Technology, 40 (6), 946-954.

LOCKETT, T.J., 1992.Numerical Simulation of Inelastic Non-Newtonian Fluid Flows in Annuli. PhD thesis, Imperial College, University of London.

LUCCA, P.A., TEPPER, B.J., 1994. Fat replacers and the functionality of fat in foods. *Trends in Food Science & Technology*, 5 (1), 12-19.

LINKAM SCIENTIFIC INSTRUMENTS, Optical Rheology System CSS450, brochure.

LOEWENBERG, M., HINCH, E.J., 1996. Numerical simulation of a concentrated emulsion in shear flow. *Journal of Fluid Mechanics*, 321, 395-419.

LYU, S-P., BATES, F.S., MACOSCO, W., 2000. Coalescence in polymer blends during shearing. *American Institute of Chemical Engineers (AIChE) Journal, 46 (2), 229-238.*

MAFFETTONE, P. L., MINALE, M., 1998. Equation of change for ellipsoidal drops in viscous flow. *Journal of Non-Newtonian Fluid Mechanics*, 78, 227-241.

MARTIN, H.P., BROOKS, N.J., SEDDON, J.M., TERRILL, N.J., LUCKHAM, P.F., KOWALSKI, A.J., CABRAL, J.T., 2010. Complex fluids under microflow probed by SAXS: rapid microfabrication and analysis. *XIV International Conference on Small-Angle Scatterin (SAS09), Journal of Physics: Conference Series*, 247, 012050.

MARTIN, P., CARREAU, P.J., FAVIS, B.D., JEROME, R., 2000. Investigating the rheology/morphology interrelationship in immiscible polymer blends. Journal of Rheology, 44(3), 569-583.

MASON, T.G., 1999. New fundamental concepts in emulsion rheology. *Current Opinion in Colloid & Interface Science*, 4, 231-238.

McCANN, T.H., FABRE, F., DAY, L., 2011. Microstructure, rheology and storage stability of low-fat yoghurt structured by carrot cell wall particles. *Food Research International*, 44 (4), 884-892.

McKENNA, B.M., (ed.), 2003. *Texture in Food*. Woodhead Publishing Limited, England.

MEGIAS-ALGUACIL, D., WINDHAB, E.J., 2004. Viscosity of a Newtonian fluid calculated from the deformation of droplets covered with a surfactant under a linear shear flow. *Rheologica Acta*, 46(2), 223-229.

MEZGER, T.G., 2006. *The Rheology Handbook* (2nd edition). Vincentz Network GmbH & Co KG, Hannover, Germany..

MIGHRI, F., HUNEAULT, M.A., 2006. In situ visualization of drop deformation, erosion, and breakup in high viscosity ratio polymeric systems under high shearing stress conditions. Journal of Applied Polymer Science, 100, 2581-2591.

MISTRY, V.V., 2001. Low fat cheese technology. *International Dairy Journal*, 11, 413-422.

MO, L., 2009. Damage development in the adhesive zone and mortar of porous asphalt concrete. PhD Thesis, Technische Universiteit Delft.

MOBUCHON, C., CARREAU, P.J., HEUZEY, M.C., 2009. Structural analysis of non-aqueous layered silicate suspensions subjected to shear flow. *Journal of Rheology*, 53(5), 1025-1048.

MOONEY, M., 1951. The viscosity of a concentrated suspension of spherical particles. *Journal of Colloid Science*, 6(2), 162-170.

MOURS, M., LAUN, M., OOSTERLINCK, F., VINCKIER, I., MOLDENAERS, P., 2003. Morphology development of polymer blends in complex flow fields. *Chemical Engineering & Technology*, 26(7), 740-744.

MULLER, H.G., 1973. *An introduction to food rheology*. William Heinemann Ltd, UK.

NORTON, I.T., SPYROPOULOS, F., COX, P., (eds), 2011. *Practical Food Rheology An Interpretive Approach*. Wiley-Blackwell, UK.

OLDORP, K., 2007. What happens when rheological properties change? Looking into rheological properties with simultaneous collection of microscopic images. Annual Transactions of the Nordic Rheology Society, vol. 15.

OMEGA brochure for Unsheathed Fine Gage Thermocouples, at www.omega.com

PACEK, A.W., MAN, C.C., NIENOW, A.W., 1998. On the sauter mean diameter and size distributions in turbulent liquid/liquid dispersions in a stirred vessel. *Chemical Engineering Science*, 53 (11), 2005-2011.

PACEK, A. W., MOORE, P. T., NIENOW, A. W., CALABRESE, R. V., 1994. Video technique for measuring dynamics of liquid-liquid dispersion during phase inversion. *American Institute of Chemical Engineers (AIChE) Journal*, 40(12), 1940-1949.

PADRON ALDANA, G.A., 2005. Effect Of Surfactants On Drop Size Distribution in a Batch, Rotor-Stator Mixer. PhD Thesis, University of Maryland.

PAL, R., 1996. Effect of droplet size on the rheology of emulsions. *American Institute of Chemical Engineers (AIChE) Journal*, 42(11), 3181-3190.

PAL, R. 1998. A novel method to correlate emulsion viscosity data. *Colloids and Surfaces A: Physicochemical and Engineering Aspects,* 137, 275-286.

PAL, R., 2000. Shear viscosity behavior of emulsions of two immiscible liquids. *Journal of Colloid and Interface Science*, 225, 359-366.

PAL, R., 2001. Evaluation of theoretical viscosity models for concentrated emulsions at low capillary numbers. *Chemical Engineering Journal*, 81, 15-21.

PAL, R., 2001. Novel viscosity equations for emulsions of two immiscible liquids. *Journal of Rheology*, 45(2), 509-520.

PAL, R., 2007. Rheology of Particulate Dispersions and Composites. CRC Press, Taylor & Francis Group, US.

PAL, R., RHODES, E., 1989. Viscosity/concentration correlations for emulsions. *Journal of Rheology*, 33(7), 1021-1045.

PAL, R., YAN. Y., MASLIYAH, J., 1992. Rheology of emulsions. Chapter 4 of *Emulsions* (edited by Schramm, Lauriel, L.). American Chemical Society, Washington DC, USA.

PANINE, P., GRADZIELSKI, M., NARAYANAN, T., 2008. Combined rheometry and small-angle x-ray scattering. *American Institute of Physics, Review of Scientific Instruments*, 74, 2451-2455

PHAN-THIEN, N., PHAM, D.C., 1997. Differential multiphase models for polydispersed suspensions and particulate solids. *Journal of Non-Newtonian Fluid Mechanics*, 72, 305-318.

PHILIPPE, A.M., BARAVIAN, C., IMPEROR-CLERC, M., DE SILVA, J., PAINEAU, E., BIHANNIC, I., DAVIDSON, P., MENEAU, F., LEVITZ, P., MICHOT, L.J., 2011. Rheo-SAXS investigation of shear-thinning behaviour of very anisometric repulsive disk-like clay suspensions. *Journal of Physics: Condensed Matter*, 23 (19), 194112.

PU, B., CHEN, D., 2001. A study of the measurement of surface and interfacial tension by the maximum liquid drop volume method. *Journal of Colloid and Interface Science*, 235, 273-277.

PUYVELDE VAN, P., ANTONOV, Y. A., MOLDENAERS, P., 2002. A rheo-optical investigation of shear-induced morphological changes in biopolymeric blends. *Korea-Australia Rheology Journal*, 14(3), 115-119.

PUYVELDE, VAN, P., ANTONOV, Y. A., MOLDENAERS, P., 2003. Morphology evolution of aqueous biopolymer emulsions during a weak shear flow. *Food Hydrocolloids*, 17, 327-332.

PUYVELDE, VAN, P., MOLDENAERS, P., 2006. Rheology – Morphology relationships in immiscible polymer blends. In *Micro- and Nanostructured Multiphase Polymer Blend Systems* (edited by Thomas, S., Groeninckx, G., Harrats, C.), CRC Press, pp 421-440.

QUEIMADA, A.,J., MARRUCHO, I.,M., STENBY, E.,H., COUTINHO, J.,A.,P., 2003. Generalized relation between surface tension and viscosity: a study of pure and mixed n-alkanes. 15th Symposium of Thermophysical Properties, June 22-27, Colorado, USA.

RENARDY, Y., CRISTINI, V., LI, J., 2002. Drop fragment distributions under shear with inertia. International Journal of Multiphase Flow, 28, 1125-1147.

RIDES, M., ALLEN, C.R.G., 2002. Guide to the measurement of the flow properties of polymers. *National Physical Laboratory*, MATC(MN)42.

ROSCOE, R., 1952. The viscosity of suspensions of rigid spheres. *British Journal of Applied Physics*, 3, 267-269.

ROSENTHAL, A.J., 1999. Food Texture: Measurement and Perception. Aspen Publishers Inc., USA.

RYDEN, J., ALBERTSSON, P.A., 1971. Interfacial tension of dextran-polyethylene glycol-water two-phase systems. Journal of Colloid and Interface Science, 37 (1), 219-222.

SAIKI, Y., PRESTIKGE, C.A.,HORN, R.G., 2007. Effects of droplet deformability on emulsion rheology. Colloids and Surfaces A: Physicochemical and Engineering Aspects, 299, 65-72.

SEFTON, E., SINTON, D., 2010. Evaluation of selected viscosity prediction models for water in bitumen emulsions. *Journal of Petroleum Science and Engineering*, 72(2) 128-133.

SHERMAN, P., 1970. *Industrial Rheology*. Academic Press INC., London, UK.

SHERWOOD, J.D., 2006. Cell models for suspension viscosity. *Chemical Engineering Science*, 61(20), 6727-6731.

SIBREE, J.O., 1930. The viscosity of emulsions Part I. *Transactions of the Faraday Society*, 26, 26-36.

SIGILLO, I., SANTO, L. DI., GUIDO, S., GRIZZUTI, N., 1997. Comparative measurements of interfacial tension in a model polymer blend. *Polymer Engineering and Science*, 37(9), 1540-1549.

SLAYTER, E.M., SLAYTER, H.S., 1992. Light and electron microscopy. Cambridge University Press, UK.

SONDERGAARD, K., LYNGAAE-JORGENSEN, J., 1995. *Rheo-Physics of Multiphase Polymer Systems: Characterization by Rheo-Optical Techniques*. Technomic Publishing Company, Inc., U.S.A..

SPROW, F.B., 1967. Distribution of drop sizes produced in turbulent liquid-liquid dispersion. *Chemical Engineering Science*, 22, 435-442.

SPYROPOULOS, F., 2006. Biopolymer-Surfactant Aqueous Two-Phase Systems: Equilibria, Rheology and Interfacial Properties. PhD thesis, University of Birmingham.

SPYROPOULOS, F., FRITH, W. J., NORTON I. T., WOLF, B., PACEK, A. W. 2007. Morphology and shear viscosity of aqueous two-phase biopolymer-surfactant mixtures. *Journal of Rheology,* 51(5), 867-881.

STELLBRINK, J., LONETTI, B., ROTHER, G., WILLNER, L., RICHTER, D., 2008. Shear induced structures of soft colloids: rheo-SANS experiments on kinetically frozen PEP-PEO diblock copolymer micelles. *Journal of Physics: Condensed Matter*, 20 (40), 404206.

SUITTHIMEATHEGORN, O., TURTON, J.A., MIZUUCHI, H., FLORENCE, A.T., 2007. Intramuscular absorption and biodistribution of dexamethasone from non-aqueous emulsions in the rat. International Journal of Pharmaceutics, 331 (2), 204-210

SUITTHIMEATHEGORN, O., JAITELY, V., FLORENCE, A.T., 2005. Novel anhydrous emulsions: formulation as controlled release vehicles. International Journal of Pharmaceutics, 298 (2), 367-371.

SULAGES, J., SCHWEIZER, T., VENERUS, D.C., HOSTETTLER, J., METTLER, F., KROGER, M., OTTINGER, H.C., 2008. Lubricated optical rheometer for the study of two-dimensional complex flows of polymer melts. *Journal of Non-Newtonian Fluid Mechanics*, 150, 43-55.

TABILO-MUNIZAGA, G., BARBAROSA-CANOVAS, G. V., 2005. Rheology for the food industry. *Journal of Food Engineering*, 67, 147-156.

TADROS, TH. F. 1994. Fundamental principles of emulsion rheology and their applications. *Colloids and Surfaces Physicochemical and Engineering Aspects*, 91, 39-55.

TAKEDA, M., KUSANO, T., MATSUNAGA, T., ENDO, H., SHIBAYAMA, M., SHIKATA, T., 2011. Rheo-SANS studies on shear-thickening/thinning in aqueous rodlike micellar solutions. *Langmuir*, 27 (5), 1731-1738.

TAKEO, M., 1999. *Disperse Systems*. Wiley-VCH Verlag GmbH, Federal Republic of Germany.

TANNER, R.I., 2002. *Engineering Rheology*, 2nd edition. Oxford Engineering Science Series 52, Oxford University Press, US.

TANPAIBOONKUL, P., LERDWIJITJARUD, W., SIRIVAT, A., LARSON, R. G., 2007. Transient and steady-state deformations and breakup of dispersed-phase droplets of immiscible polymer blends in steady shear flow. *Polymer*, 48, 3822-3835.

TAYLOR, G.I., 1932. The viscosity of fluid containing small drops of another fluid. *Proceedings of the Royal Society of London Series A, Containing Papers of a Mathematical and Physical Character*, 138(834), 41-48.

TEIPEL, U., 2002. Influence of droplet size on the rheological behavior of emulsions. *Chemical Engineering & Technology Communications*, 25(6), 609-615.

TESTA, C., SIGILLO, I., GRIZZUTI, N., 2001. Morphology evolution of immiscible polymer blends in complex flow fields. Polymer, 42, 5651-5659.

THERMO FISHER SCIENTIFIC, RheoScope module for Haake Mars Rheometer, brochures.

TUCKER III, C. L., MOLDENAERS, P., 2002. Microstructural evolution in polymer blends. *Annual Review of Fluid Mechanics*, 34, 177-210.

UTOMO, A.T., BAKER, M., PACEK, A.W., 2008. Flow pattern, periodicity and energy dissipation in batch rotor-stator mixer. *Chemical Engineering Research and Design*, 86(12), 1397-1409.

UTRACKI, L.A., (ed), 2002. *Polymer Blends Handbook*, Volume 1. Springer.

VERVOORT, S., BUDTOVA, T., 2005. Shear-induced gel widening and solvent release in the vorticity direction. *Colloids and Surfaces A: Physicochemical Engineering Aspects*, 262, 132-138.

WANG, C.,Y., CALABRESE, R.V., (1986). Drop breakup in turbulent stirred-Tank contractors part II: Relative influence of viscosity and interfacial tension. *American Institute of Chemical Engineers (AIChE) Journal*, 32(4), 667-676.

WANG, W., ZHENG, Q., 2005. The dynamic rheological behaviour and morphology of nylon/elastomer blends. *Journal of Materials Science*, 40, 5545-5547.

WANG, Z., GUO, W., LI, L., LUK'YANCHUK, B., KHAN, A., LIU, Z., CHEN, Z., HONG, M., 2011. Optical virtual imaging at 50nm lateral resolution with a white-light nanoscope. Nature Communications, 2, article No 218.

WAGNER, N.J., 1998. Rheo-optics. *Current Opinion in Colloid and Interface Science*, 3, 391-400.

WILKES, G.J., 1974. Rheo-optical methods and their application to polymeric solids. *Journal of Macromolecular Science, Part C: Polymer Reviews*, 10 (2), 149-261.

WILLIAMS, A., JANSSEN, J.J.M., PRINS, A., 1997. Behaviour of droplets in simple shear flow in the presence of a protein emulsifier. *Colloids and Surfaces A: Physicochemical and Engineering Aspects*, 125, 189-200.

WINDHAB, E. J., DRESSLER, M., FEIGL, K., FISCHER, P., MEGIAS-ALGUACIL, D., 2005. Emulsion processing – from single-drop deformation to design of complex processes and products. *Chemical Engineering Science*, 60, 2101-2113.

WOLF, B., FRITH, W.J., 2003. String phase formation in biopolymer aqueous solution blends. Journal of Rheology, 47(5), 1151-1170.

WOLF, B., SCIROCCO, R., FRITH, W.J., NORTON, I.T., 2000. Shear-induced anisotropic microstructure in phase-separated biopolymer mixtures. *Food Hydrocolloids*, 14(3), 217-225.

XU,T., SHAW, M.T., WEISS, R.A., 2004. Rheo-optical studies of the effect of shear flow on the structure of elastomer blends. *Journal of Polymer Science Part B: Polymer Physics*, 42, (9), 1725-1738.

YANG, H., LI, B., WANG, K., EN SUN, T., WANG, X., ZHANG, Q., DONG, X., HAN, C.C., 2008. Rheology and phase structure of PP/EPDM/SiO_2 ternary composites. *European Polymer Journal*, 44(1), 113-123.

YARON, I., GAL-OR, B., 1972. On viscous flow and effective viscosity of concentrated suspensions and emulsions. *Rheologica Acta*, 11, 241-252.

YU, W., BOUSMINA, M., GRMELA, M., PALIERNE, J. F., ZHOU, C., 2002. Quantitative relationship between rheology and morphology in emulsions. *Journal of Rheology*, 46(6), 1381-1399.

YU, W., BOUSMINA, M., ZHOU, C., 2006. Note on the morphology determination in emulsions via rheology. *Journal of Non-Newtonian Fluid Mechanics Short Communication*, 133, 57-62.

YUE, P., FENG, J.J., LIU, C., SHEN, J., 2005. Viscoelastic effects on drop deformation in steady shear. *Journal of Fluid Mechanics*, 540, 427-437.

ZEFRA, M., BROOKS, B.W., 1996. Prediction of vinyl chloride drop sizes in stabilised liquid-liquid agitated dispersion. *Chemical Engineering Science*, 51(12), 3223-3233.

ZIEGLER, V., WOLF, B. A., 1999 Viscosity and morphology of the two-phase system PDMS/P(DMS-ran-MPS). *Journal of Rheology*, 43(4), 1033-1045.

APPENDIX 1

PROVISIONAL PATENT

PTO/SB/16 (10-07)
Approved for use through 06/30/2010. OMB 0651-0032
U.S. Patent and Trademark Office; U.S. DEPARTMENT OF COMMERCE
Under the Paperwork Reduction Act of 1995, no persons are required to respond to a collection of information unless it displays a valid OMB control number.

PROVISIONAL APPLICATION FOR PATENT COVER SHEET – Page 1 of 2

This is a request for filing a PROVISIONAL APPLICATION FOR PATENT under 37 CFR 1.53(c).

Express Mail Label No. _____

INVENTOR(S)		
Given Name (first and middle [if any])	Family Name or Surname	Residence (City and either State or Foreign Country)
Samiul	Amin	Solihull, UK
Andrzej	Pacek	UK
Ourania	Gouseti	UK

Additional inventors are being named on the ____none____ *separately numbered sheets attached hereto*

TITLE OF THE INVENTION (500 characters max):

HIGH SHEAR RHEO-OPTICS OF COMPLEX FLUIDS

Direct all correspondence to: **CORRESPONDENCE ADDRESS**

☑ The address corresponding to Customer Number: [redacted]

OR

☐ Firm or Individual Name [redacted]

Address [redacted]

City [redacted]	State MA	Zip [redacted]
Country US	Telephone [redacted]	Email [redacted]

ENCLOSED APPLICATION PARTS *(check all that apply)*

☐ Application Data Sheet. See 37 CFR 1.76

☑ Drawing(s) *Number of Sheets* 12

☑ Specification (e.g. description of the invention) *Number of Pages* 7 + 3

☐ CD(s), Number of CDs [redacted]

☐ Other (specify) _____

Fees Due: Filing Fee of $210 ($105 for small entity). If the specification and drawings exceed 100 sheets of paper, an application size fee is also due, which is $260 ($130 for small entity) for each additional 50 sheets or fraction thereof. See 35 U.S.C. 41(a)(1)(G) and 37 CFR 1.16(s).

METHOD OF PAYMENT OF THE FILING FEE AND APPLICATION SIZE FEE FOR THIS PROVISIONAL APPLICATION FOR PATENT

☐ Applicant claims small entity status. See 37 CFR 1.27.

☐ A check or money order is enclosed to cover the filing fee and application size fee (if applicable).

☐ Payment by credit card. Form PTO-2038 is attached

☐ The Director is hereby authorized to charge the filing fee and application size fee (if applicable) or credit any overpayment to Deposit Account Number: _____. A duplicative copy of this form is enclosed for fee processing.

[redacted]

TOTAL FEE AMOUNT ($)

USE ONLY FOR FILING A PROVISIONAL APPLICATION FOR PATENT

This collection of information is required by 37 CFR 1.51. The information is required to obtain or retain a benefit by the public which is to file (and by the USPTO to process) an application. Confidentiality is governed by 35 U.S.C. 122 and 37 CFR 1.11 and 1.14. This collection is estimated to take 8 hours to complete, including gathering, preparing, and submitting the completed application form to the USPTO. Time will vary depending upon the individual case. Any comments on the amount of time you require to complete this form and/or suggestions for reducing this burden, should be sent to the Chief Information Officer, U.S. Patent and Trademark Office, U.S. Department of Commerce, P.O. Box 1450, Alexandria, VA 22313-1450. DO NOT SEND FEES OR COMPLETED FORMS TO THIS ADDRESS. **SEND TO: Commissioner for Patents, P.O. Box 1450, Alexandria, VA 22313-1450.**

If you need assistance in completing the form, call 1-800-PTO-9199 and select option 2.

PROVISIONAL APPLICATION COVER SHEET
Page 2 of 2

PTO/SB/16 (10-07)
Approved for use through 06/30/2010. OMB 0651-0032
U.S. Patent and Trademark Office; U.S. DEPARTMENT OF COMMERCE

The invention was made by an agency of the United States Government or under a contract with an agency of the United States Government.

☐ No.
☐ Yes, the name of the U.S. Government agency and the Government contract number are: _____

WARNING:

Petitioner/applicant is cautioned to avoid submitting personal information in documents filed in a patent application that may contribute to identity theft. Personal information such as social security numbers, bank account numbers, or credit card numbers (other than a check or credit card authorization form PTO-2038 submitted for payment purposes) is never required by the USPTO to support a petition or an application. If this type of personal information is included in documents submitted to the USPTO, petitioners/applicants should consider redacting such personal information from the documents before submitting them to the USPTO. Petitioner/applicant is advised that the record of a patent application is available to the public after publication of the application (unless a non-publication request in compliance with 37 CFR 1.213(a) is made in the application) or issuance of a patent. Furthermore, the record from an abandoned application may also be available to the public if the application is referenced in a published application or an issued patent (see 37 CFR 1.14). Checks and credit card authorization forms PTO-2038 submitted for payment purposes are not retained in the application file and therefore are not publicly available.

SIGNATURE _____ Date February 14, 2011

TYPED or PRINTED NAME Kristofer E. Elbing REGISTRATION NO. 34,590 *(if appropriate)*

TELEPHONE [redacted] Docket Number: M0005-066001

HIGH SHEAR RHEO-OPTICS OF COMPLEX FLUIDS

Field of the Invention

This invention relates to rheometers and to the application of rheology.

Background of the Invention

Many commercial products ranging from body lotions to ice cream, mayonnaise and shaving creams can all be classed as a specific class of complex fluid known as an emulsion, i.e. the stable dispersions of one liquid in another. Based on whether the oil is the dispersed phase or the water is the dispersed phase, emulsions can be classified as either oil-in-water or water-in-oil emulsions. For both types of emulsions, the droplet size, volume fraction, and morphology can play a critical role in the rheological response of the fluid. On application of shear, the droplet deformability and breakup are important factors controlling the non-linear rheological (i.e. shear thinning) response of such fluids. Since many processing/manufacturing steps, such as high shear mixing, pumping as well as many consumer applications, such as rubbing a body lotion involve high shear processes, engineering/controlling the high shear non-linear rheological response becomes very important. The droplet deformability and breakup and the shear rates at which these may occur will to a large extent depend upon the nature of the continuous phase, with continuous phase viscoelasticity playing an important role. It is known to use rheometers with built-in cameras to observe morphology of fluids during the application of shear.

Summary of the Invention

Several aspects of the invention are presented in this application.

Systems according to the invention can help to develop effective formulation design rules by allowing the interaction between the rheology and morphology to be understood, especially at higher shear rates relevant to industrial processing.

Systems according to one general aspect provide devices and associated methodology to obtain simultaneous rheological and morphological data of multiphase systems at high shear rates is described. Many complex fluids, especially emulsions ,

undergo drastic morphological changes on application of shear. This change in the morphology is intimately linked to the rheology of the fluid, thereby impacting critical aspects such as the processability and manufacturing of such fluids. The exact morphology and droplet sizes due to breakup under shear can also directly impact the performance controlling aspects of such complex fluids. A direct quantitative link between the shear induced morphological changes and the associated rheological responses can be very important for deriving formulation design/optimization rules. The devices and associated methodology described here can allow such rheology-morphology linkages to be established even at very high shear rates (approaching 10,000 s-1) not seen in any prior art.

Systems according to the invention can help to establish morphology-rheology links in complex fluids, such as emulsions, by providing the capability of capturing high quality images of the complex fluid whilst the rheological testing is being carried out. This task poses challenges at higher shear rates (i.e shear rates above 100 S-1).

Brief Description of the Drawing

Fig. 1 is a diagram of an illustrative embodiment of a rheology setup according to the invention, with the following reference labels: (1) PC; (2) strobe flash; (3) synchronising trigger; (4) strobe light directed to geometry; (5) rheometer; (6) measuring geometry ; (7) microscope; (8) CCD high resolution camera.

Fig. 2 is a diagram of a compact version of the test rig of Fig. 1 where the microscope was replaced with a magnifying tube and a small camera was installed.

Figs. 3(a)-3(g) are diagrams of geometries for use with the setup of Figs. 1 and 2, with (a) being a top view of parallel plates and cone/plate (for PP40, PP60 and CP55/2 respectively: α=43mm, 63mm, 58mm and β=11mm, 14mm, 13mm); (b) and (c) being side views of main bodies of cone and top plates (d=40mm and 60mm for PP40 and PP60 respectively); (d) and (e) side being views of cone and top plates respectively; (f) being a top view of CC's main bodies; and (g) being a side view of CC.

Figs. 4(a) and 4(a') are photographs of novel geometries for use with the setup of Figs. 1-2 and Figs. 4(b) and 4(b') are photographs of the setup of Figs. 1-2.

Fig. 5 is a family of graphs showing a series of simultaneous rheo-optical recordings obtained for O/W system.

Fig. 6a is a plot for simultaneous rheo-optical recordings obtained for an aqueous two phase system.

Fig. 6b is a collection of rheo-optical recordings showing effects of shear rate on gelling structure.

Fig. 7 shows clear images taken at high shears.

Fig. 8 shows a W/O/W double emulsion at rest.

Fig. 9 shows water drops in 10000cSt silicone oil (a) at rest; (b) and (c) at 10s-1. Images were captured with Marlin utilising 20mm magnifying tube.

Fig. 10 shows air bubbles in 10000cSt silicone oil (a) at rest; (b) at 10s-1; (c) retracting drop after cessation of flow. Images were captured with Dolphin utilizing 20mm magnifying tube.

Detailed Description of an Illustrative Embodiment

Referring to Fig. 1, an illustrative embodiment of a rheology setup according to the invention combines a standard rotational rheometer with novel optical measuring geometries, stroboscopic lighting system, microscope, camera and software for recordings and data analysis. Rheological and structural data is recorded simultaneously. Particular attention is given in attaining high quality images at different shear stress and in different two phase systems by optimising image acquisition conditions.

New geometries were designed and constructed for the Gemini G2 rheometer of Malvern Instruments and are discussed below. The lighting system consists of a strobe light source (Perkin Elmer Inc. xenon strobe flash system supplied by Metax) placed opposite the objective lens and an electronic trigger that matches the pulsating frequency of the light with the camera's framing speed. Positioning of the light to flash through the sample and directly into the microscope/camera lens considerably enhances image clarity. Magnification of zoom stereo microscope (SZ1145TR-CTV supplied by Olympus) can be easily altered during the measurement. Magnification, defined as the number of microns per pixel, is currently in the range 7.79-1.33μm/pixels. Three geometries were tested: parallel plates, cone-plate and concentric cylinders.

Images are recorded with a CCD high resolution Dolphin F145B firewire black/white camera (supplied by Allied Vision Technologies, AVT) connected to the microscope, using the AVT software. Rheological data is obtained using Bohlin software. Sharp images of discrete droplets in dilute systems are analysed automatically with Morphologi (supplied by Malvern Instruments). The semi-automated, Bubble Pro software developed in School of Chem Eng has been employed for analysis of more complex images. One of ordinary skill would of course recognize that embodiments could also be based on other types of components.

Referring to Fig. 2, a compact version of the equipment was also constructed, where the microscope and relatively large CCD camera (see above) were replaced by a 20mm long magnifying tube combined with smaller Marlin camera (Allied Vision Technologies) is shown in Fig 2. Both the optics as well as camera can be optimised further.

Referring to Fig. 3, newly designed geometries used with the setups are identical to standard geometries commonly used in rheological measurements but they are partially made from glass are shown in figure 3. Two parallel plates PP40 and PP60 (diameters 40mm and 60mm respectively), a cone / plate CP55/2 (55mm base diameter, 2o angle, 0.7mm truncation (i.e. 4mm small base)) and coaxial cylinders with narrow gap, CC (1mm annular gap, inner to outer ratio 0.97) were constructed and tested. The main parts (exposed to shear stress) are made from polished glass to ensure good transparency. Frames and shafts that hold the glass fix geometries in the rheometer are made of stainless steel and provide robustness without compromising transparency. Glass parts are precisely fitted into frames so the accuracy of rheological measurements is not affected and it was tested with geometries supplied by manufacturers.

Features of the setup include:

1. Geometries: B-ham geometries for simultaneous measurements of rheology and morphology glass plates/cones/cylinders are combined with appropriate metallic frame ensuring high transparency and structural robustness.

2. Strobe light: Stroboscopic lighting system can be synchronised with (or fed from) video camera to provide very high quality, sharp images on both low and high

shears. This direct synchronization is presently preferred, although other methods can be provided to allow for the capture of very high quality, sharp images.

3. Magnification: Two features are provided in current setting with the microscope: (i) ability to rapidly adjust magnification according to the characteristic dimension of analysed morphology, the response of morphology to the change of shear rate can be followed in real time. This feature can be automated using a computer running dedicated software and/or special-purpose hardware. (ii) Magnification is defined in terms of the size of the pixel (μm/pixel).

4. Setup: Enhanced quality images can be obtained through utilising an optical geometry in conjunction with the microscope/camera/light setting illustrated in figure 1. Positioning the strobe light opposite the analysed object/ lens of microscope/camera provides optimal lighting conditions.

High quality images obtained under different, often difficult, experimental conditions are shown in Figs. 5-10.

Simultaneous high shear rheo-optics.

O/W emulsions recorded at an increasing-decreasing triangle shear profile are shown in Fig. 5, with:

Continuous phase: 68% hexylene glycol + 32% water

Dispersed phase: 350cSt silicone oil

Aqueous two-phase system

Morphology of aqueous two-phase systems can be difficult to analyse because refractive indices of both phases are very similar. Results obtained with the system described above are shown in Fig. 6, with:

Continuous phase: 10% gelatine in water

Dispersed phase: 15% dextran in water

Images at increasing shears and very high shears

Clear images at very high shears were obtained using the method described above as illustrated in Fig. 7.

Double emulsions

The system described above enables complex structures to be recorded and analysed. Fig. 8 shows complex emulsion with drops within drops.

Compact version

Clear images were obtained using the compact setup with the two cameras and are depicted in Figs. 9 and 10.

Advantages and applications of systems and methods according to the invention can include:

- Simultaneous measurement of shear induced morphological changes in complex fluids and associated rheological response.
- Ability to extend simultaneous rheology and morphology measurement capabilities to very high shear rates, whilst maintaining clarity of images.
- Possibility of automated morphology analysis

Specific Application Areas are:

- Understanding rheological phenomena in complex shear thinning/thickening fluids including analysis of relaxation dynamics and other linear and non-linear rheological effects.
- Following aggregation and flocculation under shear.
- Following droplet breakup/coalescence and deformation (see Figure above)
- Following shear induced directional changes in morphology of complex fluid
- Generate design rules and optimise complex fluid formulations across a wide range of industries such as: personal care, home care, foods, pharmaceutical and life sciences.
- Wide scale applicability in academic research not only to liquid/liquid but also to more complex multiphase systems such as: liquid/liquid/gas or liquid/gas/solid.

The present invention has now been described in connection with a number of specific embodiments thereof. However, numerous modifications which are contemplated as falling within the scope of the present invention should now be apparent

to those skilled in the art. Therefore, it is intended that the scope of the present invention be limited only by the scope of the claims appended hereto. In addition, the order of presentation of the claims should not be construed to limit the scope of any particular term in the claims.

What is claimed is:

CLAIMS

1. A rheometer, comprising:

a rotary actuator,

a first sample contact part having a contact surface for contacting the sample, having a drive portion operatively connected to the rotary actuator,

a second sample contact part having a contact surface for contacting the sample,

wherein at least a portion of at least one of the first sample contact part and the second sample contact part is transparent,

a camera having a field of view and being positioned with the field of view extending over at least a portion of the transparent portion of the first sample contact part,

a strobe light positioned to illuminate the sample under the transparent portion of the first sample contact part, and

a synchronization control for adjusting an illumination rate of the strobe light.

2. The apparatus of claim 1 wherein the synchronization control is linked to an acquisition rate of the camera.

3. The apparatus of claim 1 wherein the acquisition rate of the camera is linked to a rheological characteristic.

4. The apparatus of claim 1 wherein the acquisition rate of the camera is linked to a predetermined points in a rheometric sequence.

5. The apparatus of claim 1 wherein the strobe light is positioned opposite the camera with respect to an axis of rotation of the rotary actuator.

6. The apparatus of claim 1 wherein the camera is a CCD camera.

7. The apparatus of claim 1 wherein the camera includes a front-end optic with a single lens to define its field of view.

8. The apparatus of claim 1 wherein the camera includes a front-end optic with an adjustable magnification.

9. The apparatus of claim 8 further including an automatic magnification adjustment controller responsive to morphological characteristics of the sample as detected by the camera and having an output provided to a magnification input of the camera.

10. The apparatus of claim 8 further including an automatic magnification adjustment controller having a pixel-based magnification selection input and having an output provided to a magnification input of the camera.

11. The apparatus of claim 1 wherein the camera includes a front-end optic that includes a magnifying tube.

12. The apparatus of claim 1 wherein a geometry defined by the first sample contact part and the second sample contact part is an optically clear parallel plate geometry.

13. The apparatus of claim 1 wherein a geometry defined by the first sample contact part and the second sample contact part is an optically clear cone and plate geometry.

14. The apparatus of claim 1 wherein a geometry defined by the first sample contact part and the second sample contact part is an optically clear couette geometry.

15. A rheometric method, comprising:

applying shear to a sample,

acquiring images of at least a portion of the sample during the step of applying shear to the sample, and

intermittently illuminating the sample during the steps of applying shear and acquiring images at a rate related to a rate of acquisition for the step of acquiring images.

16. The apparatus of claim 15 wherein the shear is applied to the sample at a rate of rotation of at least on the order of 100 reciprocal seconds.

17. The apparatus of claim 15 wherein the shear is applied to the sample at a rate of rotation of at least on the order of 1000 reciprocal seconds.

18. The apparatus of claim 15 wherein the shear is applied to the sample at a rate of rotation of at least on the order of 10,000 reciprocal seconds.

19. The apparatus of claim 15 further including the step of adjusting the rate of application of shear during the step of acquiring images.

20. The apparatus of claim 15 further including the step of adjusting a magnification setting for the step of acquiring images.

21. The apparatus of claim 20 wherein the step of adjusting a magnification is responsive to changes in morphology within the sample.

22. The apparatus of claim 21 wherein the step of adjusting is automatic.

23. The apparatus of claim 15 wherein the steps of applying shear, intermittently illuminating, and acquiring images are applied to a complex fluid.

24. The apparatus of claim 23 wherein the steps of applying shear, intermittently illuminating, and acquiring images are applied to an emulsion.

10

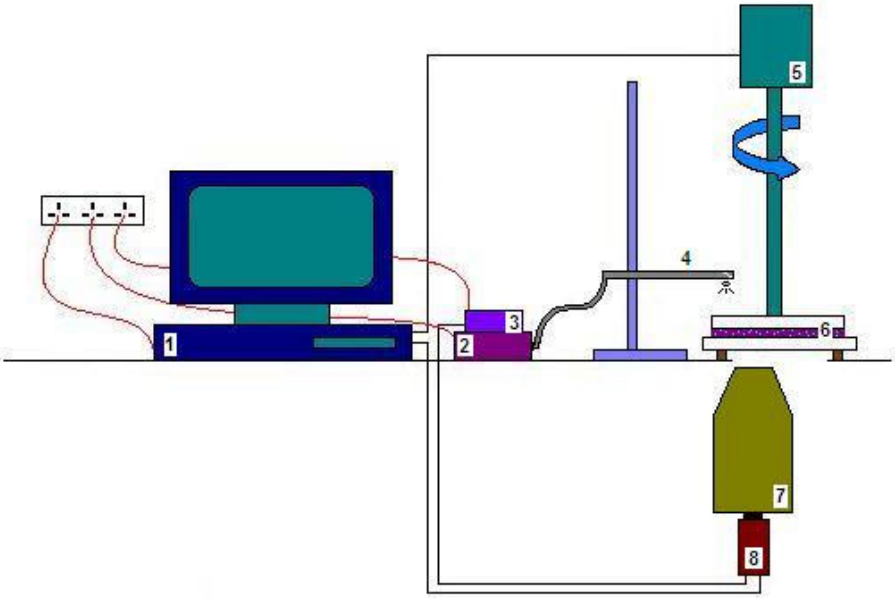

FIG. 1

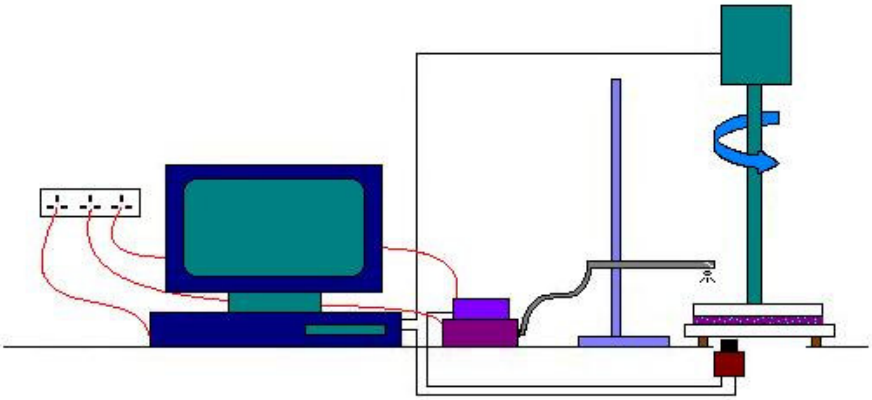

FIG. 2

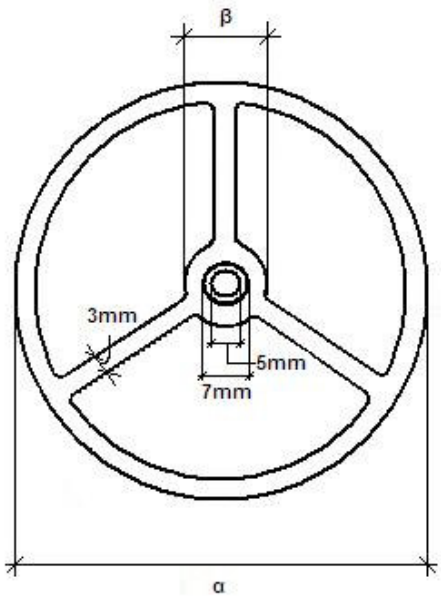

FIG. 3(a)

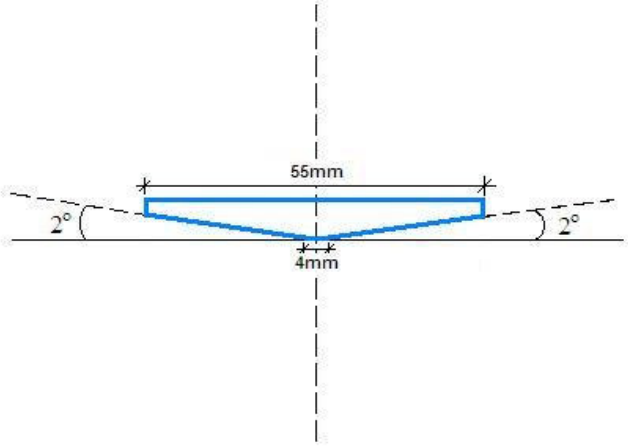

FIG. 3(b)

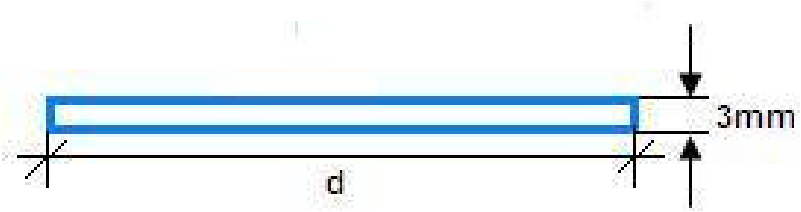

FIG. 3(c)

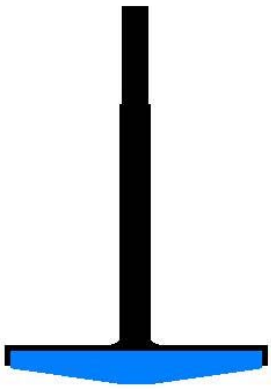

FIG. 3(d)

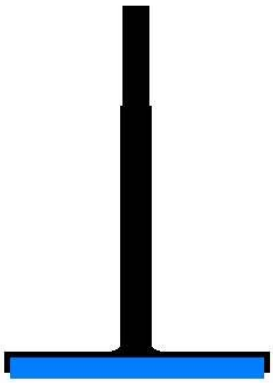

FIG. 3(e)

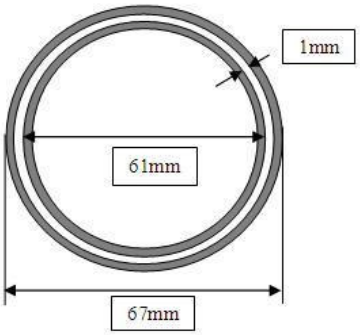

FIG. 3(f)

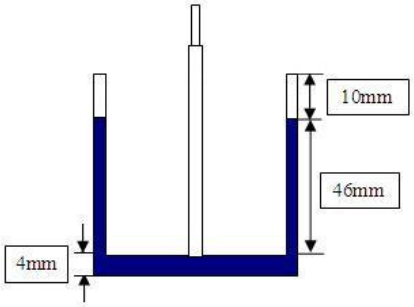

FIG. 3(g)

FIG. 4(a)

FIG. 4(a')

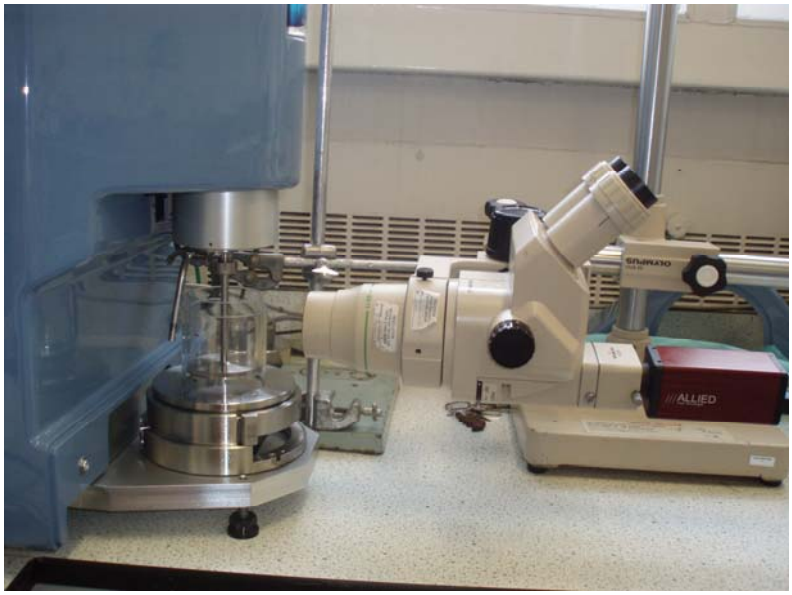

FIG. 4(b)

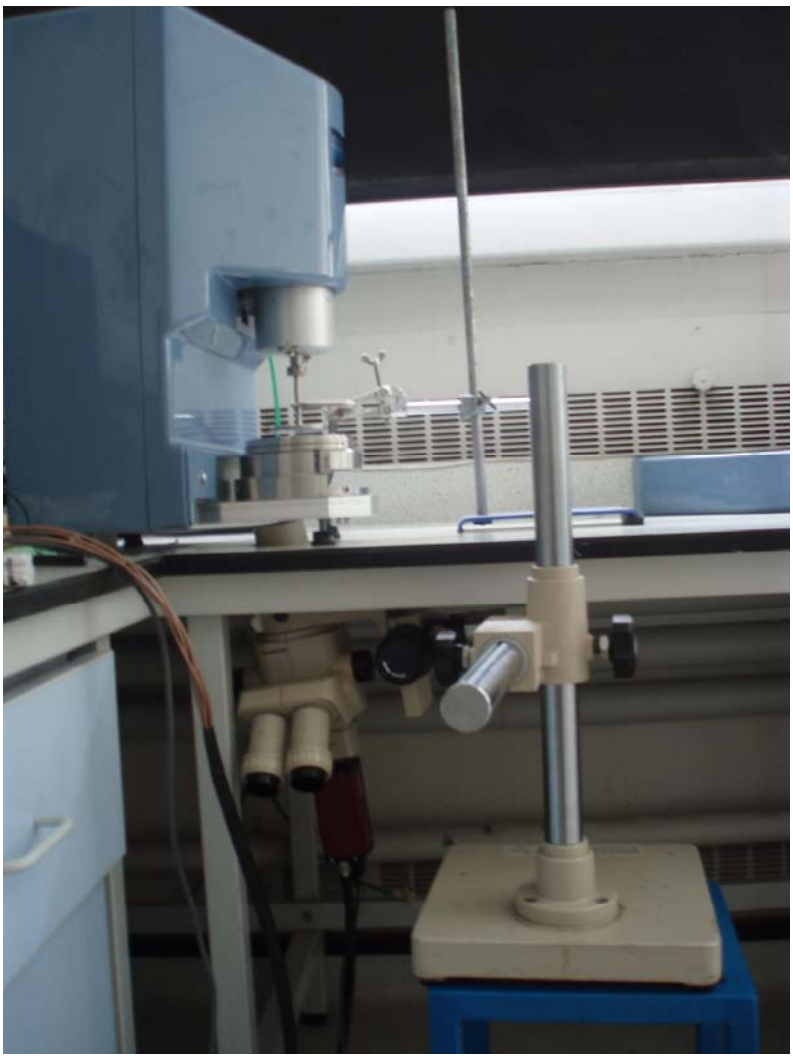

FIG. 4(b')

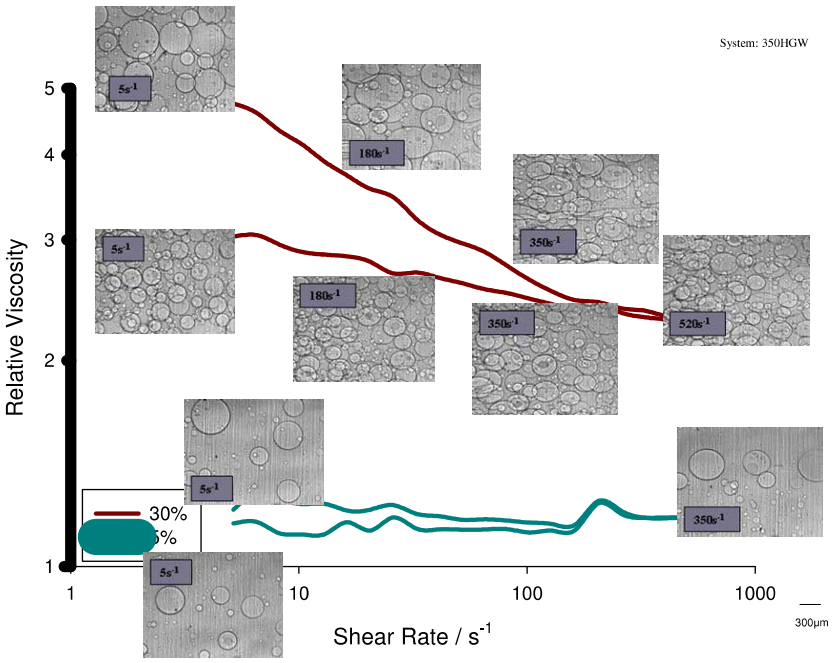
System: 350HGW
Relative Viscosity
5
4
3
2
1
1
10
100
1000
Shear Rate / s-1
5s-1
180s-1
350s-1
520s-1
30%
300µm

FIG. 5

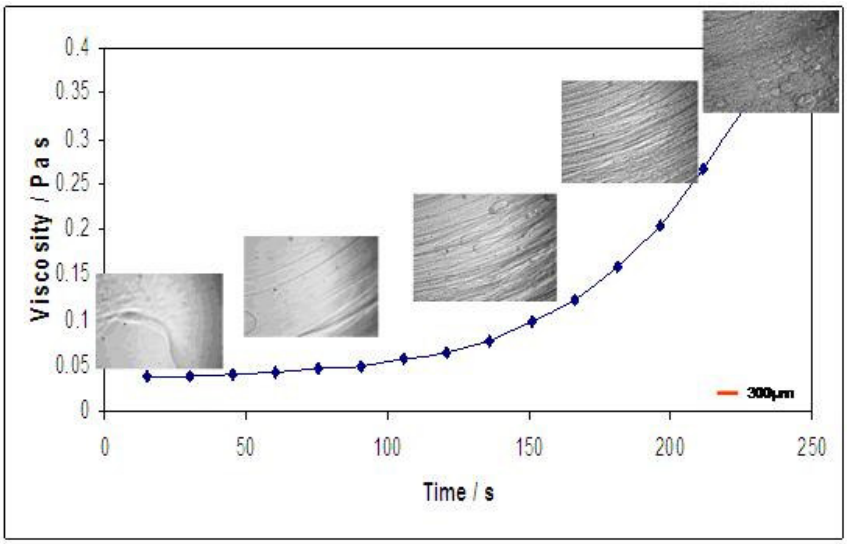
Viscosity / Pa s
0.4
0.35
0.3
0.25
0.2
0.15
0.1
0.05
0
0
50
100
150
200
250
Time / s
300µm

FIG. 6(a)

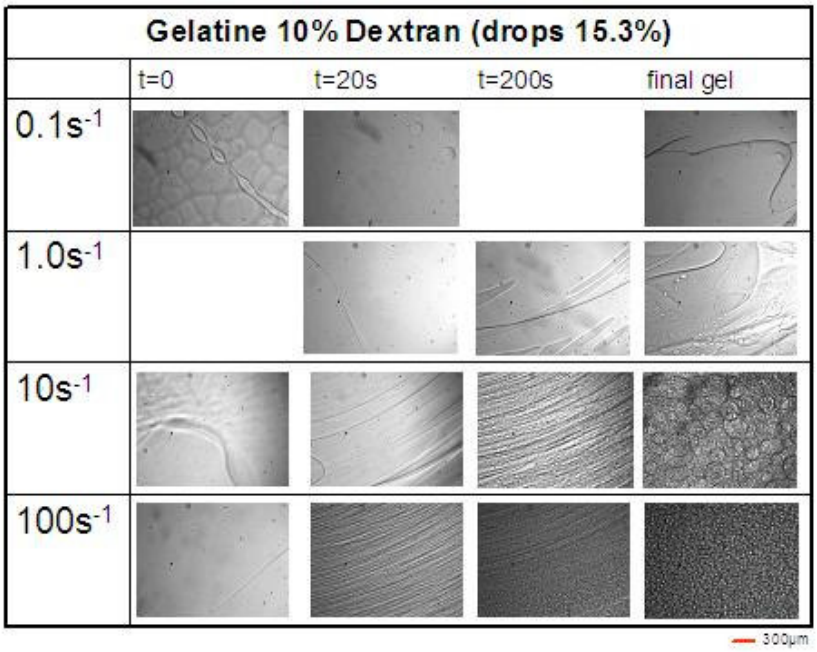
Gelatine 10% Dextran (drops 15.3%)
t=0
t=20s
t=200s
final gel
0.1s-1
1.0s-1
10s-1
100s-1
300µm

FIG. 6(b)

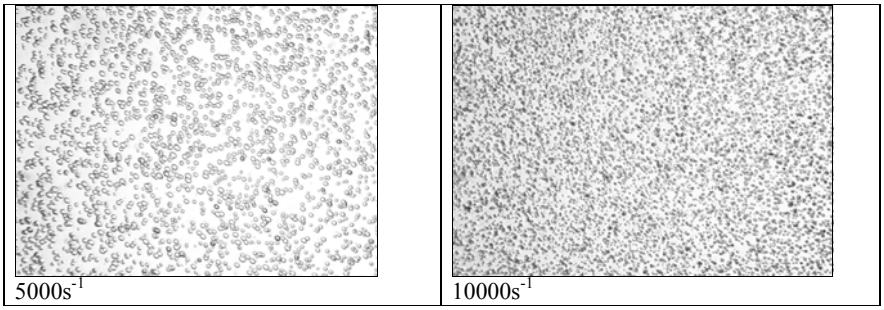
5000s-1
10000s-1

FIG. 7

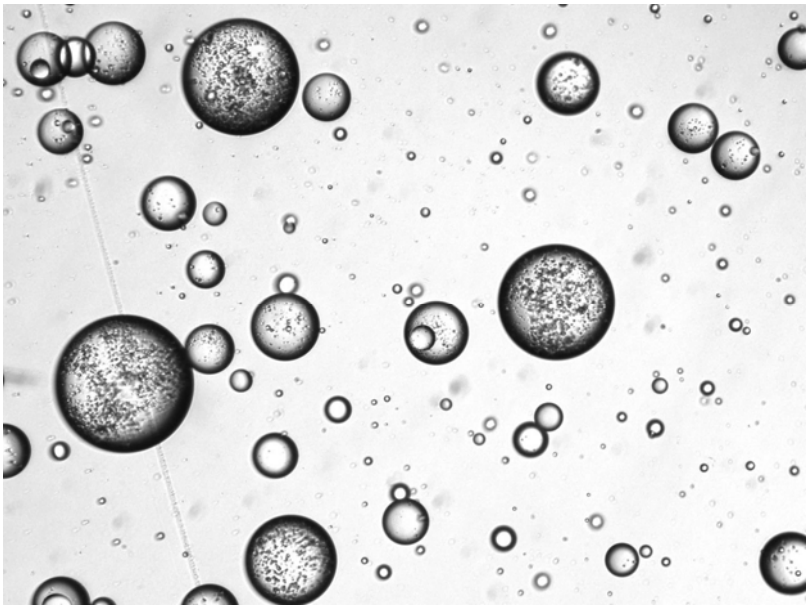

FIG. 8

FIG. 9

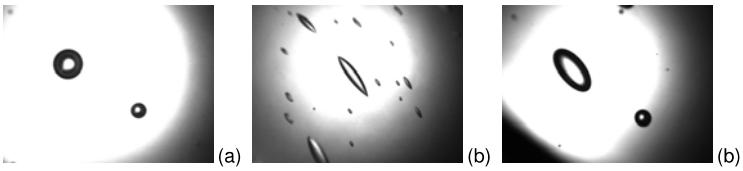

FIG. 10

APPENDIX 2

PHOTO GALLERY

PHOTO GALLERY

Figure A.1: The following images show a gelled dextran/gelatin system exposed to shear after gelation has occurred. They demonstrate destruction of the structured system (from (a) to (j) in time order)

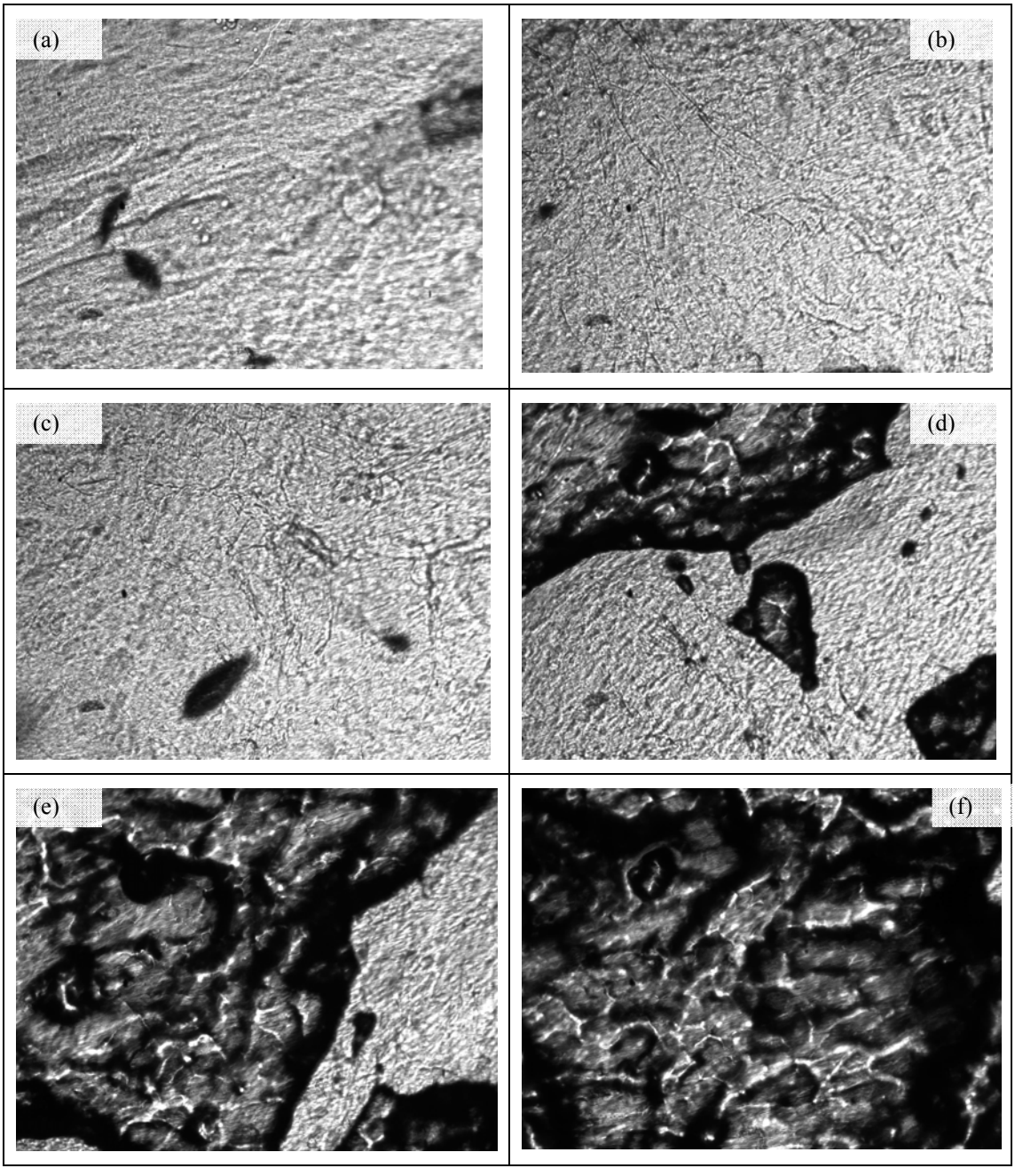

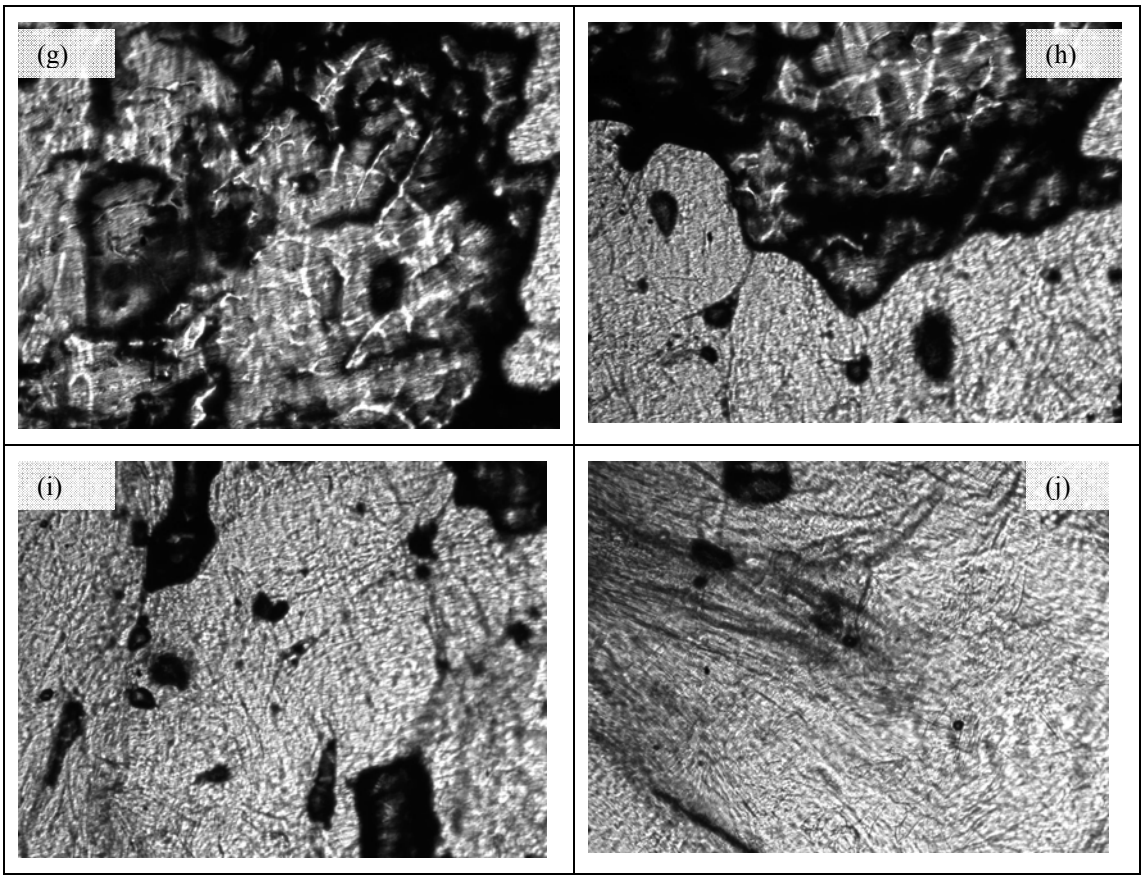

Figure A.2: Kinetically stable microstructure of oil drops capured in a gelatin gel.

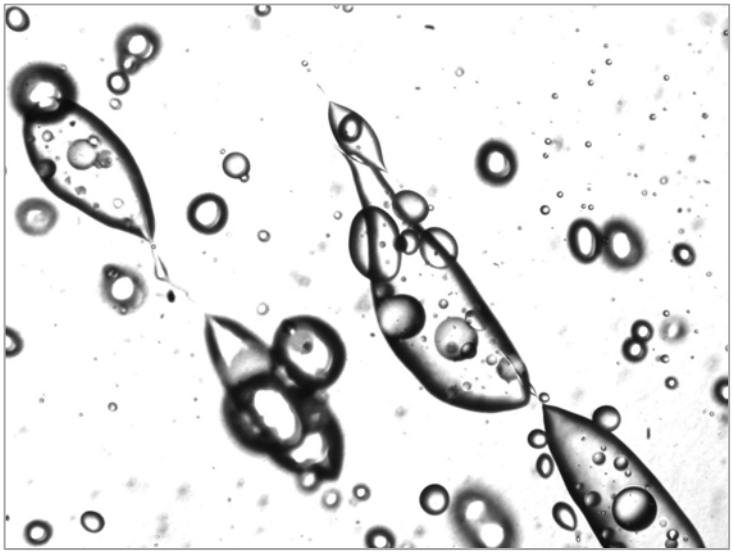

Figure A.3: Elongated air bubbles in silicone oil under shear.

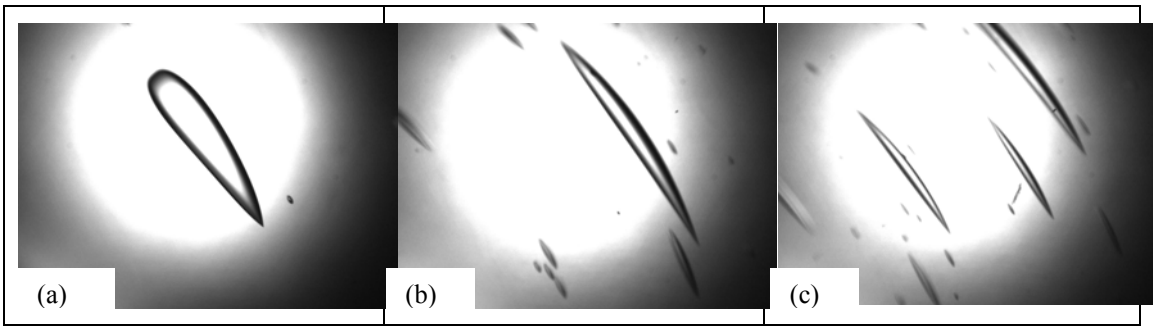

Figure A.4: Oil/Aqueous system (20cSt silicone oil in hexylene glycol / glycerol mixture), volume fraction of oil is 0.3. System is subjected to shear rate 250s^{-1}. Images (a) and (b) captured few seconds and 10min after initiation of shearing, respectively.

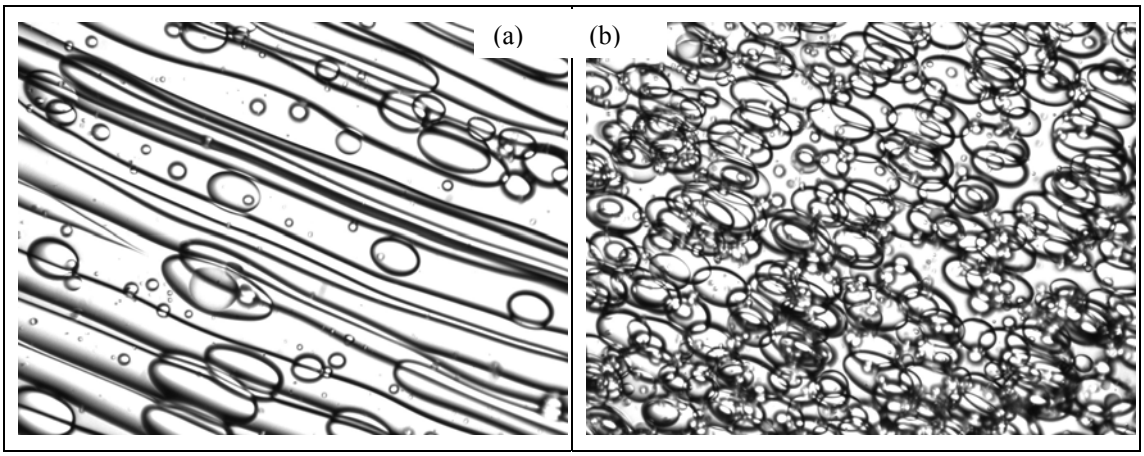

Figure A.5: Oil/Aqueous system, volume fraction of the oil is 0.3. Shows drops deviating from the elliptical shape due to interactions between crowded drops.

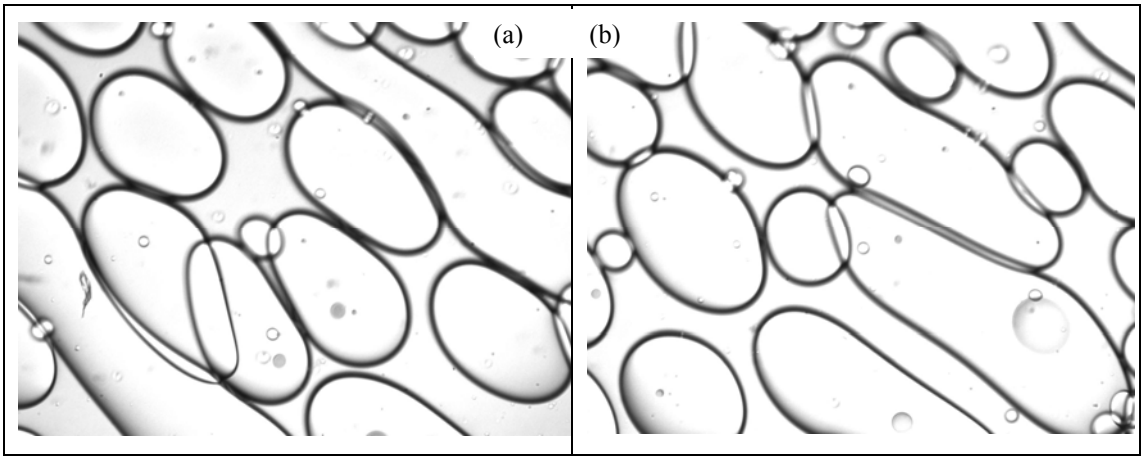

Figure A.6: oil drops exposed to increasing shear rate (from (a) to (d)).

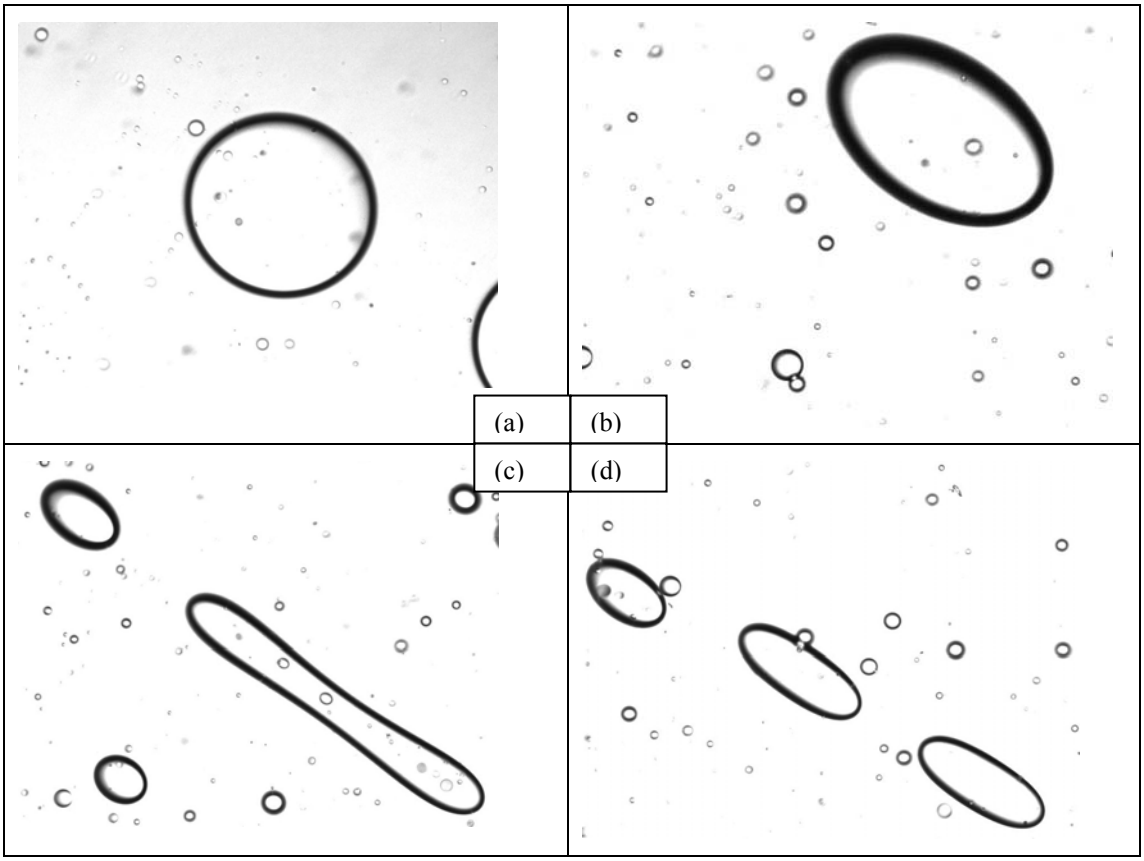

Figure A.7: Examples of isolated oil drops in aqueous phases.

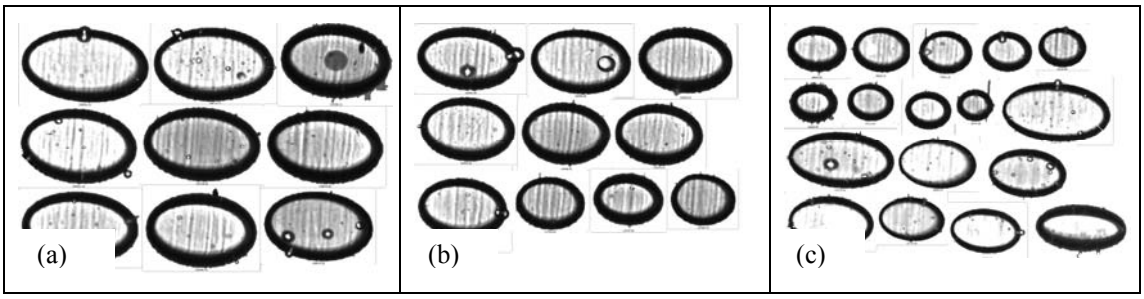

Figure A.8: pendant oil drop in hexylene glycol as it detaches from the edge of the syringe. Such images can be used to measure the interfacial tension between the two phases.

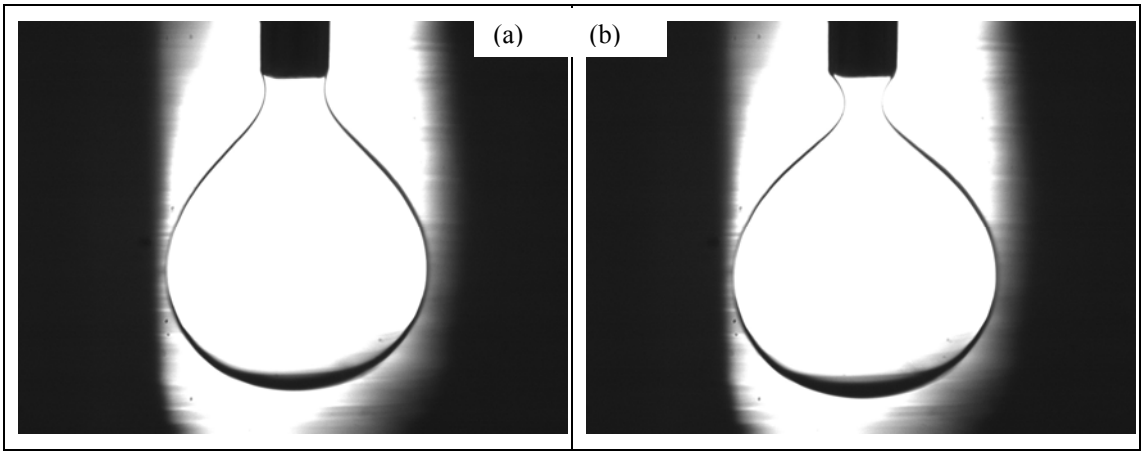

Figure A.9: Drop coalescing in dextran / peg system (time intervals: (1/5)s except from (i) to (j), where it is 1s).

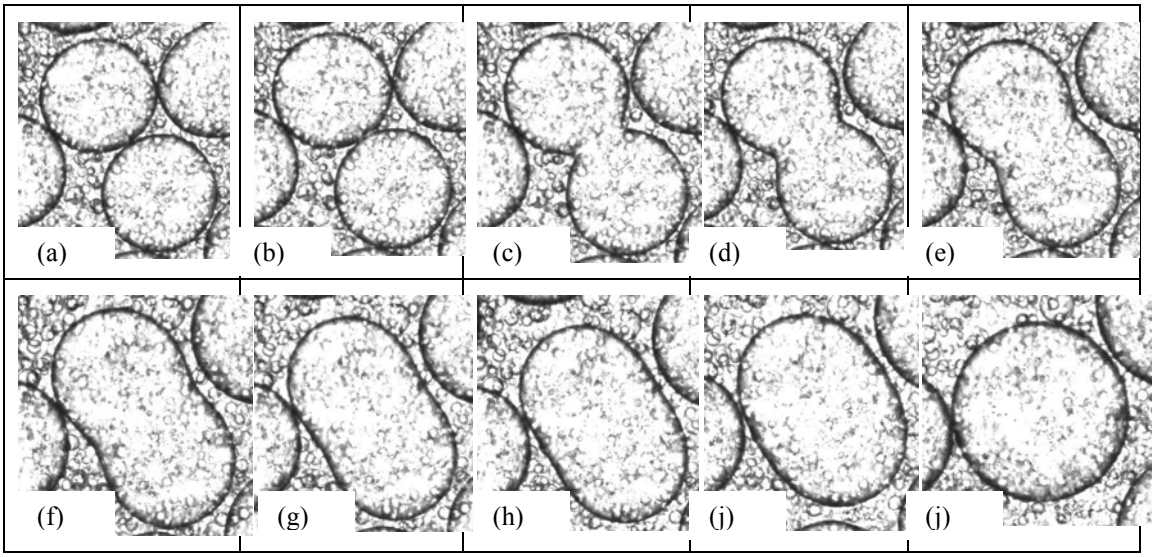

Figure A.10: dumbbell breakage of oil drop in aqueous continuous phase